
Multi-frequency Study on Markarian 421 during the First Two Years of Operation of the MAGIC Stereo Telescopes

Shang-yu Sun



München 2014

Multi-frequency Study on Markarian 421 during the First Two Years of Operation of the MAGIC Stereo Telescopes

Shang-yu Sun

Dissertation
an der Fakultät für Physik
der Ludwig–Maximilians–Universität
München

vorgelegt von
Shang-yu Sun
aus Kaohsiung, Taiwan

München, den 22.09.2014

Erstgutachter: Prof. Dr. Christian Kiesling
Zweitgutachter: Prof. Dr. Masahiro Teshima
Tag der mündlichen Prüfung: 22.09.2014

Abstract

Markarian 421 (Mrk 421) is one of the classical blazars at X-ray and very high energies (VHE; >100 GeV). Its spectral energy distribution (SED) can be accurately characterized by current instruments because of its close proximity, which makes Mrk 421 one of the best sources to study the nature of blazars. The goal of this PhD thesis is to better understand the mechanisms responsible for the broadband emission and the temporal evolution of Mrk 421. The results might be applied to other blazars which cannot be studied with this level of detail because their emissions are weaker, or they are located further away. This thesis reports results from ~ 70 hours of observations with MAGIC in 2010 and 2011 (the first two years of the operation of the MAGIC stereo telescopes), as well as the results from the multi-wavelength (MW) observation campaigns in 2010 and 2011, where more than 20 instruments participated, covering energies from radio to VHE.

The MW data from the 2010 and 2011 campaigns show that, for both years, the fractional variability F_{var} increases with the energy for both the low-energy and the high-energy bumps in the SED of Mrk 421. Furthermore, $F_{\text{var}}(\text{optical})$ was similar to $F_{\text{var}}(\text{HE-}\gamma\text{-ray}; >100 \text{ MeV})$, and $F_{\text{var}}(\text{X-ray})$ was similar to $F_{\text{var}}(\text{VHE-}\gamma\text{-ray})$. This observed characteristic is expected from the strong correlation between the synchrotron photons and the up-scattered photons by inverse-Compton effect within the synchrotron self-Compton (SSC) emission model, thus allowing for the first time of the consistency test on this widely used theoretical model.

During the MW campaign in 2010, we measured the decay of a flaring activity during 13 days in March. We could perform MW observations every day, which enables an unprecedented characterization of the time-evolution of the radio to γ -ray emission of Mrk 421. The broadband SEDs during this flaring episode, resolved on timescales of one day, were characterized with two leptonic scenarios: a one-zone SSC model, and a two-zone SSC model where one zone is responsible for the quiescent emission while the other (smaller) zone, which is spatially separated from the former one, contributes to the daily-variable emission occurring mostly at X-rays and VHE γ rays. Both the one-zone SSC and the two-zone SSC models can describe the daily SEDs. However, the two-zone SSC model provides a better agreement to the observed SED at the narrow peaks of the low- and high-energy bumps during the highest activity. The proposed two-zone scenario would naturally lead to the correlated variability in the X-ray and VHE bands without variability in the optical/UV band, as well as to shorter timescales for the variability in the X-ray and VHE bands with respect to the variability in the other bands. This concept of a second small emission region containing a narrow electron spectrum in order to explain the short timescale flaring activity in the X-ray and VHE bands could be generalized to other blazars.

The results from the 2010 March flaring activity of Mrk 421 are reported in Sections 5.3 – 5.5, and they are the main scientific achievement of this PhD thesis. Preliminary results were reported (as an oral contribution) in the 33rd International Cosmic Ray Conference (Rio de Janeiro, July

2013), one of the most prestigious conferences in the field of the VHE astronomy and astroparticle physics in general. The final results (reviewed and approved within the *Fermi*, MAGIC, and VERITAS Collaborations) have been submitted for publication in the *Astronomy and Astrophysics* journal in 2014 June.

During the MW campaign in 2011, Mrk 421 had an atypically high activity in the optical band, together with a very low state in the X-ray/VHE band. Typically, blazar emission models for Mrk 421 focus on the explanation of the variability in the X-ray and γ -ray bands. This data set is suitable for examining emission models and estimate if they can describe the evolution of the whole broadband SEDs including the variabilities in optical, X-ray, and γ -ray bands. We found that the one-zone SSC model can describe the relatively slow variation of the 2011 broadband SEDs. The modeling of these SEDs shows that the main factor dominating the spectral evolution could be the electron energy distribution (EED), instead of the environmental parameters like the blob size and the Doppler factor. To explain the featured high optical state together with the low X-ray/VHE state, several changes were needed in comparison to the typical state from 2009: a harder power-law index in the first segment in the EED, a lower first break in the EED, and a softer power-law index in the second segment in the EED. Besides, these optical high states had synchrotron peak frequencies 10 times lower than the typical state, while their synchrotron peak energy-fluxes were similar to those of the typical state. On the contrary, the 2010 March flaring activity showed that a high peak energy-flux was accompanied by a high peak frequency in comparison to the typical state, which has also been observed on several other blazars. This contrast showed that the broadband variability in the emission of Mrk 421 during 2011 had a different *flavor* with respect to the typical blazar broadband flaring activity.

This PhD thesis shows that most variations in the SED of Mrk 421 can be produced through changes in the EED, which could shed light into how particles get accelerated in the vicinity of super-massive black holes, or within the relativistic jets of the active galactic nuclei. However, the results also show a large complexity in the evolution of the broadband (radio to VHE γ -rays) SED. Thus longer and deeper observations are needed to understand what characteristics get repeated over time and hence typical, what characteristics are atypical, and ultimately, whether the lessons learned with Mrk 421 can be extended to high-synchrotron-peaked blazars in general.

Kurzfassung

Markarian 421 (Mrk 421) einer der klassischen Blazare in Röntgen- und hochenergetischen Gammastrahlen (VHE; >100 GeV). Seine spektrale Energieverteilung (SED) kann mit den aktuellen Instrumenten aufgrund seiner Nähe sehr genau untersucht werden, was Mrk 421 zu einem exzellenten Kandidaten für die Untersuchung von Blazaren macht. Das Ziel dieser Doktorarbeit ist ein besseres Verständnis der Mechanismen, die für die Breitband Emission und zeitliche Entwicklung von Mrk 421 verantwortlich sind. Die Ergebnisse können anschließend auch auf andere Blazare übertragen werden, die jedoch nicht mit dieser Genauigkeit untersucht werden können, sei es weil die Emission zu schwach ist oder das Objekt zu weit entfernt ist. Diese Arbeit umfasst die Ergebnisse von 70 Beobachtungsstunden mit MAGIC in den Jahren 2010 und 2011 (den ersten zwei Jahren von MAGIC im Stereo-Betrieb), ebenso wie die Ergebnisse von Multi-Wellenlängen (MW) Beobachtungen (auch Kampagnen genannt) in 2010 und 2011, an denen mehr als 20 Experimente teilgenommen haben und die den Energiebereich von Radio bis zu VHE abdeckten.

Die MW Daten von Kampagnen in 2010 und 2011 zeigen für beide Jahre einen Anstieg der anteiligen Variabilität F_{var} mit der Energie jeweils für den niederenergetischen und den hochenergetischen Teil der SED von Mrk 421. Des Weiteren zeigten sich jeweils ähnliche Werte für $F_{\text{var}}(\text{optisch})$ und $F_{\text{var}}(\text{HE-}\gamma\text{-ray; } >100 \text{ GeV})$, sowie für $F_{\text{var}}(\text{Röntgen})$ und $F_{\text{var}}(\text{VHE-}\gamma\text{-ray})$. Diese Charakteristik wird aufgrund der starken Korrelation zwischen den Synchrotron-Photonen und den durch den inversen Compton-Effekt beschleunigten Photonen innerhalb des Synchrotron Self-Compton (SSC) Modells erwartet. Daher erlauben die Beobachtungen zum ersten Mal einen Konsistenztest dieses häufig verwendeten Modells.

Während der MW Kampagne 2010, maßen wir im März einen Abfall der Flair-Aktivität über 13 Tage. Wir konnten für jeden Tag MW Beobachtungen durchführen, die eine bislang nicht erreichte Charakterisierung der Zeitentwicklung der Radio bis Gammastrahlungsemission von Mrk 421 erlaubte. Die Breitband SEDs während der Flair-Episode, mit einer Zeitauflösung von einem Tag, wurden mit zwei leptonenischen Modellen beschrieben: Einem Ein-Zonen SSC Modell und einem Zwei-Zonen SSC Modell, bei dem eine Zone für die dauerhafte Emission verantwortlich ist, während die zweite (kleinere und räumlich getrennte) Zone zur zeitlich variablen Emission beiträgt, die hauptsächlich die Röntgen- und VHE Gammastrahlung betrifft. Beide, das Ein-Zonen SSC Modell und das Zwei-Zonen SSC Modell, können die SED der jeweiligen Tage beschreiben. Allerdings zeigt das Zwei-Zonen SSC Modell während der höchsten Aktivität der Quelle eine größere Übereinstimmung mit den beobachteten SEDs im Bereich der schmalen Maxima im nieder- und hochenergetischen Bereich. Das vorgeschlagene Zwei-Zonen Szenario würde automatisch zu einer Korrelation der Variabilität im Röntgen und VHE Band ohne einer Variabilität im Optischen/UV Wellenlängenbereich führen, sowie zu Variabilitäten auf kürzeren Zeitskalen im Röntgen und VHE Band im Vergleich zu den anderen Wellenlängen. Dieses

Konzept einer kleinen Emissionsregion, die nur mit einem schmalbandigen Elektronenspektrum gefüllt wird, um Flair-Aktivitäten auf kurzen Zeitskalen zu erklären, könnte für andere Blazare verallgemeinert werden.

Die Resultate der Flair-Aktivität vom März 2010 von Mrk 421 sind in Abschnitt 5.3-5.4 dargestellt und stellen die hauptsächlich wissenschaftliche Erkenntnis dieser Doktorarbeit dar. Vorläufige Ergebnisse wurden in einem Vortrag auf der 33rd International Cosmic Ray Conference in Rio de Janeiro im Juli 2013 vorgestellt, einer der prestigeträchtigsten Konferenzen auf dem Gebiet der VHE Astronomie und Astrophysik. Die abschließenden Ergebnisse (geprüft und anerkannt innerhalb der Fermi, MAGIC und VERITAS Kollaboration) sind im Juni 2014 erfolgreich für die Publikation im Journal Astronomy and Astrophysics eingereicht worden.

Während der MW Kampagne 2011 zeigte Mrk 421 eine außergewöhnlich hohe Aktivität im optischen Bereich zusammen mit einem ruhigen Zustand im Röntgen/VHE Band. Typischerweise zielen Blazar Emissionsmodelle für Mrk 421 auf eine Erklärung der Variabilität der Röntgen und Gammastrahlungsemission. Dieser Datensatz ist geeignet für eine Untersuchung der Emissionsmodelle und einer Überprüfung, ob sie die Entwicklung der SED im gesamten Wellenlängenbereich einschließlich der Variabilität im optischen, Röntgen und VHE Band beschreiben können. Wir fanden heraus, dass das Ein-Zonen SCC Modell die relativ langsame Veränderung der Breitband-SED von 2011 beschreiben kann. Die Modellierung dieser SEDs zeigt, dass der Hauptfaktor für die spektrale Entwicklung die Elektronen-Energieverteilung (EED) sein könnte, anstatt Umgebungsparameter wie die Größe der Region oder der Wert des Dopplereffektors. Um den gezeigten hohen optischen Zustand zusammen mit dem niedrigen Röntgen/VHE Zustand zu erklären, sind viele Veränderungen im Vergleich zum typischen Zustand von 2009 notwendig: Ein härterer Exponent im ersten Segment der EED, ein niedrigerer, erster Knickpunkt in der EED und ein weicherer Exponent im zweiten Segment der EED. Zudem zeigten die hohen optischen Zustände ein zehnmal niedrigeres Synchrotron Maximum als der typische Zustand, während die Energieflüsse am Synchrotron Maximum ähnlich zum typischen Zustand waren. Im Gegensatz dazu zeigte die Flair-Aktivität im März 2010, dass das hohe Maximum im Energiefluss von einer hohen Frequenz im Bereich des Maximums im Vergleich zum Normalzustand begleitet wurde, der auch für mehrere andere Blazare beobachtet wurde. Dieser Gegensatz zeigt, dass die Breitband Variabilität in der Emission von Mrk 421 2011 von einer anderen Art war als die Breitband Flair-Aktivitäten von typischen Blazaren.

Diese Doktorarbeit zeigt, dass der Großteil der Veränderung in der SED von Mrk 421 durch Veränderungen in der EED erzeugt werden kann, was Aufschluss darüber geben kann wie Teilchen in der Nähe eines supermassiven schwarzen Loches oder in relativistischen Jets von Aktiven Galaktischen Kernen beschleunigt werden. Dennoch zeigen meine Ergebnisse auch die große Komplexität in der Entwicklung der SED über viele Wellenlängen (Radio bis VHE Gammastrahlung). Mit längeren und tieferen Beobachtungen können wir verstehen welche der gefundenen Charakteristika sich zeitlich wiederholen oder eventuell atypisch sind und schließlich überprüfen, ob diese Erkenntnisse über Mrk 421 auf andere high-synchrotron-peaked Blazare verallgemeinert werden können.

List of Acronyms, Abbreviations, and Modified Julian Day Conversion

AGASA	Akeno Giant Air Shower Array
AGILE	Astro-rivelatore Gamma a Immagini Leggero (γ -ray satellite)
AGN	Active Galactic Nuclei
AMC	Active Mirror Control
ARA	Askaryan Radio Array (neutrino experiment)
ARGO	Astrophysical Radiation with Ground-based Observatory at YangBaJing (γ -ray experiment)
AUGER	Pierre Auger Cosmic Ray Observatory
BH	Black Holes
BL Lac	BL Lacertae object
CCD	Charge-Coupled Device
CMB	Cosmic Microwave Background
COG	Center Of Gravity
CR	Cosmic Ray
c.u.	Crab Units; the VHE flux of the Crab Nebula, integrated above 200 GeV, is $2.2 \times 10^{-10} \text{ cm}^{-2}\text{s}^{-1}$
DC	Direct Current
DM	Dark Matter
DRS4	Domino Ring Sampler 4
EBL	Extragalactic Background Light
EC	External Compton
EED	Electron Energy Distribution
em	electromagnetic
EVP	Electrical Vector Polarization
EVPA	Electrical Vector Polarization Angle
FoV	Field of View
FWHM	Full Width Half Maximum
GASP	GLAST-AGILE Support Program
GC	Galactic Center

GLAST	Gamma-ray Large Area Space Telescope
GRB	Gamma-Ray Burst
GZK	Greisen-Zatsepin-Kuzmin
H.E.S.S.	High Energy Stereoscopic System
HN	HyperNova
HSP	High Synchrotron Peaked
IACT	Imaging Atmospheric Cherenkov Telescope
IPRC	Individual Pixel Rate Control
IR	InfraRed
ISP	Intermediate Synchrotron Peaked
KASCADE	KARlsruhe Shower Core and Array DETector (CR experiment)
LAT	Large Area Telescope (on <i>Fermi</i> gamma-ray space telescope)
LC	Light Curve
LSP	Low Synchrotron Peaked
M1	MAGIC I
M2	MAGIC II
MAGIC	Major Atmospheric Gamma-ray Imaging Cherenkov telescope
MAXI	Monitor of All-sky X-ray Image
MC	Monte Carlo simulation
MJD	Modified Julian Day
MW	Multi-Wavelength
<i>ndf</i>	number of degrees of freedom
NN	Next Neighboring
NSB	Night Sky Background
NS	Neutron Star
ph.e.	PhotoElectron
PMT	PhotoMultiplier Tube
PSR	Pulsar
PWN	Pulsar Wind Nebula
QE	Quantum Efficiency
RF	Random Forest
RMS	Root Mean Square
RPC	Resistive Plate Counter
RUNJOB	RUSSIA-NIPpon JOint Balloon collaboration (CR experiment)
RXTE	the Rossi X-ray Timing Explorer

SB	starburst galaxy
SED	Spectral Energy Distribution
SMBH	SuperMassive Black Hole
SN	SuperNova
SNR	SuperNova Remnant
SSC	Synchrotron Self-Compton
Super-K	Super-Kamioka Neutrino Detection Experiment
TD	Topological Defect
UHE	Ultra High Energy (> EeV)
UV	UltraViolet
VCSEL	Vertical-Cavity Surface-Emitting Laser
VERITAS	Very Energetic Radiation Imaging Telescope Array System
VHE	Very High Energy (>100 GeV)
WD	White Dwarf
WEBT	Whole Earth Blazar Telescope
XRB	X-ray Binary
ZA	Zenith Angle

Date (year.month.day) Modified Julian Day (MJD)

2010.01.01	55197
2010.02.01	55228
2010.03.01	55256
2010.04.01	55287
2010.05.01	55317
2010.06.01	55348
2011.01.01	55562
2011.02.01	55593
2011.03.01	55621
2011.04.01	55652
2011.05.01	55682
2011.06.01	55713

List of Units, Physics Constants

eV	1.602×10^{-12} erg
keV	10^3 eV
MeV	10^6 eV
GeV	10^9 eV
TeV	10^{12} eV
PeV	10^{15} eV
EeV	10^{18} eV
ZeV	10^{21} eV
pc	3.086×10^{18} cm
Mpc	10^6 pc

c	speed of light	2.998×10^{10} cm/s
e	electric charge of an electron	4.803×10^{-10} esu, 1.602×10^{-19} C
m_e	mass of an electron	9.109×10^{-28} g, 511 keV/c ²
m_p	mass of proton	938.3 MeV/c ²
r_e	$= e^2/m_e c^2$, classical electron radius	2.818×10^{-13} cm
σ_T	$= 8\pi r_e^2/3$, Thomson cross section	6.652×10^{-25} cm ²

Acknowledgement

I thank particularly Dr. David Paneque's careful academic guide, Prof. Dr. Masahiro Teshima's, Prof. Dr. Christian Kiesling's, and Dr. Bela Majorovits's advices. I also receive help and support from my both parents, Selinna Sun, Randy Lin, Dr. Jiwoo Nam, Prof. Pisin Chen, Xiao-Yuan Huang, Xin Gao, Yan-Yan Bu, Xu Zhang, Bauer Ly, Tung-te Wang, Heng-Ye Liao, Ana Solaguren-Beascoa, Alessandro Manfredini, Sebastian Passehr, Sebastian Nowak, Marlene Eder, Hsien-Yu Hung, Nu Nguyen, Li-Sen Wang, She-Rong Lin, Chien-wen Chen, Jian-Yau Sun, Ching-Cheng Hsu, In-Ping Tien, Ming Li, Larisa Huang, Yu-Chien Sun, Karsten Berger, Andrea Boller, Daniela Borla Tridon, Daniela Hadasch, Tobias Jogler, Stefan Klepser, Julian Krause, Nijil Mankuzhiyil, Javier Moldón, Nina Nowak, Stefan Rügamer, Nicola Strah, Robert Wagner, Frederik Beaujean, Emiliano Carmona, Iva Snidaric, Gessica De Caneva, Markus Garzarczyk, Eduardo Colombo, Diego Tesaro, Miquel Barcelo, Oscar Blanch, Adiv González Muñoz, Rubén López-Coto, Abelardo Moralejo, Julian Sitarek, Konstancja Satalecka, Saverio Lombardi, Laura Maraschi, Giovanni Pareschi, Antonio Stamerra, Fabrizio Tavecchio, Susumu Inoue, Masaaki Hayashida, Alexander Hahn, Kazuhito Kodani, Daisuke Nakajima, Koji Saito, Takayuki Saito, Hajime Takami, Wojciech Idec, Marcos López, Priyadarshini Bangale, Ulisses Barres de Almeida, Francesco Borracci, Pierre Colin, Francesco Dazzi, David Fink, Christian Fruck, Dennis Häfner, Jürgen Hose, Christopher Jablonski, Hanna Kellermann, Eckart Lorenz, Daniel Mazin, Uta Menzel, Razmik Mirzoyan, Koji Noda, Sybille Rodriguez, Jezabel Rodriguez Garcia, Thomas Schweizer, Burkhard Steinke, Marcel Strzys, Takeshi Toyama, Ievgen Vovk, Ina Wacker, Cornelia Schultz, Michele Doro, Massimo Rebeschini, Elina Lindfors, Roberta Zanin, Alessandro De Angelis, Michele Palatiello, Daniela Dorner, Thomas Bretz. Thank you all.

Preface

This PhD thesis reports on the mechanisms responsible for the broadband emission and temporal evolution of the classical TeV blazar Markarian 421 (Mrk 421).

Chapters 1 – 3 are the introductions to the research background knowledge:

What are the current main channels (through what particle) to study astrophysical sources? It is good to understand what information could be obtained through each channel. This information can be found in **Chapter 1: High-Energy-Astrophysics Messengers**.

What are the TeV emitters? What are AGN? What are blazars? What do we know about Mrk 421? This information is provided in **Chapter 2: Blazars as Prominent Very-High-Energy (VHE;> 100 GeV) γ -ray Astrophysical Sources**.

In this PhD thesis, the main instrument used to study the VHE emission from Mrk 421 is MAGIC. A description of this instrument and a detailed report on how the MAGIC data is analyzed is given in **Chapter 3: the MAGIC Telescopes and Data Analysis**.

Chapters 4 – 6 are the main body of this research report:

Results from MAGIC observations in 2010 and 2011 (the first two years of the operation of the MAGIC stereo telescopes) are reported in **Chapter 4**.

Not only MAGIC data, but also the data from other wavelengths are gathered to give a comprehensive view on the behavior of Mrk 421 in 2010 and 2011. This is reported in **Chapter 5: Multi-wavelength Campaign on Mrk 421 in 2010** and **Chapter 6: Multi-wavelength Campaign on Mrk 421 in 2011**.

Chapter 7 gives the Summary of the Study on Mrk 421.

Appendices A, B, C are some secondary/supporting results related to this study. In the main body of the thesis, the links to these auxiliary materials are given.

Contents

Abstract	v
Kurzfassung	vii
Lists of Acronyms, Abbreviations, Units, and Physical Constants	ix
Acknowledgement	xv
Preface	xvii
1. High-Energy-Astrophysics Messengers	1
1.1. Three Messengers	1
1.1.1. Protons	1
1.1.2. Neutrinos	4
1.1.3. Photons	6
1.2. Detection	7
1.2.1. Detection of Protons	7
1.2.2. Detection of Neutrinos	9
1.2.3. Detection of Photons	11
1.3. Remarks on the Study of Active Galactic Nuclei	12
2. Blazars as Prominent Astrophysical Very-High-Energy γ-ray Sources	13
2.1. AGN and Their Classification	13
2.2. Blazar	16
2.2.1. The Concept of the Blazar: the Beaming Effect and Its Spectrum	16
2.2.2. Blazar Emission Models	18
2.3. The TeV Blazar Markarian 421	22
2.3.1. TeV Blazar Discovery	22
2.3.2. Markarian 421	23
3. The MAGIC Telescopes and Data Analysis	25
3.1. The MAGIC Telescopes	25
3.2. MAGIC Data Analysis	29
4. Observations of Markarian 421 with MAGIC in 2010 and 2011	35
4.1. Very-High-Energy Flux Variability	36

4.2. Very-High-Energy Spectral Variability	42
5. Multi-wavelength Campaign on Markarian 421 in 2010	53
5.1. Observation and Data Analysis	53
5.1.1. MAGIC	53
5.1.2. VERITAS	55
5.1.3. Whipple	55
5.1.4. <i>Fermi</i> -LAT	56
5.1.5. X-ray Observations	56
5.1.6. Optical Observations	57
5.1.7. Radio Observations	58
5.2. Multi-band Variabilities in 2010	59
5.3. Multi-band Variability in the March Flaring Activity	63
5.4. Temporal Evolution of the Broadband Spectral Energy Distribution in the March Flaring Activity	68
5.4.1. Characteristics of the Measured Broadband SEDs	68
5.4.2. Description of the Synchrotron Self-Compton Model	74
5.4.3. SED Modeling: One-zone SSC Model	78
5.4.4. SED Modeling: Two-zone SSC Model	83
5.5. Discussion on the March Flaring Activity	89
6. Multi-wavelength Campaign on Markarian 421 in 2011	97
6.1. Observation and Data Analysis	97
6.2. Multi-band Variabilities	97
6.3. Temporal Evolution of the Broadband Spectral Energy Distribution	102
6.3.1. Characteristics of the Measured Broadband SEDs	102
6.3.2. SED Modeling	107
6.4. Discussion	110
7. Summary of the Study on Markarian 421	113
A. Markarian 421 MAGIC Light Curve Archive	119
A.1. Intra-night Light Curves of March 2010	119
B. Markarian 421 MAGIC Spectrum Archive	121
B.1. Spectra and Fit Functions	121
C. Test and Cross-check for MAGIC Markarian 421 Data Analysis	143
C.1. Analysis Chain Testing on the Crab Nebula Very-High-Energy Spectrum	143
C.2. Markarian 421 Very-High-Energy Light Curve Cross-check with Other Analyzers	145
C.3. Markarian 421 Very-High-Energy Spectrum Cross-check with Other Analyzers .	147
Bibliography	153

1. High-Energy-Astrophysics Messengers

In the following, the properties of three high-energy astrophysical messengers are discussed: protons, photons, and neutrinos. I take the proton as the representative of charged cosmic-ray particles because it is dominant in population. The three messengers are discussed with respect to different energy ranges, different astronomical sources and detection methods for different particles.

1.1. Three Messengers

1.1.1. Protons

The information of the astrophysical proton is summarized in Table 1.1. A few points from this table are described in the following. The proton energy starts from its rest mass 0.938 GeV. The lowest-energy part ($\lesssim 0.1$ TeV) of the proton or heavier nuclei in cosmic rays (CRs) primarily come from the nuclear synthesis in stars. On the next energy level, 0.1 TeV–10 PeV, some galactic high-energy sources such as supernovae (SN) or supernova remnants (SNR) can accelerate protons to this level. Below 1 PeV, no point-like proton source is expected because the galactic magnetic field can trap protons. Above 1 PeV, the magnetic field cannot work so effectively. Ultra-high-energy (UHE) ($> \text{EeV}$) protons are expected from extragalactic sources like active galactic nuclei (AGN) or gamma ray bursts (GRBs), or hypernovae (HN). These models are called bottom-up astrophysical acceleration models [Torres and Anchordoqui, 2004] because the proton is accelerated from lower to higher energies. There are also exotic top-down particle-physics models [Bhattacharjee and Sigl, 2000] to explain UHECRs, including annihilation of dark matter (DM), super-heavy dark-matter-particle decays, topological defects (TDs) etc. Between PeV and EeV is the transition range of galactic and extragalactic sources. Although UHE protons are less deflected by the magnetic field, those from distant sources might be blocked by cosmic microwave background (CMB) photons.

The interaction of the UHECR with (CMB) photons:

$$p^+ + \gamma_{\text{CMB}} \rightarrow \Delta^+ \rightarrow n + \pi^+ \quad \text{or} \quad p^+ + \pi^0 \quad (\Delta^+ \text{ resonance}), \quad (1.1)$$

$$\pi^+ \rightarrow \mu^+ + \nu_\mu, \quad (1.2)$$

$$\pi^0 \rightarrow 2\gamma, \quad (1.3)$$

$$\mu^+ \rightarrow e^+ + \bar{\nu}_\mu + \nu_e, \quad (1.4)$$

$$n \rightarrow p^+ + e^- + \bar{\nu}_e. \quad (1.5)$$

Table 1.1. Sources of astrophysical protons.

energy[eV]	possible source	particle flux	index	galactic B trapping or $\langle t \rangle / r_g$	point-like or diffuse	anisotropy
1G-0.1T	stellar nucleosynthesis, SN			effective	diffuse	isotropic
0.1T		$1 \text{ m}^{-2} \text{ s}^{-1}$				
0.1T-10P	SN,SNR		-2.7	effective	diffuse	the highest excess: $\sim 10^{-3}$ ^(b)
10P		$1 \text{ m}^{-2} \text{ yr}^{-1}$	knee	10 pc		
1P-10E	galactic/extragalactic		-3	ineffective	diffuse	isotropic ^(c)
10E		$1 \text{ km}^{-2} \text{ yr}^{-1}$	ankle	10 kpc		
10E-50E	AGN,GRB,HN,DM,TD	absorption by CMB	-2	ineffective	diffuse	isotropic ^(e)
50E-0.3Z	AGN,GRB,HN,DM,TD	absorption by CMB	-2	ineffective	possibly point-like ^(d)	anisotropic ^(e)
0.3Z	-	highest-energy CR ever detected	-	-	-	-

Note. —

^(a) The gyroradius in the galactic magnetic field. Calculated with 10^{-10} Tesla. The acronyms and abbreviations in this table are explained in the text or in the Lists of Acronyms, Abbreviations, Units, and Physical Constants. The content of this table refers to [Grupen, 2005].

^(b) Reported by ARGO-YBJ [Bartoli et al., 2013]; a patch of the sky has the highest excess ratio of CR events, $\sim 10^{-3}$, at energies $\sim 30 \text{ GeV} - 100 \text{ TeV}$ with the significance of $\sim 15 \sigma$.

^(c) Reported by KASKADE [Maier et al., 2005].

^(d) Pierre Auger Observatory [de Mello Neto and Pierre Auger Collaboration, 2013] reports a correlation between arrival directions of cosmic rays above 55 EeV and the positions of AGNs with $z < 0.018$. The fraction of correlating cosmic rays is 33% compared with 21% expected for isotropy.

^(e) Reported by the Telescope Array [Fukushima et al., 2013]; the events with $E > 57 \text{ EeV}$ are anisotropic with significance of $\geq 3\sigma$ with the smearing angle $\geq 5^\circ$.

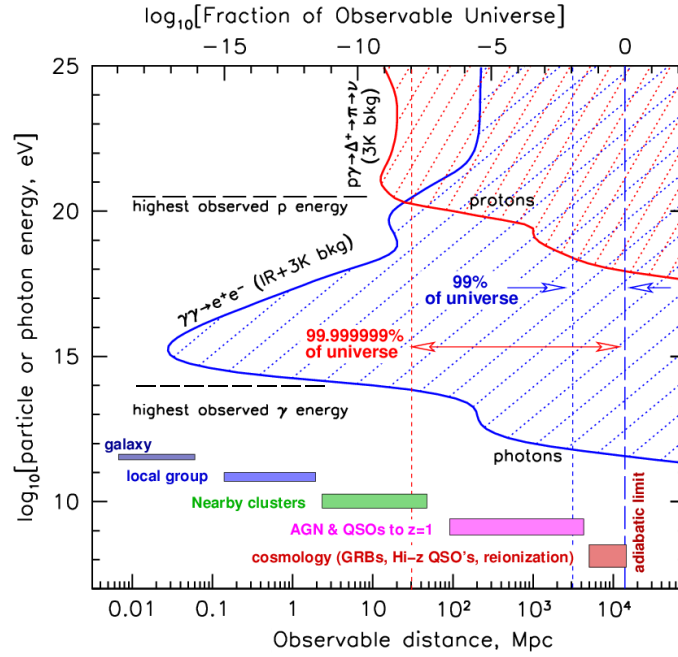


Figure 1.1.: The range and the energy limitation of photons or protons as astrophysical messengers. Plotted by P. Gorham [Gorham, 2005].

These interactions, called Greisen-Zatsepin-Kuzmin (GZK) process, cause the GZK cutoff [Greisen, 1966, Zatsepin and Kuzmin, 1966], in the CR spectrum, at the energies above the threshold of the interaction in Formula 1.1, 6×10^{19} eV (for CBM photons with $E_\gamma = 2.7$ kT), and the UHE neutrinos produced in the interactions in Formulae 1.2, 1.4 and 1.5 are called GZK neutrinos or cosmogenic neutrinos. The proton mean free path of this interaction for $E_p = 6 \times 10^{19}$ eV is around 50 Mpc. This distance also implies the distance limit of UHE protons as astrophysical messengers. We can see this point in Figure 1.1 plotted by P. Gorham [Gorham, 2005]. The red curve inside denotes the threshold energy and the mean-free-path length of the Δ^+ resonance, and the red-slashed region represents the part of the universe where protons are forbidden to observe due to the GZK process. The conclusion is that above the highest energy (around 3×10^{20} eV) of observed protons, more than 99.999999% of the universe is invisible. In contrast, the UHE neutrinos produced in the GZK process can be used as a probe of this invisible but major part of the universe, but the difficulty of the low flux and the small cross-section should be solved by the effective-volume increase of the detector. On the other hand, it is possible to receive UHECRs above the pion-resonance threshold energy from local astrophysical objects (< 50 Mpc) such as AGNs within the Virgo supercluster (the local supercluster which our Milkyway galaxy belongs to). These CRs, which are not blocked by CMB, are called trans-GZK cosmic rays, and can possibly be used to study the sources. For example, Auger had found that 19 out of 98 events are around a radiogalaxy, Centaurus A, which is the nearest AGN (3.8 Mpc away). In this case, only 7.6 events are expected by the chance correlation.

Table 1.2. Sources of astrophysical neutrinos.

energy[eV]	source	point-like or diffuse
1 μ -1m	cosmological	possibly diffuse
1m-1	- - -	energy too low to measure
1 -1k		
1k-1M	solar/stellar	dependence on separation angle to the Sun
1M-1G	SN	point-like source
	atmospheric	secondary particles ^(a)
1G-1T	atmospheric	secondary particles ^(a)
1T-1P	atmospheric	secondary particles ^(a)
1P	- - -	highest-energy ν ever detected
1P-1E	AGN,GRB,HN,DM,TD(+GZK)	possibly point-like
1E-1Z	AGN,GRB,HN,DM,TD(+GZK)	possibly point-like

Note. — The acronyms and abbreviations in this table are explained in the text or in the Lists of Acronyms, Abbreviations, Units, and Physical Constants.

^(a) These neutrinos are produced in the atmospheric showers induced by CRs, which are diffuse. The content of this table refers to [Grupen, 2005].

1.1.2. Neutrinos

Here we review the astrophysical sources of neutrinos. Cosmological 1.9 K background neutrinos have the lowest energy, with a peak around 0.16 meV. Between keV and MeV, solar neutrinos dominate. The proton-proton fusion produces up to 86% of the solar neutrinos:



which peaks around 200 keV. The remaining 14% primarily come from the electron capture by Be:



which gives an emission line around 900 keV. A bump at a higher energy, around 7 MeV, results from β^+ decays:

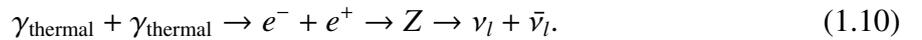


which contributes 0.02%.

At higher energies, there is a contribution from supernova. The deleptonization during the formation of a neutron star gives the neutrino burst:



And at a temperature around 10^{11} K, which corresponds to 10 MeV, the neutrino is an efficient channel to bring away the energy of a supernova:



The supernova neutrinos peak just around this energy (10 MeV).

The atmospheric neutrinos result from high-energy CR interacting with the atmosphere (See Subsection 1.2.1). Its spectrum dominates in the whole neutrino spectrum between MeV and PeV. The GZK neutrino (See Subsection 1.1.1) might dominate around EeV. A summary can be seen in Table 1.2.

Table 1.3. Sources of astrophysical photons.

energy[eV]	source	point-like or diffuse
1k-1M	Sun,star,WD,NS,SNR,BH,star cluster normal galaxy,active galaxy,galaxy cluster	point-like source point-like source
1M-1G	Sun,PSR,XRB,SNR, globular cluster,normal galaxy,active galaxy	point-like source point-like source
1G-1T	PSR,XRB,SNR,active galaxy	point-like source
1G-100T	PSR,XRB,SNR,active galaxy (interacting with EBL)	point-like source
100T	- - highest-energy γ ever detected - -	- -
100T-1E	AGN (interacting with EBL)	possibly point-like source

Note. — The acronyms and abbreviations in this table are explained in the text or in the Lists of Acronyms, Abbreviations, Units, and Physical Constants. The content of this table refers to [Gruppen, 2005].

1.1.3. Photons

Here we review the astrophysical sources of high-energy photons. The nearest star, the Sun, can effectively produce photons up to X-ray, and even γ -rays [Brigida and Fermi LAT Collaboration, 2011]. Other possible X-ray sources could be normal stars, white dwarfs (WDs), neutron stars (NSs), SNRs, black holes (BHs), star clusters, normal galaxies, active galaxies, or galaxy clusters. The γ -ray sources might be pulsars (PSRs), X-ray binaries (XRBs), SNRs, globular clusters, normal galaxies, active galaxies, or cluster of galaxies. Besides, our galactic center (GC) and disk could also also emit more γ -rays than the diffuse γ -ray background. Scientists also try to look for dark matter signals from the GC, low surface-brightness galaxies, dwarf spheroidals, or central parts of nearby clusters of galaxies.

The γ -rays above 10 GeV can interact with the extragalactic background light (EBL) and the CMB, and result in pair productions:

$$\gamma + \gamma_{\text{EBL}} \rightarrow e^- + e^+, \quad (1.11)$$

and hence they can be absorbed considerably if they travel for a long distance. The EBL is the second dominating part (just second to CMB) of the whole diffuse extragalactic background-radiation spectrum. Between 10 GeV and 1 PeV, the higher energy of the γ -ray, the higher probability of the interaction. Above 1 PeV, the probability of interaction decreases. The mean-free-path length for this interaction as a function of the photon energy is also shown in Figure 1.1, like the GZK process for protons. In the figure, the blue-slashed region means the part of the universe blocked by this pair production. Above 100 TeV, up to 99.999999% of the universe cannot be seen, but at the γ -ray energies of < 300 GeV, already more than 1% of the universe could be seen.

1.2. Detection

In this section, the different detection methods of these messengers are presented. To detect a high-energy particle, the detector should have a large volume to contain its long track. We observe the signals from its interaction with the target. Here, the interactions of the messengers with the matter, and the instruments for the reception of the interaction signals are discussed.

1.2.1. Detection of Protons

The proton interacts with matter in the following ways:

$$p^+ + N \rightarrow X + \pi^\pm \text{ or } \pi^0, \quad (1.12)$$

$$\pi^0 \rightarrow 2\gamma, \quad (1.13)$$

$$\pi^+ \rightarrow \mu^+ + \nu_\mu, \quad (1.14)$$

$$\pi^- \rightarrow \mu^- + \bar{\nu}_\mu, \quad (1.15)$$

$$\mu^+ \rightarrow e^+ + \bar{\nu}_\mu + \nu_e, \quad (1.16)$$

$$\mu^- \rightarrow e^- + \nu_\mu + \bar{\nu}_e, \quad (1.17)$$

where N stands for a nucleus, and X is a nucleus in its excited state. The outgoing μ^\pm would emit the Cherenkov radiation and also have a chance to cause an EM shower through Bremsstrahlung and the pair production, or a hadronic shower through the photonuclear interaction. As for e^\pm , they would result in EM showers transiently because of their large cross-sections with matter. On the other hand, X would cause a hadronic shower. Typical instruments are scintillation counters, water Cherenkov counters, resistive plate chambers and drift chambers, streamer tube detectors, and Geiger tube detectors. For the protons with lower energies (\lesssim PeV), the direct observation of the cascade in the detector is possible. The flux of high-energy protons is small and the longitudinal and the lateral developments of its particle cascades are long and wide, so a detector array covering a large area is necessary for measuring higher-energy protons. Table 1.4 gives the examples of the experiments for different energy ranges.

Table 1.4. The detection of astrophysical protons.

energy[eV]	instrument	mechanism involved	detector
1G-1T	AMS(satellite)	magnetic bending shower in calorimeter	silicon tractor calorimeter
1T-1P	RUNJOB(balloon)	shower in solid target	calorimeter
1P-1E	KASCADE(ground array)	hadronic air-shower→charged particles hadronic air-shower→muon	scintillator, hadron calorimeters muon tracking detector
1E-0.3Z	AUGER(ground array)	hadronic air-shower→water-shower→Cherenkov light hadronic air-shower→fluorescence	Cherenkov detector fluorescence detector
0.3Z	- - -	highest-energy CR ever detected	- - -

Note. — The acronyms and abbreviations in this table are explained in the text or in the Lists of Acronyms, Abbreviations, Units, and Physical Constants.

1.2.2. Detection of Neutrinos

There are three possible neutrino interactions. These are the elastic scattering

$$\nu_l + e^- \rightarrow \nu_l + e^-, \quad (1.18)$$

the charge current (CC) interaction

$$\nu_l + N \rightarrow l^- + X \quad \text{or} \quad \bar{\nu}_l + N \rightarrow l^+ + X, \quad (1.19)$$

and the neutral current (NC) interaction

$$\nu_l + N \rightarrow \nu_l + X \quad \text{or} \quad \bar{\nu}_l + N \rightarrow \bar{\nu}_l + X, \quad (1.20)$$

where l^\pm can be e^\pm , μ^\pm , or τ^\pm ; N stands for a nucleus, and X is a nucleus in its excited state. In the elastic scattering, the ν_e dominates the total interaction rate because ν_e can interact through the exchange of a charged W boson or a neutral Z boson, while ν_μ and ν_τ can interact only through the exchange of a neutral Z boson. In the CC interaction, if the neutrino energy is below 100 MeV, l^\pm is always e^\pm ; the production of μ^\pm , or τ^\pm requires a higher energy of the neutrino. Therefore, ν_μ and ν_τ with energies below 100 MeV can only have a NC interaction or an elastic scattering.

The outgoing μ^\pm or τ^\pm would emit the Cherenkov radiation and also have a chance to cause an electromagnetic (EM) shower through Bremsstrahlung and a pair production, or a hadronic shower through a photonuclear interaction. As for e^\pm , they would result in EM showers transiently because of their large cross-sections with matter. On the other hand, X would cause a hadronic shower. Table 1.5 gives examples for astrophysical neutrino experiments for different energy ranges. In this table, we can see many experiments observe the Cherenkov radiation from the shower particles produced in the CC interaction or the elastic scattering. The cosmological and the UHE neutrinos are not yet observed.

Table 1.5. The detection of astrophysical neutrinos.

energy[eV]	instrument	mechanism involved	detector
1 μ -1m	- -	- - - energy too low to measure - - -	
1m-1	- -		
1-1k	- -		
1k-1M	Super-K	electron-neutrino elastic scattering \rightarrow water em-shower \rightarrow Cherenkov radiation	Cherenkov counter
	Davis exp.	perchloroethylene electron-charge-current	X-ray and Auger e counting(radiochemical methods)
1M-1G	Super-K	electron-neutrino elastic scattering \rightarrow water em-shower \rightarrow Cherenkov radiation	Cherenkov counter
	SNO	charge-current $\rightarrow e \rightarrow$ Cherenkov radiation neutral-current $\rightarrow n \rightarrow^{(a)} p \rightarrow e \rightarrow$ Cherenkov radiation	PMT PMT
1G-1T	Super-K	electron-neutrino elastic scattering \rightarrow water em-shower \rightarrow Cherenkov radiation	PMT
	IceCube	electron-neutrino elastic scattering \rightarrow water em-shower \rightarrow Cherenkov radiation	Cherenkov counter
1T-1P	IceCube	charge-current \rightarrow muon \rightarrow Cherenkov radiation	PMT
1P	IceCube	charge-current \rightarrow muon \rightarrow Cherenkov radiation	PMT
1P-1E	IceCube	- - - highest-energy γ ever detected - - -	
	ARA	charge-current \rightarrow ice hadronic/leptonic shower \rightarrow Cherenkov radiation	PMT
1E-1Z	IceCube	charge-current \rightarrow muon \rightarrow Cherenkov radiation	antenna PMT
	ARA	charge-current \rightarrow ice hadronic/leptonic shower \rightarrow Cherenkov radiation	antenna

Note. — The acronyms and abbreviations in this table are explained in the text or in the Lists of Acronyms, Abbreviations, Units, and Physical Constants.

^(a) The neutron is captured by the deuterium in the heavy water and then a γ -ray (~ 6 MeV) is produced. The γ -ray then up-scatters the electron to a higher energy.

Table 1.6. The detection of astrophysical photons.

energy[eV]	instrument	mechanism involved	detection
1k-1M	Swift(satellite)	photo-electric	Wolter telescope → CCD
	RXTE(satellite)	photo-electric	proportional counter
1M-100M	COMPTEL(satellite)	Compton effect	scintillator
100M-100G	Fermi(satellite)	pair production	converter tracker calorimeter
100G-10T	MAGIC(ground-based)	em air-shower → Cherenkov radiation	collection mirror → PMT
	Milagro(ground array)	em air-shower → water-shower → Cherenkov radiation	PMT
	Argo-YBJ(ground array)	em air-shower → plastic-shower	RPC
10T-1P	HiScore(ground array)	em air-shower → Cherenkov radiation	PMT
100T	- -	- - highest-energy γ ever detected - -	
1P-1E	AUGER(ground array)	em air-shower → water-shower → Cherenkov radiation	PMT
		em air-shower → fluoresce	collection mirror → PMT

Note. — The acronyms and abbreviations in this table are explained in the text or in the Lists of Acronyms, Abbreviations, Units, and Physical Constants.

1.2.3. Detection of Photons

High-energy photons may interact with matter in the following ways: the photoelectric effect when $E_\gamma < 100$ keV

$$\gamma + \text{atom} \rightarrow \text{atom}^+ + e^-, \quad (1.21)$$

the Compton effect when $E_\gamma < 1$ MeV

$$\gamma + e^-_{\text{at rest}} \rightarrow \gamma' + e^-_{\text{fast}}, \quad (1.22)$$

the pair production when $E_\gamma \gg 1$ MeV

$$\gamma + N \rightarrow N' + e^+ + e^-. \quad (1.23)$$

Table 1.6 gives examples for observatories for different energy ranges. The absorption of X-rays and γ -rays in the atmosphere is high, so direct observations should be in space, for example, *Swift*, *RXTE*, *Fermi* satellites. They directly detect photons through the photoelectric effect, the Compton effect, or the pair production in the instruments. For very-high-energy (VHE; $E > 100$ GeV) photons, it becomes possible to observe the indirect signals of the air-shower triggered by the pair production in the atmosphere. Some observatories like *Argo-YBJ* detect shower particles directly, and some observatories like *MAGIC* or *Milagro* detect the Cherenkov radiation from the shower. Currently the highest-energy γ 's ever detected are around 100 TeV. For higher energies, the flux is so low that a large array should be used to catch the rare photons of these energies.

1.3. Remarks on the Study of Active Galactic Nuclei

If we want to have a rather detailed study on AGNs, it is necessary to consider whether the messenger is blocked before reaching the Earth, how much it is deflected by the magnetic field, and how high the event rate is with the help of the contemporary technology. Considering neutrinos, we need to observe them above 1 PeV. However, this energy is roughly the highest energy we can reach nowadays; the detected events are too few. Therefore, the neutrino is not a suitable channel for this study. As for protons, energies >10 EeV are needed if we want the gyroradius to be smaller than 10 kpc at the strength of the galactic magnetic field. At this energy, the flux is around $1\text{km}^{-2}\text{yr}^{-1}$. This number is too limited to have a detailed study. Another constraint results from the GZK process, which allows only those from neighboring sources (trans-GZK protons) to reach the Earth. The mean free path of 10 EeV protons is around 1 Gpc, which implies that only a small fraction (3×10^{-7}) of our universe can be seen. In contrast, the photon is not deflected by the magnetic field, but there is still the problem of absorption by the EBL. The mean free path of 1-TeV photons is similar to 10-EeV protons, around 1 Gpc, but that of < 10 GeV photons is already longer than the horizon of the observable universe. In conclusion, it is the most probable to have a detailed AGN study with high-energy photons.

2. Blazars as Prominent Astrophysical Very-High-Energy γ -ray Sources

There are many categories of astrophysical VHE γ -ray sources, and the AGN is one of them. In Section 2.1, the AGN and its various classes are described. The blazar is a subclass of the AGN, also a prominent kind of VHE γ -ray sources in terms of the number. In Section 2.2, the physics and the emission models of blazars are reported. In Section 2.3, a subclass of blazars, TeV blazars, is introduced, and a brief research note on the source Markarian 421 is given.

2.1. AGN and Their Classification

A galaxy with an active galactic nucleus (AGN) is one class of active galaxies. Active galaxies include starburst (SB) galaxies, mergers, and active galactic nuclei (AGNs). To date¹, only two SB galaxies and 56 AGNs are VHE γ -ray sources. An AGN has a higher luminosity than a normal galaxy in most parts of the electromagnetic spectrum. In current knowledge of AGN, people classify them into two categories: radio-quiet and radio-loud. An AGN with a jet structure is radio-loud, while an AGN without a prominent jet is radio-quiet. Most of the AGNs with jets are hosted in elliptical galaxies, and most of the AGNs with no jet are hosted in spiral galaxies. Figure 2.2 shows the classification of AGNs.

Figure 2.1 shows the structure of an AGN with a jet, including the broad-emission-line region, the narrow-emission-line region, and the torus. The direction of viewing the AGN determines what is seen and results in different types (see Figure 2.2): type 1 refers to those with their galactic planes rather facing the Earth, type 2 those with their galactic planes rather extending through the Earth. We observe only the narrow-emission-line region of the type 2 AGN, but the broad-emission-line region cannot be seen because it is blocked by the torus. For the type 1 AGN, both regions are at the line of sight, but the broad-emission-line region dominates in the spectrum. For radio-quiet AGNs, type 1 is called Seyfert 1, and type 2 is called Seyfert 2. For radio-loud AGNs, traditionally we call their hosts radio galaxies, but in the current classification, the radio galaxy refers to only type 2, and type 1 is called a quasar. An additional kind for the radio-loud AGN is type 0, which is also called a blazar. Its jet is almost toward the line of sight. The BL Lac objects (BL Lacs) and flat-spectrum radio quasars (FSRQ) are two subclasses of blazars. FSRQs have optical emission lines, but BL Lacs have very weak lines or no line. The

¹May of 2014, according to the TeV catalog: <http://tevcat.uchicago.edu/>

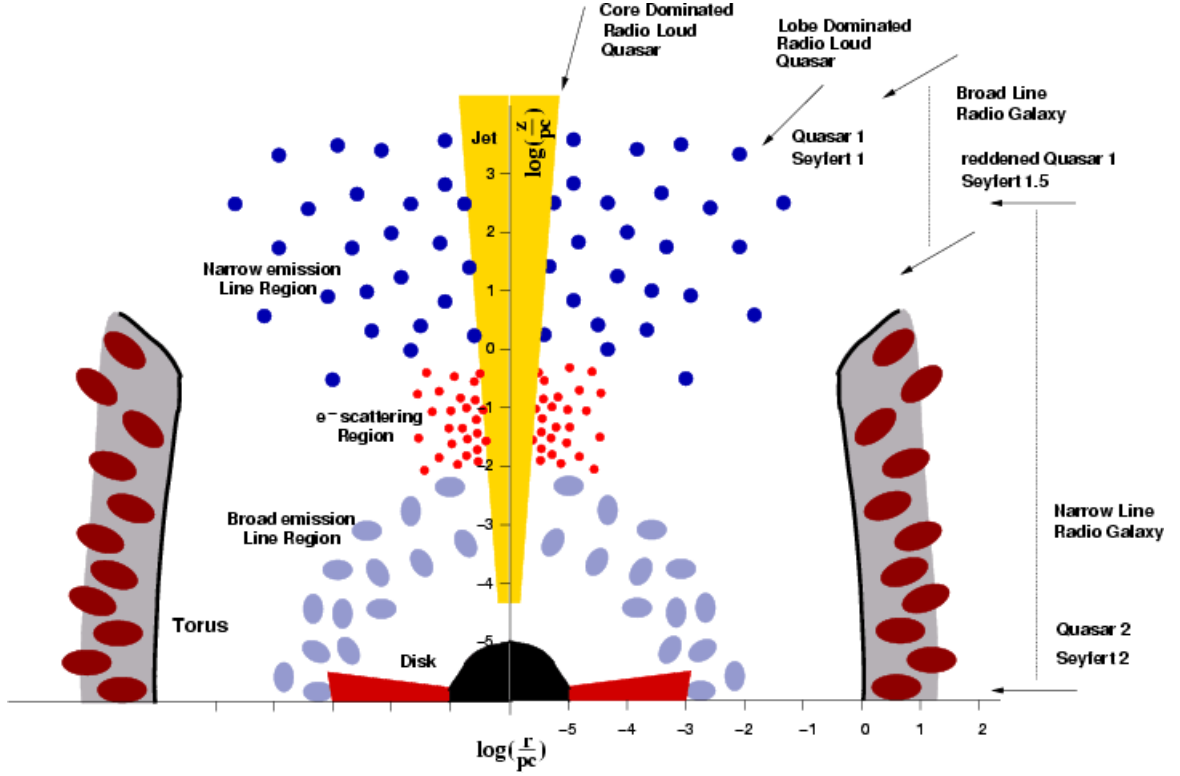


Figure 2.1.: The structure of an active galactic nucleus with a jet. The size scale and the classification according to the viewing angle are also shown. The image is produced by C. Zier and P. L. Biermann [Zier and Biermann, 2002].

equivalent width of a line, EW , is used to divide these two classes:

$$EW = \left| \int \frac{F_0 - F_\lambda}{F_0} d\lambda \right|. \quad (2.1)$$

where λ is the wavelength, F_0 the flux of the continuum, F_λ the flux of both the continuum and the line. Blazars with $EW < 5 \text{ \AA}$ are called BL Lacs, and those with $EW > 5 \text{ \AA}$ are FSRQs. Furthermore, the BL Lacs are classified into the low-synchrotron-peaked (LSP) BL Lac, the intermediate-synchrotron-peaked (ISP) BL Lac, and the high-synchrotron-peaked (HSP) BL Lac according to the peak frequency ($\nu_{\text{peak}}^{\text{syn}}$) of the synchrotron bump in the spectral energy distribution (SED). LSP: $\nu_{\text{peak}}^{\text{syn}} < 10^{14} \text{ Hz}$; ISP: $10^{14} \text{ Hz} < \nu_{\text{peak}}^{\text{syn}} < 10^{15} \text{ Hz}$; HSP: $\nu_{\text{peak}}^{\text{syn}} > 10^{15} \text{ Hz}$ [Ackermann et al., 2011b].

	Edge-on (~90 deg.) Type 2 Narrow line	Type 1 Broad line	Face-on (~0 deg.) Type 0	
Radio quiet (in general spiral galaxy) No jet	Sey2	Sey1=QSO Near Far <i>Seyfert Galaxy</i> $10^{-4}[\text{Mpc}^{-3}]$	X	Seyfert=Sey Radio Galaxy=RG Broad Line=BL Narrow Line= NL Quasi-stellar Radio Source =quasar Quasi-stellar Object=QSO ----- loose definition: quasar=QSO Radio-loud quasar/QSO=>quasar Radio-quiet quasar/QSO=>QSO
Radio loud (in general elliptical galaxy) Jet dominated	NLRG •FRI(lower luminosity)  •FRII(higher luminosity) 	BLRG •SSRQ •FSRQ, OVV <i>Quasar</i> $10^{-9}[\text{Mpc}^{-3}]$ <i>Radio Galaxy</i> $10^{-6}[\text{Mpc}^{-3}]$ (strict definition) <i>Radio Galaxy</i> (original definition)	Blazar •FSRQ, OVV, HPQ •BL Lac $10^{-7.5}[\text{Mpc}^{-3}]$ •LSP •ISP •HSP	Fanaroff & Riley=FR Flat Spectrum Radio Quasar=FSRQ Steep Spectrum Radio Quasar=SSRQ Optically Violent Variable=OVV Highly Polarization Quasar=HPQ Low-Synchrotron-Peaked= LSP Intermediate-Synchrotron-Peaked= ISP High-Synchrotron-Peaked= HSP

Field Galaxy $10^{-1}[\text{Mpc}^{-3}]$

Figure 2.2.: The AGN classification: primarily by radio-quiet/radio-loud (in rows) and by viewing angles (in columns). The abbreviations used in the table are explained on the right-hand side. Additional classifications are shown by dashed lines with different colors: a box defines a category; the name of a certain category and its number density is shown on the right-bottom corner. Subclasses of a class are denoted by black dots below that class. The patterns beside FR I and FR II explain general characters of their jets: the jet image of a FR I radio galaxy in general has a brighter end close to the core; FR II away from the core. The classification ideas refer to the explanations at <http://ned.ipac.caltech.edu/level5/Urry1/UrryP2.html>.

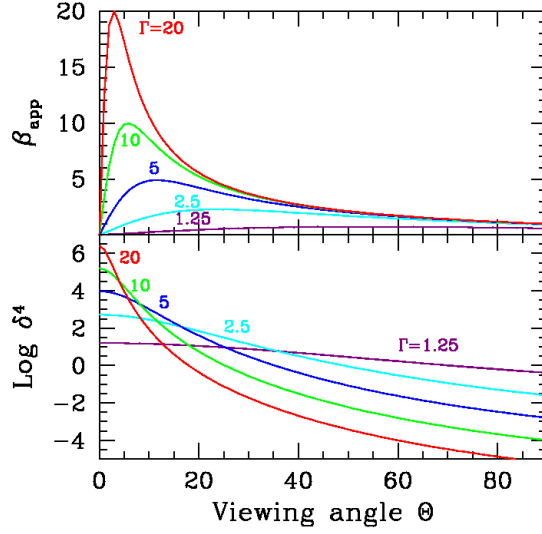


Figure 2.3.: Top: The apparent velocity, β_{app} , as a function of the viewing angle θ for different values of Γ , as labeled. Bottom: the amplification δ^4 as a function of the viewing angle, for the same Γ as in the top panel. The Γ in this figure is the same as γ in the text; the Θ here is the θ in the text; β_{rmap} is β in the text. The image was created by G. Ghisellini[Ghisellini, 2013].

2.2. Blazar

2.2.1. The Concept of the Blazar: the Beaming Effect and Its Spectrum

A blazar is an AGN with a relativistic jet flowing toward observers/the Earth. The jet is powered by accretion onto its central supermassive black hole. The emission from a blazar is dominated by components originating from the relativistic jet due to the relativistic beaming effect: a blob of particles inside the jet can be boosted to almost the speed of light so that the apparent luminosity of the blob can be enhanced by a factor of δ^4 , where δ is the Doppler factor, defined as

$$\delta = \gamma^{-1}(1 - \beta \cos \theta)^{-1},$$

$$\beta = v/c,$$

$$\gamma = (1 - \beta^2)^{-1/2}, \quad (2.2)$$

where v is the speed of the blob, and θ the separation angle between the jet and the line of sight. At small θ , a smaller θ or a larger γ results in a larger δ . The enhancement of the luminosity with respect to θ assuming several γ 's, is shown in Figure 2.3. Taking a non-extreme example of a blazar, the enhancement is above 10^4 times with $\gamma = 10$ ($\beta \sim 0.995c$) and $\theta = 5^\circ$. The high enhancement in the luminosity is one of the reasons why blazars are much brighter than ordinary

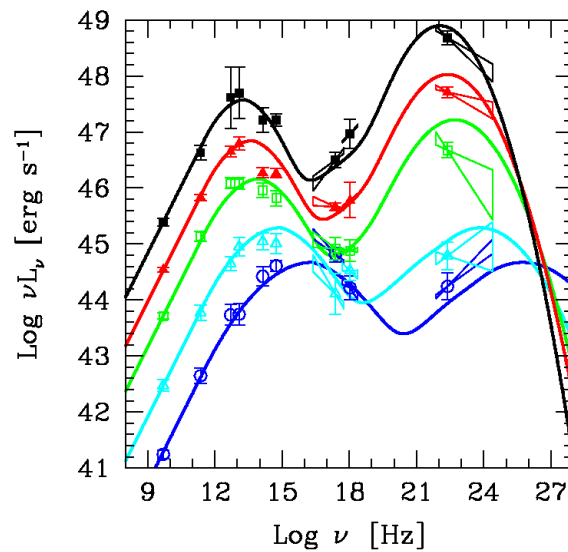


Figure 2.4.: The blazar sequence: SEDs of several subclasses of the blazar. They can be sorted according to their peak frequencies: the FSRQ, the LSP BL Lac, the ISP BL Lac, the HSP BL Lac (the last one has highest peak frequency). Also note that not only peak frequencies but also peak luminosities of the two bumps are in a sequence. The image was created by D. Donato, G. Ghisellini, G. Tagliaferri, G. Fossati, G. Celotti, L. Maraschi, and A. Comastri [Ghisellini et al., 1998, Donato et al., 2001].

galaxies at the same distance. This enhancement resulting from the relativistic motion in the jet is called the beaming effect.

The typical SED of a blazar has two characteristic bumps: the low- and the high-energy bumps. Figure 2.4 shows spectra of different types of blazars. All of them have two bumps, with a tendency of a higher peak luminosity coming along with a higher peak frequency. Furthermore, "the luminosity ratio of the high-energy bump to the low-energy one" increases as the peak frequency decreases. Among the subclasses of blazars, they can be sorted according to their peak frequencies: FSRQ, LSP BL Lac, ISP BL Lac, HSP BL Lac (the last one has the highest peak frequency). This sequence of blazar peak frequencies is called the blazar sequence. Also note that not only peak frequencies but also peak luminosities of the two bumps are in a sequence.

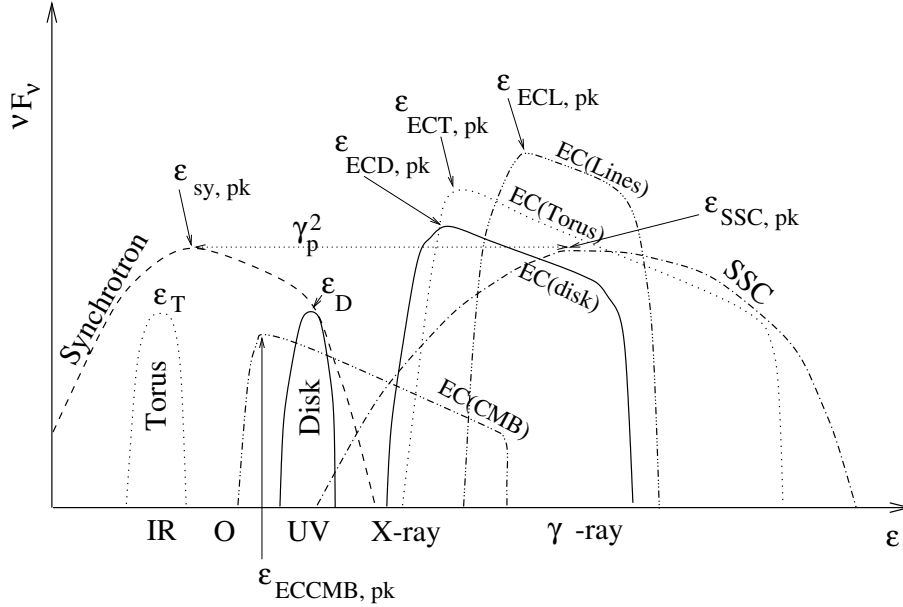


Figure 2.5.: A schematic plot of the synchrotron self-Compton (SSC) and the external-Compton (EC) models. For the EC models, there could be several components contributing to the up-scattered photon field: the cosmic microwave background (CMB), the torus, the disk, and the emission-line regions. The image was created by H. Krawczynski, M. Boettcher, and A. Reimer [Boettcher et al., 2012].

2.2.2. Blazar Emission Models

There are two categories of models describing the broadband emission in blazars: one is leptonic, the other one is hadronic. They are described in this subsection.

Leptonic models

In leptonic models, the low-energy bump is attributed to the synchrotron radiation of electrons in turbulent magnetic fields in the jet on the basis of the observed spectrum and the polarization.

$$e \xrightarrow{B} e + \gamma_{\text{syn}} \quad \text{electron synchrotron} \quad (2.3)$$

There are several models developed to describe the high-energy bump. Synchrotron self-Compton (SSC) models attribute it to the inverse Compton scattering of the same population of electrons and synchrotron photons.

$$e(\text{high E}) + \gamma_{\text{syn}}(\text{low E}) \rightarrow e(\text{low E}) + \gamma(\text{high E}) \quad \text{inverse-Compton scattering: SSC} \quad (2.4)$$

, where "E" stands for "energy". As alternatives, external-Compton (EC) models use external photon fields as target, rather than synchrotron photons.

$$e(\text{high E}) + \gamma_{\text{ext}}(\text{low E}) \rightarrow e(\text{low E}) + \gamma(\text{high E}) \quad \text{inverse-Compton scattering: EC} \quad (2.5)$$

The external photon fields could result from the emission of the accretion disk of the AGN, the broad line region, the torus, or CMB. These external photon fields have different spectra, which are peaked at energies of the UV, the optical, the IR, and the microwave bands respectively. Figure 2.5 shows all the emission spectra mentioned above. In this figure, we see the distribution of the inverse-Compton peaks. From the low to the high energies, they result from the EC(CMB), the EC(disk), the EC(torus), the EC(lines), and the SSC models. In these models, electrons need to be accelerated to at least TeV energies, which can be explained by many mechanisms (for example, the shock acceleration).

Hadronic models

In hadronic models, the main composition of the relativistic particles is the proton and the electron or the relativistic pair. Relativistic protons can interact with target photons or material. In the nuclear rest frame, the threshold of the $p\gamma$ interaction for the photo-meson production is 0.15 GeV, and that of the pp inelastic interaction is 1.22 GeV. The pp inelastic interaction demands the ambient matter density to be high enough to produce the observed spectrum. Besides, the pp inelastic interaction also needs high matter density if the interaction time is required to be shorter than the variability timescale. The jet is *radiation dominated* if the particle-photon interaction dominates, and the jet is *heavily mass-loaded* if the particle-particle interaction dominates. In the following, the interactions in a radiation dominated jet are listed:

$$e \xrightarrow{B} e + \gamma_{\text{syn}} \quad \text{primary-electron synchrotron,} \quad (2.6)$$

$$p \xrightarrow{B} p + \gamma_{\text{syn}} \quad p\text{-synchrotron and cascade,} \quad (2.7)$$

$$p + \gamma_{\text{syn}} \rightarrow \begin{cases} p \\ \pi^0 \end{cases} \rightarrow \begin{cases} \gamma \rightarrow e^+e^- \\ \gamma \rightarrow e^+e^- \end{cases} \quad \pi^0 \text{ cascade,} \quad (2.8)$$

$$\rightarrow \begin{cases} n \\ \pi^+ \end{cases} \rightarrow \begin{cases} \mu^+ \rightarrow e^+ \bar{\nu}_\mu \nu_e \\ \xrightarrow{B} \mu^+ \gamma_{\text{syn}} \\ \nu_\mu \end{cases} \quad \begin{array}{l} \pi^+ \text{ cascade,} \\ \mu^+ \text{-synchrotron,} \end{array} \quad (2.9)$$

$$\rightarrow \begin{cases} \Delta^{++} \\ \pi^- \end{cases} \rightarrow \begin{cases} \mu^- \rightarrow e^- \nu_\mu \bar{\nu}_e \\ \xrightarrow{B} \mu^- \gamma_{\text{syn}} \\ \bar{\nu}_\mu \end{cases} \quad \begin{array}{l} \pi^- \text{ cascade,} \\ \mu^- \text{-synchrotron,} \end{array} \quad (2.10)$$

$$\xrightarrow{\text{Bethe-Heitler pair production}} pe^+e^- \quad \text{Bethe-Heitler cascade.} \quad (2.11)$$

In order to discuss the model in detail, we take the one in [Abdo et al., 2011] as an example. See Figure 2.6b. This is a hadronic model for a HSP BL Lac, Mrk 421, in its typical state. We find that the π^\pm or the π^0 cascade results in a flat bump in the SED. On the other hand, μ -synchrotron

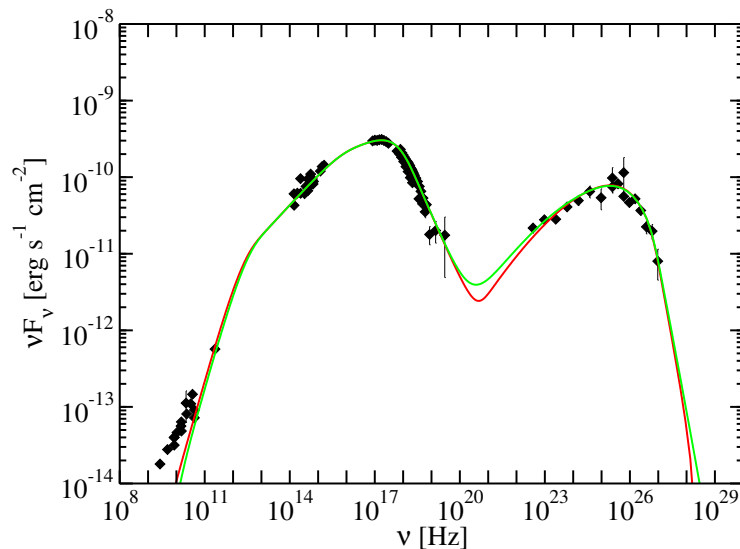
and -cascade” or ” p -synchrotron and -cascade” results in two bumps. Among all the channels, primary-electron synchrotron contributes to the X-ray bump the most, and μ -synchrotron and -cascade to the γ -ray bump the most. The p -synchrotron and -cascade contribute to the γ -ray bump in the second order, and to the energy below the peak of the γ -ray bump.

In hadronic models, protons are needed to be accelerated to 10^{20} eV energy level to provide efficient γ -ray emission mechanisms.

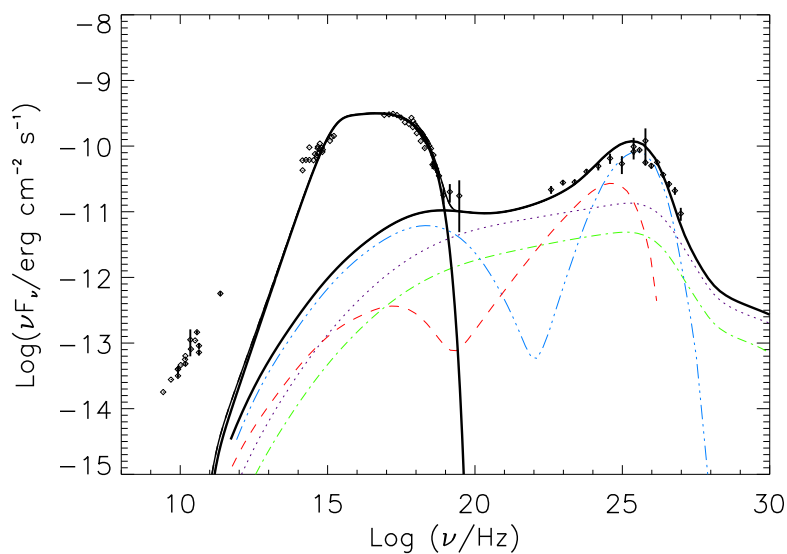
Discussion on models

There have been much simultaneous broadband SEDs (containing VHE spectra) collected for HSP blazars. There have been also many discussions on the degeneracy between different emission models for them. As an example, Figure 2.6 shows the SED of one HSP Mrk 421, modeled with a leptonic model (SSC) and a hadronic model. Both can fit the observed SED well. A possibility to distinguish between them is the variability correlation among different energy bands.

Leptonic models predict multi-wavelength (MW) correlations between the variation of the low-energy bump and that of the high-energy bump when a blazar flares or decays, and this feature has been observed in several HSP blazars. Another observed phenomenon also favors leptonic models: fast variabilities observed in some flaring activities. Because of the mass difference, it is easier for electrons to be accelerated or decelerated quickly, compared with protons. For example, although both leptonic and hadronic models can reproduce the time averaged broadband SED of Mrk 421 (Figure 2.6), it is difficult to produce short time variability (< 1 hour) with hadronic models, which has been observed in Mrk 421 (e.g., [Gaidos et al., 1996]). Besides, a strong magnetic field and a high matter density might be needed in hadronic models. This extreme condition also happens in the case of [Abdo et al., 2011]. Therefore, the leptonic model is favored, at least for active states.



(a) Two 1-zone SSC model fits obtained with different minimum variability timescales: $t_{var} = 1$ day (red curve) and $t_{var} = 1$ hour (green curve).



(b) Hadronic model fit components: π^0 -cascade (black dotted line), π^\pm cascade (green dashed-dotted line), μ -synchrotron and cascade (blue dashed-triple-dotted line), proton synchrotron and cascade (red dashed line). The black thick solid line is the sum of all emission components (which also includes the synchrotron emission of the primary electrons at optical/X-ray frequencies).

Figure 2.6.: Leptonic and hadronic model fits for the Mrk 421 SED from 2009. The image was created by J. Finke, M. Georganopoulos, D. Paneque, T.Reichardt, A. Reimer et al.[Abdo et al., 2011].

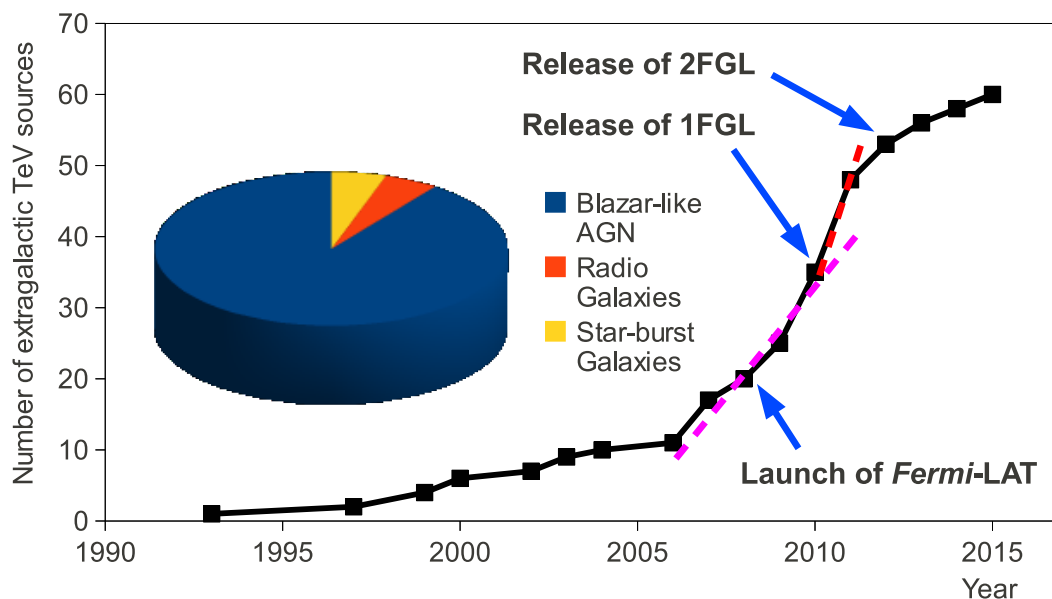


Figure 2.7.: The number of discovered extragalactic VHE sources vs. time: 60 until 2014 June, including three starburst galaxies, three FRI radio galaxies, and all the others are blazars.

2.3. The TeV Blazar Markarian 421

2.3.1. TeV Blazar Discovery

The first extragalactic source detected at TeV energies was the blazar Markarian 421 in 1992 by the Whipple collaboration [Punch et al., 1992], and then the number of the detected sources has increased to 60 until 2014 June. Figure 2.7 shows the growth of the number with respect to time. Not only the number has been increasing, but also the rate of the discovery, partially because of the improved TeV telescopes, partially because of the expansion of the target selection strategy. In the beginning, targets were selected based on radio and X-ray spectral properties [Holder, 2012], later on spectral and variability information from GeV energies became available due to *Fermi* catalogs, which boosted the discovery rate of TeV AGNs. Among these 60 extragalactic TeV sources, there are only three starburst galaxies, three FRI radio galaxies, and all the others are blazars. From this point, we can see that TeV telescopes are particularly suitable for the blazar study.

2.3.2. Markarian 421

Markarian 421 (Mrk 421; RA=11^h4^m27.31^s, Dec=38°12'31.8", J2000) is one of the BL Lac objects, which are believed to have pairs of relativistic jets flowing in opposite directions closely aligned to our line of sight. Mrk 421 is one of the closest ($z = 0.031$; [de Vaucouleurs et al., 1991]) and brightest BL Lac objects in the extragalactic X-ray and VHE sky. This object is the first BL Lac object detected by the Energetic Gamma Ray Experiment Telescope (EGRET; [Lin et al., 1992]) at energies above 100 MeV, and is also the first extragalactic source detected by Imaging Atmospheric Cherenkov Telescopes (IACTs; [Punch et al., 1992]). This is one of the best studied BL Lac objects at VHE because it can be detected by modern IACTs within several minutes, and its broadband SED can be well measured by operating instruments covering energies from radio to VHE. Nearly all the IACTs have measured its VHE γ -ray spectrum [Krennrich et al., 2002, Aharonian et al., 2002, Okumura et al., 2002, Aharonian et al., 2003, Aharonian et al., 2005] [Albert et al., 2007a].

Its integral flux of very-high-energy γ -rays is usually around 0.5 Crab Units (c.u.)² [Acciari et al., 2014], but it may reach > 11 c.u.³ when it flares. The timescale of the flux variation could be occasionally as short as 15 minutes [Gaidos et al., 1996].

The SED from a blazar is dominated by the emission components from its relativistic jet flowing toward observers, which is enhanced by the relativistic beaming effect. The observed spectrum and polarization indicates that the low energy bump is attributed to the synchrotron radiation of electrons in turbulent magnetic fields in the jet. Mrk 421 has a peak frequency of the low-energy bump above 10^{15} Hz, and therefore it is categorized as a high-synchrotron-peaked (HSP) BL Lac object based on the classification criterion presented in [Abdo et al., 2010]. The peak frequency of the high-energy bump for a HSP blazar is usually below 2.4×10^{25} Hz (100 GeV). This bump is interpreted as the inverse Compton scattering of the same population of electrons off synchrotron photons (synchrotron self-Compton, SSC; [Maraschi et al., 1992, Dermer and Schlickeiser, 1993, Bloom and Marscher, 1996]). Alternatively, hadronic models can also explain this bump (e.g., [Mannheim, 1993, Mücke et al., 2003]). Although both leptonic and hadronic models can reproduce the time averaged broadband SED of Mrk 421 (e.g., [Abdo et al., 2011]), it is difficult to produce short time variability (< 1 hour) with hadronic models, which has been observed in Mrk 421 (e.g., [Gaidos et al., 1996]). Thus, leptonic models are favored, at least in active states. In leptonic scenarios, one-zone SSC models with an electron distribution described by one or two power-law functions can typically describe the observed SEDs (e.g., [Katarzyński et al., 2003, Błażejowski, 2005, Rebillot et al., 2006, Fossati et al., 2008, Horan et al., 2009]).

As Mrk 421 is bright and highly variable, long-term multi-wavelength (MW) monitoring campaigns have been organized to deeply study its SED and its temporal evolution from radio to VHE γ rays. Since 2009, an exceptionally long and dense monitoring of the broadband emission of Mrk 421 has been performed. The results of the 2009 MW campaign, which relate to Mrk 421 during non-flaring (typical) activity, were reported in [Abdo et al., 2011]. The SED

²The VHE flux of the Crab Nebula used in this work is 2.2×10^{-10} cm⁻²s⁻¹. This value is obtained by integrating the fit function published in [Aleksić et al., 2012a] from 200 GeV to 10 TeV.

³Mrk 421 emitted in a flux > 11 c.u. in 2013 April. See ATel:<http://www.astronomerstelegram.org/?read=4976>.

is successfully modeled by both a leptonic and a hadronic model, but the authors commented that the hadronic model required extreme conditions for particle acceleration and confinement. Moreover, the exquisite sample of the SED revealed that the leptonic one-zone SSC model required two breaks in the electron energy distribution (EED) to satisfactorily describe the smooth bumps in the quiescent state SED.

Mrk 421 showed high activity during the entire multi-instrument campaign in 2010. During the temporal period spanning from March 10 (Modified Julian Day (MJD) 55265) to March 22 (MJD 55277), the VHE activity decreased from a high flux ~ 2 c.u. down to the typical value ~ 0.5 c.u., hence offering the possibility to study the evolution of the SED during the decay of a flaring event. The extensive MW data collected allow for the measurement of the complete SED with simultaneous observations (mostly within 2-3 hours) during 13 consecutive days. This does not only represent the first time that such a study has been possible for Mrk 421, but more importantly for any blazar, which allows for an unprecedented study of the broadband emission from this object. The SED and indicated physical parameters in the emission region in different epochs and their temporal evolution have been studied (e.g., [Mankuzhiyil et al., 2011, Aleksić et al., 2012b]), but based on sparse sampling. The observational data for 13 consecutive days provides a first opportunity to directly study the temporal evolution of the SED. These are presented in **Chapter 5**, and they are the **main scientific achievement of this PhD thesis**, which was presented in the **33rd International Cosmic Ray Conference**, one of the most prestigious conference in the field of the VHE astronomy and astro-particle in general. It also has just been submitted for the publication in the **Astronomy and Astrophysics journal**. During 2011, the VHE flux from Mrk 421 was between 0.6 and 0.1 Crab units. There were three periods of time when Mrk 421 emitted in very low VHE flux: MJD 55598 (6 February)– 55621 (1 March), MJD 55676 (25 April) – 55688 (7 May), MJD 55714 (2 June) – 55716 (4 June). With the 2011 data, another unprecedented detailed study is made with the evolution of Mrk 421 between its typical state and its very low states. This is presented in Chapter 6.

3. The MAGIC Telescopes and Data Analysis

3.1. The MAGIC Telescopes

The Major Atmospheric Gamma-ray Imaging Cherenkov (MAGIC) telescope system consists of two 17-meter telescopes, which are located on the island La Palma (28°N, 18°W), 2200 m above the sea level. MAGIC I (M1) started operation in 2004; MAGIC II (M2), at a distance of 85 m from MAGIC I, has begun in late 2009. They observe the air showers induced by VHE γ -rays from many astrophysical sources, such as pulsars, supernova remnants, and active galactic nuclei. The stereoscopic mode of the air-shower observation with a parallax angle allows for a three-dimensional event reconstruction, which improves the resolutions and the sensitivity. The integral sensitivity (> 200 GeV): from 2% c.u. to 1% c.u.; the energy resolutions at different energies: from 20–30% to 16–20%. See more explanation in this section.

Mirror and Mount. Both telescopes have a large reflecting dish of a parabolic shape with a diameter of 17 meters. The focal length, f/D , is 1.03. The dish consists of aluminum mirrors. Each mirror panel has two motors behind it to adjust the angle in order to keep the light precisely focused. The control system is named as Active Mirror Control (AMC). The supporting frame of the telescope is made of lightweight carbon fiber. Each telescope is also equipped with quick-rotation drives. The average time for reposition is 20 seconds. The fast repositioning allows for the observation of an abrupt short event such as γ -ray bursts.

Camera. At the focal point of the reflecting dish lies the camera. Its hexagonal active area has a (maximum) diameter of 1.05 meters, and consists of hemispherical photomultipliers (PMTs), which allow for the record of short light pulses. Each PMT has 6 dynodes; the gain is 20000–30000; the effective quantum efficiency (QE) is 25–35%. Each PMT has a Winstoncone outside for the collection and the collimation of photons. The total field of view (FoV) of the camera is 3.6 degrees. At the center is a calibration box emitting pulses of a constant intensity in order to calibrate the signal in each pixel/PMT.

Readout Electronics and Trigger. The electrical pulses from PMTs are converted through the vertical cavity laser diodes (VCSELs) into light pulses (analog signal), and then transmitted through optical fibers to the counting house. There the receiver boards split the signals into the trigger branch and the readout branch. The readout electronics, the Domino Ring Sampler 2 (DRS2)¹ chip, digitizes the signal in a frequency of 2 GHz, with a deadtime of 26 ns for each shower event. In the trigger branch, the software Individual Pixel Rate Control (IPRC) sets the discriminator threshold for each pixel (level-zero trigger; L0 trigger), in order to maintain the

¹This digitizing sampler had been used when the data in this work were taken.



Figure 3.1.: MAGIC telescopes. Image owned by the MAGIC collaboration.

accidental event rate coming from the night sky background (NSB) and the electronic noise at a constant level. Then another trigger condition for each telescope demands a topology of x next neighbors (xNN; level-one trigger; L1 trigger). For stereo observations, the 3NN condition is typically used. Finally, only the events triggering both telescopes are recorded (level-three trigger; L3 trigger).

Performance: the integral sensitivity. Figure 3.2 shows the integral sensitivity of MAGIC. Reading from this figure, MAGIC stereo has an integral sensitivity of $\sim 1\%$ c.u. for the energies > 200 GeV, which means that for a source emitting in a flux of 1% c.u., it takes MAGIC stereo an effective observation time of 50 hours to accumulate the signal significance to 5σ , which is the threshold for declaring the detection of an astronomical source. A lower value of the sensitivity means a higher/better sensitivity. From the MAGIC mono mode to the stereo mode, the integral sensitivity for the energies > 200 GeV has improved from 2% c.u. to 1% c.u.

Performance: the angular resolution. Figure 3.3 shows the angular resolution of MAGIC telescopes. The angular resolution here is defined as the standard deviation from 2-dimensional Gaussian fitting to the distribution of the reconstructed γ -ray direction. The events within 1σ of a 2-dimensional Gaussian distribution take up 39% of the total. Figure 3.3 also shows the radius wherein 68% of the events are distributed. The angular resolution for γ -rays > 100 GeV is better than 0.1° .

Performance: the energy resolution. Figure 3.4 shows the energy resolution and the energy bias of MAGIC telescopes. The energy resolution here is defined as the standard deviation from a Gaussian function fit to the distribution of $(E_{rec} - E_{true})/E_{true}$ from MC γ -ray events. The events within 1σ of a Gaussian distribution take up 68% of the total. The energy bias is defined as the mean of the distribution. The energy resolution and the energy bias slightly depends on the $Hadronness^2$ and the θ^2 ³ cuts. Stricter cuts usually enhance the resolution and reduce the bias. Figure 3.4 results from $Hadronness < 0.6$, $\theta^2 < 0.03$.

²See Section 3.2 for explanation.

³ θ is the separation angle between the source direction and the reconstructed γ -ray direction.

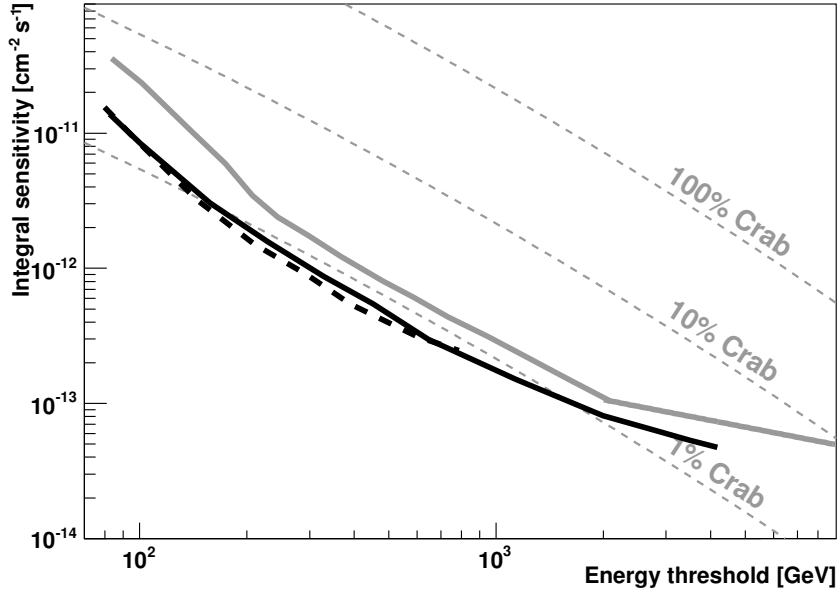


Figure 3.2.: The integral sensitivity of the MAGIC telescopes. Solid black line: calculated from MAGIC stereo data; dashed line: from MAGIC stereo MC data; solid gray line: from MAGIC I. For comparison, fractions of the integral Crab Nebula spectrum are plotted in thin dashed gray lines. Image created by the MAGIC collaboration [Aleksić et al., 2012c].

The energy resolution is 16–20% between 100 GeV and 10 TeV. For higher energies it is slightly worse because of a larger fraction of the shower image is truncated, and showers with higher *Impact* parameters⁴ and poorer statistics in the training sample; for lower energies, it is also worse because of a lower photon number, higher relative noise, and a worse estimation of the arrival direction, which spoil the precision of the *Impact* parameter reconstruction.

The energy bias is below 20% at the energies > 100 GeV. For lower energies, the bias is larger because of the threshold effect. In the spectrum analysis, the process of *unfolding* corrects for this bias as well as for the finite resolution of the energy reconstruction. The *unfolding* is explained in Section 3.2.

Performance: systematic uncertainties. The systematic uncertainties in the spectral measurements with MAGIC stereo observations are 11% in the normalization factor (at > 300 GeV) and 0.15–0.20 in the photon index. The error on the flux does not include uncertainty on the energy scale. The energy scale of the MAGIC telescopes is determined with a precision of about 17% at low energies ($E < 100$ GeV) and 15% at medium energies ($E > 300$ GeV). Further details are reported in [Aleksić et al., 2012a].

⁴See Section 3.2 for explanation.

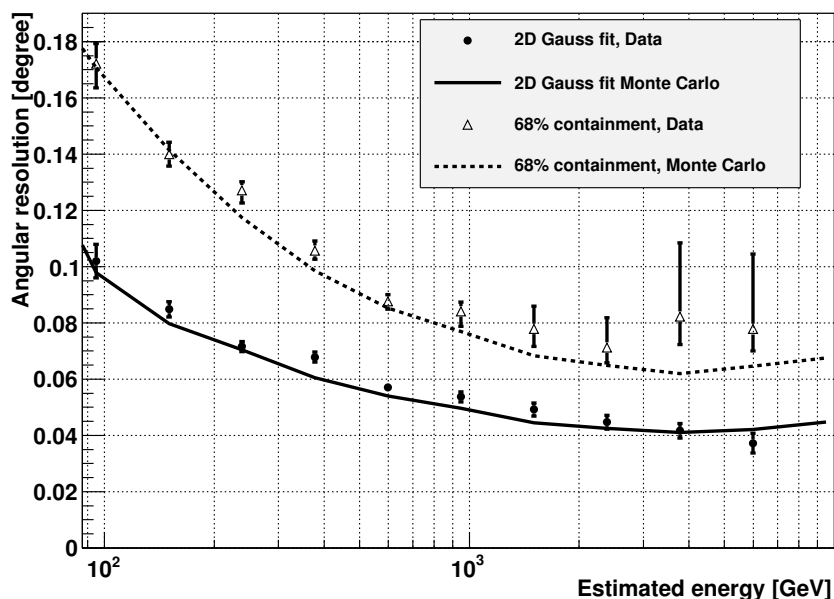


Figure 3.3.: The angular resolution of MAGIC telescopes. The angular resolution here is defined as the standard deviation from a 2-dimensional Gaussian fitting to the distribution of the reconstructed γ -ray direction. The events within 1σ of a 2-dimensional Gaussian distribution take up 39% of the total. The angular radius within which 68% of events are distributed is also shown for comparison. Image created by the MAGIC collaboration [Aleksić et al., 2012c].

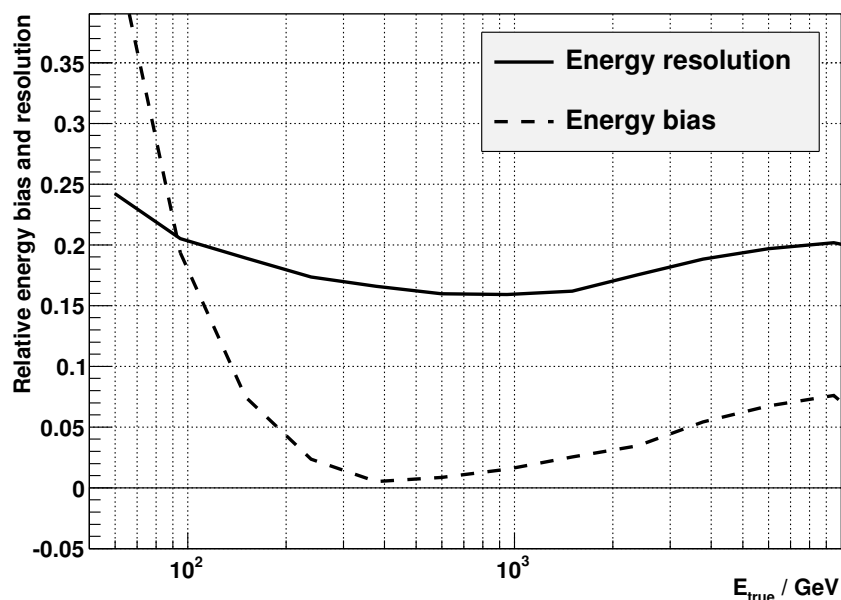


Figure 3.4.: The energy resolution (solid line) and the energy bias (dashed line) of the MAGIC telescopes. Image created by the MAGIC collaboration [Aleksić et al., 2012c].

3.2. MAGIC Data Analysis

The data are analyzed through the MARS analysis framework [Moralejo et al., 2009], using the standard routine for the data taken in the stereoscopic mode. In this work, the version up to V2-13-5 has been used for the data analysis. The goal of the analysis is to compute the number of γ -ray events from a particular direction of the sky per unit time and per unit area in different particle-energy ranges. To achieve this, we have to extract possible signals, to reconstruct the arrival time, the energy and the direction of a particle by the shower image on the camera, to reject background events, and to calculate the effective area of the telescopes. The procedures are described in the following.

Signal Extraction and Calibration

The original information given by a pixel of the camera is a waveform. The arrival time and the strength of the signal are to be determined from it. The relative time delays among different pixels/channels are considered. The goal of the signal-strength analysis is to convert the size of the wave to the equivalent number of photo-electrons. To achieve this, the pedestal level and the signal-strength-calibration information are measured. The pedestal is subtracted from the waveform, and the integral of the resulting waveform over time S is calculated. Then S is converted to the number of photo-electrons N through a conversion factor k ($N = kS$). In order to estimate k , a calibration pulsing light with a stable intensity is used for emitting signals to the camera. The conversion factor k is computed through the *F-factor method* [Shockley and Pierce, 1938]:

$$k = \frac{F^2 \mu_C^2}{\sigma_C^2}, \quad (3.1)$$

$$F = \sqrt{1 + \frac{\mu_G^2}{\sigma_G^2}}, \quad (3.2)$$

where C is the integral value from the calibration pulse, G the gain of the PMT, μ the mean of many measured values of C or G , and σ the root mean square of many measured values of C or G . F can be measured in the laboratory.

Image Cleaning

The contribution from the night sky background and the electronic pixel noise is removed through the so-called image cleaning. The method consists in identifying the pixels with the signal and setting the charge of all the other pixels to 0. The definition of the shower image is subject to change according to different situations, such as the moon light condition, the MAGIC I or the MAGIC II camera, the trigger mode. To define the shower image, the core pixels are found out firstly: for the data condition in this work, at least 3 neighboring pixels with a charge of at least $6(M1)/9(M2)$ photo-electrons, whose arrival time are within a window of 4.5 ns required. The boundary pixels are defined as those which surround the core pixels, have a charge of at least $3(M1)/4.5(M2)$ photo-electrons, and an arrival-time difference to the neighboring core pixels of within 1.5 ns.

Data Quality Selection

Data are grouped into several sets according to the observation zenith angle (ZA) and the moon light condition, and treated in separate analysis pipelines. In this work, data are grouped as: 5–28 degrees, 28–40 degrees, 40–50 degrees⁵; the data that can be analyzed as in the dark condition are picked up: the direct current (DC) < 1500 nA or the trigger rate > 90 Hz (for MAGIC I data); 80 Hz (for MAGIC II data); the total charge (in photo-electrons) contained in the shower image (*Size*) > 50.

The weather condition also affects the data quality: a cloudy condition might lead to the underestimation of the flux from a source. We usually use the number of the stars seen by the star guider, and the cloudiness measured by the pyrometer⁶, as parameters to choose the data. Data with too low a number of stars or with too high cloudiness are not used. Sometimes data are taken under some hardware technical problems. The trigger rate is an important parameter to remove not-optimal data because it is sensitive to the light condition and the hardware condition. Typically it should stay in a reasonable range, and the data outside the group are to be excluded because it might mean unexpected disturbances. In this work, the following conditions are used: the cloudiness < 50, the number of stars in the star-guider > 15, the trigger rate range: within 30% of the mean in that observation.

Stereoscopic Shower Image Parameterization

The shower images were parameterized with an extended set of Hillas parameters [Hillas, 1985a]. They are calculated to describe the characteristics of the image, in order to use them for the event reconstruction.

Size: the total charge (in photo-electrons) contained in the image.

Length: the root mean square of the charge distribution along the major axis of the image ellipse.

Width: the root mean square of the charge distribution along the minor axis of the image ellipse.

Conc(N): the fraction of the total charge contained by the N brightest pixels

COG: center of gravity; the mean (charge-weighted) position of the image

TimeGradient: the velocity of the temporal evolution along the major axis of the ellipse; it shows how fast the arrival time changes along this axis; the sign of this parameter depends on the expected source location on the camera plane: it is positive if the arrival time increases when moving away from the source location.

⁵The values of $\cos(5^\circ)$, $\cos(28^\circ)$, $\cos(40^\circ)$, and $\cos(50^\circ)$ are evenly distributed. The event rate is affected by the ZA. The $\cos(ZA)$ can approximately normalize the event rates at different ZAs to the same value. This data grouping makes the event rates similar in a group.

⁶The pyrometer measures the integral radiant flux between 8 and 14 mm in a FOV of 2 degree. From this, a temperature according to the black body radiation is calculated. In optimal conditions, the sky temperature at zenith is 198 K. It increases with increasing zenith distance. At 60 degrees, it is about 220 K. The sky temperature $T(ZA)$ at optimal conditions is a function of ZA. At $T_b=250$ K, the sky is covered with clouds for sure (the clouds reflect the thermal radiation of the earth). The cloudiness c is calculated as follows: $c = [T_m - T(ZA)]/[T_b - T(ZA)]$, where T_m is the measured sky temperature at the zenith angle ZA. See <http://www.astro.uni-wuerzburg.de/wikineu/index.php/Cloudiness>.

Dist: the angular distance between the COG and the expected source location on the camera plane

Impact: the distance between the center of the telescope and the extended shower axis

MaxHeight: the altitude of the location of the shower maximum; this value is zero at the telescope altitude; the location of the shower maximum corresponds to the COG on the camera plane

CherenkovRadius: the radius of the Cherenkov light pool on the ground; assuming the Cherenkov light produced by a single electron of 86 MeV at the height of the shower maximum

CherenkovDensity: the Cherenkov photon density on the ground with the previous assumptions

Gamma-Hadron Separation

To distinguish γ -rays from hadrons, a method called "Random Forests" (RF; [Bock et al., 2001], Breiman, L., "Random Forests", Machine Learning, 45, p5, 2001) is used to obtain a linear discerning parameter called hadronness, which ranges between 1 and 0 in order to describe how much a shower event is γ -like (*Hadronness* = 0). The first step is to build up the decision trees with the training samples: Monte-Carlo(MC)- γ -event simulations and real data. In this work, the following MC data are used:

- MC superstar files for lower zenith angles(5–35 deg) with tags of Ringwobble, Dortmund, Image cleaning: M1_6-3 , M2_9-4.5
- MC superstar files for higher zenith angles(35–50 deg) with tags of Ringwobble, Dortmund, Image cleaning M1_6-3, M2_9-4.5

Several event parameters, such as *Size*, *Length*, *Width*, *Conc*, *Impact*, *MaxHeight* and *TimeGradient*, are used to separate γ events from hadronic ones. For each separation, a parameter is chosen randomly. The best separation value of this parameter is obtained by minimizing the Gini index Q_{Gini} [Gini, 1921]. Taking an example with *MaxHeight* as separation parameter,

$$Q_{Gini} = 2 \times \left(\frac{N_g^{MaxHeight>q} + N_h^{MaxHeight>q}}{N_g^{MaxHeight>q} N_h^{MaxHeight>q}} + \frac{N_g^{MaxHeight<q} + N_h^{MaxHeight<q}}{N_g^{MaxHeight<q} N_h^{MaxHeight<q}} \right), \quad (3.3)$$

where q is the parameter cut value to be optimized, N_g is the number of γ events, N_h is the number of hadron events, $N_g^{MaxHeight>q}$ is the number of γ events with the parameter *MaxHeight* larger than q . The separation process continues with other parameters until the samples are dominated by one class or there are too few rest samples. Finally for this tree i , at the end of each branch, the parameter hadronness is calculated as:

$$Hadronness_i = \frac{N_g^p + N_h^p}{N_h^p}, \quad (3.4)$$

where N_h^p means the number of hadron events in the condition of p . Many trees are generated in this way. A to-be-judged real event can be put into all the trees, and the hadronness will be

the average of all Hadronness_{*i*}'s. In this work, official RFs produced and examined by J. Krause⁷ (a former post-doc at MPI) are used. The following hadronness conditions are used to pick up the γ -ray events: the 95% efficiency for the MC data in ZA 5-28 degrees, the 99% efficiency for 28-40 degrees and 40-50 degrees. These conditions are examined by application onto Crab Nebula data from 2009 November to 2010 March. The resulted Crab Nebula spectra are shown in Appendix C.1, with comparison from the spectrum fit function in [Zanin, 2011].

Arrival Direction Reconstruction

The point on the camera corresponding to the arrival direction is one point on the major axis of the shower ellipse. The angular distance between the *COG* and the arrival direction, *Disp* can be determined by another random forest with the parameters *Size*, *Length*, *Width*, *Dist*, *MaxHeight*, *Impact*, and *TimeGradient*. Each telescope can find its own *Disp*. Another possibility (stereo) is to combine two shower images and find the cross-over of the two major axes, and the estimated arrival direction is at the cross-over. Since three estimated arrival directions from *Disp*₁, *Disp*₂, and the stereo cross-over are obtained, a decision process is used to determine the direction, and it can also reject possibly-badly-reconstructed event. It is designed to reduce the ambiguity in reconstruction particularly for low-energy shower events or the events with two somewhat parallel shower ellipses.

Once the arrival direction is determined, comparing with the expected source direction, the separation angle of these two directions, θ_{on} , can be calculated. Those with $\theta_{\text{on}} < 0.1^\circ$ give N_{on} . The source direction and the telescope pointing direction together define the off-direction (the most-frequently used one): the pointing direction has equal angular distances to the source- and off- directions. The separation angle between the arrival direction and the off-direction is θ_{off} . Those with $\theta_{\text{off}} < 0.1^\circ$ give N_{off} . Then the number of γ events from the source, N_{excess} , is $N_{\text{on}} - \alpha N_{\text{off}}$, where α is the ratio between on-events and off-events with $\theta > 0.1^\circ$. The significance for the γ events can be estimated as [Li and Ma, 1983]

$$N_\sigma = \sqrt{2} \left(N_{\text{on}} \cdot \ln \left[\frac{1 + \alpha}{\alpha} \cdot \frac{N_{\text{on}}}{N_{\text{on}} - N_{\text{off}}} \right] + N_{\text{off}} \cdot \ln \left[(1 + \alpha) \cdot \frac{N_{\text{off}}}{N_{\text{on}} - N_{\text{off}}} \right] \right)^{1/2}. \quad (3.5)$$

Energy Reconstruction

One look-up table for each telescope is used to reconstruct the energy of the γ -ray and its uncertainty. This table is constructed with γ -ray MC data. The table has two dimensions: *Size* and *Impact/CherenkovRadius*. Each *Size* value and each *Impact/CherenkovRadius* value together determine a distribution of $E_{\text{true}} \cdot \text{CherenkovDensity}/\text{Size}$, including its mean and the RMS. E_{true} is the true γ -ray energy, which is proportional to *Size/CherenkovDensity*. The estimated energy of the γ -ray, E_{est} , and its uncertainty is obtained at first in this way. Then the values from both telescopes together give an average value according to the weighting from the energy uncertainty. Finally, E_{est} is corrected for its empirical ZA dependence by a factor of $0.4 \times \cos(\text{ZA})$.

⁷<https://www.mpp.mpg.de/jkrause/>

Energy Spectrum Calculation

To calculate the energy spectrum of the γ -ray source $\frac{d^3 N_{\text{excess}}}{dAdEdt}$ (A : the effective area of the MAGIC telescopes, E : γ -ray energy, t : the effective observation time), the estimation of the effective area and observation time is necessary beside the N_{excess} obtained in the previous procedure.

The effective area is estimated from γ -ray Monte-Carlo simulations. For each ZA and energy bin, the corresponding effective area $A_{E_j}^{ZA_i}$ is obtained through the ratio between the number of the detected γ -ray events $\text{det}N_{E_j}^{ZA_i}$ and the total number of the generated ones $\text{gen}N_{E_j}^{ZA_i}$:

$$A_{E_j}^{ZA_i} = A_0 \cdot \frac{\text{det}N_{E_j}^{ZA_i}}{\text{gen}N_{E_j}^{ZA_i}}, \quad (3.6)$$

where A_0 is a circular area (radius 450 m) within which the γ -ray events are generated.

The effective observation time τ is estimated through fitting the distribution of the time separation between one event and the next, δt , with the following function:

$$ce^{-\frac{\delta t}{\tau}}, \quad (3.7)$$

which results from Poisson statistics, describing the probability that no event is detected within a time-interval δt :

$$P(\delta t) = e^{-p\delta t}, \quad (3.8)$$

where p is the probability to detect an event during a unit time-interval.

After obtaining the effective area, γ -ray energy, and the effective observation time, the preliminary energy spectrum is calculated. The preliminary spectrum still needs to undergo an unfolding process in order to correct the errors resulting from the limited energy resolution and the low-energy bias around the energy threshold [Albert et al., 2007b]. The true spectrum, vector T , is mis-constructed (M), to a biased reconstructed spectrum, vector R :

$$R = M \cdot T, \quad (3.9)$$

where the matrix M is called the migration matrix, which contains the relation between E_{true} and E_{est} . M and R are known, and the goal is to get $T = M^{-1}R$. The non-diagonal matrix M brings large statistical errors of T , so another process, the *regularization*, is used to smoothen the resulted spectrum. Different regularization methods are used to check whether the results can meet each other. The process mentioned above gives the corrected (unfolded) spectral points. The parameters describing the spectral shape are obtained with the so-called *forward folding*, which does not involve any regularization. The forward folding determines the spectral shape parameters through the minimum- χ^2 fit function to the excess distribution over the estimated energy.

4. Observations of Markarian 421 with MAGIC in 2010 and 2011

In this chapter, the results from MAGIC observations of Mrk 421 in 2010 and 2011 are presented. The methods of data analysis are given in Section 3.2. In Section 4.1, the observed VHE flux is presented. A derived parameter from different energy bands in the Light Curves (LCs), the hardness ratio, is calculated for each date, and its relations with the time and the flux are also shown. In Section 4.2, the spectra for single observations and their fit parameters are reported and discussed.

The MAGIC observations are classified according to their reliability:

Class A: Excellent data: low zenith angles, good weather conditions and no technical problems. All these data can be analyzed with the same analysis pipeline (and MC data)

Class B: Data that require some "extra work" to analyze, and that "potentially" could have larger systematics. These data could be split into the following categories:

Class B1: high zenith angles ($ZA > 28$ deg)

Class B2: the observations performed with moonlight or twilight

Class B3: the data which suffer from some technical problems (e.g. calibration runs for that particular day did not work, but one could use calibration constants from previous or posterior days)

Class C: the data that cannot be used

4.1. Very-High-Energy Flux Variability

We analyze the flux of each date in different energy bands:

Full-energy band: > 200 GeV

Low-energy band: $100 - 300$ GeV

Medium-energy band: 300 GeV – 1 TeV

High-energy band: > 1 TeV

The daily LC of the full-energy band from 2010 is shown in Figure 4.1. There were large flux increases (flaring activities) in January, February, March, and May, with peak VHE fluxes (> 200 GeV) of 6.3, 2.6, 4.7, $2.6 \times 10^{-10} \text{cm}^{-2} \text{s}^{-1}$ respectively. The VHE emission from the Crab Nebula is about $2.2 \times 10^{-10} \text{cm}^{-2} \text{s}^{-1}$. These flares correspond to 2.9, 1.2, 2.1, 1.2 c.u., while the typical Mrk 421 VHE emission is about 0.5 c.u.. The calculated flux is very accurate for most of the observations. (See the high significances of the observations.) Exceptions arose the occasions where the source was in its low state, the observation condition was not perfect, and/or the observation time was very short. Typical disadvantageous observation conditions are bad weather, bright moonlight, bright twilight, or technical problems. In Figure 4.1, there were some dates when the ratio of effective time to observation time was lower than 0.4. During the observations on those dates, there were moonlight or twilight. The data taken under too bright a condition were removed (as explained in Section 3.2).

The 2011 daily LC of the full-energy band, the significance of flux observation, and the observation time are shown in Figure 4.2. During this period, the VHE flux from Mrk 421 was between 0.6 and 0.1 c.u., and hence showing a flux that was often lower than its typical flux level of 0.5 c.u. With 2011 data, it is possible to study the evolution of Mrk 421 between its typical states and its very low states. There were three periods of time when Mrk 421 showed very low VHE activities: MJD 55598 (6 February) – 55621 (1 March), MJD 55676 (25 April) – 55688 (7 May), MJD 55714 (2 June) – 55716 (4 June).

The LCs of the low-, medium-, and high-energy bands (F_L , F_M , and F_H) are shown in Figure 4.3. From any two of them, the hardness ratio is calculated as follows:

$$H_{H/L} = \frac{F_H}{F_L}, \quad H_{H/M} = \frac{F_H}{F_M}, \quad H_{M/L} = \frac{F_M}{F_L}.$$

The three hardness ratios, $H_{H/L}$, $H_{H/M}$, and $H_{M/L}$ are reported in Figure 4.4. Comparing Figure 4.3 with Figure 4.4, the evolution of the hardness ratio with the time seems to be correlated to the evolution of the flux: a higher hardness ratio is related to a higher flux. In order to study the relation between the hardness ratio and the flux, three plots of "hardness ratio vs. flux" are shown in Figure 4.5. In order to have small uncertainties in the fluxes reported in the x-axis of the plots, the flux from the medium-energy band F_M is chosen. The uncertainties in F_L and F_H are higher than in F_M because MAGIC has small effective areas at low energies, and the number of photons from the source is very low at high energies.

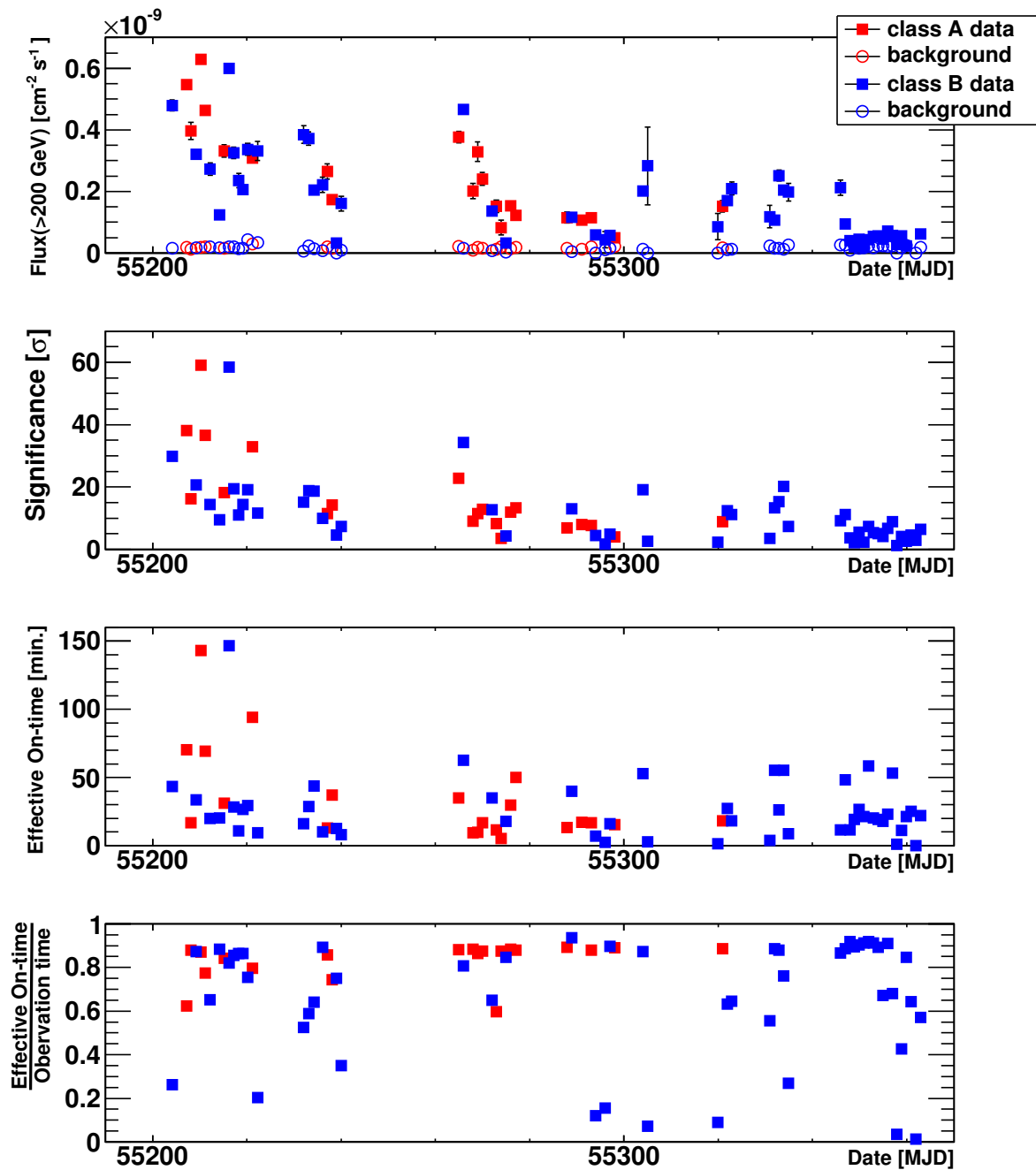


Figure 4.1.: The 2010 LC of > 200 GeV (the 1st panel), the significance of flux observation computed according to Equation 17 in [Li and Ma, 1983] (the 2nd panel), the observation time (the 3rd panel), the ratio of the effective time to the observation time (the 4th panel). The definition of the class A/B data is given in the beginning of this chapter.

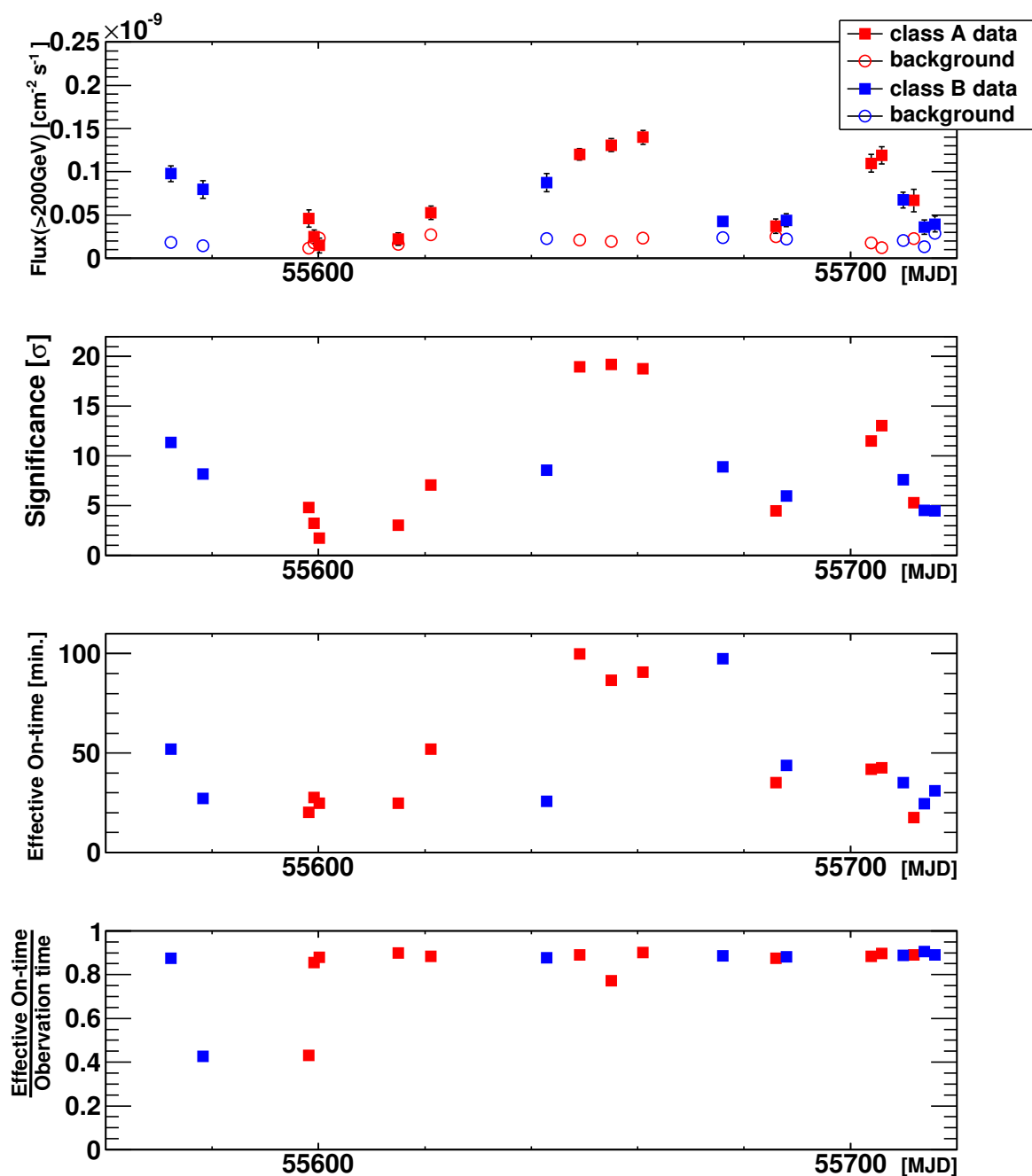
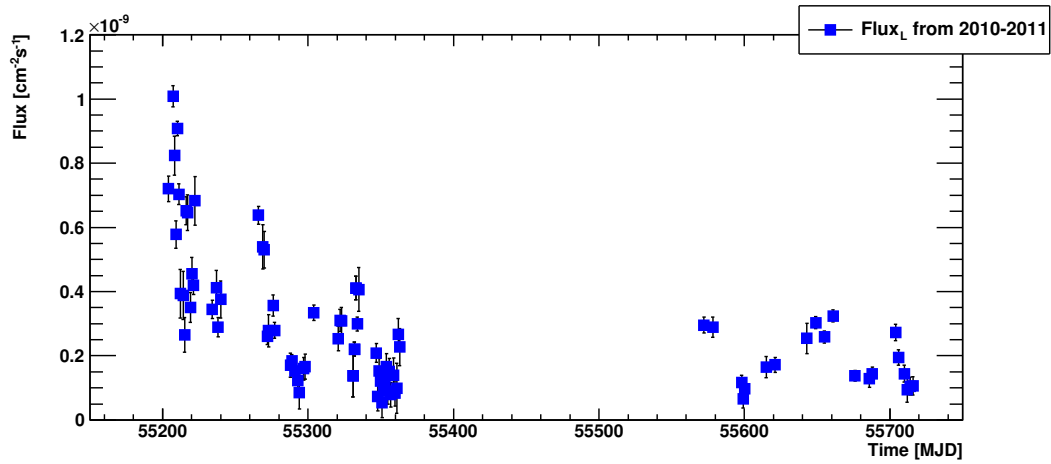
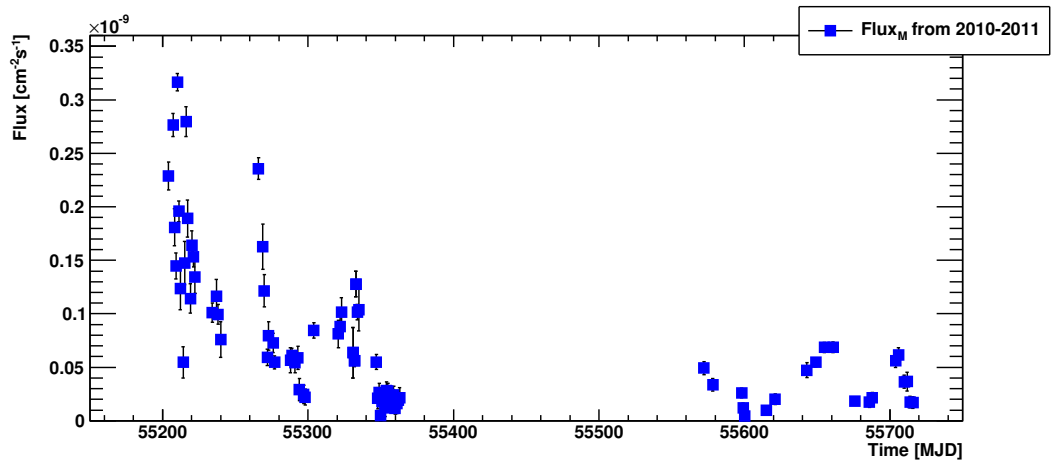


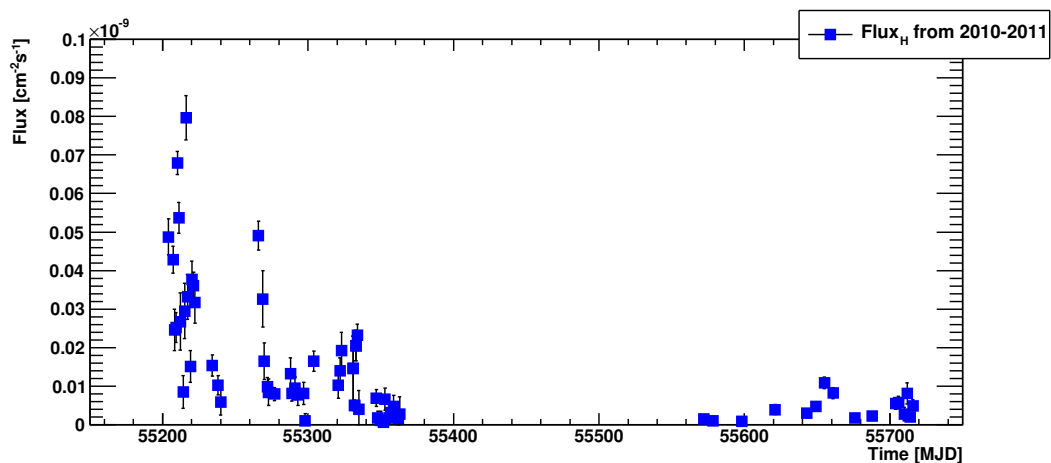
Figure 4.2.: The 2011 LC of > 200 GeV (the 1st panel), the significance of flux observation computed according to Equation 17 in [Li and Ma, 1983] (the 2nd panel), the observation time (the 3rd panel), the ratio of the effective time to the observation time (the 4th panel). The definition of the class A/B data is given in the beginning of this chapter



(a) The flux at the low-energy band.

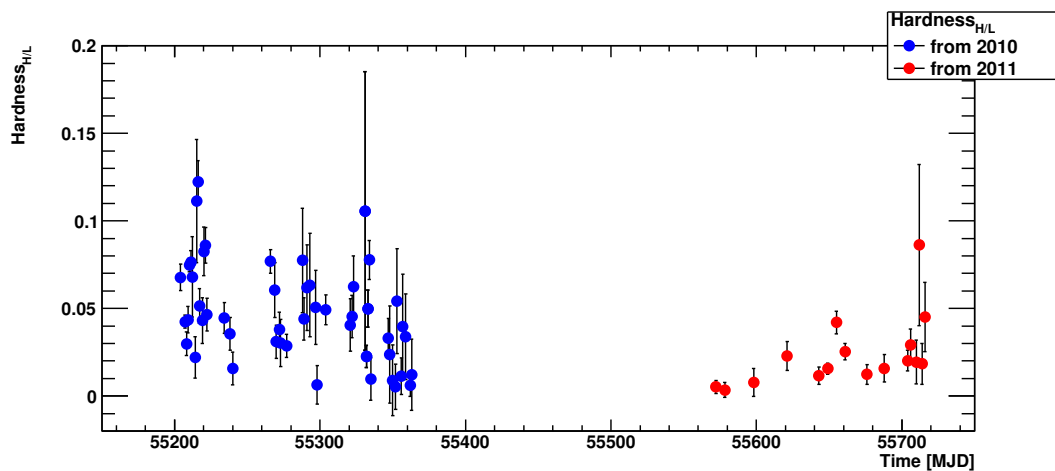
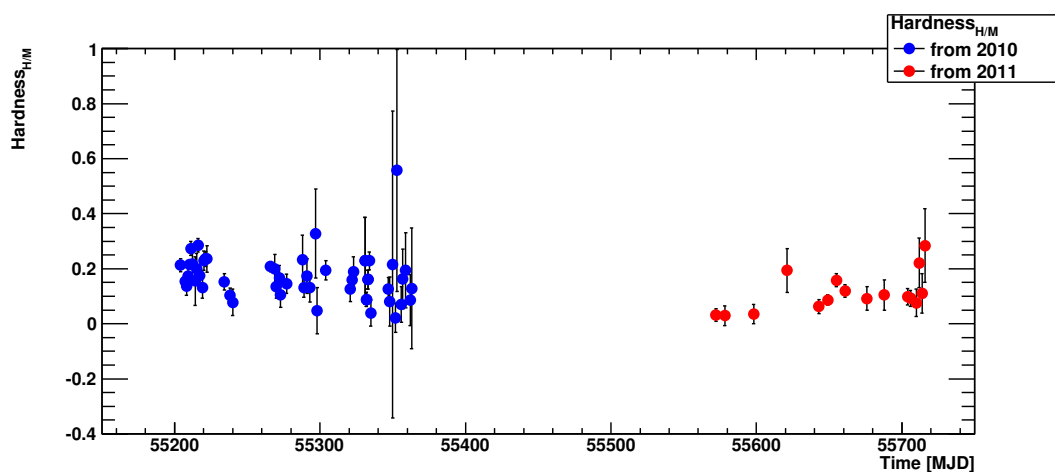
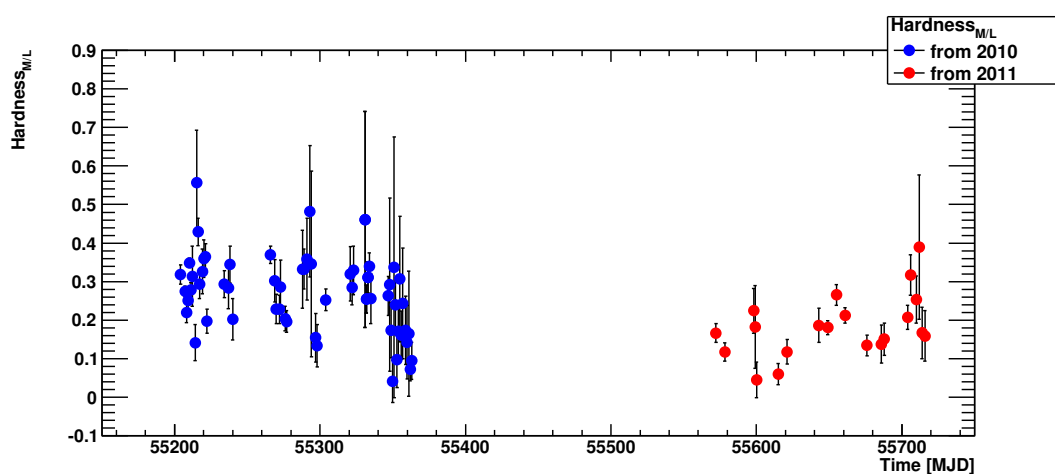


(b) The flux at the medium-energy band.



(c) The flux at the high-energy band.

Figure 4.3.: The 2010–2011 LCs at three energy bands: 100–300 GeV (low-energy band), 300–1000 GeV (medium-energy band), > 1 TeV (high-energy band).

(a) $H_{H/L} = F_H/F_L$.(b) $H_{H/M} = F_H/F_M$.(c) $H_{M/L} = F_M/F_L$.Figure 4.4.: 2010–2011 hardness ratio vs. time: $H_{H/L}$, $H_{H/M}$, $H_{M/L}$.

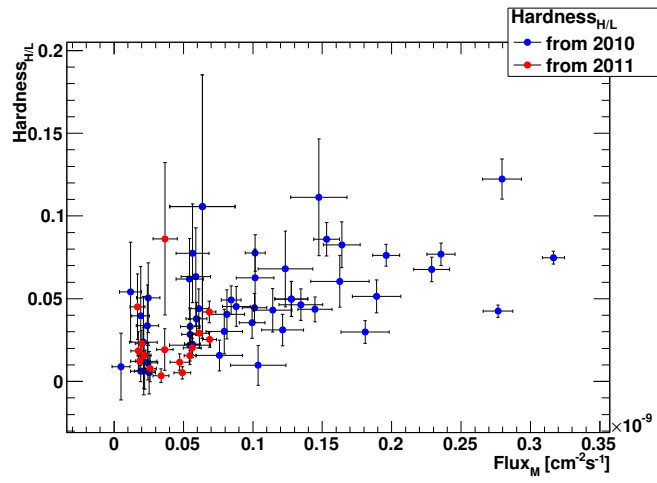
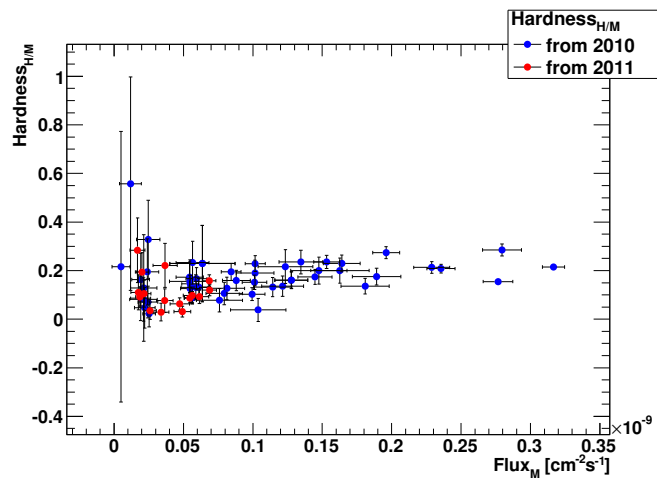
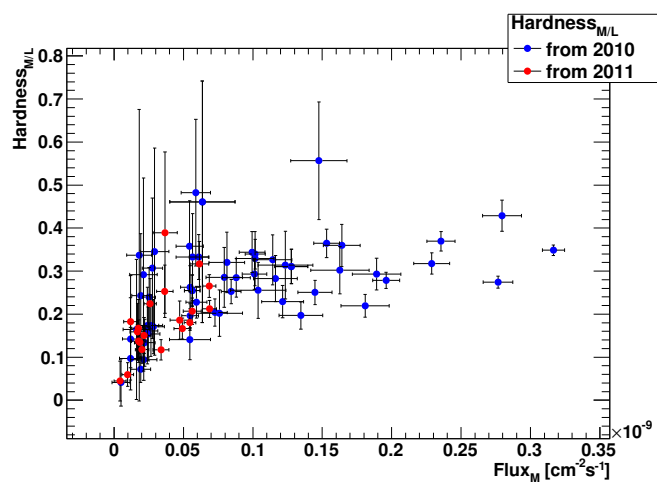
(a) $H_{H/L}$ vs. medium-band flux.(b) $H_{H/M}$ vs. medium-band flux.(c) $H_{M/L}$ vs. medium-band flux.

Figure 4.5.: Hardness ratio vs. flux.

As F_H has large error bars (because of poorer photon statistics), the error bars of $H_{H/L}$ and $H_{H/M}$ are larger, and the trends in them are rather difficult to read. There is a clear trend in the " $H_{M/L}$ vs. F_M " plot: the hardness ratio increases with the flux until $F_M \sim 0.1 \times 10^{-9} \text{ cm}^{-2}\text{s}^{-1}$, and then the hardness ratio remains approximately constant at a value of $H_{M/L} \sim 0.3$. This saturation in the hardness ratio for high photon fluxes could be produced by a lower efficiency in the inverse-Compton scattering in the Klein-Nishina regime to produce high-energy γ -rays.

4.2. Very-High-Energy Spectral Variability

We resolved the VHE spectrum of Mrk 421 in 2010 and 2011 day-by-day. In order to describe the features of the spectra quantitatively, several functions are used to fit each spectrum:

- A power-law function

$$f_0 \cdot \left(\frac{E}{300\text{GeV}} \right)^\alpha \quad [\text{TeVcm}^{-2}\text{s}^{-1}], \quad (4.1)$$

There are 2 free parameters in this function: the flux constant f_0 , and the photon index α .

- A power-law function with an exponential cutoff

$$f_0 \cdot \left(\frac{E}{300\text{GeV}} \right)^\alpha e^{-\frac{E}{E_0}} \quad [\text{TeVcm}^{-2}\text{s}^{-1}], \quad (4.2)$$

There are 3 free parameters in this function: the flux constant f_0 , the photon index α , and the cutoff energy E_0 .

- A power-law function with a fixed exponential cutoff at 4 TeV

$$f_0 \cdot \left(\frac{E}{300\text{GeV}} \right)^\alpha e^{-\frac{E}{4\text{TeV}}} \quad [\text{TeVcm}^{-2}\text{s}^{-1}], \quad (4.3)$$

There are 2 free parameters in this function: the flux constant f_0 , and the photon index α . This function fixes the cutoff energy E_0 at 4 TeV, in comparison to the previous function. With the cutoff energy fixed, the change of spectra reflects on the flux constant and the photon index, and thus the relation between the flux and the photon index becomes easier to study.

- A log-parabola function

$$f_0 \cdot \left(\frac{E}{300\text{GeV}} \right)^{\alpha + \beta \log\left(\frac{E}{300\text{GeV}}\right)} \quad [\text{TeVcm}^{-2}\text{s}^{-1}], \quad (4.4)$$

There are 3 free parameters in this function: the flux constant f_0 , the photon index α , and the log-parabola index. The purpose of fitting with this function is to test the effectiveness of describing the electron energy distribution with a log-parabola function, which is supported by some particle acceleration theories.

Table 4.1. Fit Parameters from the Fit Function 4.1 (power-law) for the spectra in Figures 4.6 – 4.7.

Date	$f_0[\text{TeV cm}^{-2}\text{s}^{-1}]$	α	χ^2/ndf	Prob.	Sig.
2010.01.08	$(6.79 \pm 0.32) \times 10^{-11}$	-2.23 ± 0.03	47.1/12	4.3×10^{-6}	4.59
2010.01.14	$(9.22 \pm 0.21) \times 10^{-11}$	-2.18 ± 0.01	136./13	8.8×10^{-23}	9.82
2010.01.20	$(9.15 \pm 0.19) \times 10^{-11}$	-2.11 ± 0.01	129./12	6.2×10^{-22}	9.63
2010.01.25	$(4.88 \pm 0.18) \times 10^{-11}$	-2.15 ± 0.02	30.4/13	4.0×10^{-3}	2.88
2010.02.07	$(2.83 \pm 0.27) \times 10^{-11}$	-2.27 ± 0.06	14.0/10	1.7×10^{-1}	1.37
2010.02.11	$(2.70 \pm 0.29) \times 10^{-11}$	-2.23 ± 0.06	15.9/12	1.9×10^{-1}	1.30
2010.05.17	$(3.77 \pm 0.39) \times 10^{-11}$	-2.23 ± 0.06	11.9/12	4.4×10^{-1}	0.76
2010.06.10	$(9.03 \pm 1.78) \times 10^{-12}$	-2.39 ± 0.15	9.5/13	7.2×10^{-1}	0.35
2011.04.10	$(1.66 \pm 0.13) \times 10^{-11}$	-2.51 ± 0.04	15.2/12	2.3×10^{-1}	1.20
2011.04.25	$(3.82 \pm 0.78) \times 10^{-12}$	-2.81 ± 0.12	17.3/8	2.6×10^{-2}	2.21
2011.05.23	$(1.48 \pm 0.20) \times 10^{-11}$	-2.46 ± 0.08	6.5/12	8.8×10^{-1}	0.15
2011.05.31	$(1.29 \pm 0.45) \times 10^{-11}$	-2.04 ± 0.28	4.5/8	8.0×10^{-1}	0.24

Note. — Prob. is the probability for χ^2 to be larger; if it is smaller than 0.05, the model significantly (with a 95% confidence level) deviates from the data. Sig. is the significance of the deviation, in unit of σ .

The spectra for the single MAGIC observations, fitted with the four functions mentioned above, are reported in Appendix B. In Figures 4.6 and 4.7, we show spectra only for few selected dates. They are selected according to the integral flux and the spectra shape. The flux is dominated by how high the low-energy spectral point is. In these figures, spectra are put in the order of "with very high, high, medium, and low integral fluxes". The shapes of spectra are classified into "with hard, medium, or soft photo-indices". Seeing the variation of the spectra, one can realize the complexity of the blazar behavior in the VHE band. We present the spectra in the form of $E^2 \frac{dN}{dE}$, the so-called spectral energy distribution (SED). The power-law index of the VHE spectra are typically between -2 and -3, and hence the term E^2 makes the decline tendency of the spectra smaller and thus features of index variations in the spectra can be noticed more easily.

In Figures 4.6 and 4.7, not only spectra but also the 4 fit results are provided. These fits are correlated fits. The fit contours are the lines enclosing the spectra points from the forward folding of the original spectra (see Section 3.2). The forward folding shows the data distribution expected from the input fit function and the original data distribution. The contours denote the 68% uncertainties of the fits. Note that the ranges of the fits and that of the SED data points could be slightly different because they are computed with the forward folding and the unfolding methods respectively.

Note that the ranges of the fits and that of the SED data points could be slightly different because they are computed with the forward folding and the unfolding methods respectively. The energy binnings in these two foldings are different, so the number of spectrum points cannot be directly used for the ndf calculation in the fit. The fit parameters for the spectra in Figures 4.6 and 4.7 are listed in Tables 4.1 – 4.4. The parameters for all the dates can be found in Appendix B.

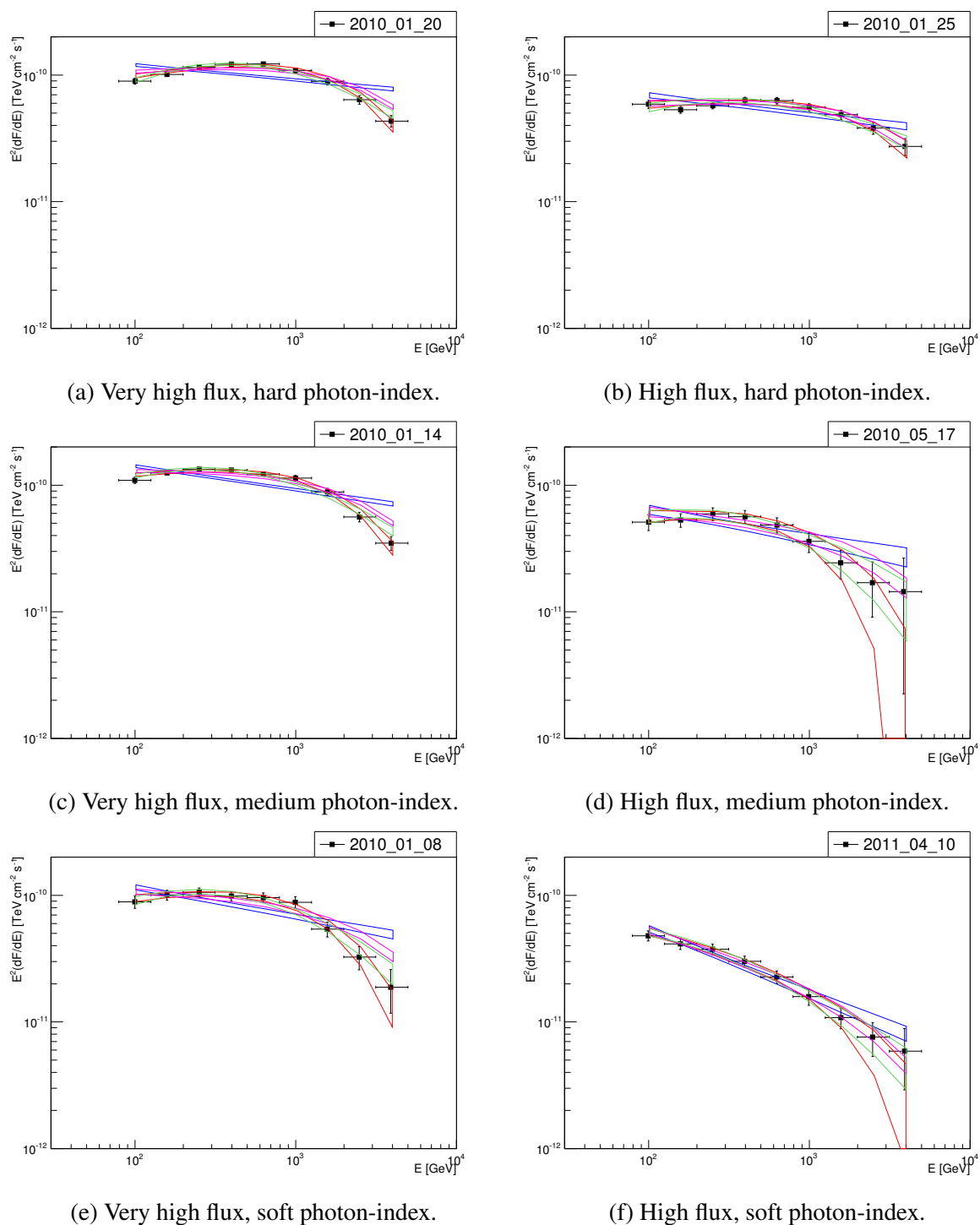


Figure 4.6.: VHE spectra for 6 observations in 2010 and 2011: with a very high flux or a high flux. The fits from the forward folding: **blue contour** (power law, Equation 4.1); **red contour** (power law with an exponential cutoff, Equation 4.2); **magenta contour** (power law with the exponential cutoff fixed at 4 TeV, Equation 4.3); **green** (log-parabola, Equation 4.4). The fit parameters are listed in Tables 4.1 – 4.4.

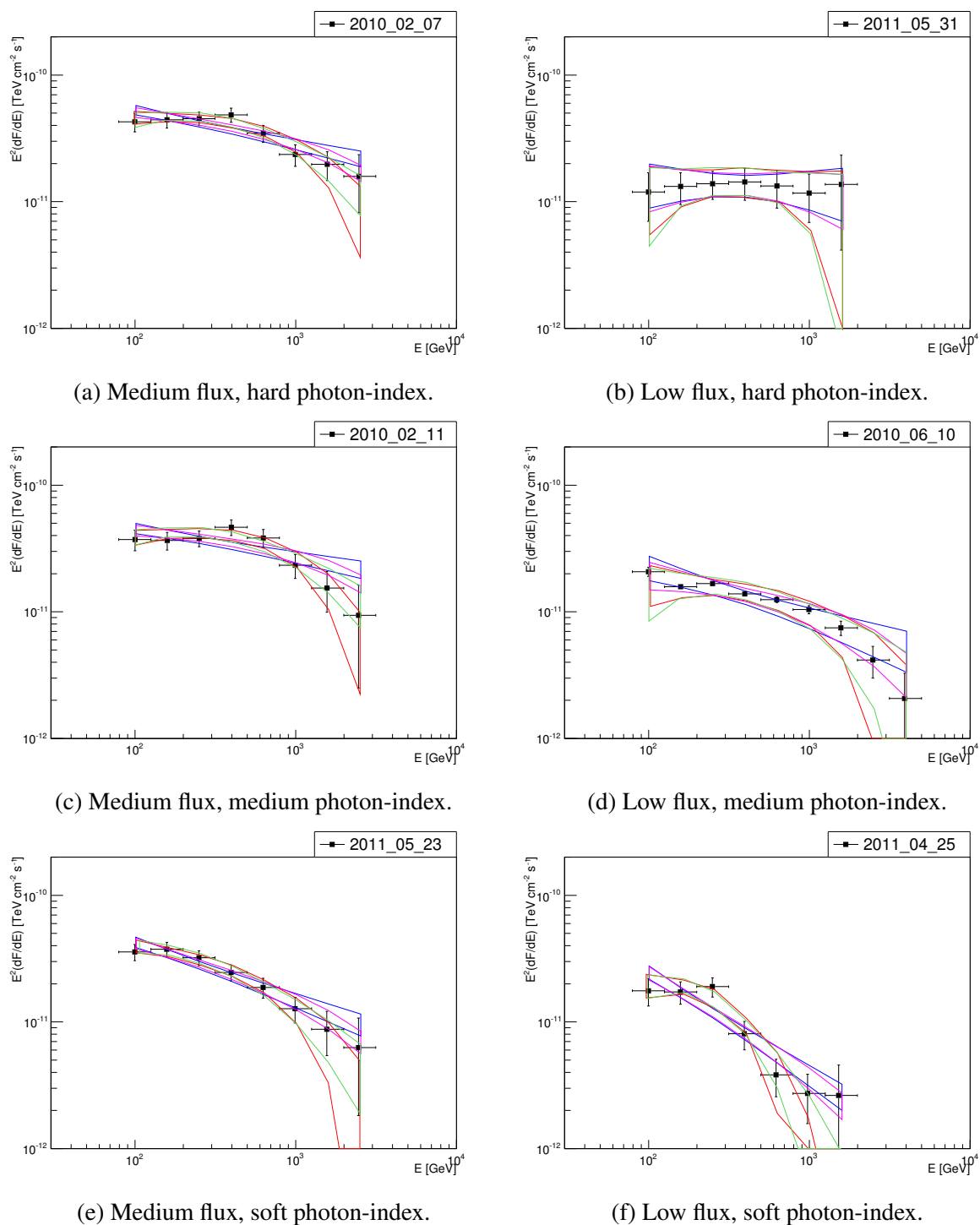


Figure 4.7.: VHE spectra for 6 observations in 2010 and 2011: with a medium flux or a low flux. The fits from the forward folding: **blue contour** (power law, Equation 4.1); **red contour** (power law with an exponential cutoff, Equation 4.2); **magenta contour** (power law with the exponential cutoff fixed at 4 TeV, Equation 4.3); **green** (log-parabola, Equation 4.4). The fit parameters are listed in Tables 4.1 – 4.4.

Table 4.2. Fit Parameters from the Fit Function 4.2 (power-law with an exponential cutoff) for the spectra in Figures 4.6 – 4.7.

Date	$f_0[\text{TeV cm}^{-2}\text{s}^{-1}]$	α	$E_0[\text{TeV}]$	χ^2/ndf	Prob.	Sig.
2010.01.08	$(1.40 \pm 0.11) \times 10^{-09}$	-1.80 ± 0.09	$(1.44 \pm 0.34) \times 10^{+0}$	11.6/11	3.8×10^{-1}	0.86
2010.01.14	$(1.67 \pm 0.05) \times 10^{-09}$	-1.84 ± 0.03	$(2.05 \pm 0.25) \times 10^{+0}$	8.6/12	7.3×10^{-1}	0.34
2010.01.20	$(1.46 \pm 0.04) \times 10^{-09}$	-1.77 ± 0.03	$(2.23 \pm 0.27) \times 10^{+0}$	7.5/11	7.5×10^{-1}	0.31
2010.01.25	$(7.47 \pm 0.34) \times 10^{-10}$	-1.89 ± 0.06	$(3.34 \pm 0.91) \times 10^{+0}$	8.9/12	7.1×10^{-1}	0.37
2010.02.07	$(6.34 \pm 1.35) \times 10^{-10}$	-1.88 ± 0.21	$(1.17 \pm 0.68) \times 10^{+0}$	9.2/9	4.1×10^{-1}	0.82
2010.02.11	$(6.54 \pm 1.56) \times 10^{-10}$	-1.72 ± 0.24	$(8.80 \pm 4.37) \times 10^{-1}$	9.1/11	6.1×10^{-1}	0.51
2010.05.17	$(8.15 \pm 1.69) \times 10^{-10}$	-1.84 ± 0.20	$(1.17 \pm 0.65) \times 10^{+0}$	6.4/11	8.4×10^{-1}	0.20
2010.06.10	$(2.05 \pm 0.62) \times 10^{-10}$	-1.98 ± 0.44	$(1.59 \pm 1.87) \times 10^{+0}$	8.1/12	7.7×10^{-1}	0.28
2011.04.10	$(4.27 \pm 0.62) \times 10^{-10}$	-2.31 ± 0.13	$(2.17 \pm 1.49) \times 10^{+0}$	11.9/11	3.6×10^{-1}	0.90
2011.04.25	$(7.11 \pm 10.1) \times 10^{-10}$	-1.39 ± 1.06	$(1.93 \pm 1.61) \times 10^{-1}$	13.3/7	6.5×10^{-2}	1.84
2011.05.23	$(4.38 \pm 1.34) \times 10^{-10}$	-2.10 ± 0.26	$(9.89 \pm 7.45) \times 10^{-1}$	3.7/11	9.7×10^{-1}	0.03
2011.05.31	$(2.12 \pm 1.67) \times 10^{-10}$	-1.67 ± 0.90	$(1.13 \pm 2.62) \times 10^{+0}$	4.2/7	7.4×10^{-1}	0.32

Note. — See the caption of Table 4.1 for detailed explanation.

Table 4.3. Fit Parameters from the Fit Function 4.3 (power-law with the exponential cutoff fixed at 4 TeV) for the spectra in Figures 4.6 – 4.7.

Date	$f_0[\text{TeV cm}^{-2}\text{s}^{-1}]$	α	χ^2/ndf	Prob.	Sig.
2010.01.08	$(1.14 \pm 0.03) \times 10^{-09}$	-2.05 ± 0.03	22.8/12	2.8×10^{-2}	2.19
2010.01.14	$(1.49 \pm 0.02) \times 10^{-09}$	-1.99 ± 0.01	30.5/13	3.9×10^{-3}	2.89
2010.01.20	$(1.34 \pm 0.02) \times 10^{-09}$	-1.90 ± 0.01	24.4/12	1.7×10^{-2}	2.38
2010.01.25	$(7.32 \pm 0.23) \times 10^{-10}$	-1.93 ± 0.03	9.3/13	7.4×10^{-1}	0.32
2010.02.07	$(4.91 \pm 0.28) \times 10^{-10}$	-2.15 ± 0.06	11.3/10	3.3×10^{-1}	0.97
2010.02.11	$(4.46 \pm 0.29) \times 10^{-10}$	-2.10 ± 0.07	12.8/12	3.7×10^{-1}	0.88
2010.05.17	$(6.26 \pm 0.38) \times 10^{-10}$	-2.10 ± 0.06	8.7/12	7.2×10^{-1}	0.35
2010.06.10	$(1.79 \pm 0.23) \times 10^{-10}$	-2.21 ± 0.17	8.5/13	8.0×10^{-1}	0.24
2011.04.10	$(3.88 \pm 0.18) \times 10^{-10}$	-2.39 ± 0.05	12.4/12	4.1×10^{-1}	0.82
2011.04.25	$(1.25 \pm 0.12) \times 10^{-10}$	-2.73 ± 0.12	16.6/8	3.4×10^{-2}	2.12
2011.05.23	$(3.21 \pm 0.24) \times 10^{-10}$	-2.36 ± 0.08	5.1/12	9.5×10^{-1}	0.06
2011.05.31	$(1.67 \pm 0.34) \times 10^{-10}$	-1.93 ± 0.29	4.4/8	8.2×10^{-1}	0.23

Note. — See the caption of Table 4.1 for detailed explanation.

Table 4.4. Fit Parameters from the Fit Function 4.4 (log-parabola) for the spectra in Figures 4.6 – 4.7.

Date	$f_0[\text{TeV cm}^{-2}\text{s}^{-1}]$	α	β	χ^2/ndf	Prob.	Sig.
2010.01.08	$(1.18 \pm 0.05) \times 10^{-09}$	-2.06 ± 0.04	$(-4.48 \pm 0.90) \times 10^{-1}$	13.7/11	2.4×10^{-1}	1.16
2010.01.14	$(1.50 \pm 0.03) \times 10^{-09}$	-2.04 ± 0.02	$(-3.53 \pm 0.37) \times 10^{-1}$	17.8/12	1.2×10^{-1}	1.56
2010.01.20	$(1.34 \pm 0.02) \times 10^{-09}$	-1.91 ± 0.02	$(-3.81 \pm 0.40) \times 10^{-1}$	7.4/11	7.6×10^{-1}	0.30
2010.01.25	$(7.04 \pm 0.25) \times 10^{-10}$	-2.00 ± 0.04	$(-2.57 \pm 0.69) \times 10^{-1}$	13.5/12	3.2×10^{-1}	0.98
2010.02.07	$(5.05 \pm 0.42) \times 10^{-10}$	-2.19 ± 0.08	$(-4.65 \pm 2.28) \times 10^{-1}$	8.5/9	4.7×10^{-1}	0.71
2010.02.11	$(4.64 \pm 0.43) \times 10^{-10}$	-2.16 ± 0.09	$(-4.68 \pm 2.38) \times 10^{-1}$	10.7/11	4.6×10^{-1}	0.74
2010.05.17	$(6.37 \pm 0.54) \times 10^{-10}$	-2.17 ± 0.08	$(-3.90 \pm 2.03) \times 10^{-1}$	7.1/11	7.8×10^{-1}	0.27
2010.06.10	$(1.76 \pm 0.27) \times 10^{-10}$	-2.18 ± 0.26	$(-4.65 \pm 4.84) \times 10^{-1}$	8.2/12	7.6×10^{-1}	0.30
2011.04.10	$(3.77 \pm 0.24) \times 10^{-10}$	-2.49 ± 0.05	$(-2.47 \pm 1.41) \times 10^{-1}$	11.4/11	4.0×10^{-1}	0.83
2011.04.25	$(1.45 \pm 0.21) \times 10^{-10}$	-3.02 ± 0.27	$(-1.39 \pm 0.84) \times 10^{+0}$	12.3/7	8.8×10^{-2}	1.70
2011.05.23	$(3.28 \pm 0.33) \times 10^{-10}$	-2.48 ± 0.11	$(-4.55 \pm 2.86) \times 10^{-1}$	3.2/11	9.8×10^{-1}	0.02
2011.05.31	$(1.67 \pm 0.43) \times 10^{-10}$	-1.98 ± 0.36	$(-4.85 \pm 9.03) \times 10^{-1}$	4.1/7	7.5×10^{-1}	0.31

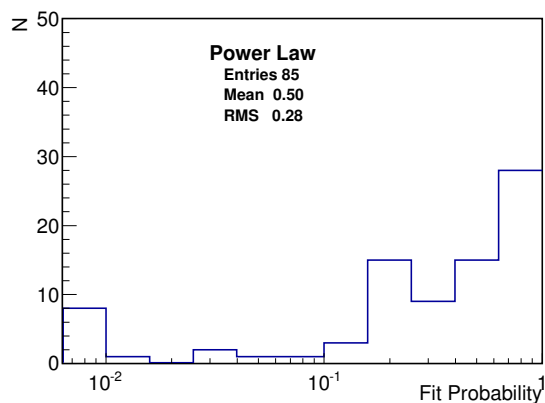
Note. — See the caption of Table 4.1 for detailed explanation.

In Figures 4.6 and 4.7, it can be seen that many of the measured SEDs with MAGIC contain the peak of the high-energy bump. Because the peak position is important in the interpretation of the observational data within theoretical scenarios, MAGIC spectra extending to the energies below 100 GeV can play a crucial role (see Chapter 5).

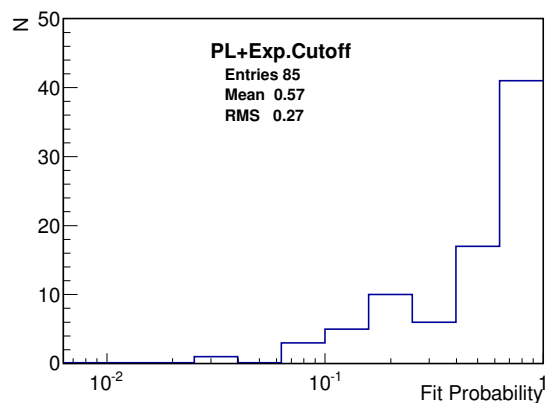
In order to have an overview of the fits, the distributions of the fit probabilities (p -value from χ^2) for these three functions to all the SEDs of 2010 are shown in Figure 4.8. The first bin of each histogram contains the entries with $p < 0.01$. The height of this peak shows the number of times that a particular function could not fit the observations. In view of this, a simple power-law function is not sophisticated enough to describe the spectra, and an extra fixed cutoff at 4 TeV improves the validity of the power-law function. A power-law function with an exponential cutoff and a log-parabola function describe the spectra similarly well.

The likelihood ratio tests are used to examine whether there is improvement or not when a more complicated fit function (with more free parameters) is applied to describe the observed spectrum. Four pairs of fit functions are compared, and the distributions of the p -values from the tests between these four pairs are presented in Figure 4.9. The first bin of each distribution contains the entries with $p < 0.01$. The height of this peak shows the number of times that the simple function (2 free parameters) is rejected (with a 99% confidence level) in favor of the more complicated function (3 free parameters).

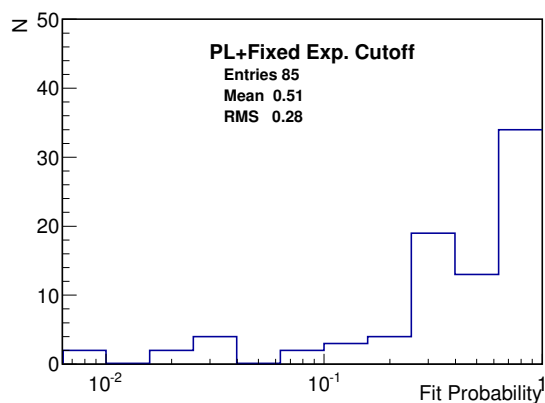
In order to compare the goodness of the two fit functions with 2 free parameters (the simple power-law fit and the power-law with an exponential cutoff fixed at 4 TeV), and the two fit functions with 3 free parameters (the log-parabola function and the power-law function with an exponential cutoff), a simple cross-examination on the likelihood ratio tests is made in the following. The accumulated numbers of entries with $p < 0.1$ are 37, 31, 19, and 32 in Figures 4.9a, 4.9b, 4.9c, and 4.9d respectively. For the case of 2 free parameters, a power-law function has 37+31 times worse fits (than a log-parabola function or a power-law function with an exponen-



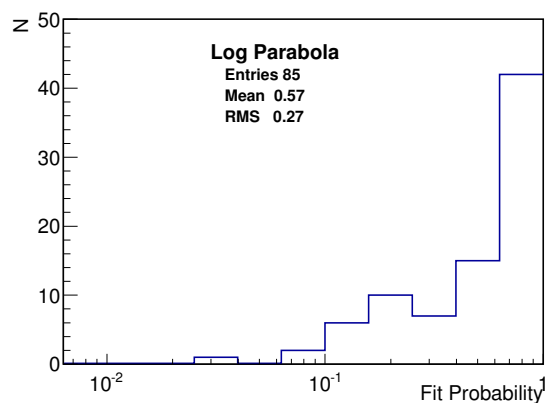
(a) A power-law function, Equation 4.1.



(b) A power-law function with an exponential cut-off, Equation 4.2.



(c) A power-law function with a fixed exponential cutoff at 4 TeV, Equation 4.3.



(d) A log-parabola function, Equation 4.4.

Figure 4.8.: Distributions of fit probabilities (the p -values from χ^2) resulting from the fits to the VHE spectra with the four different functions. The first bin of each histogram contains the entries with $p < 0.01$).

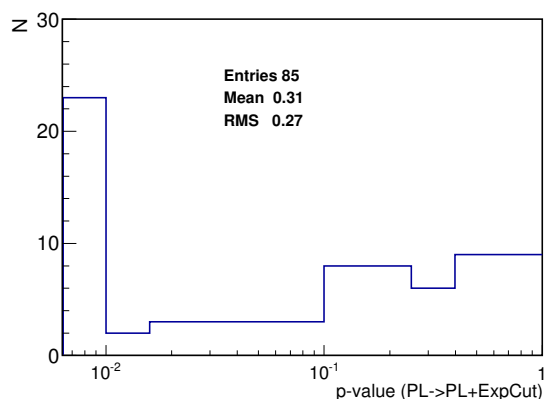
tial cutoff), while a power-law function with a fixed exponential cutoff at 4 TeV only has 19+32 times worse fits (also than a log-parabola function or a power-law function with an exponential cutoff). In view of this, the extra exponential cutoff fixed at 4 TeV represents an improvement for the power-law function. Similarly for the case of the functions with 3 free parameters, a log-parabola function has 31+32 better fits (than a power-law function function or a power-law function with a fixed exponential cutoff at 4 TeV), while a power-law function with an exponential cutoff has 37+19 better fits (also than a power-law function function or a power-law function with a fixed exponential cutoff at 4 TeV). In view of this, the log-parabola function is slightly better than the power-law with an exponential cutoff.

The photon index, α , in the power-law function with a fixed exponential cutoff at 4 TeV can serve as a simple quantification for the spectrum hardness, alternative to the hardness calculation in Section 4.1. Figure 4.10, the "VHE photon index α vs. flux F_M " distribution, shows the relation between the spectrum hardness and the flux, like Figure 4.5. The relation in Figure 4.10 is even clearer because of small error bars. These smaller error bars in α than those in $H_{M/L}$ result from better statistics in the total flux. The figure shows a saturation in the photon index α at -1.8 at VHE fluxes $\gtrsim 10^{-10} \text{ cm}^{-2}\text{s}^{-1}$ ($\sim 0.8 \text{ c.u.}$ ¹).

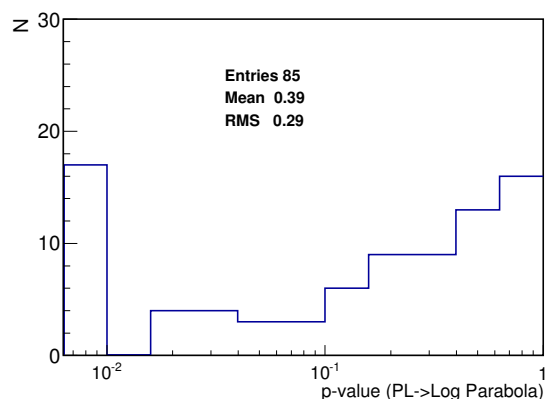
There are several possible reasons for this saturation: the extragalactic background light (EBL), the Klein-Nishina effect, and/or intrinsic characteristics in particle-acceleration mechanism. The first one, EBL, could be excluded if the spectrum-hardness saturation can also be seen in the low-energy VHE regime ($< \text{TeV}$; the absorption $e^{-\tau} < 0.75$ [Franceschini et al., 2008]). Figure 4.5c shows that the saturation occurs in the low-energy regime, and hence it can be removed from the list of the potential causes. The second one, the Klein-Nishina effect, results in a lower efficiency in the inverse-Compton scattering to produce high-energy γ -rays. This might lower the increase rate of α with the increasing flux F_M , and result in a less steep slope in the α - F_M distribution, although no substantial effect is expected below the energy at which the peak of the high-energy bump is located. The third candidate, the characteristic in the particle acceleration, is plausible given that the saturated index α is about -1.8, which coincides with the steady photon index measured with *Fermi*-LAT at energies above 100 MeV [Abdo et al., 2011]. It is possible that the hardest α that can be measured in the VHE regime is limited by the α at energies below the peak of the high-energy bump during the non-flaring (typical) state.

Within the SSC scenario model, the spectral shapes/hardness of the low-energy and high-energy bumps are strongly correlated. Therefore, examining the spectral shape of the low-energy bump (in the X-ray band) may help diagnose the factors resulting in the photon index saturation in the VHE band. The Klein-Nishina effect does not affect the X-ray spectra, so it could be excluded if there is a saturation in the hardness at high X-ray fluxes. On the other hand, the particle-acceleration mechanism should result in similar spectral features in the X-ray emission if it is really the primary factor. In order to clarify the situation, the spectral hardness in the X-ray band during observations in 2010 and 2011 (hence coincident with the VHE MAGIC observations) is examined. For this, I use the X-ray observations performed with *Swift*-XRT, which were taken in the framework of the extensive multi-instrument observing campaigns in 2010 and 2011, that will be reported in Chapters 5 and 6. The X-ray hardness ratio ($F_{2-10\text{keV}}/F_{0.3-2\text{keV}}$) vs. X-ray

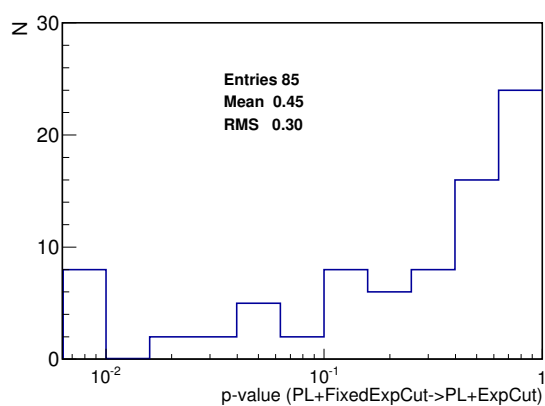
¹1 c.u. of the integral flux $> 300 \text{ GeV}$ is $\sim 1.2 \times 10^{-10} \text{ cm}^{-2}\text{s}^{-1}$.



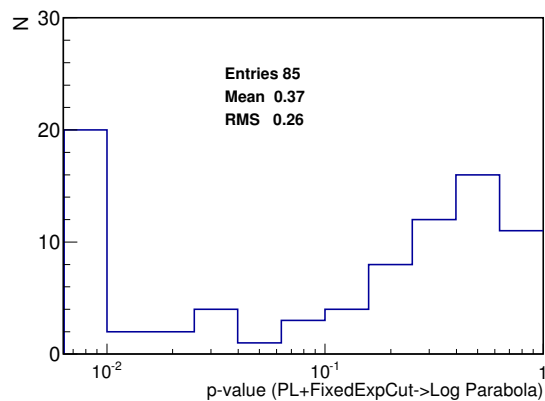
(a) A power-law function (2) and a power-law function with an exponential cutoff (3).



(b) A power-law function (2) and a log-parabola function (3).



(c) A power-law function with a fixed exponential cutoff at 4 TeV (2) and a power-law function with an exponential cutoff (3).



(d) A power-law function with a fixed exponential cutoff at 4 TeV (2) and a log-parabola function (3).

Figure 4.9.: Distributions of the p -values from the likelihood ratio tests between pairs of the fit functions. The first bin of each histogram contains the entries with $p < 0.01$. The numbers of free parameters in a fit function are reported in the parentheses in the sub-captions above.

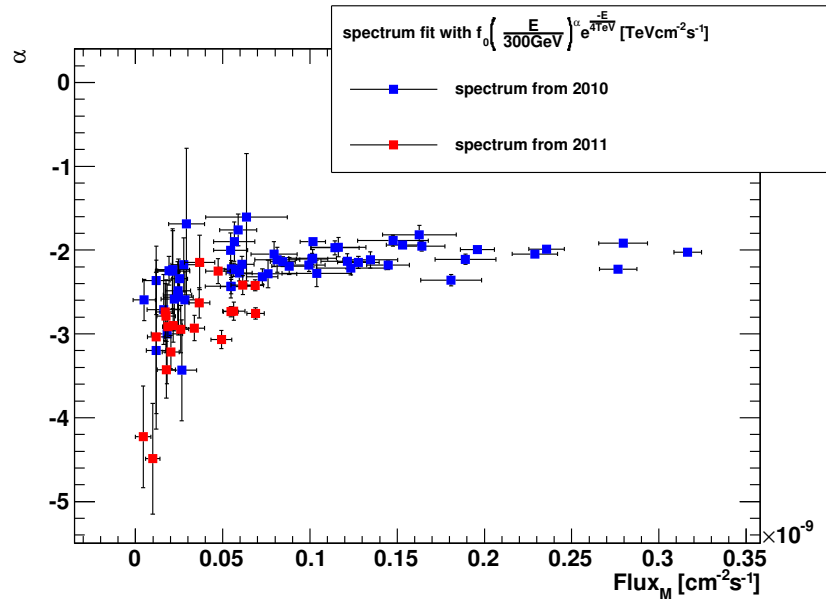
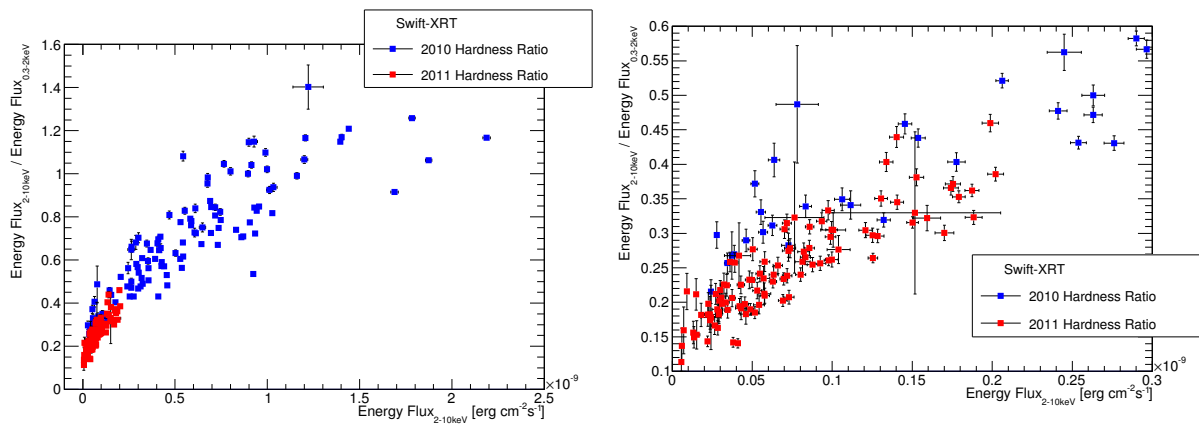


Figure 4.10.: The VHE photon index α vs. flux F_M for all the VHE spectra from 2010 and 2011. The α is from the Fit Function 4.3 (power-law with a fixed exponential cutoff at 4 TeV).



(a) The full data set.

(b) A zoom-in view containing only changes fluxes below $0.3 \times 10^{-10} \text{ erg cm}^{-2} \text{ s}^{-1}$.

Figure 4.11.: The X-ray hardness ratio vs. flux.

energy flux ($F_{2-10\text{keV}}$) is reported in Figure 4.11. It shows that the slope in the hardness ratio vs. energy flux is not constant. In particular, it seems the slope below an energy flux of $(0.5 - 1) \times 10^{-10} \text{ erg cm}^{-2}\text{s}^{-1}$ is higher than the slope above. That is, the growth rate of the hardness ratio decreases with the increasing X-ray energy flux, and above $10^{-9} \text{ erg cm}^{-2}\text{s}^{-1}$, it seems the X-ray hardness ratio saturates. However, above $10^{-9} \text{ erg cm}^{-2}\text{s}^{-1}$ there are only few observations and hence it is difficult to make a definite statement. The change in the slope in the X-ray hardness ratio vs. flux implies a lower efficiency in the production of high-energy photons, which is similar to what occurs in the VHE band. Consequently, these data suggest that the saturation in the VHE spectral slope is caused by the mechanism producing the electron energy distribution responsible for the X-ray and VHE emission. A more detailed analysis, possibly with additional X-ray/VHE data, would be required to fully understand this observation.

5. Multi-wavelength Campaign on Markarian 421 in 2010

In this chapter, the multi-wavelength (MW) campaign on Mrk 421 performed in 2010 is reported. In Section 5.1, the observations and the data analysis performed with the various instruments are reported. In Section 5.2, the results obtained with the data from the whole 2010 year are shown, including all the MW LCs and the variability from each band. The rest of the chapter focuses on the 13-day flaring episode recorded in 2010 March. The following sections report the main scientific achievement of this PhD thesis, which has just been submitted for the publication in the *Astronomy and Astrophysics* journal. The observation results on the multi-band variability are given in Section 5.3, all the broadband SEDs during the flaring activity, as well as the characterization of the SEDs within two SSC scenarios in Section 5.4, the discussion and the interpretation of the experimental results in Section 5.5.

5.1. Observation and Data Analysis

All the instruments that made observations of Mrk 421 during this period are reported in Table 5.1.

5.1.1. MAGIC

The MAGIC stereoscopic system is a crucial instrument in this observing campaign. The MAGIC telescopes were described in Section 3.1. All the observations of Mrk 421 in 2010 were conducted with both the telescopes, in the false-source tracking (wobble) mode: alternatively tracking two positions in the sky which are symmetric with respect to the true source position and 0.4° away from it. The data that suffered from bad weather and occasional technical problems and are removed from the analysis. The data were analyzed as described in Section 3.2, and results reported in Chapter 4. This is a substantial fraction of the work done during my PhD thesis.

Table 5.1.: List of participating instruments in the campaign on Mrk 421 during 2010.

Instrument/Observatory	Energy range covered	Web page
MAGIC	0.08-5.0 TeV	http://www.magic.mppmu.mpg.de/
VERITAS	0.2-5.0 TeV	http://veritas.sao.arizona.edu/
Whipple	0.4-2.0 TeV	http://veritas.sao.arizona.edu/content/blogsection/6/40/
<i>Fermi</i> -LAT	0.1-400 GeV	http://www-glast.stanford.edu/index.html
<i>Swift</i> -BAT	14-195 keV	http://heasarc.gsfc.nasa.gov/docs/swift/swiftsc.html/
RXTE-PCA	3-32 keV	http://heasarc.gsfc.nasa.gov/docs/xte/rxte.html
<i>Swift</i> -XRT	0.3-9.6 keV	http://heasarc.gsfc.nasa.gov/docs/swift/swiftsc.html
RXTE-ASM	2-10 keV	http://heasarc.gsfc.nasa.gov/docs/xte/rxte.html
MAXI	2-10 keV	http://www.nasa.gov/mission_pages/station/research/experiments/MAXI.html
<i>Swift</i> -UVOT	UVW1, UVM2, UVW2	http://heasarc.gsfc.nasa.gov/docs/swift/swiftsc.html
Abastumani [†]	R band	http://www.oato.inaf.it/blazars/webt/
Lulin [†]	R band	http://www.oato.inaf.it/blazars/webt/
Roque de los Muchachos (KVA) [†]	R band	http://www.oato.inaf.it/blazars/webt/
St. Petersburg [†]	R band polarization	http://www.oato.inaf.it/blazars/webt/
Goddard Robotic Telescope (GRT)	R band	http://asd.gsfc.nasa.gov/Takanori.Sakamoto/GRT/index.html
The Remote Observatory for Variable Object Research (ROVOR)	B, R, V bands	http://rovor.byu.edu/
New Mexico Skies (NMS)	R, V bands	http://www.itelescope.net/
Bradford Robotic Telescope (BRT)	B, R, V bands	http://www.telescope.org/
Perkins	R band polarization	http://www.lowell.edu/researchtelescopes_perkins.php
Steward	R band polarization	http://james.as.arizona.edu/~psmith/90inch/90inch.html
Crimean	R band polarization	http://www.perekop.net/crao-crimean-astrophysical-observatory/
Submillimeter Array (SMA)	225 GHz	http://sma1.sma.hawaii.edu/
Metsähovi Radio Observatory [†]	37 GHz	http://www.metsahovi.fi/
University of Michigan Radio Astronomy Observatory (UMRAO) [†]	8.0, 14.5 GHz	http://www.oato.inaf.it/blazars/webt/
Owens Valley Radio Observatory (OVRO)	15 GHz	http://www.ovro.caltech.edu/

Note— The energy range shown in Column 2 is the actual energy range covered during the Mrk 421 observations, and not the instrument nominal energy range, which might only be achievable for bright sources and in excellent observing conditions.

[†] through GASP-WEBT program

5.1.2. VERITAS

VERITAS is an array of four 12-m diameter imaging atmospheric Cherenkov telescopes located in southern Arizona [Weekes et al., 2002]. Designed to detect emission from astrophysical objects in the energy range from ~ 100 GeV to greater than 30 TeV. VERITAS has an energy resolution of $\sim 15\%$ and an angular resolution (68% containment) of $\sim 0.1^\circ$ per event at 1 TeV. A source with a flux of 1% of the Crab Nebula flux is detected in ~ 25 hours of observations, while a 5% Crab Nebula flux source is detected in less than 2 hours. The field of view of the VERITAS cameras is 3.5° . For more details on the VERITAS instrument and the imaging atmospheric Cherenkov technique, see [Perkins et al., 2009].

All the Mrk 421 data were taken in “wobble” mode [Fomin et al., 1994] where the telescopes are pointed away from the source by 0.5° North/South/East/West to allow for simultaneous background estimation using events from the same field of view.

Prior to event selection and background subtraction, all shower images are calibrated and cleaned as described in [Cogan, 2006] and [Daniel, 2008]. Following the calibration and cleaning of the data, the events are parametrized using a moment analysis [Hillas, 1985b]. From this moment analysis, scaled parameters are calculated and used for the selection of the γ -ray-like events [Aharonian et al., 1997, Krawczynski et al., 2006]. The event selection cuts are optimized *a priori* for a Crab-like source (power-law spectrum photon index $\Gamma = 2.5$ and Crab Nebula flux level).

5.1.3. Whipple

The Whipple 10 m γ -ray telescope was situated at the Fred Lawrence Whipple Observatory in southern Arizona, USA. It operated in the 300 GeV – 20 TeV energy range, with a peak response energy (for a Crab-like spectrum) of approximately 400 GeV. The telescope has a 10-meter optical reflector with a camera consisting of 379 photomultiplier tubes, covering a field of view of 2.6° , which detects the short-duration Cherenkov light flashes emitted by secondary particles generated in cosmic- and γ -ray-induced atmospheric cascades [Kildea et al., 2007].

Whipple made observations performed in the ON/OFF and TRK (tracking) modes, in which the telescope tracks the source, which is centered in the field of view for 28 minutes (ON and TRK runs). The corresponding OFF run is collected at an offset of 30 minutes from the source’s right ascension for a period of 28 minutes. The two runs are taken at the same declination over the same range of telescope azimuth and elevation angles. This removes systematic errors that depend on slow changes in the atmosphere. In the TRK mode, only ON runs are taken with no corresponding OFF observations, and the background is estimated from events whose major axis points are away from the center of the camera. The data were analyzed using the official data analysis package since 2008, the UCD code developed in the University College Dublin [Acciari, 2011]. The photon fluxes, initially derived in Crab units for energies above 400 GeV, were converted into photon fluxes above 200 GeV using a Crab nebula flux $2.2 \times 10^{-10} \text{cm}^{-2} \text{s}^{-1}$ [Aleksić et al., 2012a].

5.1.4. *Fermi*-LAT

The *Fermi*-LAT is a γ -ray telescope operating from 20 MeV to > 300 GeV [Atwood et al., 2009, Ackermann et al., 2012]. The analysis of the *Fermi*-LAT data are performed with the ScienceTools software package version v9r32p5. We use the reprocessed *Fermi*-LAT events¹ belonging to the P7REP_SOURCE_V15 [Abdo, 2014] class and located in a circular Region Of Interest (ROI) of 10° radius around Mrk 421, after applying a cut of $< 52^\circ$ in the rocking angle, and $< 100^\circ$ on the zenith angle to reduce contamination from the Earth limb γ -rays. The background model used to extract the γ -ray signal includes a Galactic diffuse emission component and an isotropic component. The model that we adopt for the Galactic component is given by the file `gll_iem_v05.fits`, and the isotropic component, which is the sum of the extragalactic diffuse emission and the residual charged particle background, is parametrized by the file `iso_source_v05.txt`². The normalization of both components in the background model are allowed to vary freely during the spectral point fitting. The spectral parameters are estimated using the unbinned maximum likelihood technique [Mattox et al., 1996] in the energy range 300 MeV – 300 GeV. We use the P7REP_SOURCE_V15 instrument response function [Abdo, 2014], and take into account all the sources from the second *Fermi*-LAT catalog (2FGL, [Nolan et al., 2012]) located within 15° of Mrk 421. When performing the fit, the spectral parameters of sources within 10° of Mrk 421 are allowed to vary while those within 10° – 15° are fixed to their values from the 2FGL. When performing the likelihood fit in differential energy bins (spectral bins in the SED), the photon indices of the sources are frozen to the best-fit values obtained from the full spectral analysis.

The sensitivity of *Fermi*-LAT is not good enough to detect Mrk 421 within a few hours and hence we integrate over two days in order to have significant detections and to be able to produce γ -ray spectra. Despite the two-day integration window, the number of collected photons is only about 8–15 for each of the two-day intervals. Most of these photons concentrate at energies below few GeV, being rare the detection of photons above 10 GeV during each of these two-day time intervals. Upper limits at the 95% confidence level are calculated for the differential energy bins with a maximum likelihood test statistic (TS)³ below 4.

The systematic uncertainty in the flux is dominated by the systematic uncertainty in the effective area, which is estimated as 10% below 0.1 GeV, 5% in the energy range between 316 MeV and 10 GeV and 10% above 10 GeV⁴. The systematic uncertainties are substantially smaller than the statistical uncertainties of the data points in the LC and spectra.

5.1.5. X-ray Observations

All 11 *Swift*-XRT [Burrows et al., 2005] observations were carried out using the Windowed Timing (WT) readout mode. The data set is first processed with the XRTDAS software package (v.2.9.3) developed at the ASI Science Data Center (ASDC) and distributed by HEASARC within

¹See http://fermi.gsfc.nasa.gov/ssc/data/analysis/documentation/Pass7REP_usage.html

²<http://fermi.gsfc.nasa.gov/ssc/data/access/lat/BackgroundModels.html>

³The maximum likelihood test statistic TS [Mattox et al., 1996] is defined as $TS=2\Delta\log(\textit{likelihood})$ between models with and without a point source at the position of Mrk 421.

⁴See http://fermi.gsfc.nasa.gov/ssc/data/analysis/LAT_caveats.html

the HEASoft package (v. 6.15.1). Event files were calibrated and cleaned with standard filtering criteria with the *xrtpipeline* task using the calibration files as available in the *Swift*-XRT CALDB version 20140120. Events for the spectral analysis are selected within a 20-pixel (~46 arcsec) radius, which encloses about 90% of the PSF, centered on the source position. The background is extracted from a nearby circular region of 40 pixel radius. The ancillary response files (ARFs) are generated with the *xrtmkarf* task applying corrections for PSF losses and CCD defects using the cumulative exposure map. Before the spectral fitting, the 0.3-10 keV source energy spectra are binned to ensure a minimum of 20 counts per bin. The spectra are corrected for absorption with a neutral hydrogen column density N_H fixed to the Galactic 21 cm value in the direction of Mrk 421, namely $1.9 \times 10^{20} \text{ cm}^{-2}$ [Kalberla et al., 2005].

The *Rossi* X-ray Timing Explorer (RXTE; [Bradt et al., 1993]) satellite performed daily pointing observations of Mrk 421 during the time interval from MJD 55265 to MJD 55277. The data analysis are performed using FTTOOLS v6.9 and following the procedures and filtering criteria recommended by the NASA RXTE Guest Observer Facility. The observations are filtered following the conservative procedures for faint sources. Only the first xenon layer of PCU2 is used. We use the package *pcabackest* to model the background and the package *saextrct* to produce spectra for the source and background files and the script⁵ *pcarsp* to produce the response matrix. The PCA average spectra above 3 keV are fitted using the XSPEC package using a PL function with an exponential cutoff (*cutoffpl*) with a non-variable neutral hydrogen column density N_H fixed to the Galactic value in the direction of the source ($1.9 \times 10^{20} \text{ cm}^{-2}$; [Kalberla et al., 2005]). However, since the PCA bandpass starts at 3 keV, the value for N_H used does not significantly affect our results.

We also use data from the all-sky X-ray instruments available in 2010, namely RXTE/ASM, MAXI and *Swift*/BAT. The data from RXTE/ASM are obtained from the ASM web page⁶, and filtered out according to the provided prescription in the ASM web page. The daily fluxes from *Swift*/BAT are gathered from the BAT web page⁷, and the daily fluxes from MAXI are retrieved from a dedicated MAXI web page⁸.

5.1.6. Optical Observations

The optical fluxes reported in this study were obtained within the GASP-WEBT program (e.g., [Villata et al., 2008, Villata et al., 2009]), with various optical telescopes around the globe, and by Perkins, Rovor, New Mexico Skies and the Bradford telescopes. Optical polarization measurements are also included from the Steward Observatory, Crimean and St Petersburg observatories. All the instruments use the calibration stars reported in [Villata et al., 1998] for calibration, and the Galactic extinction is corrected with the coefficients given in [Schlegel et al., 1998]. The flux from the host galaxy (which is significant only below $\nu \sim 10^{15} \text{ Hz}$) is estimated using the flux values across the R band from [Nilsson et al., 2007] and the colors reported in [Fukugita et al., 1995], and then subtracted from the measured flux.

⁵The CALDB files are located at <http://heasarc.gsfc.nasa.gov/FTP/caldb>

⁶See http://xte.mit.edu/ASM_lc.html

⁷See <http://swift.gsfc.nasa.gov/docs/swift/results/transients/>

⁸See <http://maxi.riken.jp/top/index.php?cid=1&jname=J1104+382>

The *Swift* Ultraviolet/Optical Telescope (UVOT; [Roming et al., 2005]) obtained data cycling through each of three ultraviolet pass bands, UVW1, UVM2, and UVW2 with central wavelengths of 260 nm, 220 nm, and 193 nm, respectively. The photometry is computed using a 5 arcsec source region around Mrk 421 using a custom UVOT pipeline that performs the calibrations presented in [Poole et al., 2008]. Moreover, the custom pipeline also allows for separate, observation-by-observation, corrections for astrometric mis-alignments [Acciari et al., 2011]. The flux measurements obtained are corrected for Galactic extinction $E_{B-V} = 0.019$ magnitude [Schlegel et al., 1998] in each spectral band [Fitzpatrick, 1999].

5.1.7. Radio Observations

The radio data reported in this manuscript are taken with the 14-m Metsähovi Radio Observatory at 37 GHz, the 40-m Owens Valley Radio Observatory (OVRO) telescope at 15 GHz, and the 26-m University of Michigan Radio Astronomy Observatory (UMRAO). Details of the observing strategy and data reduction are given by Metsähovi [Teraesranta et al., 1998]; OVRO [Richards et al., 2011]; and UMRAO [Aller et al., 1985]. The 225 GHz (1.3 mm) light curve was obtained at the Submillimeter Array (SMA) near the summit of Mauna Kea (Hawaii). During the period covered in this work, Mrk 421 was observed as part of a dedicated program to follow sources on the *Fermi*-LAT Monitored Source List (PI:A. Wehrle). Observations of available LAT sources were observed periodically for several minutes, and the measured source signal strength calibrated against known standards, typically solar system objects (Titan, Uranus, Neptune, or Callisto).

Mrk 421 is a point-like and unresolved source for the three above-mentioned single-dish radio instruments and for SMA, which means that the measured fluxes report the flux densities integrated over the full source extension, and hence should be considered as upper limits in the SED model fits reported in this paper. However, It is worth noting that the radio flux of Mrk421 resolved with VLBA for a region of $1-2 \times 10^{17}$ cm (hence comparable to the size of the blazar emission) is actually a very large fraction of the radio flux measured with the single-dish radio instruments (see [Abdo et al., 2011]), and thus it is reasonable to assume that the blazar emission contributes substantially to the radio flux measured by single-dish radio telescopes like Metsähovi, OVRO and UMRAO. Moreover, there are several works reporting a radio-to-GeV correlation in blazars as a population (see e.g. [Ackermann et al., 2011a]), which implies that at least a fraction of the radio emission is connected to the γ -ray (blazar) emission. The 225 GHz from SMA connects the bottom (radio) to the peak (optical/X-rays) of the synchrotron (low-energy) bump of the SED, and hence it is also expected to be strongly dominated by the blazar emission of the source. Therefore, it seems reasonable to adjust the theoretical model in such a way that the predicted energy flux for the millimeter band is close to the SMA measurement, and the predicted energy flux for the radio band is not too far below the measurements performed by the single-dish instruments.

5.2. Multi-band Variabilities in 2010

In this subsection, we show the observational results derived with the MW campaign observations described in 5.1. Figure 5.1 shows the multi-band LCs from 2009 December to 2010 July. This period is defined by the observation time of the VHE instruments. Between July and November, the sunlight and the zenith angle are disadvantageous for the observation of ground-based telescopes.

In the top left panel, the VHE band includes 94 observations from MAGIC, 33 from VERITAS, and 15 from Whipple. As stated in Section 4.1, MAGIC observed VHE high states in January, February, March, and May, with peak fluxes of 2.9, 1.2, 2.1, 1.2 c.u. However, in the same January flaring activity, VERITAS observed another flux peak of 4 c.u. Besides, VERITAS also observed a very high flux of 8 c.u. in February. In the panel below the VHE panel, *Fermi*-LAT provides the γ -ray flux above 100 MeV on a timescale of 7 days. The variance in this band is basically small except a number of peaks: 3 peaks close to each other, corresponding to the VHE January flaring activity; 2 peaks in February, the second one corresponding the VERITAS 8-c.u. observation; 1 peak in the end of April. All the X-ray LCs (MAXI, RXTE-ASM and -PCA, *Swift*-BAT and -XRT) show very similar behaviors to the VHE band.

In the second panel in the right column of Figure 5.1, the LCs of three UV bands from *Swift*-UVOT are shown and the optical bands are depicted in the panel below. They show rather small variations in contrast to the VHE or X-ray bands. There are totally 14 LCs shown in the optical band panel, 2 in the B band, 4 in the V band, 7 in the R band, and 1 in the I band. The GASP-WEBT LC contains data from six telescopes. The flux contribution from the host galaxy cannot be ignored in optical bands. It is estimated through the *R* band flux calculated in [Nilsson et al., 2007] and the color reported in [Fukugita et al., 1995]. As a result, for ROVOR, New Mexico Skies, and Bradford Robotic Telescope, the host fluxes in I, R, V, and B bands are 9.73, 6.23, 4.23, 2.07 mJy, with errors 0.6, 0.4, 0.3, and 0.1 mJy respectively. For the R band of GRT and GASP, their apertures correspond to a flux of 8 mJy with an error of 0.4 mJy. The values reported in the optical LCs exclude the flux contribution from the host galaxy. Mrk 421 showed some variability in these bands although it was not as active as in the VHE- γ or X-ray bands. In radio bands, Mrk 421 had rather small variations, which were comparable to the statistical errors.

To compare and summarize the flaring activities in different bands, 5 representative LC panels are selected and displayed in Figure 5.2: VHE γ -ray, HE γ -ray, X-ray, optical and radio. The *Swift*-XRT and RXTE-PCA, which have the highest accuracy, are chosen to represent the X-ray bands; the optical R band, which has the densest temporal coverage, to represent the UV and optical bands. Different *flavors* of flares are seen in this figure. For example, the activities around MJD 55220 and 55245 are not similar. They had not only different VHE peak fluxes, but also different behavior in the HE γ -ray band and optical bands: the former had an active HE γ -ray band, but the latter had only high states in the beginning days; the former had somewhat high states in optical bands, but the latter had almost no high states in optical bands.

In order to quantify the overall variabilities, we followed the method provided in

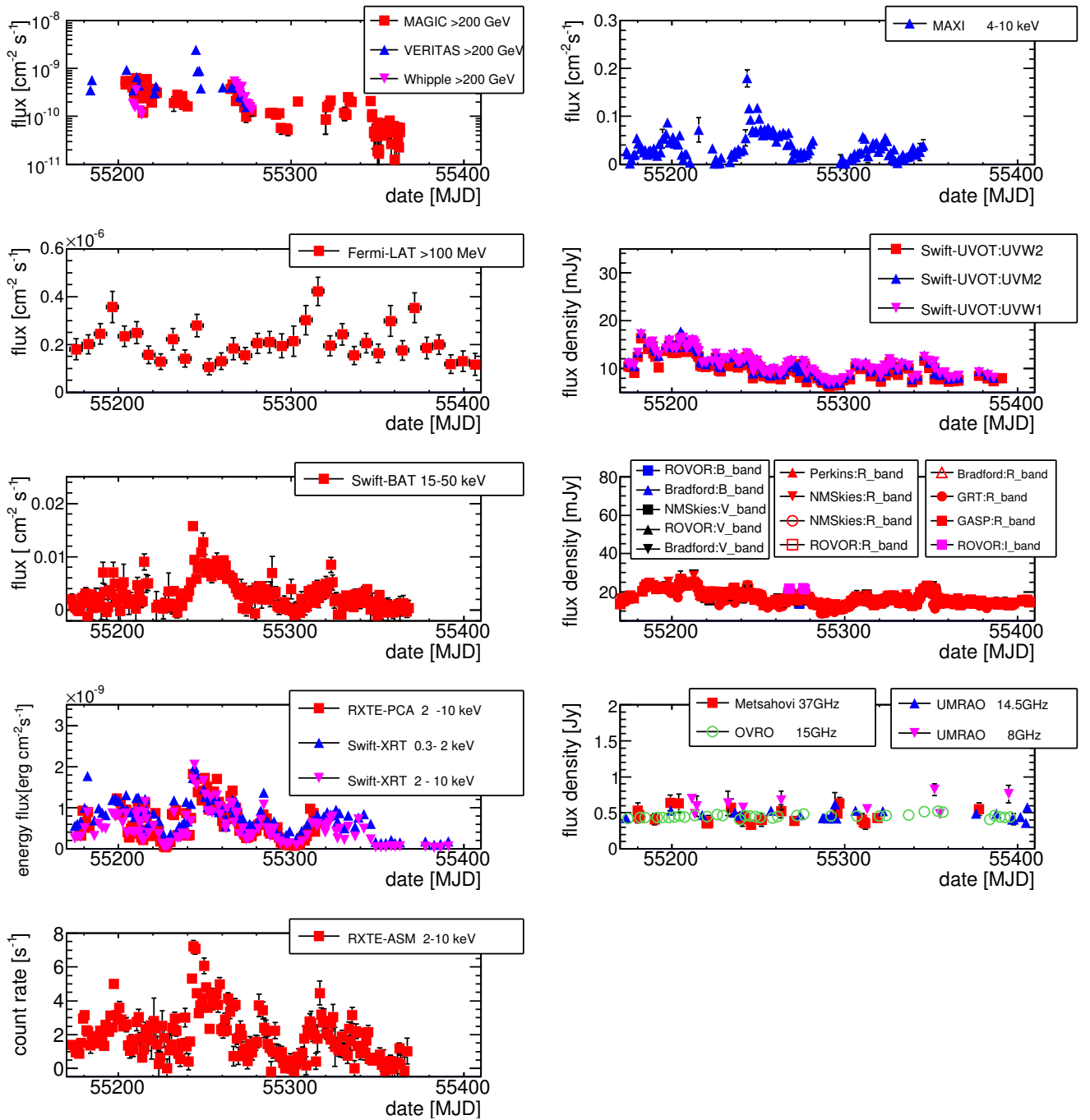


Figure 5.1.: LCs of Mrk 421 between 2009 December and 2010 July, from VHE to radio, and curves of the optical polarization. The original Whipple data reported fluxes above 400 GeV in c.u., and we converted to flux above 200 GeV using that 1 c.u. is $2.2 \times 10^{-10} [\text{cm}^{-2}\text{s}^{-1}]$. For optical bands, the contribution of the host is subtracted, as described in Section 5.2.

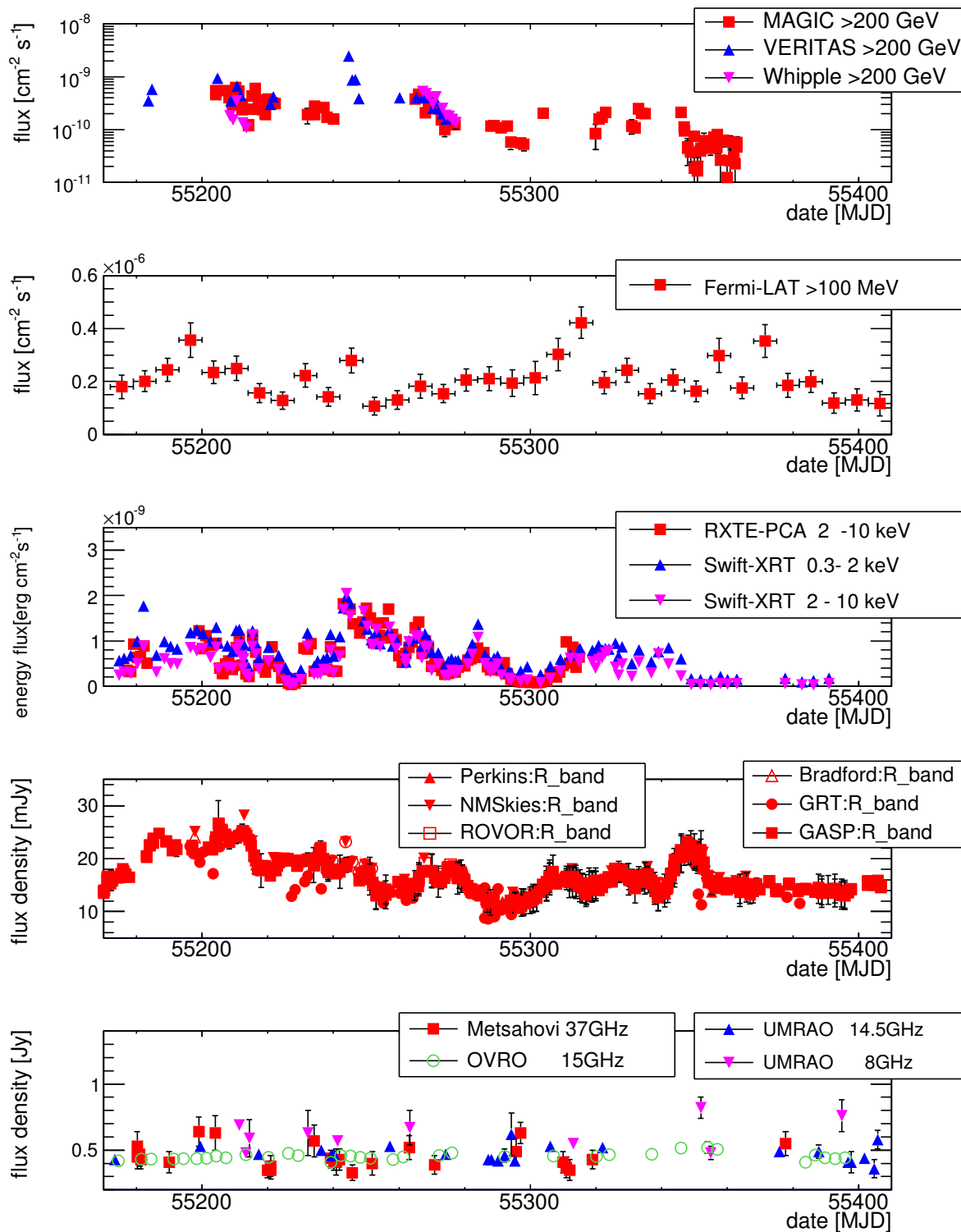


Figure 5.2.: LCs of Mrk 421 between 2009 December and 2010 August. See more description in the caption of Figure 5.1.

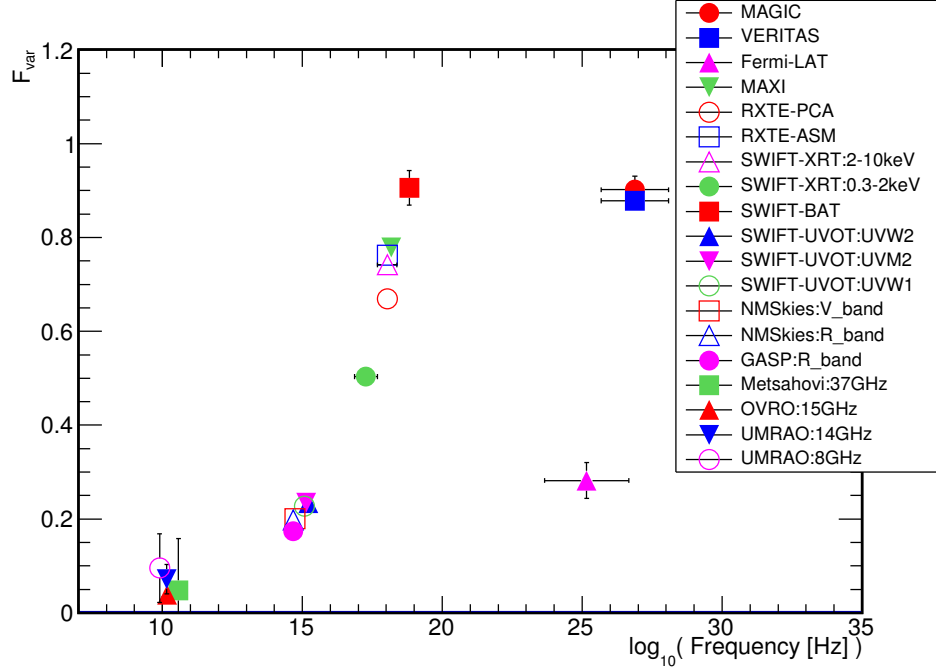


Figure 5.3.: Fractional variability F_{var} as a function of frequency derived with the MW data from 2010.

[Vaughan et al., 2003]. The F_{var} for each energy band is computed as

$$F_{\text{var}} = \sqrt{\frac{S^2 - \langle \sigma_{\text{err}}^2 \rangle}{\langle F \rangle^2}}, \quad (5.1)$$

where $\langle F \rangle$ is the mean photon flux, S is the standard deviation of the N flux points, and $\langle \sigma_{\text{err}}^2 \rangle$ is the mean squared error. The error of F_{var} is calculated according to the prescription in the Section 2.2 of [Poutanen et al., 2008]:

$$\sigma_{F_{\text{var}}} = \sqrt{F_{\text{var}}^2 + \sqrt{\frac{2\langle \sigma_{\text{err}}^2 \rangle^2}{N\langle F \rangle^4} + \frac{4\langle \sigma_{\text{err}}^2 \rangle F_{\text{var}}^2}{N\langle F \rangle^2}} - F_{\text{var}}}. \quad (5.2)$$

This prescription is more precise than the method used in [Vaughan et al., 2003] when the σ_{err} is comparable or larger than S .

Figure 5.3 shows the F_{var} of each instrument. Note that there are only instruments with $S^2 > \sigma_{\text{err}}^2$ in the figure. $S^2 < \sigma_{\text{err}}^2$ might occur when there is no variability detectable with the resolution of the instrument.

In Figure 5.3, the F_{var} increases with the emission energy from both the synchrotron and the inverse-Compton bumps:

$$F_{\text{var}}(\text{VHE } \gamma\text{-ray}) > F_{\text{var}}(\text{HE } \gamma\text{-ray}),$$

$$F_{\text{var}}(\text{high-E X-ray}) > F_{\text{var}}(\text{low-E X-ray}) > F_{\text{var}}(\text{UV}) > F_{\text{var}}(\text{optical}) > F_{\text{var}}(\text{radio}),$$

where E stands for energy. The variability in the rising segment of the bumps is lower by factors of a few than that in the falling segment of the bumps.

5.3. Multi-band Variability in the March Flaring Activity

In this section, we present the experimental results derived from the MW campaign observations described in Section 5.1. Figure 5.4 shows the multi-band LCs during the decline observed between 2010 March 10th (MJD 55265) and 2010 March 22nd (MJD 55277). In the top left panel, the VHE band includes 9 observations from MAGIC, 9 from VERITAS, and 10 from Whipple, densely distributed during this 13-day interval.

The VHE flux roughly decreases with time. Before MJD 55272 the fluxes are $\sim 1\text{--}2$ c.u., while after this day they are below 1 c.u., showing that only the decay (perhaps including the peak) of the flare was observed with the VHE γ -ray instruments in 2010 March. It is worth noting that the VHE flux measured with MAGIC for MJD 55268 is roughly 50% smaller than that measured with VERITAS for that day: 2.1 ± 0.3 vs. 4.0 ± 0.6 in units of $10^{-10}\text{cm}^{-2}\text{s}^{-1}$. Taking into account the measured errors, these fluxes are different by 3–4 standard deviations. This might result (at least partially) from systematics related to the instruments/observations during that night, but it might also be due to intra-night variability over the MAGIC and VERITAS observation windows, which are ~ 7 hours apart.

The photon flux above 300 MeV (measured by *Fermi*-LAT in two-day long time intervals) does not show any significant variability. A fit with a constant line gives a flux level of $(6.8 \pm 0.9) \times 10^{-8}\text{cm}^{-2}\text{s}^{-1}$, with $\chi^2/\text{ndf} = 2.5/6$ (the probability of a steady flux is 87%; 0.2σ to be variable).

The variability in the X-ray band, as measured with RXTE, *Swift* and MAXI is high, with LCs that resemble the ones at VHE.

At UV and optical frequencies, the variability is again rather small, in contrast to the VHE and X-ray bands. The optical data were corrected for the host galaxy contribution, which is estimated using [Nilsson et al., 2007] and the color reported in [Fukugita et al., 1995]. Therefore, the optical fluxes depicted in Figure 5.4 are the ones attributed to blazar emission. The contribution of the host galaxy to the UV fluxes is negligible and hence not considered. The emission in the UV bands and optical bands is variable. For instance, a constant fit yields χ^2/ndf of 174/11 and 144/60 for the UVOT-UVM2 and GASP/R band (12σ , 5.8σ to be variable). Hence Mrk 421 showed some variation in these bands, although it is substantially smaller than that shown at VHE and X-rays.

Optical polarization measurements are also reported in the following two panels in the right column of Figure 5.4. One depicts the polarization degree in percentage and the other reports the direction of the polarization vector, none of them showing variations. Note that the errors of these measurements are too small to be seen in the plot. The errors of in these observations are smaller than 0.1% and 3° respectively for the polarization degree and the electric vector polarization angle.

In the radio bands, there were only four observations during this period: Metsähovi, UMRAO and OVRO. All of them reported a flux of about 0.5 Jy. We did not find significant variability in

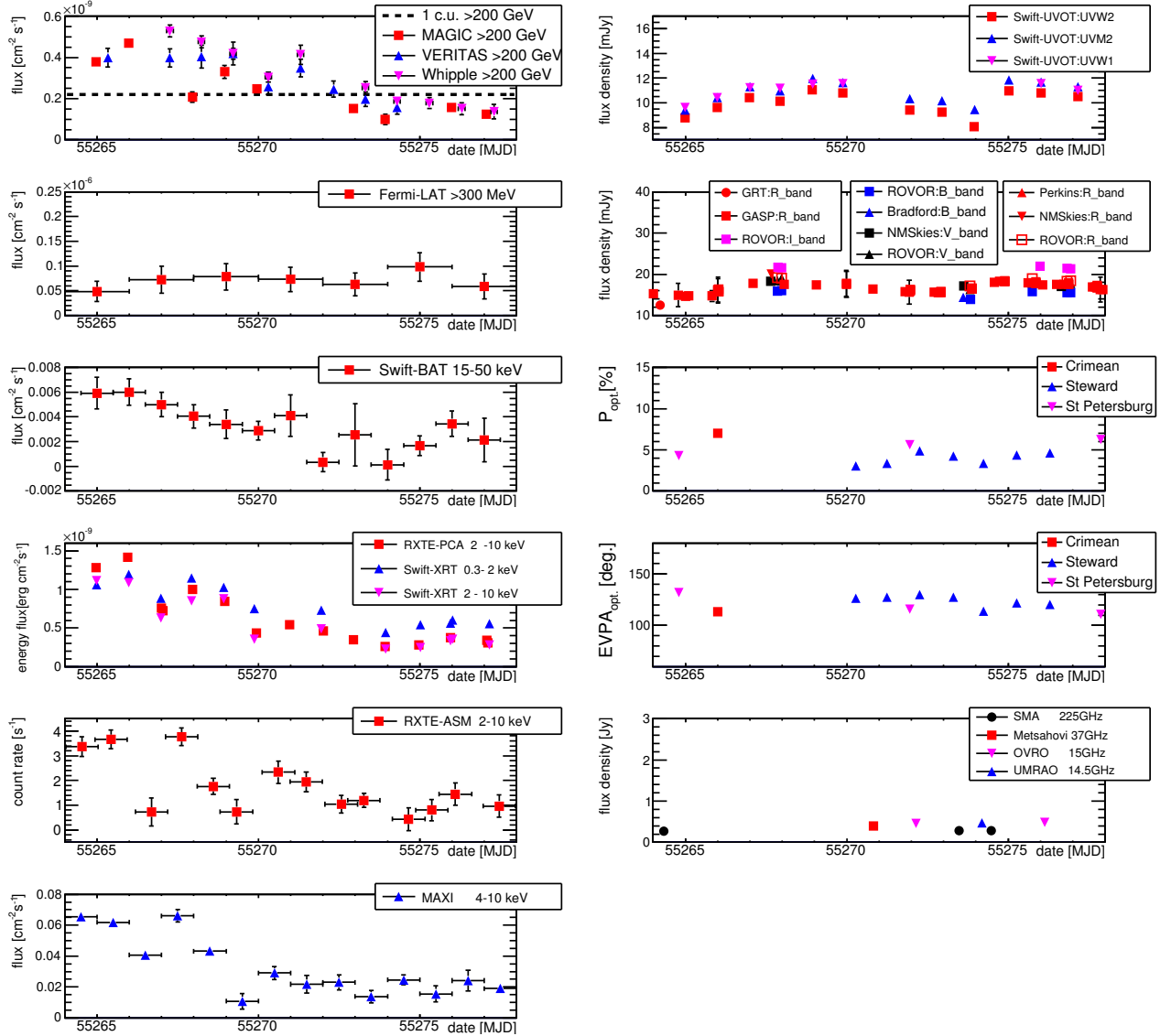


Figure 5.4.: LCs of Mrk 421 between MJD 55264 and 55278, from VHE to radio (including optical polarization). The Whipple data were converted to VHE fluxes above 200 GeV, and the host galaxy contribution was subtracted in the reported optical fluxes. P_{opt} and EVPA_{opt} stand for the polarization degree and the Electric Vector Polarization Angle. For details, see text in Section 5.3.

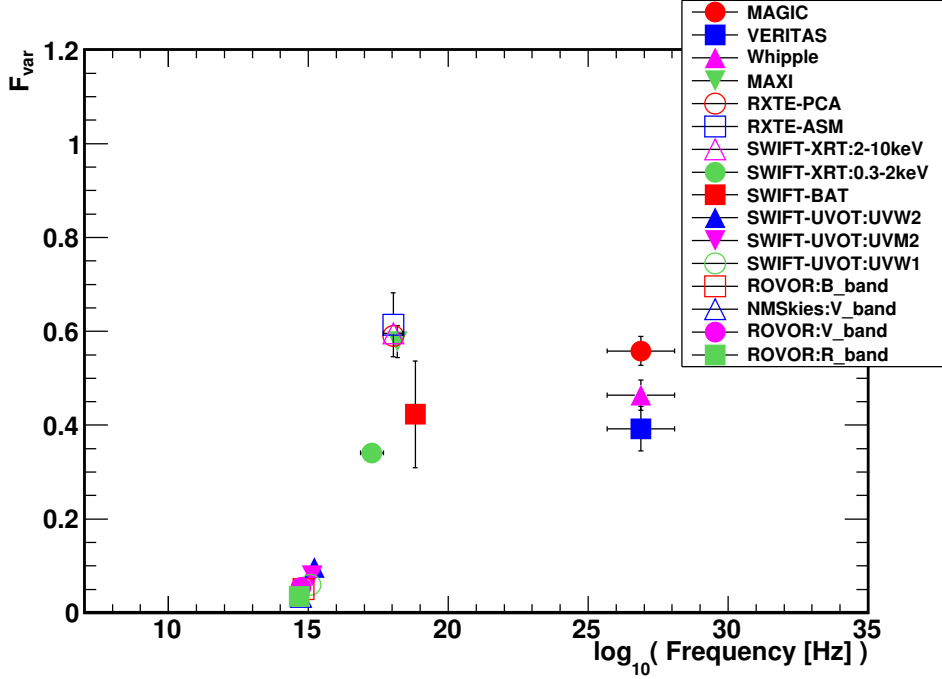


Figure 5.5.: Fractional variability F_{var} as a function of frequency derived with the MW data from 2010 March.

any of the single-dish radio observations, which are $\lesssim 1$ hour long.

In order to quantify the overall variability during these 13 consecutive days, F_{var} for each energy band is computed with Equations 5.1 and 5.2.

The F_{var} values derived from the LCs from Figure 5.4 are reported in Figure 5.5. The values of F_{var} are plotted only for instruments with $S^2 > \sigma_{\text{err}}^2$. When there is no variability detectable with the resolution of the instrument, $S^2 < \sigma_{\text{err}}^2$ might occur (as it is the case for *Fermi*-LAT).

The F_{var} is the highest in the X-ray band. The values of F_{var} measured by *Swift*-XRT and RXTE-PCA agree well in the 2-10 keV band. It is worth noticing that *Swift*-XRT shows a higher F_{var} in the 2-10 keV band than in the 0.3-2 keV band. This difference cannot be attributed to different temporal coverage, as these two were observed with the same instrument (and hence the same time).

In order to explain this difference, the normalized deviations of the fluxes, $F_{\text{dev}} = (F - \langle F \rangle) / \langle F \rangle$ computed with the *Swift*-XRT LCs for both energy bands (0.3-2 keV and 2-10 keV) are calculated. Figure 5.6 shows the absolute values of F_{dev} , $|F_{\text{dev}}|$, for the 2-10 keV band are always larger than those for the 0.3-2 keV band. This shows that the flux in the 2-10 keV band is intrinsically more variable than that in the 0.3-2 keV band across the whole temporal range, and hence that the highest F_{var} is not due to one or a few observations, but rather dominated by a higher overall relative dispersion in the flux values during the 13 consecutive days. The F_{var} for VHE γ -rays is similar to that for X-rays. The flux points from VERITAS and Whipple are more concentrated around its mean value, which yielded a slightly lower F_{var} in comparison with that of MAGIC. In

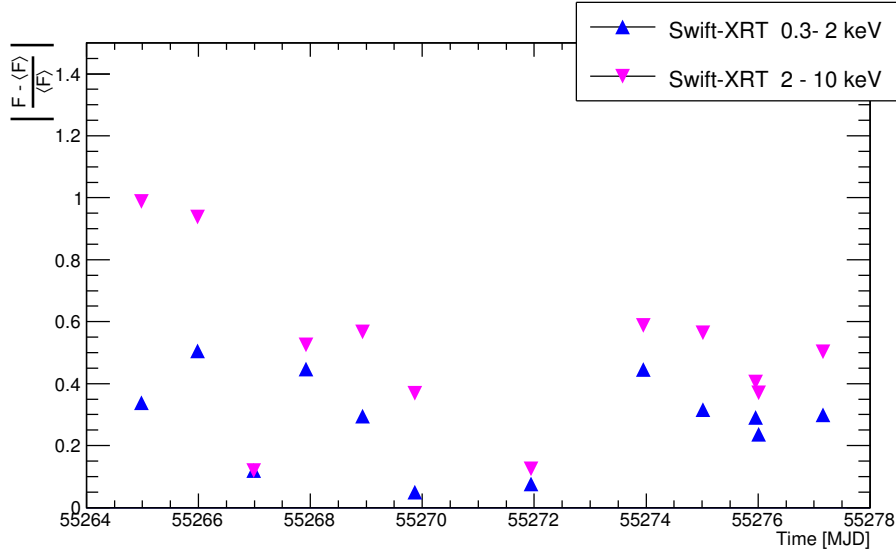


Figure 5.6.: Temporal evolution of the absolute value of the normalized deviation of the Swift-XRT flux, F_{dev} . See text for further details.

conclusion, both VHE *gamma*-rays and X-rays show higher variability than the flux in the other bands, which is another evidence that they have a closer relation to each other, as in several other Mrk 421 flaring activities (e.g., [Maraschi et al., 1999]). Consequently, the model to describe the emission mechanism of this flaring activity should also have the property that VHE γ -rays and X-rays must be closely related.

In order to understand better the relation between X-rays and VHE γ -rays, we examine the correlation between the X-ray energy flux in the 0.3-2 keV and 2-10 keV bands and the VHE γ -ray energy flux above 200 GeV. For this exercise we used the X-ray fluxes from *Swift*, RXTE and the VHE fluxes from MAGIC and VERITAS. The VHE photon fluxes given in [$\text{cm}^{-2} \text{s}^{-1}$] were converted to energy fluxes reported in [$\text{erg cm}^{-2} \text{s}^{-1}$] using a power-law spectrum with index 2.5 above 200 GeV. The top panel in Figure 5.7 shows the VHE γ -ray flux vs. X-ray flux in the 0.3-2 keV band, and the resulting fits of a linear ($F_{\text{VHE}} = k \cdot F_{\text{X-ray}}$) and a quadratic ($F_{\text{VHE}} = k \cdot F_{\text{X-ray}}^2$) function. For the fits, only MAGIC data were used, which are the VHE observations taken simultaneously or almost simultaneously to the X-ray observations (see Subsection 5.4.1 for details on simultaneity of the observations). The middle and bottom panel of Figure 5.7 show the same as the top panel, but when using the X-ray flux in the 2-10 keV band measured with *Swift* and RXTE. Neither a linear nor a quadratic function describes perfectly well the data. However, for the 2-10 keV energy range, the VHE to X-ray flux follows closely a linear trend, while it is clearly not the case for the 0.3-2 keV energy range. The scientific interpretation of these results will be discussed in Section 5.5.

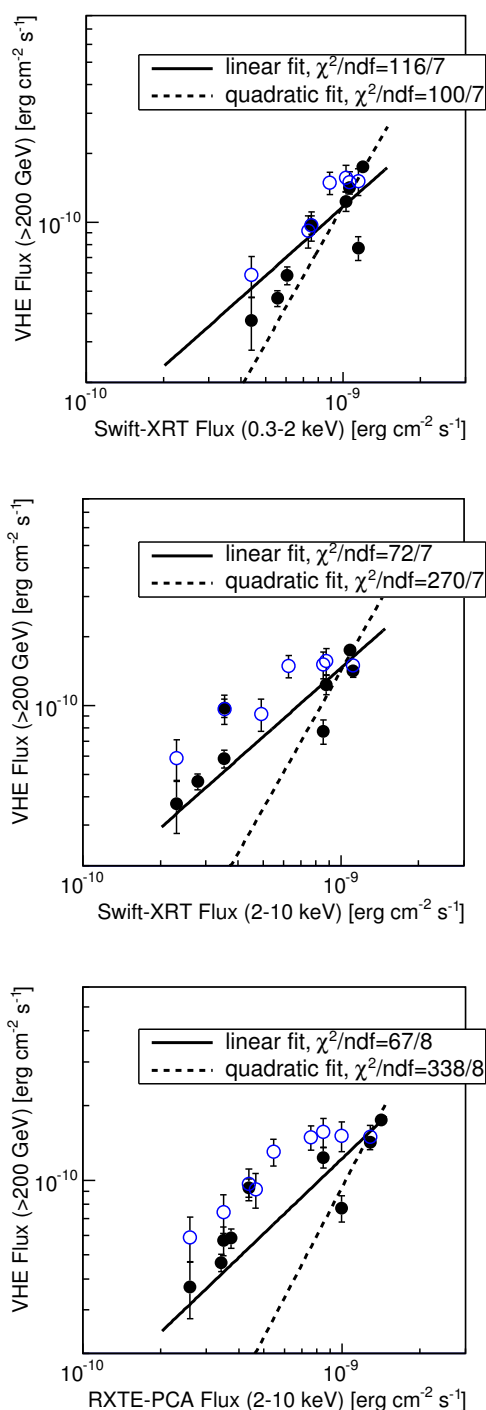


Figure 5.7.: Correlation between VHE γ -ray flux (MAGIC, depicted by black solid circles, and VERITAS, depicted with blue empty circles) and X-ray fluxes; **Top**: X-ray flux in the 0.3-2 keV band measured with *Swift*-XRT, **Middle**: X-ray flux in the 2-10 keV band measured with *Swift*-XRT, and **Bottom**: X-ray flux in the 2-10 keV band measured with RXTE-PCA. The lines show the fits with a linear ($F_{VHE} = k \cdot F_{X-ray}$) and a quadratic ($F_{VHE} = k \cdot F_{X-ray}^2$) function. Only MAGIC data points were used for the fits to ensure VHE-X-ray simultaneity (see Subsection 5.4.1).

5.4. Temporal Evolution of the Broadband Spectral Energy Distribution in the March Flaring Activity

During this flaring activity, we collected 13 successive simultaneous broadband SEDs for 13 consecutive days. In Subsection 5.4.1, we discuss characteristics of the collected MW data used to produce the SEDs. In Subsection 5.4.2, the emission model used in this study for Mrk 421 is introduced. In Subsections 5.4.3 and 5.4.4 we study these SEDs within a one-zone and a two-zone SSC scenario, respectively. Specifically, we investigate whether the temporal evolution of the EED in SSC models can explain the observed variations in the SED during the 13-day period, and hence the environment variables in the model, namely the blob radius (R), magnetic field (B), and Doppler factor (δ), were fixed (as much as possible) to their quiescent values. We cannot exclude that other model realizations with a different set of model parameters (e.g. changing the environment parameters, or varying a larger number of model parameters) can also provide a satisfactory description of the broadband SEDs, but in this study we wanted to vary only a few (as few as possible) model parameters to solidly study the evolution of the EED, which is the part of the model directly connected to the particle acceleration-and-cooling mechanisms.

5.4.1. Characteristics of the Measured Broadband SEDs

Given the known multi-band variability in the emission of Mrk 421 (and blazars in general), we paid special attention in organizing observations that are as close in time as possible. The simultaneity in the observations is depicted in Figures 5.8 and 5.9. The observations performed with MAGIC, RXTE, and *Swift* were scheduled weeks in advance, which allowed for actual observations occurring always within < 2-hour windows. The observations with VERITAS/Whipple were triggered by the high activity detected in 2010 March, and performed typically ~ 7 hours after MAGIC observations because VERITAS and Whipple are located at a different longitude from that of MAGIC. At radio frequencies we only have four observations during this period, but we do not expect variability in radio during these short (few days) timescales.

The measured SEDs for these 13 consecutive days are shown in Figures 5.10 – 5.12f. The actual MJD date for each data entry is given in the legend of each figure. For optical bands, the reported SED data points correspond to the averaged values (host-galaxy subtracted) for the specified observing night. As reported in Section 5.3, the variability in the optical band is small, and occurring on timescales of several days. Therefore, if there was no instrument observing at a particular optical energy band, then the nearest observation was used, and the corresponding MJD date is reported in the legend of the figure.

Although Mrk 421 is cosmologically nearby, at a redshift of 0.03, the absorption of γ -rays by the extragalactic background light (EBL) is not negligible at TeV energies. The VHE spectra from Figures 5.10 – 5.12f were corrected (de-absorbed) with the EBL model provided by [Franceschini et al., 2008], where $e^{-\tau_{\gamma\gamma}} = 0.58$ at 4 TeV. At this energy, which is roughly the highest energy bin in the VHE spectra, most models provide $0.5 < e^{-\tau_{\gamma\gamma}} < 0.6$, such as models from [Kneiske et al., 2004], [Finke and Razzaque, 2010], and [Domínguez et al., 2011], and hence there is no substantial difference.

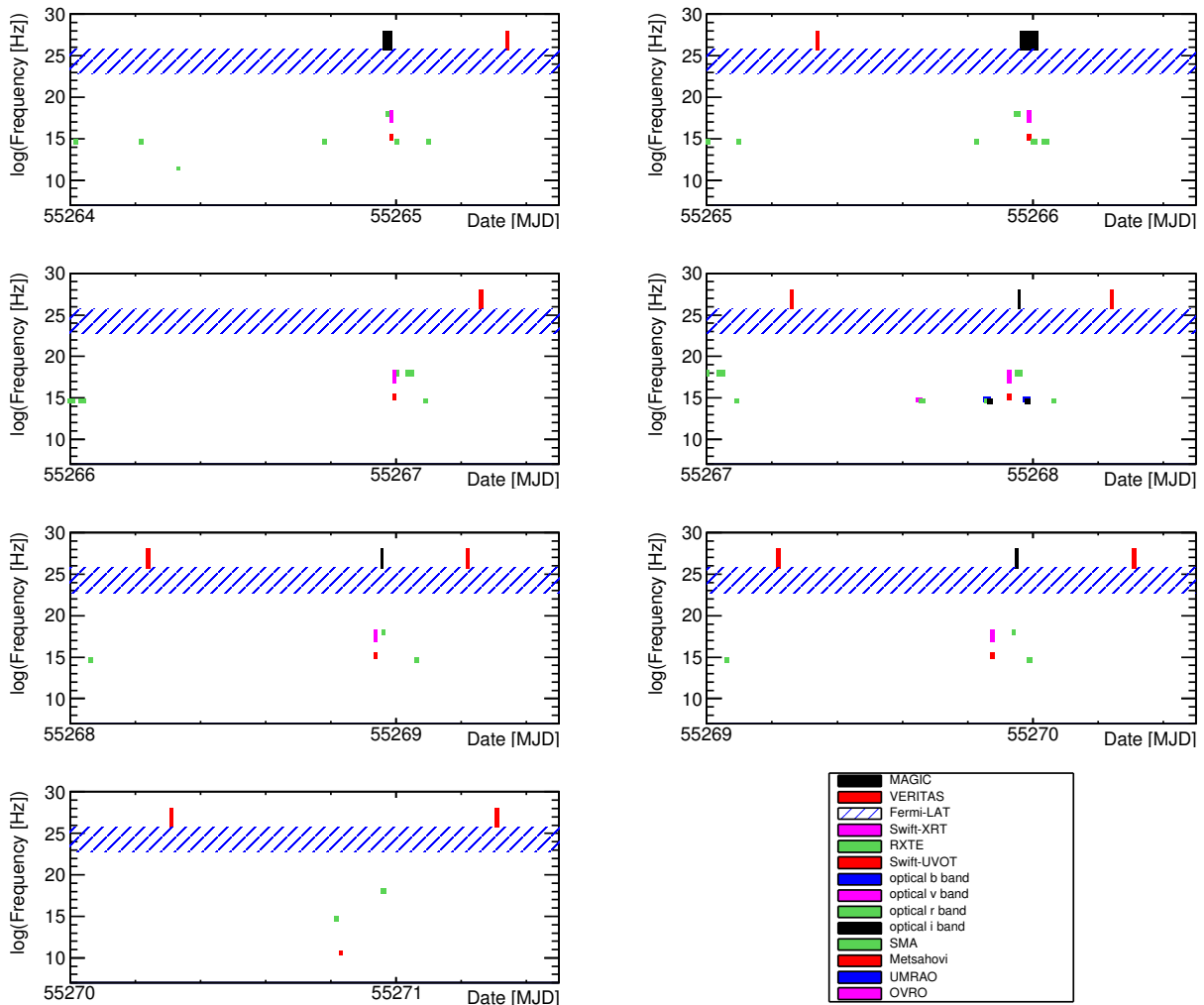


Figure 5.8.: Temporal and energy coverage during the flaring activity from 2010 March 10th (MJD 55265) to 2010 March 16th (MJD 55271). For better visibility of the observations at UV, optical, and radio band, where the observation time is usually short and the covered frequency band is narrow, additional 20 minutes in time and half a decade in frequency are used when displaying the results. The names of all the optical instruments are reported in Table 5.1.

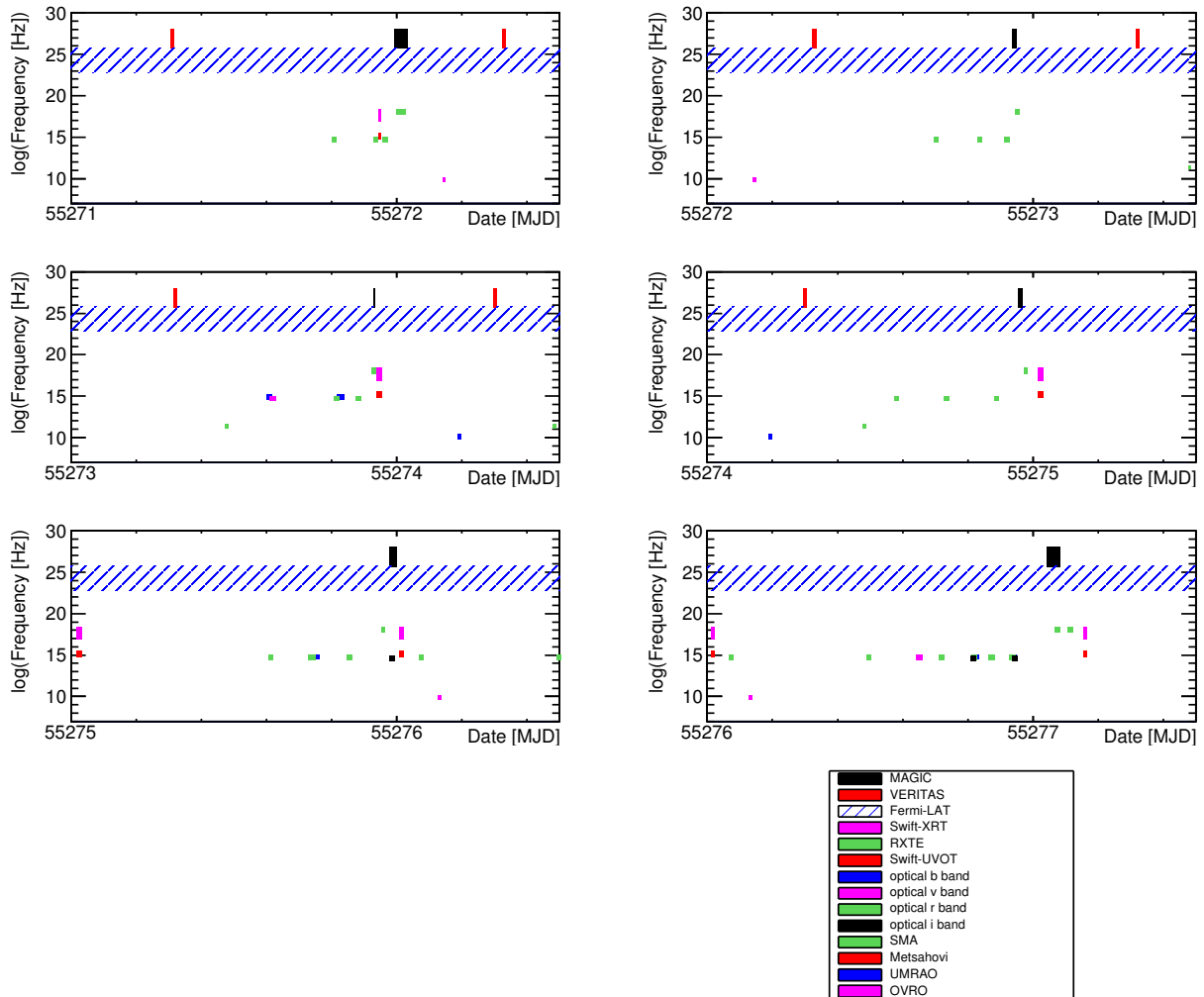


Figure 5.9.: Temporal and energy coverage during the flaring activity from 2010 March 17th (MJD 55272) to 2010 March 22nd (MJD 55277). See the caption of Figure 5.8 for further details.

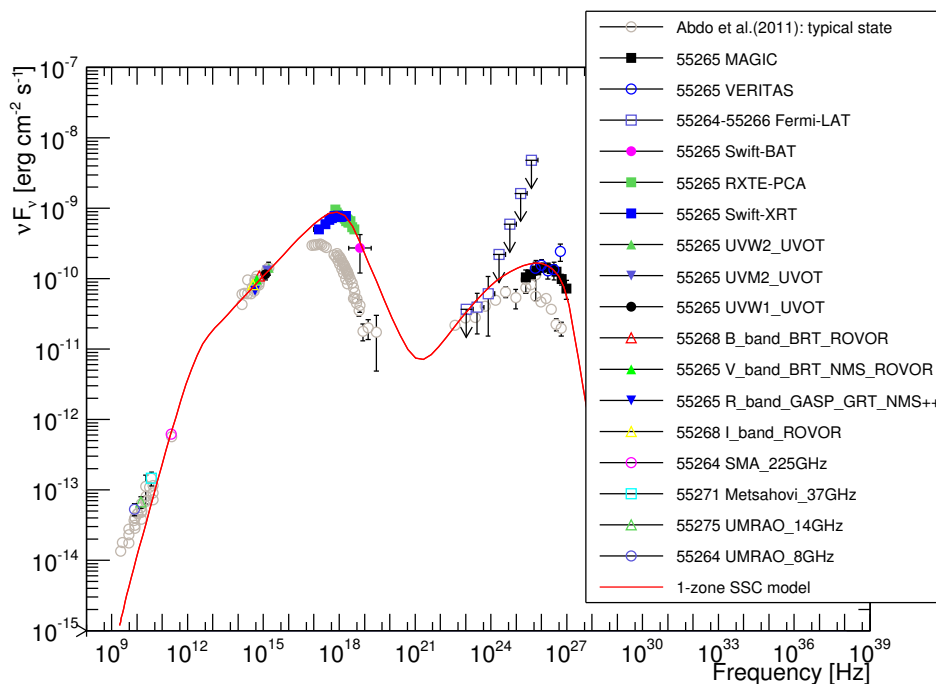
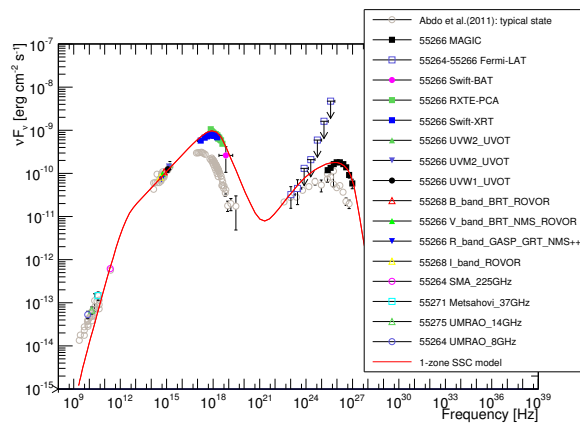


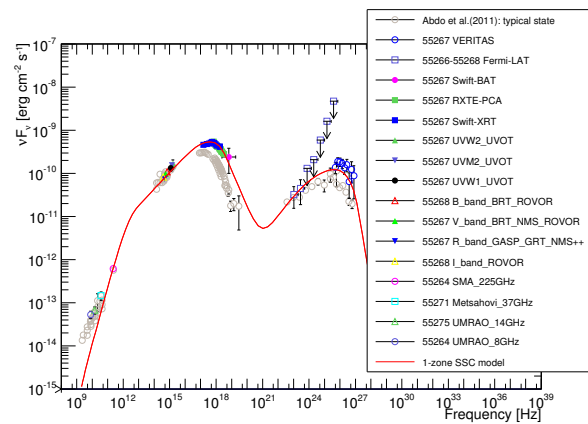
Figure 5.10.: Simultaneous broadband SED of Mrk 421 on MJD 55265. The correspondence between markers and instruments are given in the legend. The full names of the instruments can be found in Table 5.1. Many instruments contributed to the measurement of the optical R band. Due to space limitations, the symbol “++” is used to denote that there are more instruments than listed in the legend. Whenever simultaneous observations are not available, the fluxes from the closest date are reported, and its observation time in MJD is reported next to the instrument name in the legend. The red curve depicts the one-zone SSC model matching the data. The gray circles depict the averaged SED from the 2009 MW campaign reported in [Abdo et al., 2011], which is a good representation of the non-flaring (typical) SED of Mrk 421.

For comparison purposes, on each SED frame, we also show the averaged SED of the 2009 MW campaign [Abdo et al., 2011], which is a good representation of the SED of Mrk 421 during its non-flaring (typical) state. Each figure also contains its corresponding SSC model. The detail of the model and the characterization of the SED evolution will be discussed in Sections 5.4.3 and 5.4.4.

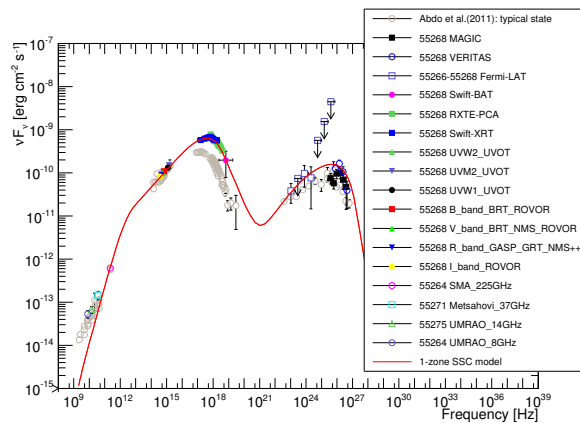
Studying the evolution of the SEDs from Figures 5.10 to 5.12f, one discerns that during high activity, both the height (peak luminosity) and the location (peak frequency) of the low- and high-energy SED bumps move. In general, both the peak frequency and the peak luminosity decrease as the flare decays. Besides the migration in the SED peak positions, we also can note a change in the shape of these SED bumps. The X-ray and γ -ray bumps of the SEDs from MJD 55265 and 55266 (Figure 5.10 and 5.11a), when Mrk 421 emitted the highest flux, are narrow, and they get wider as the flare decays. A quantitative evaluation of the widening of the two SED bumps



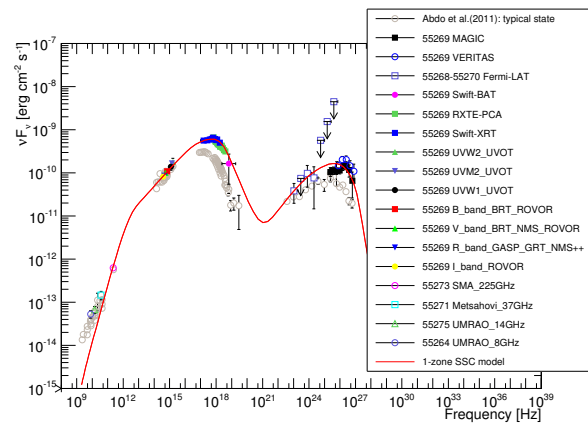
(a) MJD 55266.



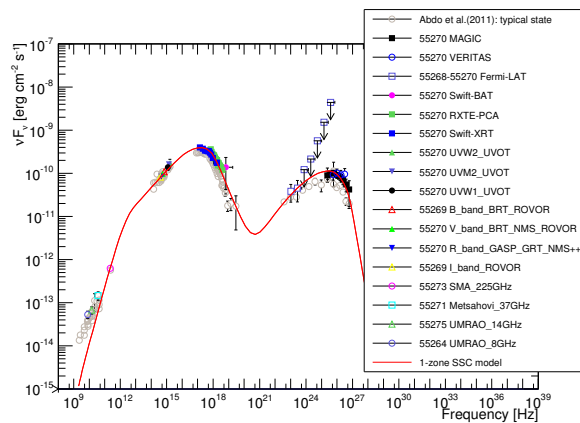
(b) MJD 55267.



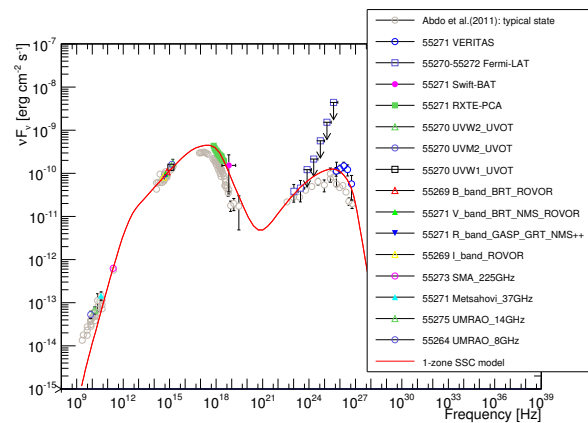
(c) MJD 55268.



(d) MJD 55269.

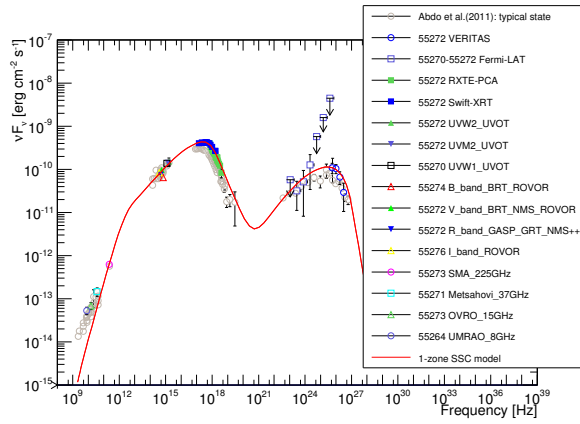


(e) MJD 55270.

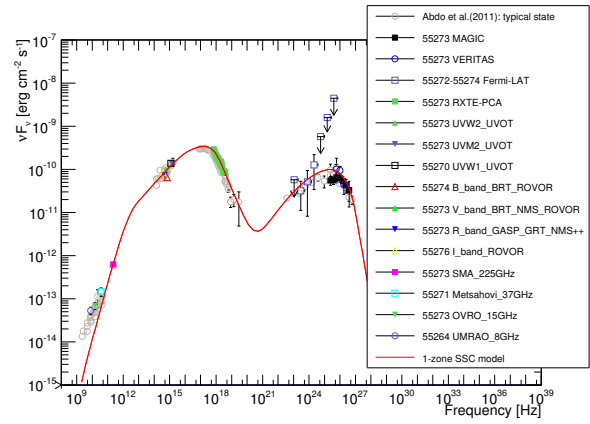


(f) MJD 55271.

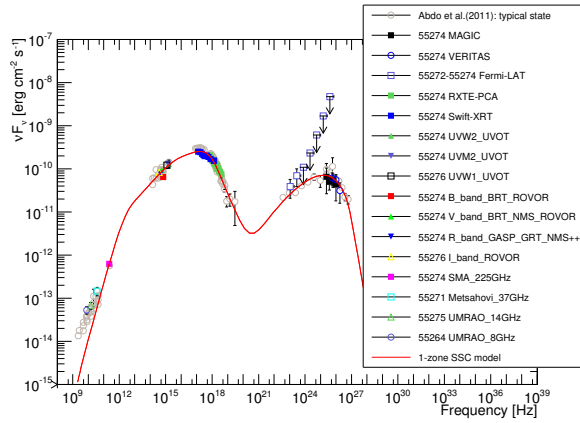
Figure 5.11.: Simultaneous broadband SEDs and their one-zone SSC model fits. See caption of Figure 5.10 for further details.



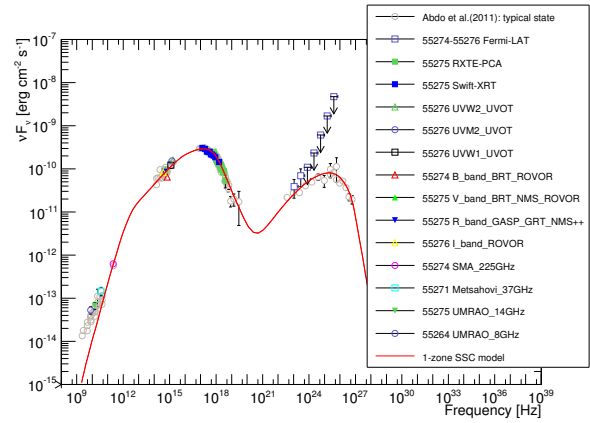
(a) MJD 55272.



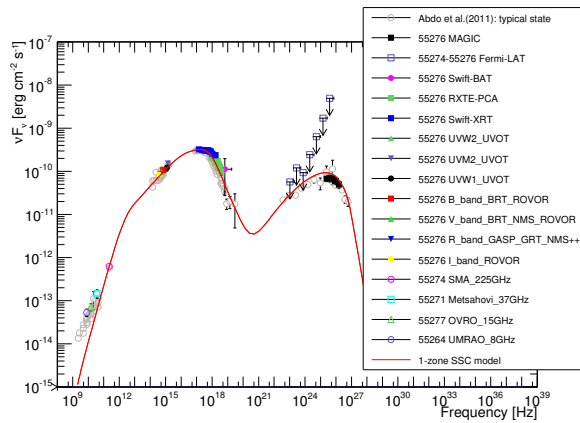
(b) MJD 55273.



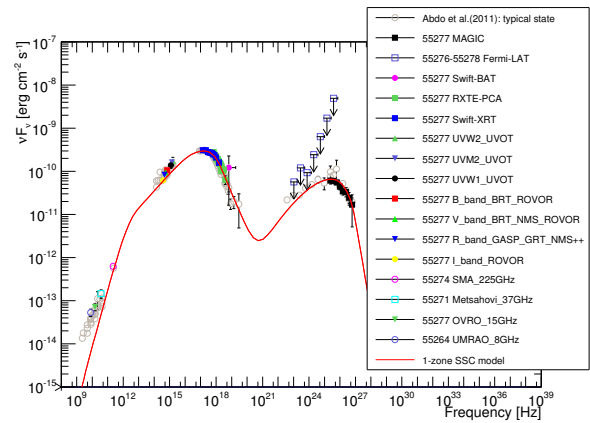
(c) MJD 55274.



(d) MJD 55275.



(e) MJD 55276.



(f) MJD 55277.

Figure 5.12.: Simultaneous broadband SEDs and their one-zone SSC model fits. See caption of Figure 5.10 for further details.

is reported in Section 5.5.

It is worth noting that SEDs during the last several nights are very similar to the averaged SED from 2009 reported in [Abdo et al., 2011]. Consequently, we decided to use the SED and SSC modeling results from [Abdo et al., 2011] as a reference for many of the studies/results reported here.

5.4.2. Description of the Synchrotron Self-Compton Model

In a one-zone synchrotron self-Compton (SSC) model, we assume that the emission comes from a single, spherical and homogeneous region in the jet, which is moving relativistically towards us. The one-zone SSC model can explain most of the measured SEDs with the smallest number of parameters, and hence it is the most widely used for HSP BL Lacs like Mrk 421.

In the SSC model, the emission from the radio to the X-ray bands, which the term synchrotron bump refers to, results from the synchrotron radiation of electrons inside a blob of a comoving radius R , with a Doppler factor δ . In this emission blob, there is a randomly-oriented magnetic field with uniform strength B . The emission of γ -rays, which the term *inverse-Compton bump* refers to, is produced by inverse Compton scattering of the synchrotron photons and the same electrons which produce them. Take the SED in Figure 5.10 as an example: the synchrotron bump is between 10^8 and 10^{21} Hz; the inverse-Compton bump is between 10^{21} and 10^{30} Hz. The electron spectrum is parameterized with as few power-law functions as possible. In the case of two power-law functions:

$$\frac{dn_e}{d\gamma_e} = \begin{cases} n_e \gamma_e^{-s_1} & \text{if } \gamma_{\min} < \gamma_e < \gamma_{\text{br}}, \\ n_e \gamma_e^{-s_2} \gamma_{\text{br}}^{s_2-s_1} & \text{if } \gamma_{\text{br}} < \gamma_e < \gamma_{\max}, \end{cases} \quad (5.3)$$

where n_e is the number density of the electron, γ_e is the Lorentz factor of the electron, γ_{\min} and γ_{\max} define the range of γ_e , s_1 and s_2 are the indices of the power-law function, and γ_{br} is the Lorentz factor where the power-law index changes. However, in order to describe the shape of the SED properly, occasionally we need three power-law functions:

$$\frac{dn_e}{d\gamma_e} = \begin{cases} n_e \gamma_e^{-s_1} & \text{if } \gamma_{\min} < \gamma_e < \gamma_{\text{br}}, \\ n_e \gamma_e^{-s_2} \gamma_{\text{br}}^{s_2-s_1} & \text{if } \gamma_{\text{br}} < \gamma_e < \gamma_{\text{br}2}, \\ n_e \gamma_e^{-s_3} e^{-\gamma_e/\gamma_{\max}} \gamma_{\text{br}1}^{s_2-s_1} \gamma_{\text{br}2}^{s_3-s_2} e^{\gamma_{\text{br}2}/\gamma_{\max}} & \text{if } \gamma_{\text{br}2} < \gamma_e, \end{cases} \quad (5.4)$$

where s_1 , s_2 and s_3 are the indices of the power-law functions, and γ_{br} and $\gamma_{\text{br}2}$ are the Lorentz factors where the power-law indices change. The electron spectrum described by these functions is called the Electron Energy Distribution (EED).

The calculation of the SSC emission model in this study is carried out by the code from Hajime Takami (a former post-doc in the MAGIC/CTA group at Max-Planck Institute for Physics), which is described in [Takami, 2011]. To make the emission model in this study comparable to previous Mrk 421 studies, the SSC code used in [Abdo et al., 2011] for Mrk 421 2009 MW data is chosen for comparison. The code was written by Justin Finke, and described in [Finke et al., 2008a]. These two codes agree if the effective confinement time of synchrotron photons is set as R/c in Hajime's code.

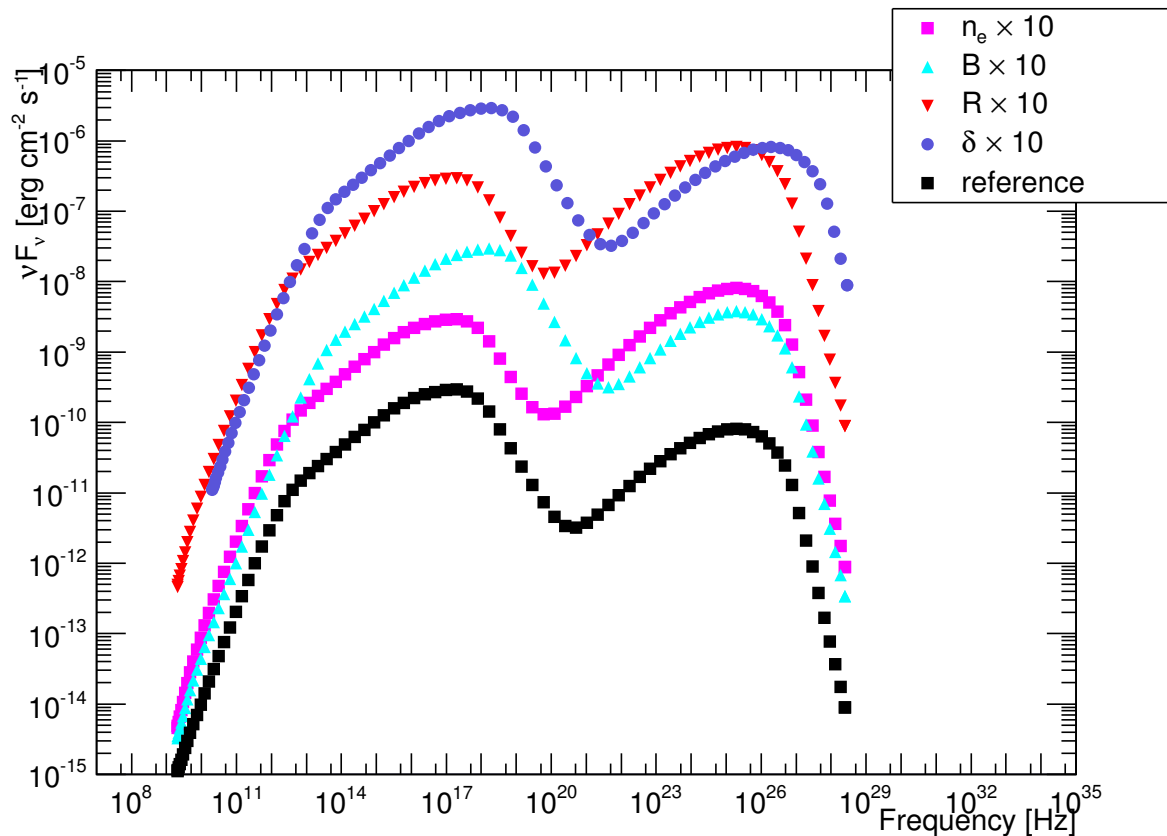


Figure 5.13.: The broadband emission determined with the one-zone SSC code from [Takami, 2011] for several sets of model parameters. The reference set of parameters are reported in Table 5.2. The other curves relate to the changes in one of the model parameters with respect to the reference set as specified in the legend.

Table 5.2. The reference set of SSC parameters.

γ_{\min}	γ_{\max}	γ_{br}	$\gamma_{\text{br}2}$	s_1	s_2	s_3	$n_e [\text{cm}^{-3}]$	$B [\text{mG}]$	$\log(R [\text{cm}])$	δ
800	1.0×10^8	3.5×10^4	3.9×10^5	2.2	2.7	4.7	900	38	16.72	21

Note. — This set of parameters produce the comparison baselines in Figures 5.13 – 5.15. They can also reproduce the model used in [Abdo et al., 2011] for the 2009 Mrk 421 SED.

In order to investigate the impact of each parameter on the resulting SED, comparisons of model SEDs by changing model parameters are shown in Figures 5.13 – 5.15. They basically show the following properties:

- The parameters γ_{\min} , s_1 , γ_{br} , s_2 , $\gamma_{\text{br}2}$, s_3 , γ_{\max} are together used to control the shape of the SED, in particular the synchrotron bump, which results directly from synchrotron emission of the electrons in the ambient magnetic field. The shape of the inverse-Compton bump is more complex because it results from the interaction of the electrons on the synchrotron photons, that also spread over a large range of energies. Moreover, the high-energy part of the inverse-Compton bump is sometimes truncated slightly by the Klein-Nishina effect.
- The parameters n_e , B , R , δ are used to control the peak positions and heights of both bumps: $(\nu|_{\text{syn.peak}}, \nu F_\nu|_{\text{syn.peak}})$ and $(\nu|_{\text{ic.peak}}, \nu F_\nu|_{\text{ic.peak}})$. A higher n_e , B , δ , or R can bring a higher peak νF_ν . However, out of these 4 parameters, only δ and B can possibly change the peak ν .

$$(\nu|_{\text{syn.peak}}, \nu|_{\text{ic.peak}}, \nu F_\nu|_{\text{syn.peak}}, \nu F_\nu|_{\text{ic.peak}}) \propto (n_e^0 B^1 \delta^1 R^0, n_e^0 B^0 \delta^1 R^0, n_e^1 B^2 \delta^4 R^3, n_e^2 B^1 \delta^4 R^4) \quad (5.5)$$

For instance, to adjust the νF_ν ratio between the two bumps, n_e and B are needed; to adjust the separation between the two peak frequencies of the two bumps, B and δ are needed. See Figure 5.13 for a visualization of the effects of changes in n_e , B , δ , or R in the broadband emission.

- The truncation of the emission at frequencies of radio part and ~ 100 keV X-ray depends on γ_{\min} , γ_{\max} respectively. See Figure 5.14 for a visualization of the effects of changes in γ_{\min} and γ_{\max} .
- The $\gamma_{\text{br}2}$ affects also the peak positions. A higher $\gamma_{\text{br}2}$ moves both of them up and towards higher energies:

$$(\nu|_{\text{syn.peak}}, \nu|_{\text{ic.peak}}, \nu F_\nu|_{\text{syn.peak}}, \nu F_\nu|_{\text{ic.peak}}) \propto (\gamma_{\text{br}2}^2, \gamma_{\text{br}2}^1, \gamma_{\text{br}2}^1, \gamma_{\text{br}2}^1). \quad (5.6)$$

See Figure 5.14 for a visualization of the effects of changes in $\gamma_{\text{br}2}$.

- The slopes on both sides of the synchrotron bump are determined by s_1 , s_2 , and s_3 . The s_1 and s_2 correspond to the slope on the low-energy side; the s_3 to the high-energy side. A softer s_1 or a softer s_2 makes νF_ν lower and the slope less steep; a harder s_2 makes νF_ν lower but the slope steeper. See Figure 5.15 for a visualization of the effects of changes in s_1 , s_2 and s_3 .

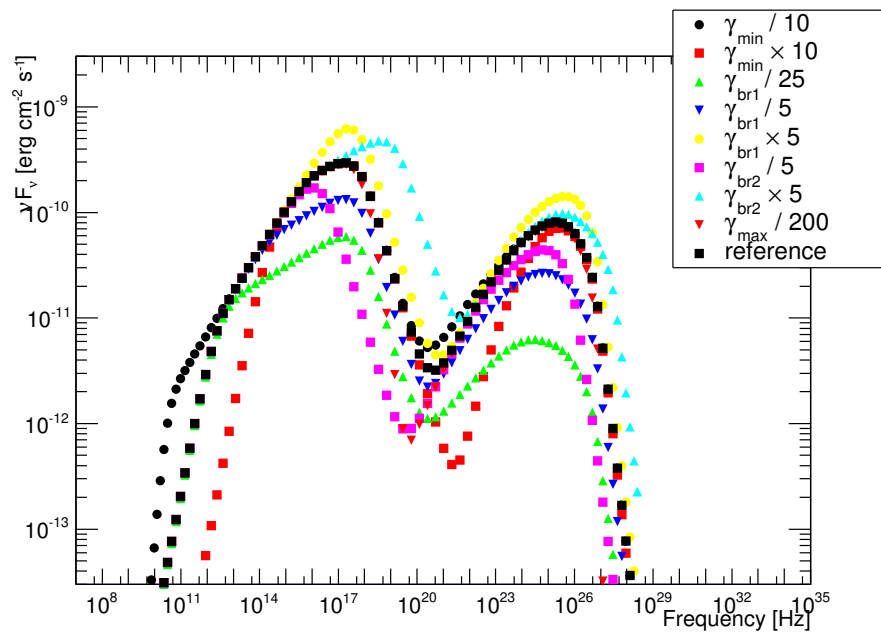


Figure 5.14.: The broadband emission determined with the one-zone SSC code from [Takami, 2011] for several sets of model parameters. See the caption of Figure 5.13 for further details.

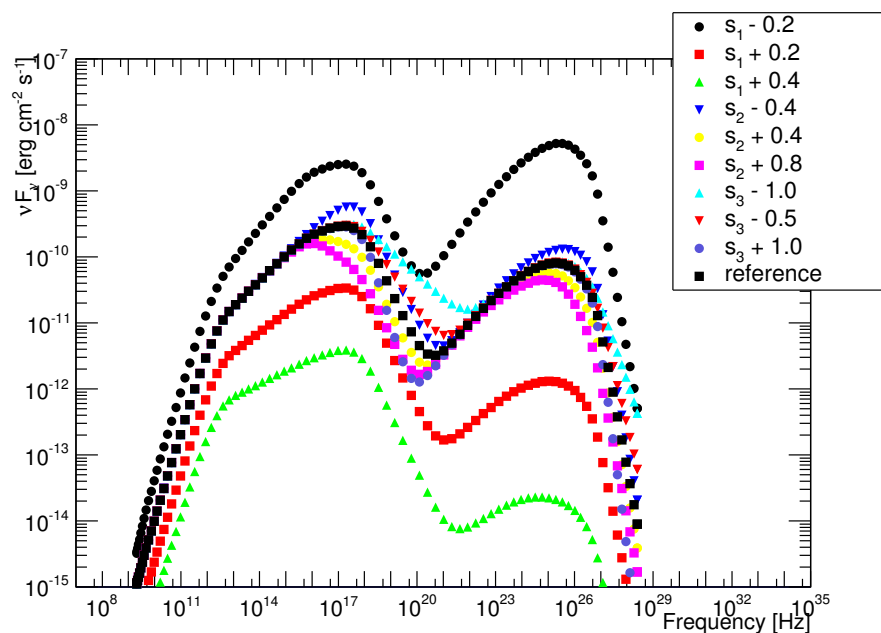


Figure 5.15.: The broadband emission determined with the one-zone SSC code from [Takami, 2011] for several sets of model parameters. See the caption of Figure 5.13 for further details.

5.4.3. SED Modeling: One-zone SSC Model

The one-zone homogeneous SSC scenario with an EED described with a broken power-law function (seven free parameters plus the two parameters defining the edges of the electron spectra) can be formally constrained from the seven characteristic observables that can be obtained from the multi-instrument data covering the two SED bumps, namely the spectral indices below and above the synchrotron peak, the peak frequencies and luminosities of the synchrotron and inverse Compton bumps, and the variability timescale [Tavecchio et al., 1998]. However, in reality the collected data do not allow us to determine these seven parameters with very good precision (particularly for the variability timescale and the peak frequency of the inverse Compton bump), which implies some degeneracy in the seven(+two) model parameters, unavoidably leading to the necessity of making some approximations or assumptions.

In previous works related to Mrk 421, it was common to use only one or two power-law functions (that is zero or one break) to describe the electron energy distribution. However, such a simple model could not adequately describe the broadband SED from the campaign organized in 2009, when Mrk 421 was in its typical non-flaring VHE state [Abdo et al., 2011]. The SED from this paper was better sampled (more instruments with higher sensitivity) than the ones reported previously, and an additional break (two additional parameters) was required to properly describe the shape of the measured synchrotron bump (from 1 eV to 100 keV), together with the full inverse-Compton bump (from 100 MeV to 10 TeV). Given the similar energy coverage and activity of the source during many days of the 13-day period, we decided to also allow for three power-law functions (i.e. two breaks) to parameterize the EED as in Equation 5.4. In total, this model has two more free parameters compared to the model with a broken power-law EED. The SEDs from the days with highest activity could be described with an EED with only one break, but for the non-flaring activity (similar to the SED from [Abdo et al., 2011]), we needed to use an EED with two breaks. The requirement for a more complex parameterization of the EED in the recent works might be due to the better energy coverage (more instruments involved in the campaigns), and better sensitivity to cover the γ -ray bump. Future observations of Mrk 421 during non-flaring states with as good or better energy coverage will tell us whether the two-break EED is always needed, or whether this is something that was required only to describe the 2009 and 2010 data.

Table 5.3.: Integral flux above 200 GeV and parameters of the one-zone SSC model. Bold-faced text is used to depict the model parameters that were varied to describe the SED during the 13-day period.

Date [MJD]	MAGIC flux [$10^{-10}\text{cm}^{-2}\text{s}^{-1}$]	VERITAS flux [$10^{-10}\text{cm}^{-2}\text{s}^{-1}$]	Whipple flux [$10^{-10}\text{cm}^{-2}\text{s}^{-1}$]	γ_{\min} [10^2]	γ_{\max} [10^8]	$\gamma_{\text{br}1}$ [10^4]	$\gamma_{\text{br}2}$ [10^5]	s_1	s_2	s_3	n_e [10^3cm^{-3}]	B [mG]	$\log(R)$ [cm]	δ
55265	3.8 ± 0.2	4.0 ± 0.5		8	1	60.	6.0	2.23	2.23	4.70	1.14	38	16.72	21
55266	4.7 ± 0.2			8	1	66.	6.6	2.23	2.23	4.70	1.16	38	16.72	21
55267		4.0 ± 0.5	5.3 ± 0.3	8	1	16.	6.0	2.23	2.70	4.70	1.10	38	16.72	21
55268	2.1 ± 0.3	4.0 ± 0.6	4.8 ± 0.3	8	1	16.	6.0	2.20	2.70	4.70	0.90	38	16.72	21
55269	3.3 ± 0.3	4.2 ± 0.6	4.2 ± 0.3	8	1	12.	7.0	2.20	2.70	4.70	0.95	38	16.72	21
55270	2.3 ± 0.2	2.6 ± 0.4	3.0 ± 0.2	8	1	8.0	3.9	2.20	2.70	4.70	0.90	38	16.72	21
55271		3.5 ± 0.4	4.1 ± 0.5	8	1	9.0	5.0	2.20	2.70	4.70	0.90	38	16.72	21
55272		2.5 ± 0.4		8	1	5.0	4.0	2.20	2.50	4.70	0.90	38	16.72	21
55273	1.5 ± 0.2	2.0 ± 0.4	2.5 ± 0.3	8	1	6.0	3.9	2.20	2.70	4.70	0.90	38	16.72	21
55274	1.0 ± 0.3	1.6 ± 0.3	1.9 ± 0.2	8	1	3.5	3.9	2.20	2.70	4.70	0.90	38	16.72	21
55275			1.8 ± 0.3	8	1	5.0	3.9	2.20	2.70	4.70	0.85	38	16.72	21
55276	1.6 ± 0.2		1.5 ± 0.3	8	1	5.7	3.9	2.20	2.70	4.70	0.90	38	16.72	21
55277	1.2 ± 0.1		1.4 ± 0.4	8	1	8.0	3.9	2.20	2.70	4.70	0.70	38	16.72	21

Note— VERITAS and Whipple fluxes were measured around seven hours after the MAGIC observations.

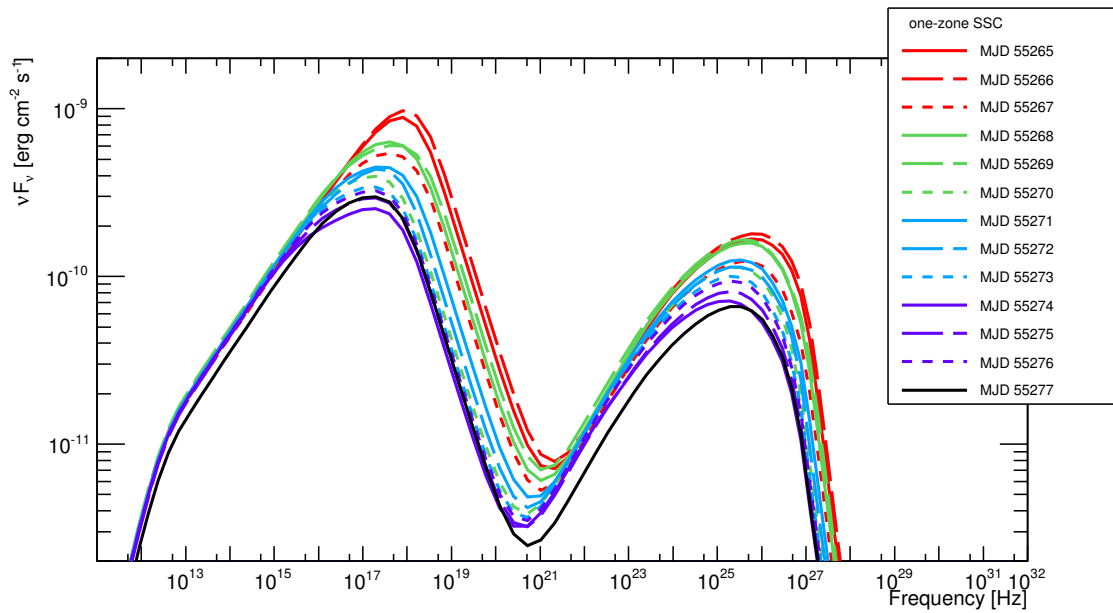
Despite the extensive MW data collected in this campaign, there is still some degeneracy in the choice of the eleven parameter values required to adjust the SED model to the observational data. Given the similarities to the SED reported in [Abdo et al., 2011] (e.g. see Figures 5.12e and 5.12f), we decided to use the SED model parameter values from [Abdo et al., 2011] as a reference for the choice of SSC parameters to describe the 2010 March broadband observations. In particular, we wanted to test whether the temporal evolution of the EED can explain the observed variations in the SED during the 13-day period, and hence we fixed the beginning and the end of the EED (γ_{\min} and γ_{\max}) and the environment parameters blob radius (R), magnetic field (B), and Doppler factor (δ) to the values reported in [Abdo et al., 2011]. The value of the Doppler factor, 21, is higher than the value inferred from VLBA measurements on the blob movement in [Piner et al., 2010]. This is actually a common problem for TeV sources, which has been dubbed the “bulk Lorentz factor crisis”, and requires the radio and TeV emission to be produced in regions with different Lorentz factors [Ghisellini et al., 2005, Georganopoulos and Kazanas, 2003].

During the adjustment of the model to the measured SED, the VHE and X-ray data provide the primary constraint because the emission in both bands had the largest variability. Therefore, a good model should explain the change in these two bands at the same time.

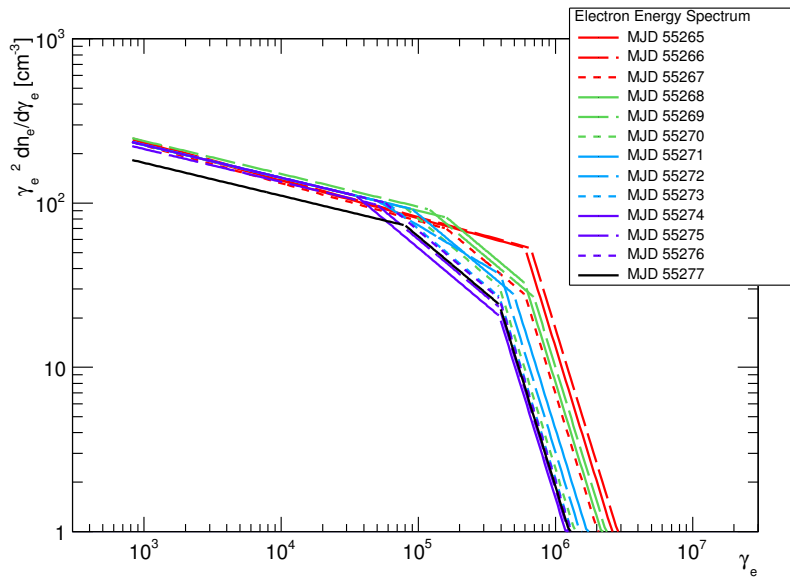
The broadband SEDs and the model results for each day are shown in Figures 5.10 – 5.12. The resulting model parameters are reported in Table 5.3. Given the values of the blob radius and Doppler factor used here, the minimum time of the flux variation $t_{\min} = (1 + z)R/c\delta$ is ~ 1 day. This value is reasonable, given the flux variations measured during the March flaring activity (see Figure 5.4), yet it would not be consistent with the potential intra-night variability that might have occurred in MJD 55268, as hinted by the disagreement in the VHE fluxes measured by MAGIC and VERITAS. The predicted radiative cooling break by synchrotron radiation⁹, $\gamma_c = 6\pi m_e c^2 / (\sigma_T B^2 R)$, where m_e is the electron mass and σ_T is the Thomson cross-section, is 3.2×10^5 in this model. The γ_{br2} values in the model range from 3.9×10^5 to 7.0×10^5 , which is comparable to γ_c , hence suggesting that the second break in the EED might be related to the synchrotron cooling break. This indicates that a flare finishes by cooling. However, the change in the power-law index does not match the canonical change expected from synchrotron cooling, $\Delta s = 1$, which is similar to the situation reported in [Abdo et al., 2011]. The result that s_3 is softer than expectation can be explained by the inhomogeneity of the emission blob, or by a weakening of the electron injection.

We can see that the X-ray and γ -ray bumps of the SEDs on MJD 55265 and 55266 (Figures 5.10 and 5.11a), when Mrk 421 emitted the highest flux, are rather narrow. In Table 5.3, we can see that we need only one break in the EED (instead of two) in order to describe these sharp bumps on MJD 55265 and 55266. On the other hand, two breaks are necessary to properly describe the characteristics of the wider X-ray and γ -ray bumps from MJD 55267 to MJD 55277 (Figures 5.11b – 5.12f), when Mrk 421 shows a somewhat lower X-ray and VHE activity. This is similar to what occurred in the non-flaring state from 2009 [Abdo et al., 2011]. Therefore, the days MJD 55265 and 55266 can be denoted as the “one-break period” in this flaring activity, and the interval from MJD 55267 to MJD 55277 as the “two-break period”. The changes in the SED

⁹In HBLs like Mrk 421, the cooling of the electrons is expected to be dominated by the synchrotron emission.



(a) SEDs.



(b) EEDs.

Figure 5.16.: One-zone SSC model curves and the related EEDs used to describe the measured SEDs during the 13-day flaring activity. The parameter values are given in Table 5.3.

during the flaring activity are dominated by the parameters, n_e , γ_{br} , and γ_{br2} : a lower activity can be parameterized with a lower n_e and a decrease in the values of the two breaks in the EED.

For MJD 55272, $s_2 = 2.5$ while for the adjacent dates is 2.7. The X-ray bump in Figure 5.12a is rather narrow, and s_2 , which affects the slope of the left side of the bump, needs to be closer to s_1 to properly describe the data.

In general, the agreement between the one-zone SSC model and the observational data is quite acceptable in Figures 5.10 – 5.12f, which shows once more the success of the one-zone SSC model to describe the SEDs of blazars. However, there are several problems to be noted. One problem is that, at the low-energy-end of the VHE spectra, the model is slightly above the data for the SEDs from MJD 55265, 55266, 55268, 55269, and 55273 (Figures 5.10, 5.11a, 5.11c, 5.11d, and 5.12b). Moreover, there is also a data-model mismatch in the X-ray bump in the one-zone SSC model for MJD 55265 and 55266. The model goes slightly above the X-ray data. If the model X-ray flux was decreased in order to better match the data, the model would under-predict the optical and VHE γ -ray fluxes.

Overall, the temporal evolution of the broadband SEDs can be described by changes in the EED, keeping constant the beginning and end of the EED (γ_{min} and γ_{max}), and the environment variables (blob radius, magnetic field, and the Doppler factor) to the values reported in [Abdo et al., 2011]. Figures 5.16a and 5.16b depict the one-zone SSC model curves and the parameterized EEDs for the 13 consecutive days. Both together provide a summary of this flaring activity when parameterized within the above-mentioned one-zone SSC scenario. We can divide the whole activity into three periods: MJD 55265-55266 (period 1), MJD 55268-55271 (period 2), and MJD 55272-55277 (period 3), which correspond to a VHE flux of ~ 2 c.u., ~ 1.5 c.u., and ~ 0.5 c.u., respectively. The EEDs of period 1 have one break; while those of period 2 and 3 have two breaks. Moreover, the EEDs of period 1 have a higher electron number density (n_e) than those of periods 2 and 3. Figure 5.16b shows that the greatest variability occurs above the first break (γ_{br}) in the EED.

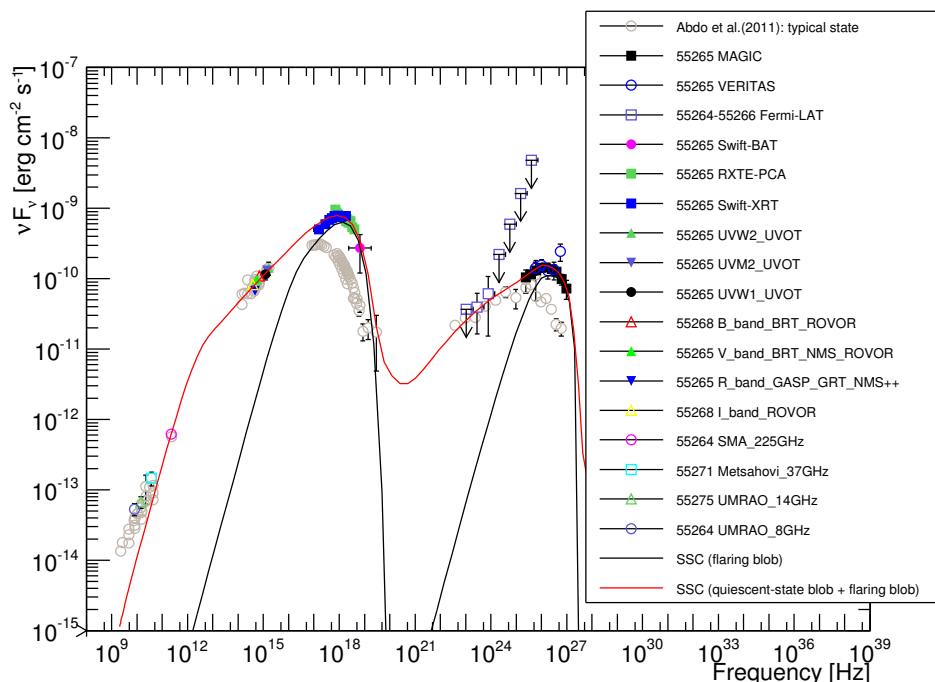


Figure 5.17.: Simultaneous broadband SED of Mrk 421 on MJD 55265. The correspondence between markers and instruments are given in the legend. The full names of the instruments can be found in Table 5.1. Whenever simultaneous observations are not available, the fluxes from the closest date are reported, and its observation time in MJD is reported next to the instrument name in the legend. Many instruments contributed to the measurement of the optical R band. Due to space limitations, the symbol “++” is used to denote that there are more instruments than listed in the legend. The red curve depicts the two-zone SSC model matching the SED data, while the black line shows the contribution of the flaring blob. The gray circles depict the averaged SED from the 2009 MW campaign reported in [Abdo et al., 2011], which is a good representation of the non-flaring (typical) SED of Mrk 421.

5.4.4. SED Modeling: Two-zone SSC Model

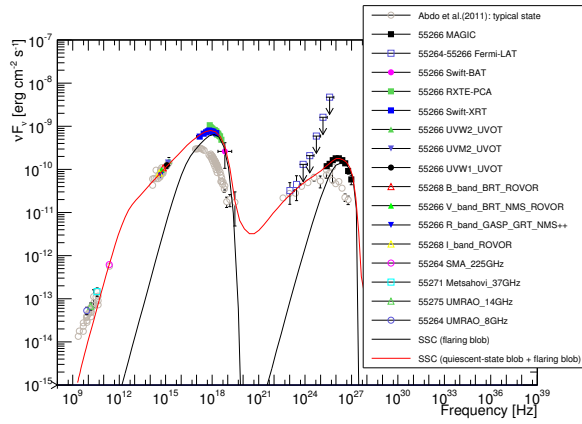
The one-zone SSC model curves reported in the previous section describe reasonably well the overall temporal evolution of the low- and high-energy bumps of the SED during this flaring activity. However, we cannot ignore the model-data mismatches mentioned in the last section, which suggest that the experimental data requires a better theoretical scenario. This was our main motivation for trying a model with two distinct blobs: one producing the steady emission, and the other one producing the temporal evolution of the SED, which mostly affects the X-ray and VHE γ -ray bands. The two blobs are assumed to be separated by a long distance and the individual radiation fields do not interact with each other. We call these the “quiescent blob” and the “flaring blob”, respectively. Since we keep the emission of the quiescent blob constant over time, and that of the flaring blob is always superimposed on that of the quiescent one, we

found it reasonable to fix the emission baseline (the quiescent blob) to the measured SED with the lowest activity among the 13 consecutive days, which is MJD 55274. Therefore, we fixed the parameters of the quiescent blob to the parameter values obtained with the one-zone SSC model (from Section 5.4.3) for MJD 55274 (Figure 5.12c). While the EED of the quiescent-state blob is described by three power-law functions, we employ only two power-law functions to describe the EED of the flaring blob as in Equation 5.3.

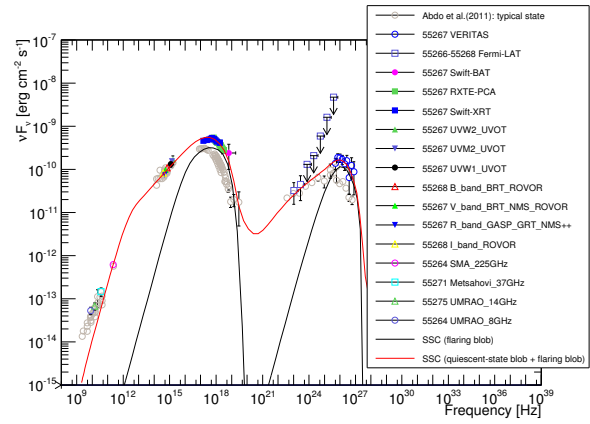
In the overall process of adjusting the model to the 13 measured SEDs, we aimed at having a flaring blob size about one order of magnitude smaller than the quiescent blob, which naturally would allow for faster variability. The size of the blob was kept constant, while the other parameters were allowed to change in order to describe the characteristics of the flare evolution. In particular, since the changes in the SED mostly occur in the X-ray and VHE range, the peak frequencies of the two SED bumps produced by the flaring blob should be higher than those produced by the quiescent-state blob.

The model curves that describe the 13 consecutive SEDs, including the model curves for the flaring blob and the overall emission of the model (quiescent blob+flaring blob) are shown in Figures 5.17 – 5.19. Table 5.4 reports the two-zone SSC model parameters that adequately describe the measured SEDs. Except for the magnetic field, which decreases during the decay of the flare, the other environmental parameters, namely the blob radius and the Doppler factor, remain constant. The changes occur in the three model parameters n_e , γ_{\min} , and γ_{br} , while s_1 , s_2 , γ_{\max} can be kept constant for all the 13 SEDs. With this two-zone SSC model, the minimum variability timescale t_{\min} is ~ 1 hour, which is comparable to the length of our single-instrument observations, where we did not measure significant variability. This short variability timescale would be consistent with the potential intra-night VHE variability on MJD 55268, when MAGIC and VERITAS/Whipple, whose observations are separated by seven hours, reported VHE fluxes that differ by a factor of two (see Figure 5.4 and Table 5.4). The predicted synchrotron cooling break γ_c for the flaring blob is 7×10^5 for MJD 55265 (the beginning of the measured flaring activity in 2010 March). For this day, the parameter γ_{br} for the flaring blob is 3×10^5 , with a change in the EED power-law index of 1, which is the canonical change for synchrotron cooling. During the following three days $\gamma_c/\gamma_{\text{br}} \lesssim 8$, and after MJD 55269 $\gamma_c/\gamma_{\text{br}}$ is much larger, which means that the break in the EED of the flaring blob is intrinsic to the acceleration mechanism, and cannot be directly related to the synchrotron cooling during those days.

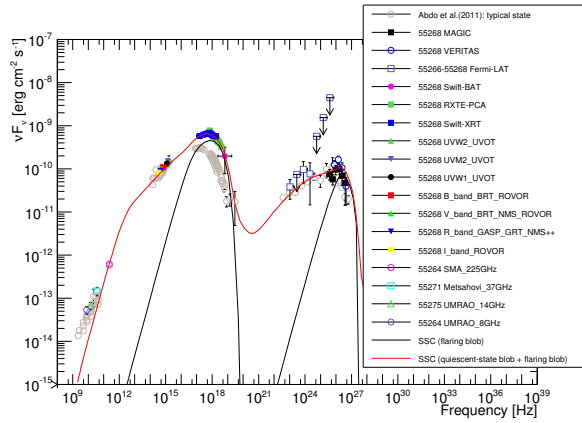
The flaring blob is characterized by an EED with a very high γ_{\min} ($> 3 \times 10^4$), which means that it lacks low-energy electrons, hence not contributing to the radio/optical emission. This is necessary for improving (with respect to the one-zone SSC model from Section 5.4.3) the description of the very narrow peaks in the X-ray and the γ -ray bumps occurring on some days (e.g. MJD 55265 and 55266).



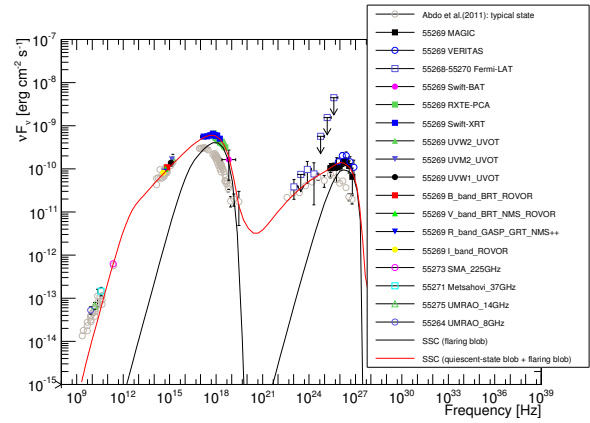
(a) MJD 55266.



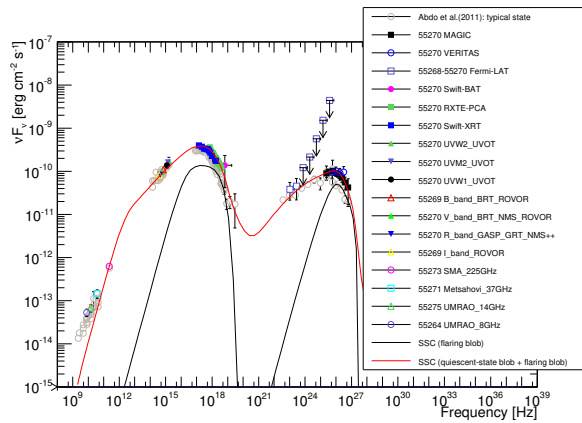
(b) MJD 55267.



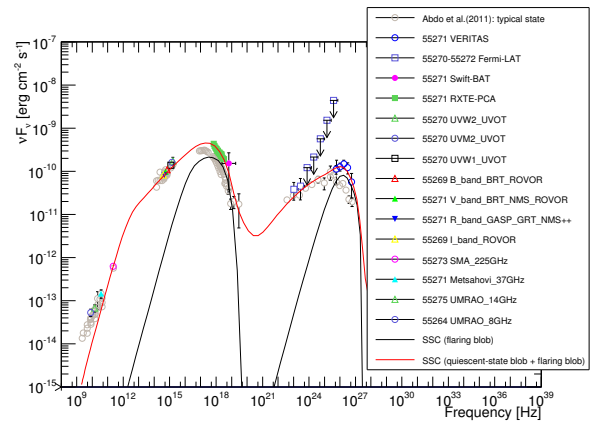
(c) MJD 55268



(d) MJD 55269.



(e) MJD 55270.



(f) MJD 55271.

Figure 5.18.: Simultaneous broadband SEDs and their two-zone SSC model fits. See caption of Figure 5.17 for further details.

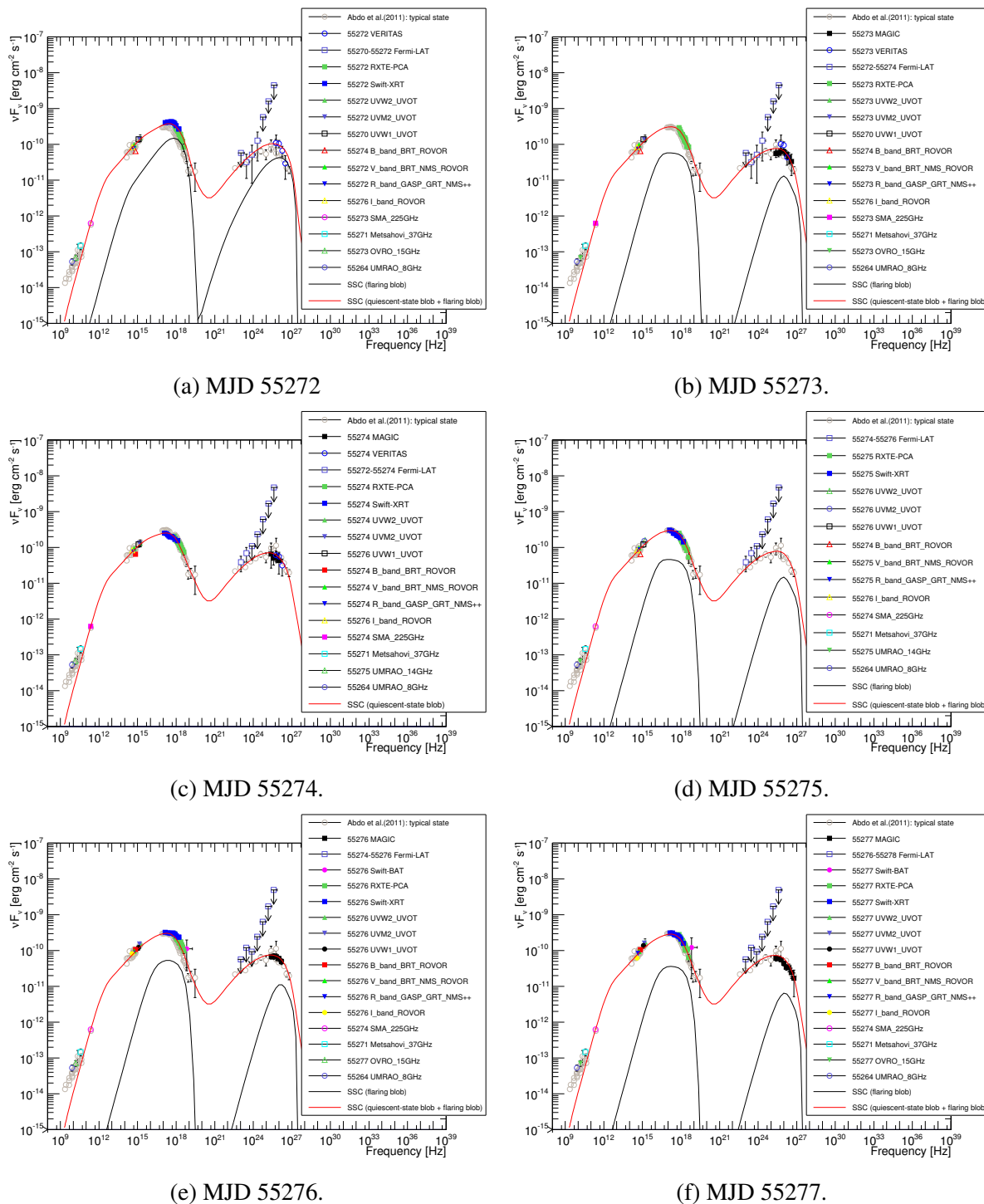
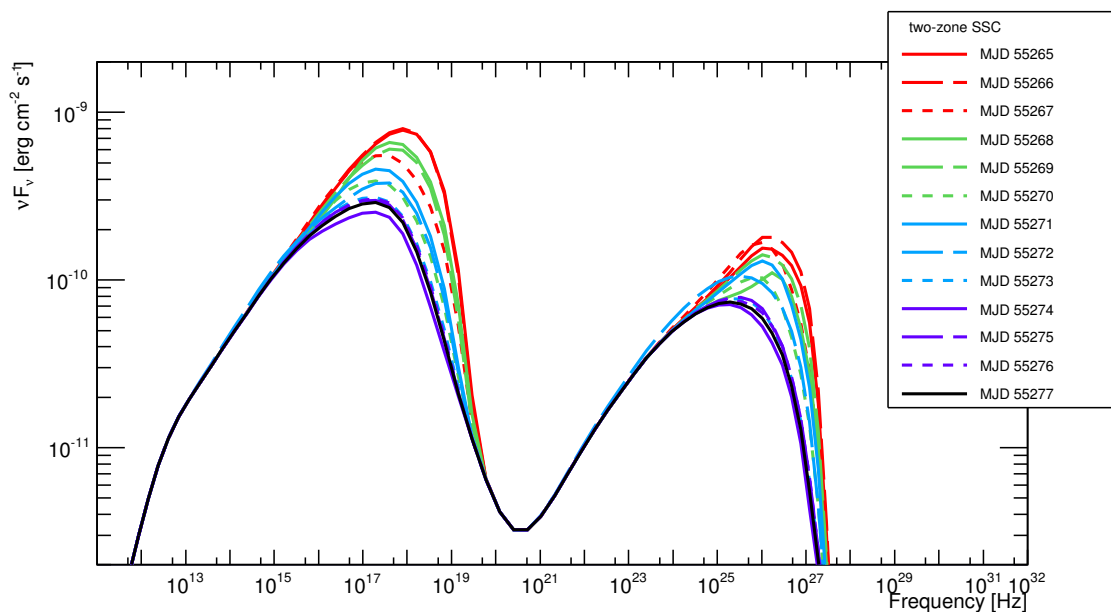


Figure 5.19.: Simultaneous broadband SEDs and their two-zone SSC model fits. See caption of Figure 5.17 for further details. The emission of the quiescent blob was set to the one describing the SED from MJD 55274, which is the lowest SED among all the 13 dates considered in this paper. Consequently, there is no flaring blob emission for MJD 55274.

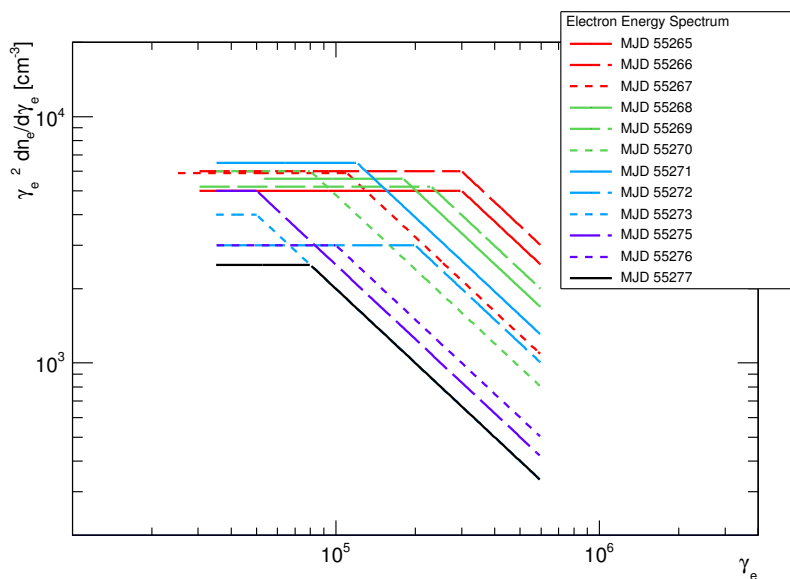
Table 5.4.: Integral flux above 200 GeV and parameters of the two-zone SSC model. Bold-faced text is used to depict the model parameters that were varied to describe the SED during the 13-day period.

Date [MJD]	MAGIC flux [$10^{-10}\text{cm}^{-2}\text{s}^{-1}$]	VERITAS flux [$10^{-10}\text{cm}^{-2}\text{s}^{-1}$]	Whipple flux [$10^{-10}\text{cm}^{-2}\text{s}^{-1}$]	γ_{\min} [10^4]	γ_{\max} [10^5]	γ_{br1} [10^5]	γ_{br2} [10^5]	s_1	s_2	s_3	n_e [10^3cm^{-3}]	B [mG]	$\log(R)$ [cm]	δ
Parameters fixed for all dates to those from MJD 55274 one-zone SSC				0.08	1000	0.35	3.9	2.2	2.7	4.7	0.9	38	16.72	21
the quiescent blob														
the flaring blob														
55265	3.8 ± 0.2	4.0 ± 0.5		3.0	6	3.0	--	2.0	3.0	--	5.0	105	15.51	35
55266	4.7 ± 0.2			3.0	6	3.0	--	2.0	3.0	--	6.0	100	15.51	35
55267		4.0 ± 0.5	5.3 ± 0.3	2.5	6	1.1	--	2.0	3.0	--	5.9	100	15.51	35
55268	2.1 ± 0.3	4.0 ± 0.6	4.8 ± 0.3	5.3	6	1.8	--	2.0	3.0	--	5.6	100	15.51	35
55269	3.3 ± 0.3	4.2 ± 0.6	4.2 ± 0.3	3.0	6	2.3	--	2.0	3.0	--	5.2	90	15.51	35
55270	2.3 ± 0.2	2.6 ± 0.4	3.0 ± 0.2	3.5	6	0.8	--	2.0	3.0	--	6.0	75	15.51	35
55271		3.5 ± 0.4	4.1 ± 0.5	3.5	6	1.2	--	2.0	3.0	--	6.5	75	15.51	35
55272		2.5 ± 0.4		3.5	6	2.0	--	2.0	3.0	--	3.0	75	15.51	35
55273	1.5 ± 0.2	2.0 ± 0.4	2.5 ± 0.3	3.5	6	0.5	--	2.0	3.0	--	4.0	75	15.51	35
55274	1.0 ± 0.3	1.6 ± 0.3	1.9 ± 0.2	--	--	--	--	--	--	--	--	--	--	--
55275			1.8 ± 0.3	3.5	6	0.5	--	2.0	3.0	--	5.0	60	15.51	35
55276	1.6 ± 0.2		1.5 ± 0.3	3.5	6	1.0	--	2.0	3.0	--	3.0	60	15.51	35
55277	1.2 ± 0.1		1.4 ± 0.4	3.5	6	0.8	--	2.0	3.0	--	2.5	60	15.51	35

Note— On MJD 55274, Mrk 421 had the lowest broadband activity among all the 13 dates. The quiescent blob emission was fixed to the SED of this date, and consequently the emission of the flaring blob on this date is null.



(a) SEDs.



(b) EEDs.

Figure 5.20.: Two-zone SSC model curves (sum of the emission from the quiescent and the flaring blobs) and the related EEDs from the flaring blob used to describe the measured SEDs during the 13-day flaring activity. The parameter values are given in Table 5.4.

Figures 5.20a and 5.20b depict the two-zone SSC model curves and the parameterized EEDs for the 13 consecutive days. Both together provide a summary of this flaring activity when parameterized within the above-mentioned two-zone SSC scenario. In this case, by construction,

all the SED variations occurs at the X-ray and the VHE bands, and the SED peaks are narrower than those from the one-zone SSC scenario. Overall, the decay of the flaring activity is dominated by a reduction in n_e and γ_{br} . The magnetic field also varies with time (not shown on this plot, see Table 5.4); lower activity is related to lower values of B .

The two-zone SSC model is described by 11+9 parameters, while the one-zone SSC model by 11. However, after fixing the parameters of the quiescent-state blob, we only needed to change the values of 4 parameters (γ_{min} , γ_{br} , n_e , and B) in the flaring blob, while in the one-zone SSC model we had to change five parameters (γ_{br} , γ_{br2} , $s1$, $s2$, n_e) to describe the SEDs during these 13 consecutive days (see Section 5.4.3). From this viewpoint, the two-zone SSC model is also more efficient to describe the measured temporal evolution of the broadband SED (once the parameters of the quiescent blob are fixed).

5.5. Discussion on the March Flaring Activity

The broadband SEDs during this flaring episode, resolved on timescales of one day, allowed for an unprecedented characterization of the time-evolution of the radio to γ -ray emission of Mrk 421. We found that both the one-zone SSC and the two-zone SSC models can describe the daily SEDs via the variation of only 4–5 model parameters, mostly related to the EED. This shows that the particle acceleration-and-cooling mechanism responsible for the EED could be the main responsible for the broadband SED variations during the flaring episodes in blazars.

The two-zone SSC model is more suitable for describing the evolution of the flaring activity because of the better agreement with the measured SED data at the peaks of the low- and high-energy bumps. Additionally, the two-zone SSC scenario presented here naturally provides shorter timescales (1 hour vs. 1 day) for variability in the X-ray and VHE bands, as well as the correlated variability in X-ray and VHE bands without any correlation to the optical and radio bands. Because low-energy electrons are absent, the peak frequency of the γ -ray bump becomes sensitive to γ_{min} due to the strong Klein-Nishina effect, which provides a rather independent channel to adjust the γ -ray bump for the flaring state. On the other hand, the X-ray bump is more sensitive to the magnetic field and γ_{br} . Hence this phenomenological scenario of two distinct zones (quiescent+flaring) allows for more flexibility in the locations and shapes of the two bumps (in comparison to the one-zone SSC model), while still varying fewer parameters. This was particularly useful to adequately describe the evolution of the width of the two SED bumps mentioned in Section 5.4.1. We can quantify this effect by computing the widths of the bumps as the full width at half maximum (FWHM) in the logarithmic scale, $\log(\nu_2/\nu_1)$, where ν_1 and ν_2 are the frequencies at which the energy flux is half of that at the peak position. The widths of the SED bumps for the 13 consecutive days are reported in Table 5.5, showing that both the synchrotron and inverse-Compton peaks increase from $\log(\nu_2/\nu_1) \sim 2$ to ~ 3 during the decay of the flare, which means that the width of the two bumps (in logarithmic scale) is about 50% wider during the non-flaring (low) activity.

The additional flexibility of the two-zone SSC model (in comparison to the one-zone SSC model) helped to improve the model-data agreement of the SEDs from MJD 55265, 55266, 55268, 55269, and 55273 (compare Figures 5.10, 5.11a, 5.11c, 5.11d, and 5.12b with Fig-

Table 5.5.: Peak positions and widths of the synchrotron and inverse-Compton bumps derived from the two-zone SSC model parameters reported in Table 5.4.

Date	$\nu_{\text{peak}}^{\text{syn}}$	$(\nu F_{\nu})_{\text{peak}}^{\text{syn}}$	ν_1^{syn}	ν_2^{syn}	$\log(\nu_2^{\text{syn}}/\nu_1^{\text{syn}})$	$\nu_{\text{peak}}^{\text{ic}}$	$(\nu F_{\nu})_{\text{peak}}^{\text{ic}}$	ν_1^{ic}	ν_2^{ic}	$\log(\nu_2^{\text{ic}}/\nu_1^{\text{ic}})$
--	[10^{17}]	[10^{-10}]	[10^{15}]	[10^{18}]	--	[10^{25}]	[10^{-11}]	[10^{23}]	[10^{26}]	--
[MJD]	[Hz]	[erg cm $^{-2}$ s $^{-1}$]	[Hz]	[Hz]	--	[Hz]	[erg cm $^{-2}$ s $^{-1}$]	[Hz]	[Hz]	--
55265	8.1	7.9	34.	6.1	2.3	10.	15.	60.	9.5	2.2
55266	8.1	8.0	34.	5.9	2.2	10.	18.	94.	9.9	2.0
55267	4.0	5.5	11.	3.3	2.5	10.	17.	56.	5.1	2.0
55268	4.0	6.6	30.	4.5	2.2	17.	11.	16.	7.3	2.7
55269	4.0	6.1	1.9	4.5	2.4	10.	14.	42.	7.8	2.3
55270	2.0	3.9	5.7	2.3	2.6	6.0	10.	11.	4.3	2.6
55271	2.0	4.6	9.0	2.6	2.5	1.0	13.	30.	5.4	2.3
55272	4.0	3.8	4.9	2.8	2.8	3.4	11.	7.4	4.5	2.8
55273	2.0	3.1	3.1	1.9	2.8	1.9	7.7	3.9	3.0	2.9
55274	2.0	2.5	1.8	1.6	2.9	1.9	7.1	3.0	2.4	2.9
55275	2.0	3.0	2.8	1.8	2.8	3.4	7.9	4.2	3.0	2.9
55276	2.0	3.1	3.1	1.8	2.8	1.9	7.5	3.6	3.2	2.9
55277	2.0	2.9	2.7	1.7	2.8	1.9	7.4	3.4	2.8	2.9

Note— $\nu_{\text{peak}}^{\text{syn}}$: the peak frequency of the synchrotron bump; $(\nu F_{\nu})_{\text{peak}}^{\text{syn}}$: the peak energy flux of the synchrotron bump; $\nu_{\text{peak}}^{\text{ic}}$: the peak frequency of the inverse-Compton bump; $(\nu F_{\nu})_{\text{peak}}^{\text{ic}}$: the peak energy flux of the inverse-Compton bump. For each bump in the SED, the value of $(\nu F_{\nu})_{\text{peak}}/2$ determines the two frequencies (ν_1 and ν_2) that are used to quantify the width of the bump in the logarithmic scale $\log(\nu_2/\nu_1)$.

ures 5.17, 5.18a, 5.18c, 5.18d, and 5.19b). The biggest data-model differences occur for the first two days, which are the ones with the highest activity and the narrowest low- and high-energy bumps. A comparison of the data-model agreement for these two days is depicted in Figures 5.21a and 5.21b. Note the better agreement of the two-zone SSC model curves with the X-ray data points and, specially, the γ -ray data points. A quantification of the agreement can be done with a χ^2 on the broadband SEDs, after exclusion of the radio data, which are considered as upper limits for the models. In total, we have 50 and 51 data points for MJD 55265 and MJD 55266, respectively. When using a one-zone SSC model we obtained a χ^2 of 4.0×10^3 for MJD 55265 and 3.6×10^3 for MJD 55266, while we obtained 1.2×10^3 for MJD 55265 and 0.7×10^3 for MJD 55266 when using the two-zone SSC model, hence showing that the agreement data-model is better for the latter theoretical scenario. An F-test on the obtained χ^2 values, and using conservatively that the one-zone model has 11 free parameters and the two-zone model has 20 free parameters (hence not considering that many of these parameters were kept constant), would reject the one-zone model (in favor of the two-zone model) with a p -value smaller than 10^{-5} . If one considers that many model parameters are kept constant, the rejection of the one-zone model in favor of the two-zone model would be even larger. The reduced χ^2 for all cases is well above 1, which shows that none of the models describe perfectly well (down to the % level) the observations. As mentioned in the previous sections, both models (with spherical homogeneous regions) oversimplify the complexity in the blazar jets, and hence we do not intend to explain the data down to the % level.

It is worth noting that the EED of the flaring blob is constrained to a very narrow range of energies, namely $\gamma_{\text{min}}-\gamma_{\text{max}} \sim 3 \times 10^4-6 \times 10^5$. One theoretical possibility to produce such narrow EED is stochastic particle acceleration via scattering by magnetic inhomogeneities in the jet, namely second order Fermi acceleration (e.g., [Stawarz and Petrosian, 2008, Lefa et al., 2011,

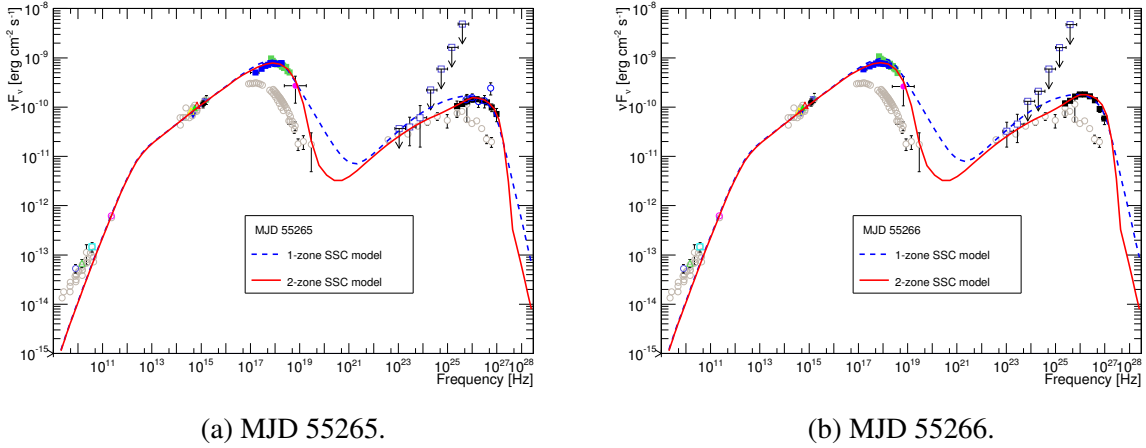


Figure 5.21.: Broadband SEDs from MJD 55265 and 55266 (the two days with the highest activity) with the one-zone and two-zone model curves described in sections 4.2 and 4.3.

Asano et al., 2014]). A spectrum in this model is localized at around a characteristic Lorentz factor γ_c , being determined by the power spectrum of magnetic turbulence q and the cooling timescale of electrons, and has the shape of $\propto \gamma_e^2 \exp[-(\gamma_e/\gamma_c)^{3-q}]$ (e.g., [Schlickeiser, 1985]). Such a spectrum can realize the narrow peaks of synchrotron radiation and inverse Compton scattering that we measured for Mrk 421 during the 2010 March flare.

The treatment made with the one- and two-zone homogeneous (spherical) SSC models could be a simplification of the problem. For instance, relativistic travel within a jet can change the properties of a blob (e.g. expansion of the size R of the emitting region, and decrease in the magnetic field B). This is a problem that has been discussed in several papers (e.g., [Tagliaferri et al., 2008] for the case of 1ES 1959+650). The fact that we can explain the temporal evolution of the SED during 13 consecutive days without changing the environment parameters could be interpreted as if the blazar emission region is not traveling relativistically, but rather stationary. Such a standing shock could be produced, for instance, by recollimation in the jet, and the particles would be accelerated as the jet flow or the superluminal knots cross it [Komissarov and Falle, 1997, Sokolov et al., 2004, Marscher, 2014]. The Lorentz factor of the plasma, as it flows through the standing shock, would be the Lorentz factor which would lead to the Doppler factor (depending on the angle) used in the model.

The SED model results described in Sections 5.4.3 and 5.4.4 allow for an estimate of several physical properties of Mrk 421 during the flaring activity from 2010 March: the total electron number density N_e , the mean electron Lorentz factor $\langle \gamma_e \rangle$, jet power carried by electrons L_e , jet power carried by the magnetic field L_B , the ratio of comoving electron and magnetic-field energy densities $U'_e/U'_B = L_e/L_B$, the synchrotron luminosity L_{syn} (integrated from $10^{9.5}$ Hz to $10^{20.5}$ Hz), inverse-Compton luminosity L_{IC} (integrated from $10^{20.5}$ Hz to 10^{28} Hz), and total photon luminosity from the SSC model $L_{\text{ph}} = L_{\text{syn}} + L_{\text{IC}}$. We also computed the jet power carried by protons L_p assuming one proton per electron ($N_p = N_e$). The total jet power is $L_{\text{jet}} = L_p + L_e + L_B$.

We followed the prescriptions given in [Celotti and Ghisellini, 2008]. Specifically, the following formulae were used:

$$N_e = \int_{\gamma_{\min}}^{\gamma_{\max}} \frac{dn_e}{d\gamma_e} d\gamma_e, \quad (5.7)$$

$$\langle \gamma_e \rangle = \frac{\int_{\gamma_{\min}}^{\gamma_{\max}} \gamma_e \frac{dn_e}{d\gamma_e} d\gamma_e}{N_e}, \quad (5.8)$$

$$L_e = \pi R^2 \Gamma^2 \beta c N_e \langle \gamma_e \rangle m_e c^2, \quad (5.9)$$

$$L_p = \pi R^2 \Gamma^2 \beta c \cdot N_e \cdot m_p c^2, \quad (5.10)$$

$$L_B = \frac{1}{8} R^2 \Gamma^2 \beta c B^2, \quad (5.11)$$

$$L_{\text{ph}} = \int \frac{\pi D_L^2 F_\nu (1+z) dv}{\Gamma^2 \delta}, \quad (5.12)$$

where $\Gamma \sim \delta$, $\beta = \sqrt{1 - \frac{1}{\Gamma^2}}$, $D_L = 134$ Mpc (derived from $H_0 = 71$ km s⁻¹ Mpc⁻¹, $\Omega_M = 0.27$, $\Omega_\Lambda = 0.73$). In the jet power calculation, only one side is considered, differently to what is done in [Finke et al., 2008b] where a two-sided jet is used. Table 5.6 reports the calculated values for the one-zone SSC model described in Section 5.4.3, while Table 5.7 reports the calculated values for the flaring blob and the sum (with the superscript "sum" on the left side of a physical-property symbol) of the two blobs in the two-zone SSC model described in Section 5.4.4. In both scenarios (one- and two-zone) the model shows a deviation from equipartition by more than one order of magnitude, as it was reported in [Abdo et al., 2011, Mankuzhiyil et al., 2011] and [Aleksić et al., 2012b]. Moreover, we found that this ratio varies little during the 13-day period considered here. It is also worth noting that, despite $\langle \gamma_e \rangle$ being 20–30 times higher for the flaring blob, the total power $L_p + L_e + L_B$ of the flaring blob is about one order of magnitude smaller than that of the quiescent-state blob (10^{43} erg s⁻¹ vs. 10^{44} erg s⁻¹). Another interesting observation is that, during the highest X-ray/VHE activity, the total photon luminosity $L_{\text{ph}} (= L_{\text{syn}} + L_{\text{IC}})$ of the flaring blob is less than half of the total photon luminosity of the quiescent-state blob. Consequently, even though the flaring blob's L_{ph} changes by one order of magnitude during the decay of the flare, the overall luminosity $^{\text{sum}}L_{\text{ph}}$ in the two-zone scenario does not change substantially during the 13-day period with the VHE flux going from ~ 2 c.u. down to ~ 0.5 c.u., remaining at about $(3-5) \times 10^{42}$ erg s⁻¹. The fact that a lower-power flaring blob dominantly contributes to the emission in X-ray and gamma rays in the first few days (when the X-ray/VHE activity is very high) indicates that the radiative efficiency of electrons is much higher than in the quiescent blob. The higher values of the magnetic field strength B and the electron number density n_e in the flaring blob with respect to those in the quiescent blob (see Table 5.5) supports the inference of high radiative efficiency. On the other hand, for the one-zone SSC scenario, the overall luminosity L_{ph} decreases from 9×10^{42} erg s⁻¹ to 3×10^{42} erg s⁻¹, compared to that from 5×10^{42} erg s⁻¹ to 3×10^{42} erg s⁻¹ in the two-zone SSC model. This means that, in terms of jet energetics, the production of the measured X-ray/VHE flaring activity is more demanding in the one-zone scenario than in the two-zone scenario.

Table 5.6.: Jet powers and luminosities derived with the parameters from the one-zone SSC model reported in Table 5.3.

Date	N_e	$\langle\gamma_e\rangle$	L_e	L_p	L_B	U'_e/U'_B	L_{jet}	L_{syn}	L_{IC}	L_{ph}
---	[10^{-1}]	[10^3]	[10^{43}]	[10^{43}]	[10^{42}]	[10^1]	[10^{44}]	[10^{42}]	[10^{41}]	[10^{42}]
[MJD]	[cm^{-3}]	---	[erg s^{-1}]	[erg s^{-1}]	[erg s^{-1}]	---	[erg s^{-1}]			
55265	2.5	3.4	7.8	4.2	6.5	1.2	1.3	6.6	14.	8.1
55266	2.5	3.4	8.0	4.3	6.5	1.2	1.3	7.2	16.	8.8
55267	2.4	3.3	7.3	4.0	6.5	1.1	1.2	4.6	11.	5.7
55268	2.5	3.5	7.9	4.2	6.5	1.2	1.3	5.4	14.	6.7
55269	2.6	3.4	8.2	4.4	6.5	1.3	1.3	5.5	14.	6.9
55270	2.5	3.3	7.5	4.1	6.5	1.2	1.2	3.5	9.8	4.5
55271	2.5	3.4	7.6	4.1	6.5	1.2	1.2	4.0	11.	5.1
55272	2.5	3.3	7.5	4.1	6.5	1.1	1.2	3.7	10.	4.7
55273	2.5	3.2	7.3	4.1	6.5	1.1	1.2	3.1	8.7	4.0
55274	2.5	3.1	7.0	4.1	6.5	1.1	1.2	2.5	6.5	3.1
55275	2.3	3.2	6.8	3.9	6.5	1.1	1.1	2.8	7.2	3.5
55276	2.5	3.2	7.3	4.1	6.5	1.1	1.2	3.0	8.2	3.8
55277	1.9	3.3	5.8	3.2	6.5	.90	.97	2.6	5.7	3.2

Note— N_e : total electron number density; $\langle\gamma_e\rangle$: mean electron Lorentz factor; L_e : jet power carried by electrons; L_p : the jet power carried by protons; L_B : jet power carried by the magnetic field; U'_e/U'_B : the ratio of comoving electron and magnetic-field energy densities; L_{jet} : total jet power; L_{syn} : the synchrotron luminosity; L_{IC} : inverse-Compton luminosity; L_{ph} : total photon luminosity from the SSC model. See the calculation explanation in Section 5.5.

Table 5.7.: Jet powers and luminosities derived with the parameters from the two-zone SSC model reported in Table 5.4.

Date	N_e	$\langle\gamma_e\rangle$	L_e	L_p	L_B	U'_e/U'_B	L_{jet}	L_{syn}	L_{IC}	L_{ph}	sum L_e	sum L_p	sum L_B	sum L_{jet}	sum L_{syn}	sum L_{IC}	sum L_{ph}
---	[10^{-1}]	[10^4]	[10^{43}]	[10^{41}]	[10^{41}]	[10^1]	[10^{43}]	[10^{41}]	[10^{40}]	[10^{41}]	[10^{43}]	[10^{43}]	[10^{42}]	[10^{44}]	[10^{42}]	[10^{41}]	[10^{42}]
[MJD]	[cm^{-3}]	---	[erg s^{-1}]	[erg s^{-1}]	[erg s^{-1}]	---	[erg s^{-1}]										
the quiescent blob																	
--	2.5	.31	7.0	410	65.	1.1	12.	25.	65.	31.							
the flaring blob																	
the quiescent blob + the flaring blob																	
55265	1.6	9.0	1.4	2.8	5.3	2.6	1.5	13.	18.	15.	8.4	4.1	7.0	1.3	3.8	8.3	4.6
55266	1.9	9.0	1.7	3.4	4.8	3.4	1.7	13.	23.	15.	8.7	4.1	7.0	1.4	3.8	8.8	4.6
55267	2.1	6.5	1.3	3.8	4.8	2.8	1.4	7.9	18.	9.7	8.3	4.1	7.0	1.3	3.3	8.3	4.1
55268	.89	12.	1.1	1.6	4.8	2.2	1.1	9.5	8.8	10.	8.1	4.1	7.0	1.3	3.4	7.4	4.1
55269	1.6	8.6	1.4	2.9	3.9	3.5	1.4	8.7	15.	10.	8.4	4.1	6.9	1.3	3.4	8.0	4.1
55270	1.3	7.6	1.0	2.4	2.7	3.7	1.1	3.4	7.3	4.2	8.0	4.1	6.8	1.3	2.8	7.2	3.5
55271	1.6	8.4	1.3	2.9	2.7	4.8	1.4	5.0	12.	6.2	8.3	4.1	6.8	1.3	3.0	7.7	3.7
55272	.77	9.3	.71	1.4	2.7	2.6	.76	3.5	9.9	4.5	7.7	4.1	6.8	1.3	2.8	7.5	3.5
55273	.74	6.9	.50	1.3	2.7	1.9	.54	1.5	1.9	1.7	7.5	4.1	6.8	1.3	2.7	6.7	3.3
55274	--	--	--	--	--	--	--	--	--	--	7.0	4.1	6.5	1.2	2.5	6.5	3.1
55275	.93	6.9	.63	1.7	1.7	3.6	.66	1.2	2.2	1.5	7.6	4.1	6.7	1.3	2.6	6.7	3.2
55276	.70	8.0	.56	1.3	1.7	3.2	.59	1.3	1.7	1.5	7.6	4.1	6.7	1.3	2.6	6.7	3.2
55277	.56	7.6	.42	1.0	1.7	2.4	.45	.92	.95	1.0	7.4	4.1	6.7	1.2	2.6	6.6	3.2

Note— N_e : total electron number density; $\langle\gamma_e\rangle$: mean electron Lorentz factor; L_e : jet power carried by electrons; L_p : the jet power carried by protons; L_B : jet power carried by the magnetic field; U'_e/U'_B : the ratio of comoving electron and magnetic-field energy densities; L_{jet} : total jet power; L_{syn} : the synchrotron luminosity; L_{IC} : inverse-Compton luminosity; L_{ph} : total photon luminosity from the SSC model. See the calculation explanation in Section 5.5. The quantities with the ^{sum} superscript report the sum of the quantities from the quiescent and the flaring blob.

This MW campaign has revealed that the correlation between the X-ray flux in the 2-10 keV band and the VHE γ -ray flux above 200 GeV shows an approximately linear trend (see Figure 5.7 middle and bottom panels), while the correlation between X-ray flux in the 0.3-2 keV band and the VHE γ -ray flux is equally close to both a linear and quadratic trend (see Figure 5.7 top panel). This is an interesting result because the 0.3-2 keV band reports the synchrotron emission before or at the low-energy (synchrotron) peak of the SED, while the 2-10 keV band reports the emission at or after the low-energy peak. During the Mrk 421 flaring activity observed in 2001 it was also noted that the VHE to X-ray (above 2 keV) correlation was linear when considering day timescales (see top rows in Table 4 of [Fossati et al., 2008]). Quadratic (or more-than-quadratic) correlation between X-rays and VHE γ -ray fluxes in the decaying phase would be problematic to explain [Katarzyński et al., 2005], but we did not see such a quadratic correlation in the MW data presented here. It is worth mentioning that, during the 2001 high activity of Mrk 421, the VHE to X-ray correlation showed a quadratic behavior when considering intra-night variability on single nights (see [Fossati et al., 2008]). During the flaring activity observed in 2010 March (reported in this manuscript), we did not detect any significant intra-night variability, which might be due to the shorter (~ 1 hour) duration of the observations (in comparison to the many-hour long observations reported in [Fossati et al., 2008], or perhaps due to the lower X-ray and VHE activity (in contrast to that of 2001).

The close-to-linear correlation for 2-10 keV X-rays can be explained as follows. In the framework of the one-zone SSC model, the SED peaks at γ -ray frequencies are produced by the smaller cross-section in the Klein-Nishina regime, rather than by the breaks $\gamma_{br,1/2}$ in the EED. Therefore, the γ -ray emission with energies above the SED peak energy are affected by the lower Klein-Nishina cross-section, and is dominated by inverse Compton scattering off infrared-to-optical photons. Since these target photons are produced by the synchrotron radiation of electrons with the Lorentz factor well below γ_{br1} , whose density is almost constant during this decaying phase (see Figure 5.16b), the density of target photons is almost constant. Thus, the change in the number density of electrons above γ_{br2} is directly reflected in the γ -ray flux, resulting in the close-to-linear correlation between X-rays and γ -ray fluxes. A similar mechanism works also in the case of the two-zone SSC model in each blob. In a flaring blob, γ -ray SED peaks originate from the Klein-Nishina effect. Therefore, γ -rays with energies above the SED peak result from inverse-Compton scattering of electrons off photons below the SED peak in the X-ray band as well as in the case of the one-zone SSC model. Thus, the close-to-linear relation is realized in both the quiescent and flaring blobs, and hence it is also realized in the total spectra.

The correlation between X-rays and γ -rays is analyzed with a great level of detail in [Katarzyński et al., 2005], where the evolution of several quantities, e.g., the number density of electrons, magnetic fields, and the size of the emission region, are simply parametrized to study their dependence to the index of the correlation. The evolution of the emission region volume is a possibility to naturally explain the reduction of the electron number density in the emission region. In the results presented here we have fixed the size R to solidly study the evolution of the electron spectrum with the steady SSC models at each moment. Further studies of the temporal broadband emission evolution involving such additional parameters will be performed elsewhere.

6. Multi-wavelength Campaign on Markarian 421 in 2011

Due to lack of time, the study of the MW data from 2011 is more superficial than that performed on the MW data from 2010 March. After my PhD thesis, I would like to deepen the study on the 2011 MW data, and later publish this work in a refereed journal as it is done with the 2010 data.

6.1. Observation and Data Analysis

Most of the instruments participating in the MW campaign on Mrk 421 in 2011 are the same as those in 2010 (see Table 5.1). Some of them did not participate in the 2011 campaign: Whipple, GRT, Abastumani, Lulin, and UMRAO. Additionally, the Brigham Young University West Mountain Observatory¹ (WMO) participated in the 2011 campaign, providing information on the R, V, and B optical bands.

6.2. Multi-band Variabilities

In this section, we show the experimental results derived with the MW campaign observations described in Section 6.1. Figure 6.1 shows the multi-band LCs from 2010 December and 2011 May.

In the top left panel of Figure 6.1, the VHE band includes 20 observations from MAGIC and 28 from VERITAS. In general, the VHE flux varied in about 1-month timescale although in some cases we can see variability occurring in a few days. The highest flux was $\sim 1.8 \times 10^{-9} \text{cm}^{-2} \text{s}^{-1}$, which is equal to ~ 0.8 c.u. above 200 GeV. This flux is low in comparison to the flux measurement in 2010, when Mrk 421 reached 8 c.u. (see Section 5.2). Mrk 421 stayed in a low state for quite some time: there are 16 observations reporting fluxes below 0.3 c.u., while the typical VHE flux is ~ 0.5 c.u. [Acciari et al., 2014].

Below the VHE panel, *Fermi*-LAT provides the γ -ray flux above 100 MeV on a timescale of 7 days. The flux in this band was similar to that in 2010. The local minima and maxima in this LC does not match with those in the VHE band.

There are 6 X-ray LCs in 5 panels after the γ -ray panel. The LCs from *Swift*-BAT, MAXI, RXTE-ASM have large error bars, whose sizes are comparable with the variabilities in the LCs. On the other hand, the LCs from RXTE-PCA and *Swift*-XRT, which have small error bars, reflect well the changes in the VHE band. There is a remarkable high flux around MJD 55630, which

¹<http://http://wmo.byu.edu/>

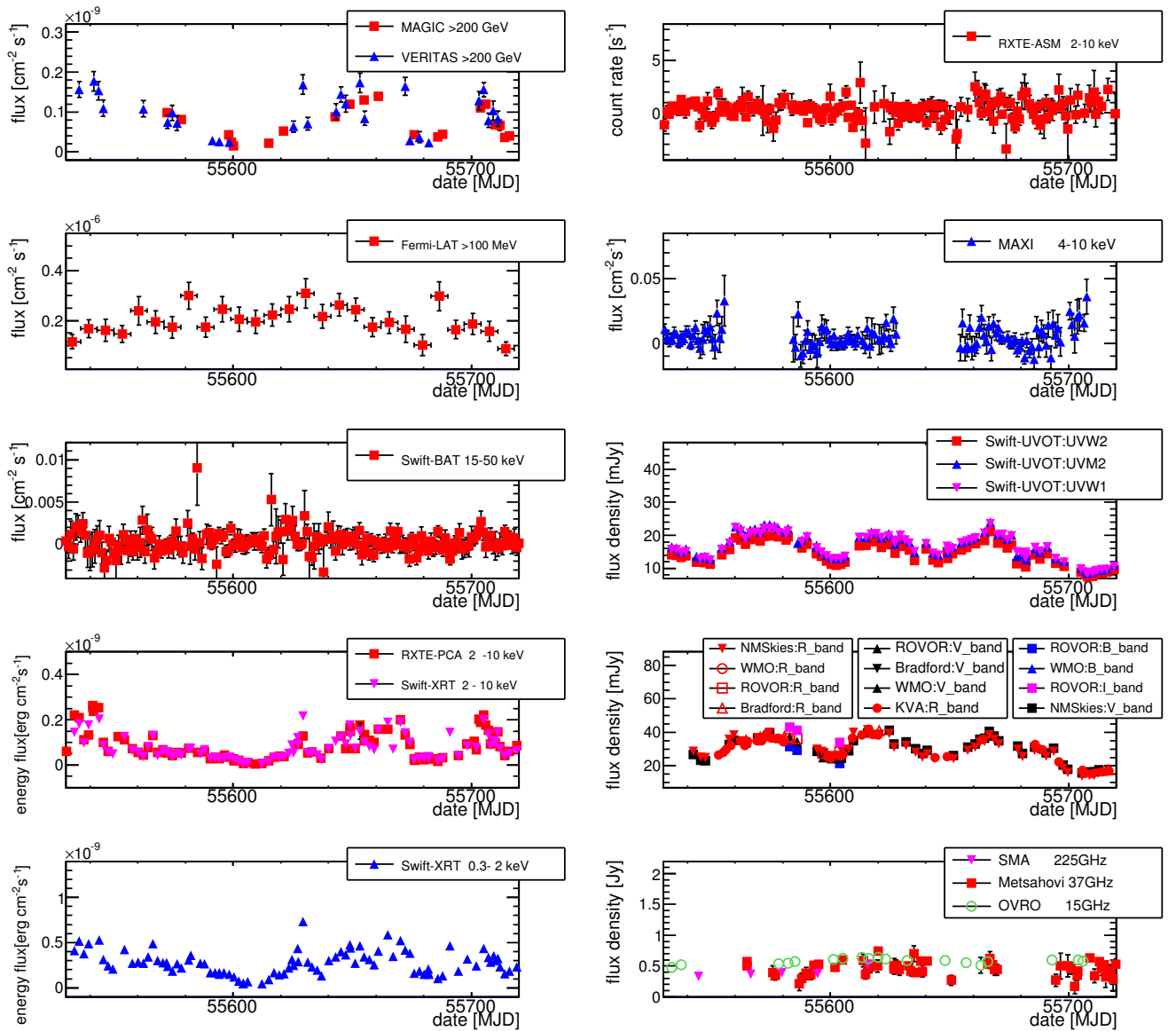


Figure 6.1.: LCs of Mrk 421 between 2010 December and 2011 May, from VHE to radio. For optical bands, the contribution of the host is subtracted, as described in Subsection 5.3.

has also a distinctive counterpart (the activity corresponding to that in another band) in the VHE band.

In the second and the third panels in the right column of Figure 6.1 are the LCs from three UV bands and four optical bands. The flux contribution from the host galaxy in the optical bands is removed (see Subsection 5.2). The shapes of UV and optical LCs are very similar. They are higher than in 2010. In 2010, the optical bands increased or decreased slowly between 10 and 25 mJy, but in 2011 there were three periods of time when the optical bands were as high as 40 mJy. This is one of the distinctive characteristics of the 2011 MW data. Typically, blazar emission models for Mrk 421 focus on the explanation of the variability in the X-ray and γ -ray bands. This data set is suitable for examining the typical emission models, for example, SSC models, and estimate if they can describe the evolution of the whole broadband SEDs including the variabilities in optical, X-ray, and γ -ray bands.

In radio bands, SMA (225 GHz), 5 observations, reported a slight gradual increase from 0.4 Jy to 0.5 Jy. OVRO (15 GHz) had denser and longer monitoring, but the value was stable around 0.5 Jy. However, Metsahovi (37 GHz) reported many flux changes in few-day-long timescale between 0.15 and 0.75 Jy although the error bars of them are large.

To compare and summarize the activities in the different bands, 6 LCs from Figure 6.2 are selected. It is found that the X-ray LCs follow well the development of that of the VHE γ -ray > 200 GeV. The LC of the HE γ -ray > 100 MeV is similar to that of the optical band. Comparing the optical LC with the X-ray LC, they are similar before MJD 55600. After that, around MJD 55630, there is a maximum in the X-ray band, but the high plateau in the optical band comes 20 days earlier. After MJD 55705, the optical band is in its lowest activity, but the X-ray band is still relatively high, and decreasing by a factor of 4 in ~ 2 weeks. In the radio band, there is a clear rise between MJD 55587 and 55595, for which no counterpart in other bands is found.

In order to quantify the overall variability, the fractional variability F_{var} , as described in Subsection 5.2, is calculated for each LC from Figure 6.1 and reported in Figure 6.3.

Comparing Figure 6.3 with Figure 5.3, one finds that the variability in the VHE- γ -ray band (MAGIC) drops from ~ 0.9 to ~ 0.55 , the HE- γ -ray (*Fermi*-LAT) reduces slightly from ~ 0.22 to ~ 0.16 , and the X-ray (0.3-2 keV and 2-10 keV) bands stay at similar values. Note that in both years, the *Swift* 2-10 keV band showed a higher variability than the 0.3-2 keV band, and the ratio $\frac{F_{\text{var}}(2-10\text{keV})}{F_{\text{var}}(0.3-2\text{keV})}$ is similar: 1.5 in 2010, 1.4 in 2011. The optical R-band increases from 0.19 to 0.25, while the radio band (OVRO) remained at essentially at the same level; from 0.04 ± 0.01 to 0.05 ± 0.02 .

The ratio $\frac{F_{\text{var}}(2011)}{F_{\text{var}}(2010)} \equiv R$ for each band mentioned above is given in Table 6.1. The change of F_{var} in the radio band was not significant compared with its large error bar. It is found that, between these two years, the change of the variability is in the inverse order of energy: $R(\text{optical}) > R(\text{X-ray}) > R(\text{HE-}\gamma\text{-ray}) > R(\text{VHE-}\gamma\text{-ray})$.

It can be concluded that the 2011 MW campaign provided a data set with a high activity and large variation in the optical band, together with a relatively low state/variability in the X-ray/VHE band. This is not typical for Mrk 421, and very different from what was observed in the 2010 MW campaign (see Chapter 5).

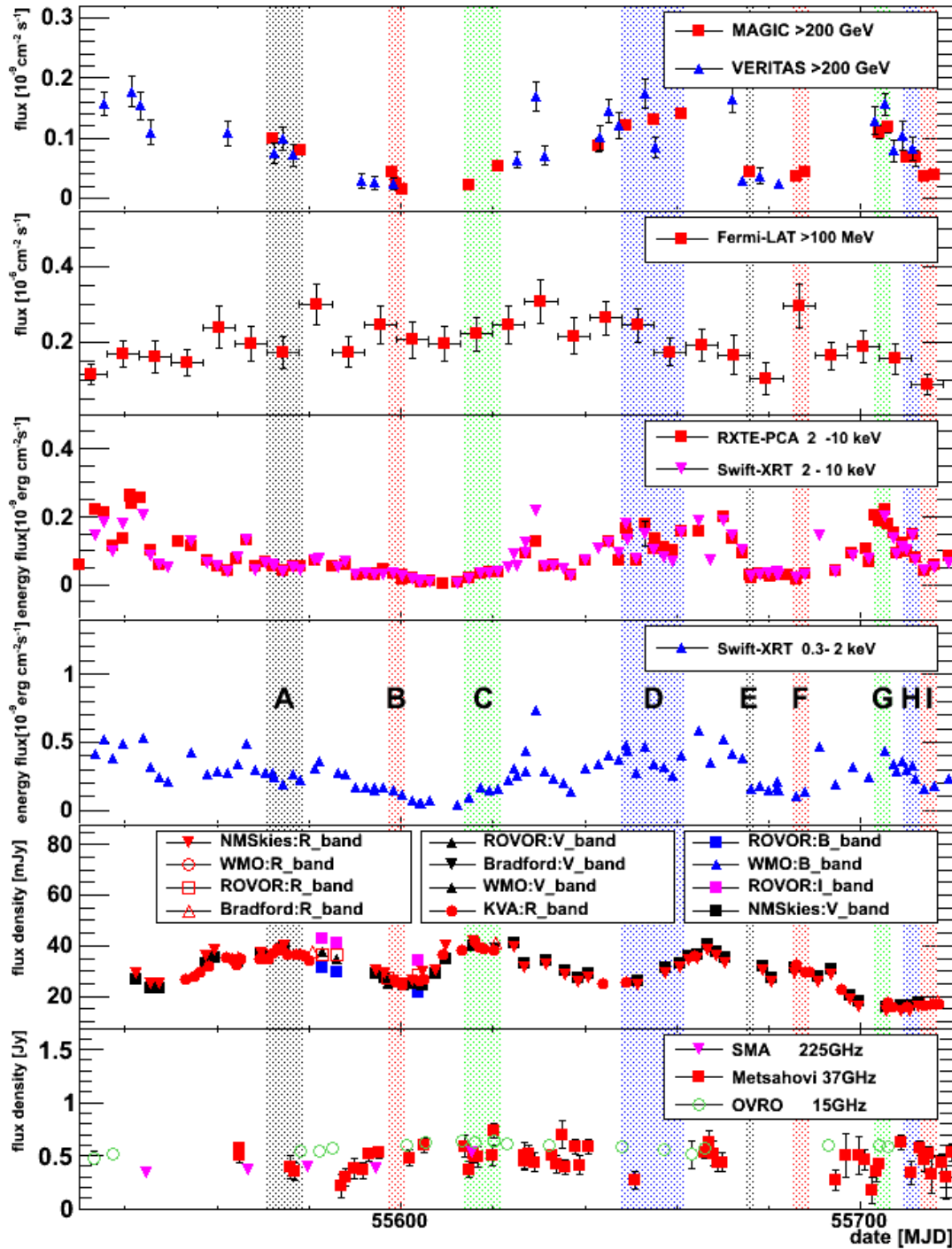


Figure 6.2.: Selected 2011 MW LCs from Figure 6.1. See the caption of Figure 6.1 for further information. The letters A – I denote the names of the time intervals defined in Section 6.3 for the study on the SED temporal evolution.

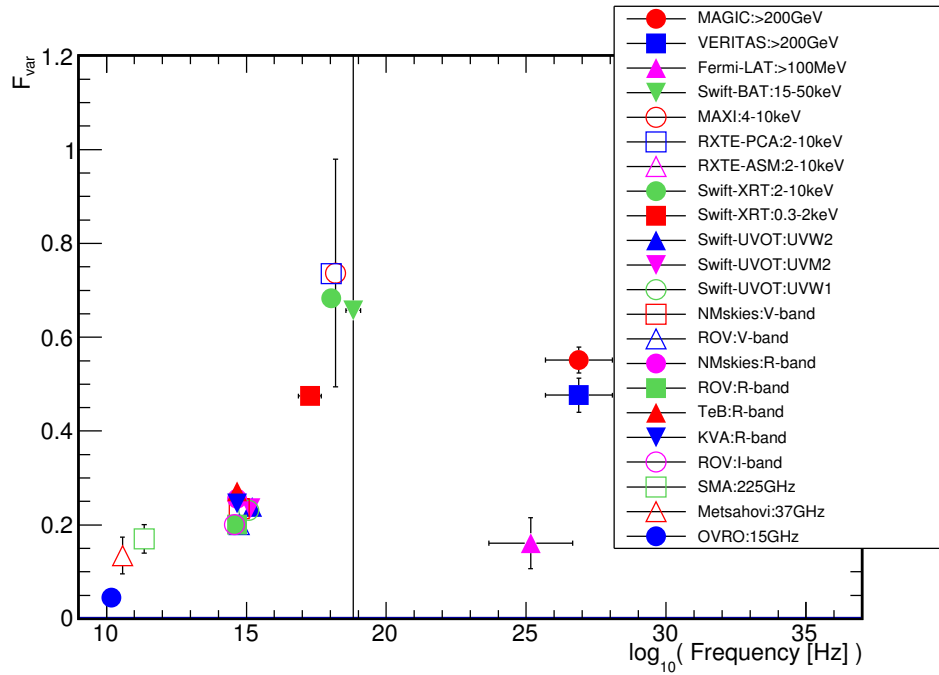


Figure 6.3.: Fractional variability F_{var} as a function of frequency derived with the MW data from 2011.

Table 6.1. Comparison of 2010 and 2011 fractional variabilities

Energy band	Instrument	$\frac{F_{\text{var}}(2011)}{F_{\text{var}}(2010)} \equiv R$
Radio	OVRO	1.17 ± 0.51
Optical r-band	all	1.28 ± 0.02
X-ray 0.3-2 keV	Swift	0.97 ± 0.01
X-ray 2-10 keV	Swift	1.00 ± 0.01
HE- γ -ray	Fermi-LAT	0.61 ± 0.25
VHE- γ -ray	MAGIC	0.51 ± 0.03

6.3. Temporal Evolution of the Broadband Spectral Energy Distribution

6.3.1. Characteristics of the Measured Broadband SEDs

In order to study the evolution of the broadband SED in 2011, the data set was split into several intervals. As Mrk 421 was in a rather low state, it is not always possible to obtain a solid VHE spectrum for each MAGIC observation. In order to have better photon statistics for the VHE spectra, it is reasonable to combine the spectra from several adjacent observations when the MW variability is small. The spectral analysis of the VERITAS observations from 2011 is not yet ready. Consequently, in this work we focus on the time intervals when MAGIC observed Mrk 421. An upgrade of this study including the VERITAS spectra and a more thorough high-level analysis will be reported elsewhere.

Based on the MW LCs from Figure 6.2, we set time periods in the following way:

- Period A: MJD 55572 – 55578 (a typical VHE state, a flux of ~ 0.4 c.u.).
- Period B: MJD 55598 – 55600 (a very low VHE state, a flux of ~ 0.2 c.u.).
- Period C: MJD 55615 – 55621 (a very low VHE state, a flux of ~ 0.2 c.u.).
- Period D: MJD 55649 – 55661 (a typical VHE state, a flux of ~ 0.6 c.u.).
- Period E: MJD 55676 (a very low VHE state, a flux of ~ 0.2 c.u.).
- Period F: MJD 55686 – 55688 (a very low VHE state, a flux of ~ 0.2 c.u.).
- Period G: MJD 55704 – 55706 (a typical VHE state, a flux of ~ 0.5 c.u.).
- Period H: MJD 55710 – 55712 (a low VHE state, a flux of ~ 0.3 c.u.).
- Period I: MJD 55714 – 55716 (a very low VHE state, a flux of ~ 0.2 c.u.).

In each period of time, all VHE γ -ray data are combined to make one spectrum. From the MW LCs in Figure 6.2, one can see that there was no outstanding variability in any of the periods except for some X-ray flux variabilities in period D (MJD 55649 – 55661). The simultaneous broadband SEDs of periods A – I are shown in Figures 6.4-6.6. According to the characteristics of the 2011 multi-band variabilities discussed in Section 6.2, the policy for displaying spectral points in the figures is made as follows. The MAGIC, *Fermi*-LAT, *Swift*-BAT spectral points integrate over the corresponding period in order to have better photon statistics. In order to show the potential variability in the X-ray band, all the X-ray spectra of single observations during the corresponding period are depicted with empty markers. The X-ray spectra from the center of the period are taken as a representative spectra, and are depicted with full markers. They are used as primary X-ray spectra for SED modeling. The UV, and optical spectral points have variability

timescales \gtrsim several weeks, and hence they integrate over the corresponding temporal period. The LC from OVRO or SMA reports stable or slowly changing fluxes. Simultaneous observations of them are depicted with full markers. Whenever simultaneous observations of them are not available, the fluxes from the closest date (with empty markers) are reported as references for theoretical modeling, and their observation time in MJD is reported next to the instrument name in the legend. Contrary to SMA and OVRO, Metsahovi reported many flux changes in a-few-day timescale, and hence one should not use Metsahovi data points from observations that are not taken simultaneously to the other observations. Consequently the spectral points from Metsahovi are shown only when the simultaneous observations are available.

To have a reference for the evolution of the SED through all the periods, the SED in each period (see Figures 6.4 – 6.6) is compared to the one from the 2009 MW campaign [Abdo et al., 2011]. Typically, the important spectral features are those around the peaks of the low- and high-energy bumps of the SED, and hence the spectra near the peaks are the most relevant and to be compared: that is the optical, X-ray, HE γ -ray, VHE γ -ray bands. However, the HE γ -ray spectra have high uncertainty, which will make the comparison unreliable. Instead, the VHE γ -ray spectra cover the peaks and the falling segments of the high-energy bump, so two ends of the spectra are compared to give a better description of the high-energy bumps. The comparison of the spectral states in the several bands mentioned above from periods A – I are reported in Table 6.2.

The SED in period G (see Figure 6.5f) is close to the 2009 SED. If the above-mentioned segments of the SED are similar to those of the 2009 SED, they are flagged as "typical": specifically, $\nu F_\nu \sim 1.5 \times 10^{-10} \text{ erg cm}^{-2} \text{ s}^{-1}$ at 10^{15} Hz , $\sim 3 \times 10^{-10} \text{ erg cm}^{-2} \text{ s}^{-1}$ at 10^{17} Hz , $\sim 10^{-10} \text{ erg cm}^{-2} \text{ s}^{-1}$ at $10^{25.5} \text{ Hz}$, $\sim 2 \times 10^{-11} \text{ erg cm}^{-2} \text{ s}^{-1}$ at $10^{26.5} \text{ Hz}$. The other descriptive terms for the activities used in Table 6.2 are *very high*, *high*, *low*, *very low*, which are used when the energy flux is $>60\%$ more, $30\% - 60\%$ more, $30\% - 60\%$ less, $>60\%$ less than the typical value. The X-ray spectra and VHE γ -ray spectra from 2011 remain typically below the reference spectra from 2009, while the optical energy fluxes from 2011 are typically above those from 2009. Note that all the dates had different states. It means that there was quite some diversity in the broadband variability.

The *Swift* spectra do not cover the peak of the synchrotron bump, as it is shown in the SEDs in Figures 6.4 – 6.6. The *Swift* and RXTE spectra have very similar photon indices in periods A and C. Although the peak frequency is not precisely known, it is clear that the peak should lie on the left-hand side of the straight line formed by the *Swift* -RXTE spectra and above the energy flux in the UV band. In view of this, for period A or C, the peak frequency is at least ~ 5 times lower than that in the 2009 average SED. In these low peak-frequency states, the optical luminosity is higher than usual. This kind of states are different from typical blazar-flare states, where there is a positive relation between the peak frequency and the peak luminosity. In period A, the luminosity at the UV frequency is already as high as the peak luminosity in the 2009 SED, and hence the peak luminosity of the low-energy bump in period A should be higher than that in the 2009 SED. And that means that during the 2011 campaign, one can see an increase in the peak luminosity together with a decrease in the peak frequency, which is a rare behavior in the broadband variability of Mrk 421 and HSP BL Lac objects in general.

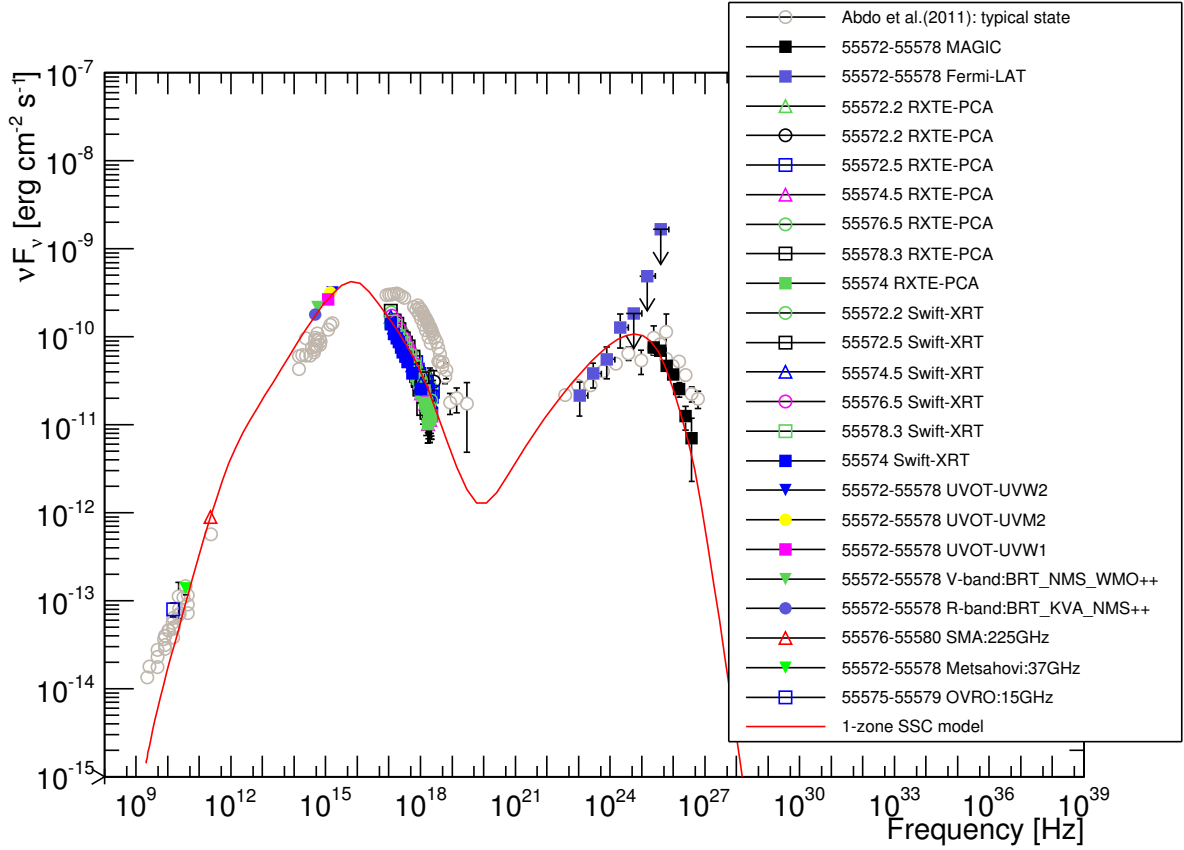


Figure 6.4.: Simultaneous broadband SED of Mrk 421 for the temporal period A, defined in Table 6.3. The correspondence between markers and instruments are given in the legend. The full names of the instruments can be found in Table 5.1. The MAGIC, *Fermi*-LAT, *Swift*-BAT, UV, and optical spectral points integrate over the corresponding period, and are depicted with full markers. All the X-ray spectra of single observations during the corresponding period are depicted with empty markers. The X-ray spectra from the center of the period are depicted with full markers. Simultaneous observations of SMA or OVRO are depicted with full markers. Whenever simultaneous observations of them are not available, the fluxes from the closest date (in empty markers) are reported, and their observation time in MJD is reported next to the instrument name in the legend. The spectral point from Metsahovi is shown only when the simultaneous observation is available. See the text in this section for the detailed display policy of the spectral points. The red curve depicts the one-zone SSC model matching the data. The parameters used in the model are listed in Table 6.3. The gray circles depict the averaged SED from the 2009 MW campaign reported in [Abdo et al., 2011], which is a good representation of the non-flaring (typical) SED of Mrk 421.

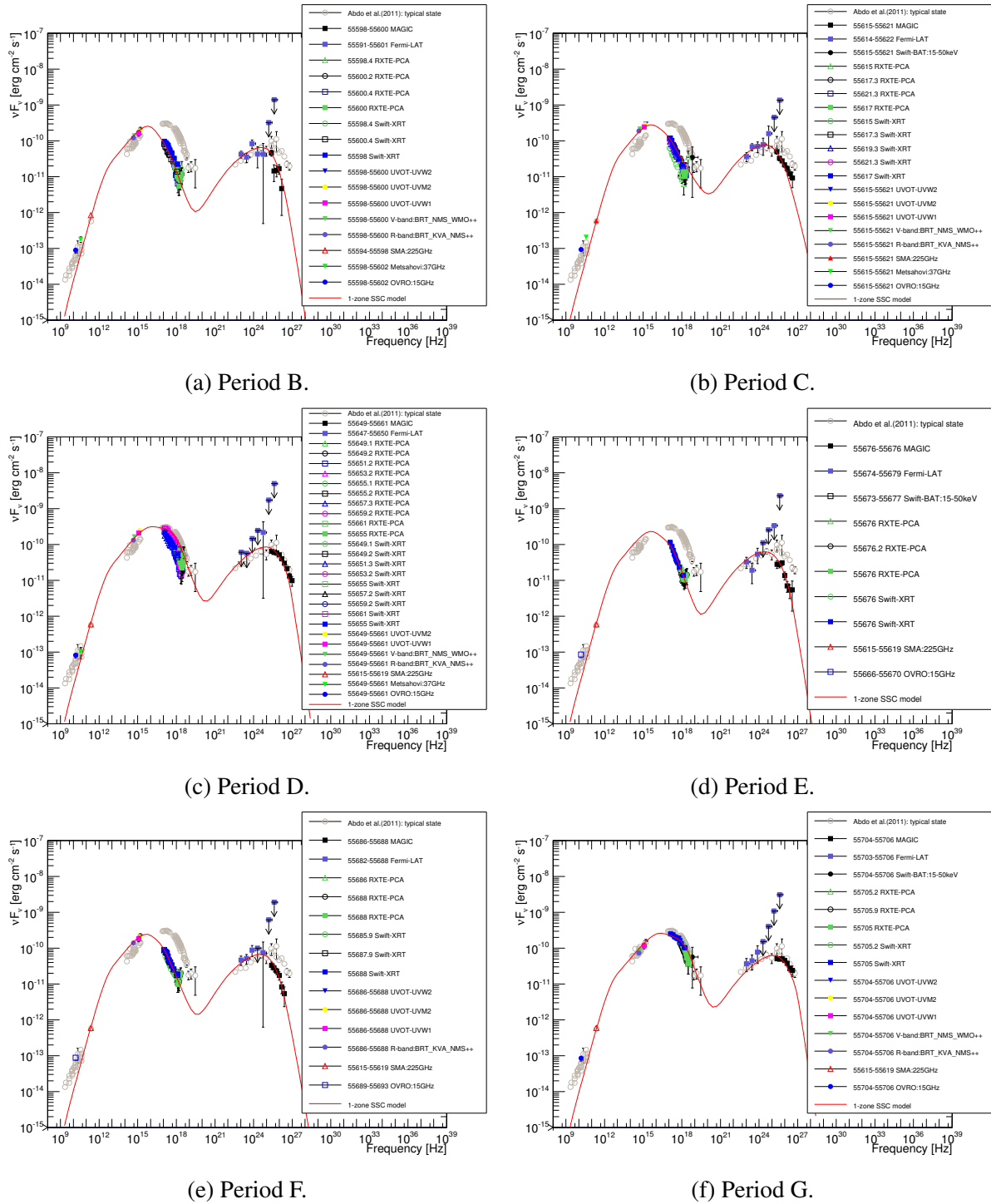


Figure 6.5.: Simultaneous broadband SED of Mrk 421 for the temporal periods defined in Table 6.3. See the description in the caption of Figure 6.4.

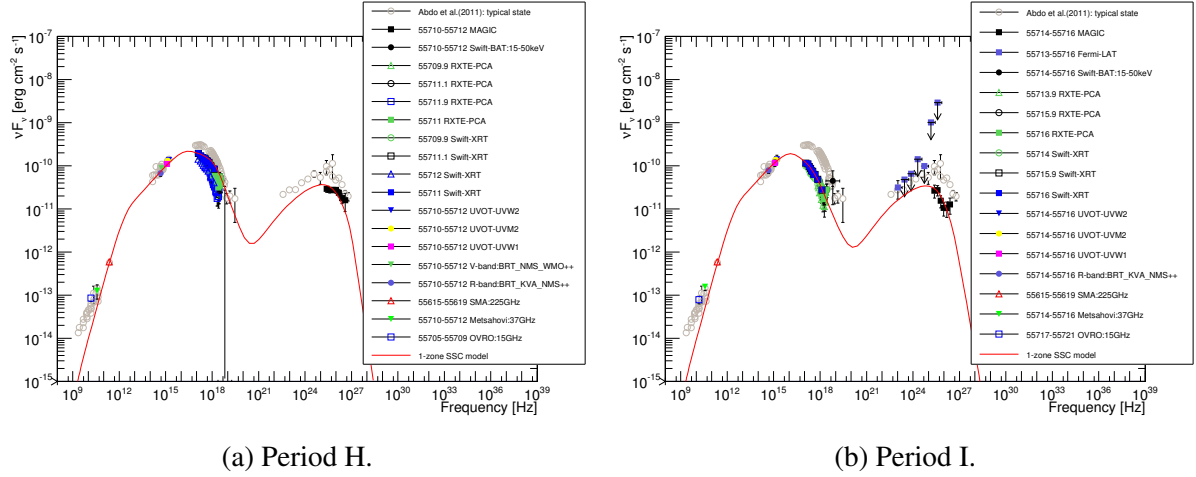


Figure 6.6.: Simultaneous broadband SED of Mrk 421 for the temporal periods defined in Table 6.3. See the description in the caption of Figure 6.4.

Table 6.2. Spectral state summary of the SEDs from Figures 6.4 – 6.6

Period Time [MJD]	optical $\sim 10^{15}$ Hz (~ 4 eV)	X-ray $\sim 10^{17}$ Hz (~ 0.4 keV)	low-energy part of MAGIC spectrum $\sim 10^{25.5}$ Hz (~ 0.1 TeV)	high-energy part of MAGIC spectrum $\sim 10^{26.5}$ Hz (~ 1 TeV)
A 55572 – 55578	very high	very low	typical	very low
B 55598 – 55600	high	very low	low	very low
C 55615 – 55621	very high	very low	low	low
D 55649 – 55661	very high	low	typical	typical
E 55676	very high	very low	low	very low
F 55686 – 55688	high	very low	low	very low
G 55704 – 55706	typical	typical	typical	typical
H 55710 – 55712	typical	low	low	typical
I 55714 – 55716	typical	very low	low	low

Note. —

“Typical” means similar to the 2009 SED [Abdo et al., 2011] (which is approximately equal to the SED from period G): $\nu F_\nu \sim 1.5 \times 10^{-10}$ erg cm $^{-2}$ s $^{-1}$ at 10^{15} Hz, $\sim 3 \times 10^{-10}$ erg cm $^{-2}$ s $^{-1}$ at 10^{17} Hz, $\sim 10^{-10}$ erg cm $^{-2}$ s $^{-1}$ at $10^{25.5}$ Hz, $\sim 2 \times 10^{-11}$ erg cm $^{-2}$ s $^{-1}$ at $10^{26.5}$ Hz. *High* means 30% – 60% more than typical. *Very high* means >60% more than typical. *Low* means 30% – 60% less than typical. *Very low* means >60% less than typical.

6.3.2. SED Modeling

The SSC model, as described in Section 5.4.2, is used to quantitatively describe the variation of the Mrk 421 broadband SED. The one-zone model is employed for the description of 2011 SEDs. The two-zone model was found to be more suitable (than the one-zone model) to describe the flaring episode from 2010 March (see Section 5.4.4). However, the SEDs built with the 2010 data show an X-ray and VHE γ -ray activity that is well below the reference data set from 2009 (typical state of Mrk 421) and hence it is impossible to apply the same two-zone SSC scenario without substantial modification in the quiescent blob. Moreover, the X-ray and VHE emission did not change on timescales as short as in 2010; in 2011, the variability timescales were much longer, and hence a slowly varying one-zone SSC blob seems to be more appropriate for the 2011 data.

In order to describe properly the smooth shape of the low-state SEDs (for example SEDs from period B, G, and H), a double-broken EED (Equation 5.4) is needed, as it was done for the data from 2010 March. The SED from period G is the first one among all the series to fit because it is the most similar one to the 2009 averaged SED, and hence it can be described with similar model parameters as in [Abdo et al., 2011]. For the other periods, we try to change as few parameters as possible.

The model parameters that described the data for each period are reported in Table 6.3. The environmental parameters, the size of the blob and the Doppler factor, were fixed to the values used in [Abdo et al., 2011] for the 2009 averaged SED. More than half of all SEDs have higher optical spectra than the 2009 averaged SED, and harder s_1 's are used to describe this feature. Then the values of γ_{br1} , s_2 , γ_{br2} , s_3 are adjusted to fit the turnpoints in the X-ray domain of the synchrotron bump. A harder s_1 brings a larger number of electrons at the energies where the characteristic synchrotron frequency (for the magnetic field) is in the optical band, and enhances the luminosity of the IC bump more efficiently than the synchrotron bump (refer to Formula 5.5), which might make the model predictions slightly above the γ -ray data. Therefore, a lower n_e and a higher magnetic field are needed to adjust the luminosity ratio between these two bumps, and make the model match the γ -ray data. Therefore, a higher magnetic field, 50 mG, is needed in comparison to the 38 mG used for the 2009 averaged SED. The model for each period is shown in Figures 6.4 – 6.6.

In this one-zone SSC model, the minimum variability timescale $t_{min} = (1 + z)R/c\delta$ is ~ 1 day, which is shorter than the variability timescales observed during the 2011 campaign, which are typically larger than a few days.

The predicted cooling break $\gamma_c = 6\pi m_e c^2 / (\sigma_T B^2 R)$ for the parameter B and R reported in Table 6.3 is in the range $2.6\text{--}4.0 \times 10^5$, which is comparable within a factor of a few with the γ_{br2} in the model. The $\frac{\gamma_{br2}}{\gamma_c}$ is from 0.29 (period C) to 2.21 (period G). In period D, γ_{br2} is the closest to γ_c ($\frac{\gamma_{br2}}{\gamma_c} = 1.06$). If VHE spectra are harder (in periods G and H), $\gamma_{br2} > \gamma_c$; if VHE spectra are softer (in periods A, B, C, E, F and I), $\gamma_{br2} < \gamma_c$. This implies that in periods D, the electron injection and the radiation cooling were in equilibrium. When the electron injection was stronger, the VHE spectrum was harder. When the radiation cooling was stronger (for most periods in 2011), the VHE spectrum was softer.

The change in the EED power-law index before and after γ_{br2} , $s_3 - s_2$ is between 0.8 and 1.9.

Table 6.3. Parameters of the One-zone SSC Model describing the SEDs from Figures 6.4 – 6.6.

Period	VHE γ -ray flux [c.u.]	γ_{\min} [10^2]	γ_{\max} [10^8]	γ_{br1} [10^4]	γ_{br2} [10^5]	s_1 --	s_2 --	s_3 --	n_e [10^2cm^{-3}]	B [mG]	$\log(R)$ [cm]	δ --
A	0.4	4	1	3.7	3.2	1.80	4.0	5.0	0.2	60	16.72	21
B	0.2	8	1	4.0	2.0	2.13	4.0	5.0	5.0	50	16.72	21
C	0.2	10	1	2.5	1.0	2.08	3.4	4.2	3.6	55	16.72	21
D	0.6	8	1	3.4	3.6	2.11	3.1	5.0	3.6	55	16.72	21
E	0.2	9	1	2.8	1.7	2.12	3.5	5.0	5.0	50	16.72	21
F	0.2	9	1	3.0	1.2	2.12	3.5	4.7	5.0	50	16.72	21
G	0.5	8	1	5.3	5.5	2.16	3.2	5.0	4.8	48	16.72	21
H	0.3	7	1	6.3	5.0	2.20	3.2	5.0	5.0	50	16.72	21
I	0.2	8	1	5.0	2.4	2.21	3.5	4.7	6.5	50	16.72	21

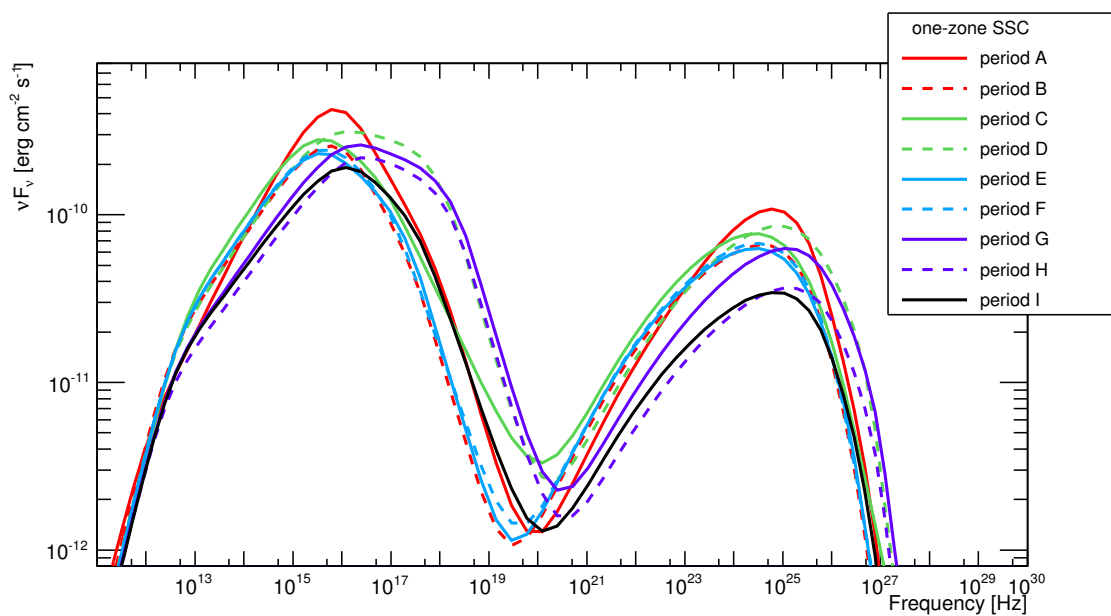
When $s_3 - s_2 \sim 1$ (in periods A, B, and I), the index change might result from the electron cooling through radiation. When $s_3 - s_2$ is much larger than 1, it may result from the combination of radiation cooling and the intrinsic efficiency-decrease in the acceleration of high-energy electrons.

The success in describing the measured SEDs keeping the environmental parameters δ , R , B constant (with only a slight change in B from 60 mG to 50 mG) shows that the broadband variability could be dominated by the temporal evolution of the EED.

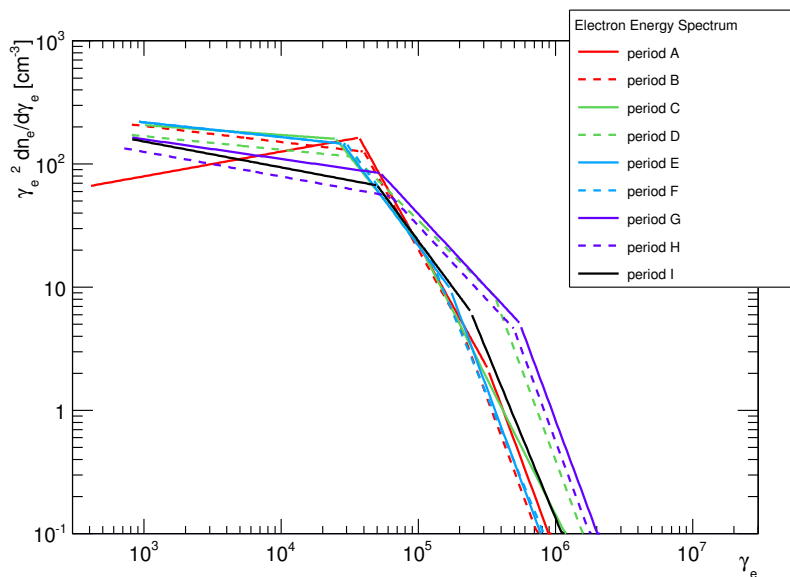
Figures 6.7a and 6.7b depict the one-zone SSC model curves and the parameterized EEDs for the 9 periods in 2011. The EED model parameters quantitatively describe the population evolution of electrons at different energies, which accounts for the spectral variations: from an optical high state (period A), to a typical state (period G) similar to the 2009 averaged SED, and then to a low state (period I).

In comparison to the typical state from 2009, a harder s_1 together with a lower γ_{br1} and a softer s_2 explain the high optical state together with the low X-ray/VHE state (period A). This means a higher acceleration efficiency to accelerate low-energy electrons to energies till γ_{br1} . Between period B and period E, the peak frequency moved between the UV and the X-ray band (see Figures 6.7a), keeping the peak synchrotron luminosity approximately constant. Then (period E→F→G) s_1 softened and γ_{br1} moved to higher energies so that the synchrotron peak moved horizontally to the right, and finally reached a typical state (period G) like that in 2009.

The decline in the X-ray /VHE emission (falling segments of the synchrotron and the inverse-Compton bumps) from period G to I is essentially achieved by decreasing γ_{br2} to a lower energy by a factor of 0.6 (from 5.5×10^5 to 2.4×10^5), which effectively reduced the number of the highest-energy electrons. The change in the broadband SED from period G to period I is the expected SED variability for Mrk 421 (and HSP BL Lac objects in general). In its SEDs, a lower synchrotron peak-frequency typically is related to a lower synchrotron peak-luminosity. But in the SED variations from B to G, one can see a very atypical behavior in which there are big changes in the synchrotron peak frequency without big changes in the synchrotron peak luminosity. See Section 6.4 for further details.



(a) SEDs.



(b) EEDs.

Figure 6.7.: One-zone SSC model curves and the related EEDs used to describe the measured SEDs during 2011. The parameter values are given in Table 6.3.

6.4. Discussion

In both years, 2010 and 2011, the fractional variability in the optical band $F_{\text{var}}(\text{optical})$ was similar to that at HE- γ -ray $F_{\text{var}}(\text{HE-}\gamma\text{-ray})$, and $F_{\text{var}}(\text{X-ray})$ was similar to $F_{\text{var}}(\text{VHE-}\gamma\text{-ray})$. Both the optical and the HE- γ -ray bands are located in the rising segments of the bumps: the former is on the low-energy bump and the latter on the high-energy bump. And both the X-ray and VHE- γ -ray bands are in the falling segments of the bumps: the former is on the low-energy bump and the latter on the high-energy bump. These correspondences might be a general phenomenon for different years in Mrk 421, as well as for other HSP BL Lac objects. This observation is expected from the strong correlation between the synchrotron photons and the up-scattered photons by inverse-Compton effect within the SSC emission model: both the variations of the optical and the HE- γ -ray photons result from the variation in the same population of electrons with relatively low energies; both the variations of the X-ray and the VHE- γ -ray photons result from the variation in another population of electrons with relatively high energies. The behavior observed in the fractional variabilities supports the interpretation of the data using the SSC theoretical model. The exquisite data set reported here allows for the first time to give this consistency test of the model.

The modeling of the broadband SEDs of several periods in 2011 shows that the main factor leading the spectral evolution could be the EED, instead of environmental parameters like R , B^2 , or δ . According to the EEDs obtained from the SSC models built to describe the SED evolution (see Figure 6.7b), the largest change among the EEDs from all the dates lies at energies $\gamma_e \gtrsim \gamma_{\text{br}2}$. The electrons at these energies are directly related to the production of X-rays and VHE γ -rays. This explains why in the SEDs νF_ν varies most in the X-ray band and the VHE γ -ray band (see Figure 6.7a), and why there are similar variabilities in the X-ray band and the VHE γ -ray band (see Figure 6.3). Similarly, there are some changes in the EED at energies $\gamma_e \lesssim \gamma_{\text{br}1}$, too. Different n_e 's, s_1 's, and $\gamma_{\text{br}1}$'s together change the population of these low-energy ($< \gamma_{\text{br}1}$) electrons. They correspond to the production of the visible light and HE γ -rays. The population variation of these low-energy electrons results in the energy-flux changes in these two energy bands in the SEDs, as well as the similar fraction variabilities in these two bands.

In the SEDs from different periods, the peak positions vary substantially. In order to quantify them, the peak frequencies, peak luminosities, and the bump widths are calculated with the one-zone SSC model SEDs whose parameters are reported in Table 6.3. The results are reported in Table 6.4. The same notations as in Section 5.5 are used. The $\nu_{\text{peak}}^{\text{syn}}$ spans over about a factor of 8, while the greatest difference in $\nu_{\text{peak}}^{\text{ic}}$'s is only about a factor of 3. The wide-spread peak-frequencies result from the changes in the $\gamma_{\text{br}1}$ and $s_2 - s_1$. Comparing these peak frequencies to those in the typical-state SED (refer to the result for MJD 55275 in Table 5.5; the SED of this day overlaps with the typical-state SED [Abdo et al., 2011] from 2009 data), these peak frequencies in 2011 are all lower than that in the typical-state SED both in the synchrotron bump and in the inverse-Compton bump. In periods C and E (the lowest $\nu_{\text{peak}}^{\text{syn}}$ in 2011, $\sim 3 \times 10^{15}$ Hz), the $\nu_{\text{peak}}^{\text{syn}}$ is ~ 70 times lower than that of the typical-state SED ($\nu_{\text{peak}}^{\text{syn}} \sim 2 \times 10^{17}$ Hz). The main difference in the parameters resulting in these SEDs with very different $\nu_{\text{peak}}^{\text{syn}}$'s is the position of the primary

²The magnetic field strength had changed slightly between 60 and 48 mG

Table 6.4.: Peak positions and widths of the synchrotron and inverse-Compton bumps derived from the one-zone SSC model parameters reported in Table 6.3.

Period	$\nu_{\text{peak}}^{\text{syn}}$ [10 ¹⁵] [Hz]	$(\nu F_{\nu})_{\text{peak}}^{\text{syn}}$ [10 ⁻¹⁰] [erg cm ⁻² s ⁻¹]	ν_1^{syn} [10 ¹⁴] [Hz]	ν_2^{syn} [10 ¹⁷] [Hz]	$\log(\nu_2^{\text{syn}}/\nu_1^{\text{syn}})$ -- --	$\nu_{\text{peak}}^{\text{ic}}$ [10 ²⁴] [Hz]	$(\nu F_{\nu})_{\text{peak}}^{\text{ic}}$ [10 ⁻¹¹] [erg cm ⁻² s ⁻¹]	ν_1^{ic} [10 ²²] [Hz]	ν_2^{ic} [10 ²⁵] [Hz]	$\log(\nu_2^{\text{ic}}/\nu_1^{\text{ic}})$ -- --
A	6.2	4.3	7.2	.64	1.9	6.0	11.	29.	4.8	2.2
B	6.2	2.6	4.0	.52	2.1	3.2	6.6	8.5	4.2	2.7
C	3.2	2.8	2.5	.79	2.5	3.2	7.7	6.3	3.8	2.8
D	12.	3.1	6.3	9.8	3.2	11.	8.5	20.	11.	2.7
E	3.2	2.3	2.5	.82	2.5	3.2	6.3	6.1	3.9	2.8
F	6.2	2.4	2.9	.71	2.4	3.2	6.8	6.6	3.9	2.8
G	24.	2.6	1.1	14.	3.1	11.	6.3	28.	15.	2.7
H	24.	2.2	1.4	14.	3.0	11.	3.7	28.	16.	2.8
I	12.	1.9	6.7	2.1	2.5	6.0	3.4	13.	8.1	2.8

Note— $\nu_{\text{peak}}^{\text{syn}}$: the peak frequency of the synchrotron bump; $(\nu F_{\nu})_{\text{peak}}^{\text{syn}}$: the peak energy flux of the synchrotron bump; $\nu_{\text{peak}}^{\text{ic}}$: the peak frequency of the inverse-Compton bump; $(\nu F_{\nu})_{\text{peak}}^{\text{ic}}$: the peak energy flux of the inverse-Compton bump. For each bump in the SED, the value of $(\nu F_{\nu})_{\text{peak}}/2$ determines the two frequencies (ν_1 and ν_2) that are used to quantify the width of the bump in the logarithmic scale $\log(\nu_2/\nu_1)$.

break $\gamma_{\text{prm}} = \gamma_e(\nu_{\text{peak}}^{\text{syn}})$ which directly relates to the value of $\nu_{\text{peak}}^{\text{syn}}$ in the SED:

$$\nu_{\text{peak}}^{\text{syn}} \propto B\gamma_{\text{prm}}^2 \delta.$$

The primary break for the period C/E EED is $\gamma_{\text{prm}} (= \gamma_{\text{br1}}) \sim 3 \times 10^4$, while that for the typical-state EED (in the one-zone SSC model) is $\gamma_{\text{prm}} (\gamma_{\text{br2}}) \sim 4 \times 10^5$. This difference in the Lorentz factor at the primary break position, together with the differences in the three electron spectral indices and the magnetic field strength, results in the large difference in the $\nu_{\text{peak}}^{\text{syn}}$ determined with the 2010 and 2011 data sets.

In order to illustrate the distribution of peak positions in the SEDs, they are shown in Figure 6.8: the synchrotron peaks in Figure 6.8a, and the inverse-Compton peaks in Figure 6.8b. For reference, not only those from 9 periods in 2011 are shown, but also those from the 2010 March flaring activity. Those of the typical state are the same as those of MJD 55275. The distribution of the $\nu_{\text{peak}}^{\text{syn}}$ spans a factor of ~ 300 , while that of the $\nu_{\text{peak}}^{\text{ic}}$ spans a factor of ~ 60 . The distribution of the $\nu_{\text{peak}}^{\text{ic}}$'s are limited more than that of the $\nu_{\text{peak}}^{\text{syn}}$'s because the Klein-Nishina effect reduces the production efficiency of the γ -ray in the higher-energy regime. On the contrary, the distribution of the $(\nu F_{\nu})_{\text{peak}}^{\text{syn}}$ spans a factor of ~ 5 , while that of the $(\nu F_{\nu})_{\text{peak}}^{\text{ic}}$ a factor of ~ 6 . The range of the $(\nu F_{\nu})_{\text{peak}}^{\text{ic}}$ is slightly larger than that of the $(\nu F_{\nu})_{\text{peak}}^{\text{syn}}$. This is consistent with the results from the modeling for the 2010 and 2011 SEDs: the primary parameter changes are in the EED. According to the SSC model as described in Section 5.4.2, the change in the n_e affects $(\nu F_{\nu})_{\text{peak}}^{\text{ic}}$ more than $(\nu F_{\nu})_{\text{peak}}^{\text{syn}}$:

$$[(\nu F_{\nu})_{\text{peak}}^{\text{syn}}, (\nu F_{\nu})_{\text{peak}}^{\text{ic}}] \propto [n_e^1, n_e^2].$$

However, the effect of changing n_e is weakened by the changes in B , and hence the distribution ranges are not dramatically different. Comparing the synchrotron-peak values for the 9 periods in 2011 to that of the 2010 March flaring activity in Figure 6.8a, the former has more variation in the frequency than in the energy flux. *Typically*, a higher peak energy flux is related to a higher

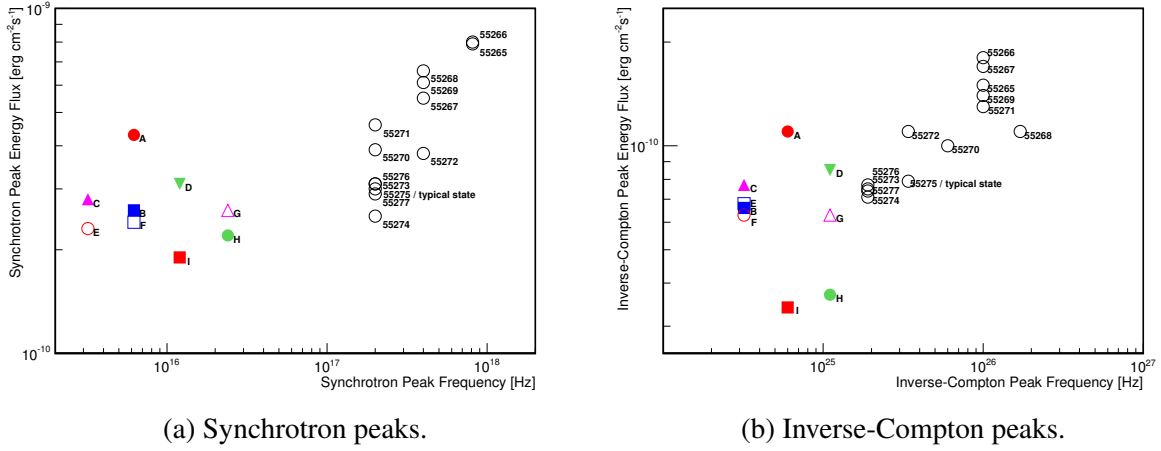


Figure 6.8.: The peak positions in the modeling SEDs from the 9 periods (A – I) in 2011 and 13 days (MJD 55265 – 55277) in the 2010 March flaring activity. For both of the panels, the x-axis spans 3 orders of magnitude; the y-axis spans 1 order of magnitude. Those of the typical state from the 2009 averaged SED [Abdo et al., 2011] are the same as those of MJD 55275. The values are given in Tables 5.5 and 6.4.

peak frequency among high and low states of Mrk 421 as it occurs to the values from the 2010 March data, depicted on the right side of Figure 6.8a. This behavior has also been observed on several other blazars. Therefore, the spread in $\nu_{\text{peak}}^{\text{syn}}$ values over one order of magnitude with similar energy fluxes observed in 2011 is *unusual*. This shows that the broadband variability observed in 2011 has a different *flavor* from the typical blazar broadband variability.

The 9 SEDs built with 2011 data could be adequately parametrized with a one-zone SSC model where most changes occur in the model parameters related to the EED. The environmental parameters R and δ remained constant, with the values used to describe the SEDs built with 2009 and 2010 data. The B was kept almost constant, with only moderate variations (from 60 mG to 48 mG, being 38 mG for the 2009 and 2010 data). This suggests that the dominant emission region could be a standing shock with an unchanged size of the shock region and an unchanged Lorentz factor of the flowing plasma. The factor to drive the evolution is supposed to relate more to the process of the particle acceleration which could happen closer to the central engine, the super-massive black hole, rather than far outside in the large-scale jet.

7. Summary of the Study on Markarian 421

Markarian 421 (Mrk 421) is a BL Lac object, which is believed to have a pair of relativistic jets flowing in opposite directions closely aligned to our line of sight. Mrk 421 is even one of the closest ($z = 0.031$), brightest, and most variable BL Lac objects in the extragalactic X-ray and very high energy (VHE; >100 GeV) sky. According to the results from the long-term monitoring, the typical VHE- γ -ray flux from Mrk 421 is 0.5 Crab Units (c.u.)¹. The typical spectral energy distribution (SED) of Mrk 421 has two characteristic bumps: the low- and the high-energy bumps. The SED from Mrk 421, and those from blazars in general, are dominated by the emission components from its relativistic beaming effect. The observed spectrum and polarization indicates that the low-energy bump is attributed to the synchrotron radiation of electrons in turbulent magnetic fields in the jet. Mrk 421 has a peak frequency of the low-energy bump above 10^{15} Hz, and therefore it is categorized as a high-synchrotron-peaked (HSP) BL Lac object. The peak frequency of the high-energy bump for a HSP blazar is usually below 2.4×10^{25} Hz (100 GeV). This bump is interpreted as the inverse-Compton scattering of the same population of electrons off synchrotron photons (synchrotron self-Compton, SSC). The goal of this PhD thesis is to better understand the mechanisms responsible for the broadband emission and the temporal evolution of Mrk 421, which might be applied to other blazars which cannot be studied with this level of detail because their emissions are intrinsically weaker, or they are located further away.

Since 2009, an exceptionally long and dense multi-wavelength (MW) monitoring of Mrk 421 has been performed. The MW campaign has been organized to deeply study its broadband emission from radio to VHE- γ rays with MAGIC, VERITAS, Whipple, *Fermi*-LAT, MAXI, RXTE, *Swift*, GASP-WEBT, and several optical and radio telescopes.

This PhD thesis reports results from ~ 70 hours of observations with MAGIC in 2010 and 2011 (the first two years of the operation of the MAGIC stereo telescopes). I also report the results from the MW observations in 2010 and 2011, where more than 20 instruments participated, covering energies from radio to VHE.

From the MAGIC stereo observations of Mrk 421 in 2010 and 2011, 85 spectra of single observations were obtained covering energies from 80 GeV to 5 TeV. In order to describe the features of the spectra quantitatively, 4 functions are used to fit each spectrum: a power-law function, a power-law function with an exponential cutoff, a power-law function with a fixed exponential cutoff at 4 TeV, and a log-parabola function. It is found that the power-law function with an

¹The VHE flux of the Crab Nebula used in this work is 2.2×10^{-10} cm⁻²s⁻¹. This value is obtained by integrating the fit function published in [Aleksić et al., 2012a] from 200 GeV to 10 TeV.

exponential cutoff and the log-parabola function can describe most of the spectra similarly well, while a power-law function or a power-law function with a fixed exponential cutoff at 4 TeV fail to describe the spectra for a fraction of the observations. The extra exponential cutoff fixed at 4 TeV improves the goodness of the fit provided by a simple power-law function.

The VHE spectral-shape changes as a function of the source's activity are also characterized. The spectral shape can be quantized through the calculation of the hardness ratio between the flux in a high-energy band and that in a low-energy band, or using the fit power-law index (photon-index, α) from the fit function with the power-law with a fixed exponential cutoff at 4 TeV². Both results show that the VHE hardness increases (the index α increases or the ratio increases) with the VHE flux until its value reaches ~ 0.8 c.u., and then the hardness saturates. In particular, the VHE photon index α found for Mrk 421 saturates at ~ -1.8 . This is the first time that such characteristic is observed in Mrk 421, as well as for any VHE blazar. The possible reason for the saturation could be the Klein-Nishina effect or the particle-acceleration mechanism. It is not yet clear.

The MW data from the 2010 and 2011 campaigns show that the highest flux variabilities occurred in the VHE γ -ray band and the X-ray band. In 2010, the VHE γ -ray flux had been as high as 4 c.u. (in January), 8 c.u. (in February), 2 c.u. (in March), and 1 c.u. (in May); its shortest variability timescale was one-day or shorter. In 2011, the VHE flux varied typically in about 1-month timescale although in some cases we can see variability occurring in a few days. The flux level was lower than the typical flux (0.5 c.u.), being $\lesssim 0.3$ c.u. for many of the observations. The highest flux detected in 2011 was ~ 0.8 c.u. From 2010 to 2011, the fractional variability F_{var} in the VHE- γ -ray band dropped from ~ 0.9 to ~ 0.55 , while in the X-ray bands (0.3-2 keV and 2-10 keV), F_{var} stayed at a similar magnitude (~ 0.5 and ~ 0.7 respectively).

This study shows that, in both years 2010 and 2011, the F_{var} increases with the energy on both the low-energy and the high-energy bumps:

$$F_{\text{var}}(\text{VHE } \gamma\text{-ray}) > F_{\text{var}}(\text{HE } \gamma\text{-ray}),$$

$$F_{\text{var}}(2\text{--}10 \text{ keV}) > F_{\text{var}}(0.3\text{--}2 \text{ keV}) > F_{\text{var}}(\text{UV}) > F_{\text{var}}(\text{optical}) > F_{\text{var}}(\text{radio}),$$

where HE stands for "high energy" (> 100 MeV). Both the optical/UV and the HE- γ -ray bands are located in the rising segments of the bumps: the former is on the low-energy bump and the latter on the high-energy bump. Both the X-ray and VHE- γ -ray bands are located in the falling segments of the bumps: the former is on the low-energy bump and the latter on the high-energy bump. Therefore, these observations show that the variability in the rising segment of the bumps is a few times lower than that in the falling segment of the bumps. Furthermore, for each year, $F_{\text{var}}(\text{optical})$ was similar to $F_{\text{var}}(\text{HE-}\gamma\text{-ray})$, and $F_{\text{var}}(\text{X-ray})$ was similar to $F_{\text{var}}(\text{VHE-}\gamma\text{-ray})$. These correspondences seem to be a general phenomenon for different years in Mrk 421, and it might also occur on other HSP BL Lac objects as Mrk 421. This characteristic is expected from the strong correlation between the synchrotron photons and the up-scattered photons by inverse-Compton effect within the SSC emission model: both the variations of the optical and

²This function describes well a large fraction of the spectra (88% with fit p -values > 0.1), and for the others, the disagreement was not very large.

the HE- γ -ray photons result from the variation in the same population of electrons with relatively low energies, while both the variations of the X-ray and the VHE- γ -ray photons result from the variation in a distinct population of electrons with relatively high energies. Consequently, the behavior observed in the fractional variabilities supports the interpretation of the data using the SSC theoretical model. The exquisite data set reported here allows for the first time to give this consistency test of the model.

During the MW campaign in 2010, we measured the decay of a flaring activity in which the VHE γ -ray flux decreased from ~ 2 c.u. to ~ 0.5 c.u. This occurred in the time interval MJD³ 55265–55277 (March 10–22). A distinctive characteristic of this interval is that we could perform MW observations every day, which enabled an unprecedented characterization of the time-evolution of the radio to γ -ray emission of Mrk 421. Such a detailed study has never been performed on Mrk 421 or any other blazar to date.

We found that flux variability is noticeable in the X-ray and VHE γ -ray bands, while it was minor or not significant in the other bands as well as optical polarization. These observations revealed a close-to-linear correlation between the X-ray flux in the 2–10 keV band and the VHE γ -ray flux above 200 GeV, consistent with the γ -rays being produced by inverse Compton scattering in the Klein-Nishina regime in the framework of SSC models.

The broadband SEDs during this flaring episode, resolved on timescales of one day, were characterized with two leptonic scenarios: a one-zone SSC model, and a two-zone SSC model where one zone is responsible for the quiescent emission while the other (smaller) zone, which is spatially separated from the former one, contributes to the daily-variable emission occurring mostly at X-rays and VHE γ rays. Both the one-zone SSC and the two-zone SSC models can describe the daily SEDs. For both cases, an electron energy distribution (EED) described by two power-law functions is sufficient to describe the emission during the very high states (MJD 55265 and 55266), which is produced by a single blob in the one-zone SSC model, and dominated by the flaring blob in the two-zone SSC model. However, an EED with three power-law functions is needed during the somewhat lower blazar activity.

We found that the two-zone SSC model is more suitable for describing the evolution of the flaring activity because of the better agreement with the measured SED data at the peaks of the low- and high-energy bumps. Additionally, the two-zone SSC scenario presented here naturally provides shorter timescales (1 hour vs. 1 day) for variability in the X-ray and VHE bands, as well as the correlated variability in X-ray and VHE bands without any correlation to the optical and radio bands. Within this two-zone SSC scenario, the EED of the flaring blob is constrained to a very narrow range of energies, namely $\gamma_{\min}\text{--}\gamma_{\max} \sim 3 \times 10^4\text{--}6 \times 10^5$, which could be produced through stochastic particle acceleration (second order Fermi acceleration) via scattering by magnetic inhomogeneities in the jet.

The results from the 2010 March flaring activity of Mrk 421 are reported in Sections 5.3 – 5.5, and they are the main scientific achievement of this PhD thesis. Preliminary results were reported (as an oral contribution) in the 33rd International Cosmic Ray Conference (Rio de Janeiro, July 2013), one of the most prestigious conference in the field of the VHE astronomy and astro-

³Modified Julian Day

particle physics in general. The final results (reviewed and approved within the *Fermi*, MAGIC, and VERITAS Collaborations) have been submitted for publication in the *Astronomy and Astrophysics* journal in 2014 June.

During the MW campaign in 2011, we observed that Mrk 421 had an atypically high activity (~ 2 times that in 2010) and a relatively large variability in the optical band, together with a very low state/variability in the X-ray/VHE band, which is very unusual for Mrk 421. Typically, blazar emission models for Mrk 421 focus on the explanation of the variability in the X-ray and γ -ray bands. This data set is suitable for examining emission models and estimate if they can describe the evolution of the whole broadband SEDs including the variabilities in optical, X-ray, and γ -ray bands.

In order to study the evolution of the broadband SED in 2011, the VHE spectra are combined from several adjacent observations for better photon statistics, and the MW data set is split into 9 intervals with distinct broadband activities. We could describe the variations in the full broadband SED with a one-zone SSC model where most changes occur in the EED, rather than in the environmental parameters (like the blob size or the Doppler factor). This also agrees with the results obtained from the 2010 March observations.

To explain the featured high optical state together with the low X-ray/VHE state, several changes were needed in comparison to the typical state from 2009: a harder power-law index in the first segment in the EED s_1 together with a lower first break in the EED γ_{br1} , and a softer power-law index in the second segment in the EED s_2 .

In overview of the SEDs from 2011, there is small variation in the synchrotron peak energy-flux $(\nu F_\nu)_{peak}^{syn}$, but the variation in the synchrotron peak frequency ν_{peak}^{syn} is large (maximum value being a factor of 8 larger than the minimum) and without correlation with the variation in the $(\nu F_\nu)_{peak}^{syn}$. Typically, a higher peak energy-flux is related to a higher peak frequency among high and low states of Mrk 421 as it occurs to the values from the 2010 March data, as well as in the broadband SEDs from many other blazars. Therefore, the broadband variability observed in 2011 has a different *flavor* from the typical blazar broadband variability. These two different flavors of the broadband variabilities can be explained with the changes in the EED. The increase of the peak frequency with the approximately constant peak energy-flux (as in 2011) could be produced by an increased primary break γ_{prm} (which is directly related to the value of ν_{peak}^{syn} in the SED), together with a *softened* EED power-law index for electron energies below the γ_{prm} ; on the other hand, the increase of the peak frequency with the increasing peak energy-flux (as in 2010 March) could be achieved by an increased primary break γ_{prm} and a *hardened* EED power-law index for electron energies below the γ_{prm} .

These studies show large complexity in the evolution of the broadband (radio to VHE γ -rays) SED. In this PhD thesis, I show that most variations in the SED of Mrk 421 can be produced through changes in the EED. However, the overall EED characteristics estimated for the 2010 and 2011 campaigns are different, and they also differ from the EED characteristics estimated for the 2009 campaign. Therefore, longer and deeper observations are needed to understand what characteristics get repeated over time and hence are typical, and what characteristics are atypical. Ultimately, one should investigate whether the lessons learned from Mrk 421 can be extended to

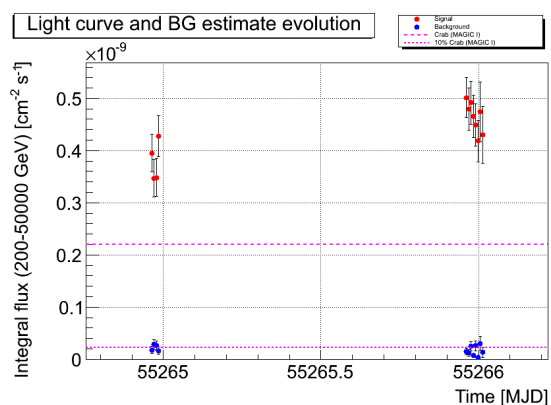
HSP blazars in general, and also how to relate the characteristics of the EED (that we need to explain the measured SEDs) with the particle acceleration in the vicinity of super-massive black holes, or within the relativistic jets of the active galactic nuclei.

A. Markarian 421 MAGIC Light Curve Archive

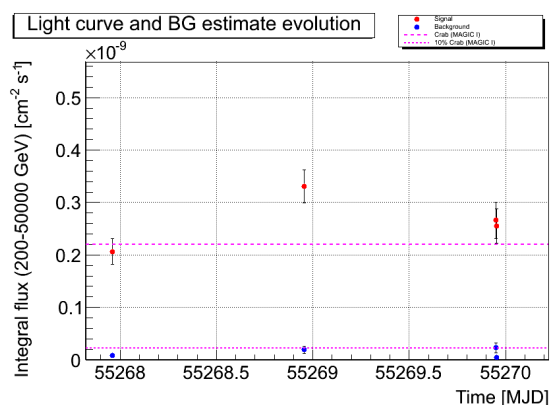
In Section 4.1, Markarian 421 LCs from MAGIC observations in 2010 and 2011 have been presented. Because of the limited space, only the plots directly related to scientific results were selected in that section. In this chapter, additional MAGIC LC plots which can support the study are presented.

A.1. Intra-night Light Curves of March 2010

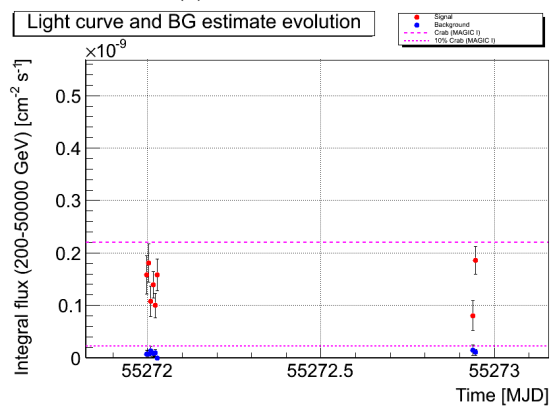
To examine if there is any fast variability during the March flaring activity in 2010, which can constrain to some extent the emission models in Chapter 5, 4 intra-night LCs in Figure A.1 are drawn. The time bin is 10-minute wide. On MJD 55266, there was a decline of 0.4 c.u. (23% of the original flux, 2.1 c.u.) in 50 minutes. The change of the flux is roughly the size of the summation of the statistical error bars. On MJD 55273, there was an increase of 0.4 c.u. (130% of the original flux, 0.3 c.u.) in 10 minutes. The change of the flux is roughly twice the summation of the statistical error bars. There is no significantly large intra-night variability detected during this period of time.



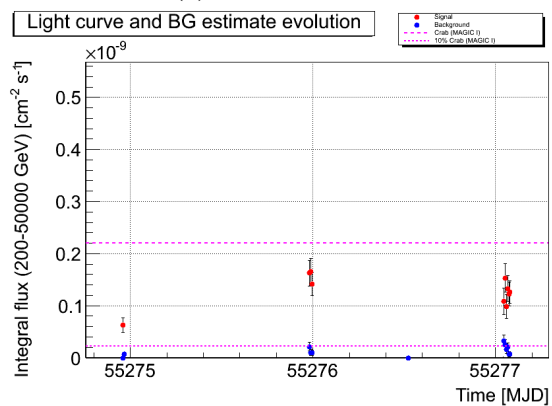
(a) MJD 55265-55267.



(b) MJD 55268-55270.



(c) MJD 55272-55273.



(d) MJD 55275-55277.

Figure A.1.: Mrk 421 intra-night LCs of 2010 March VHE flare.

B. Markarian 421 MAGIC Spectrum Archive

In Section 4.2, Markarian 421 spectra from MAGIC observations in 2010 and 2011 have been presented. Because of the limited space, only a small portion of them has been shown in that section. In this chapter, the complete results of MAGIC daily spectra are presented. In Section B.1, all the spectra, fit functions, and fit parameters for each observation are shown.

B.1. Spectra and Fit Functions

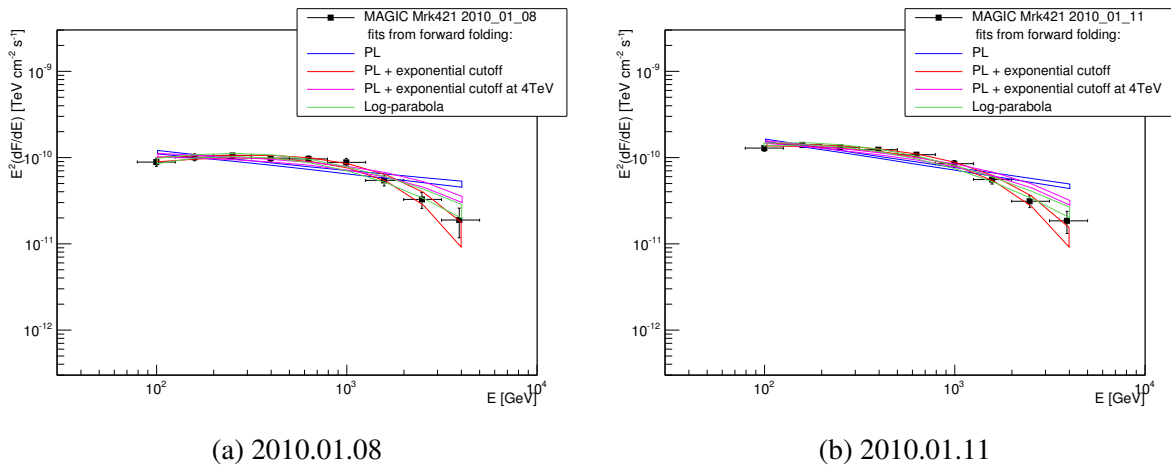
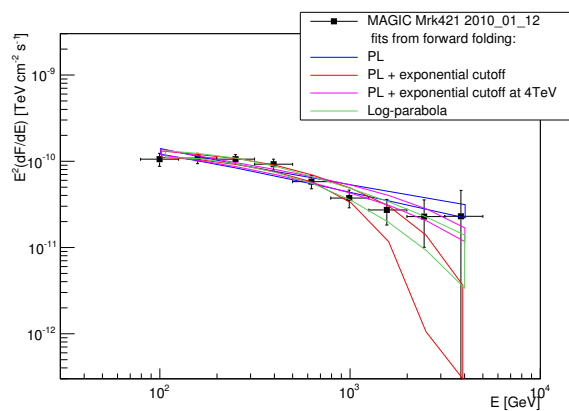
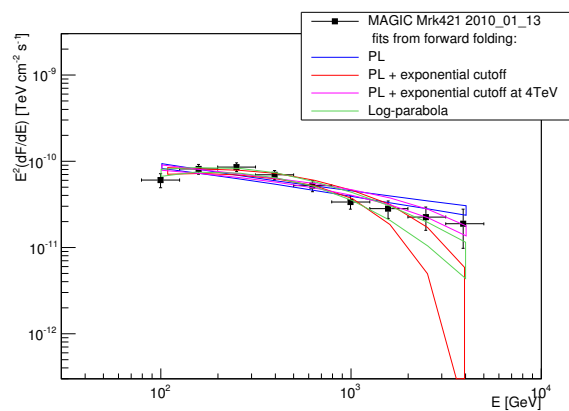


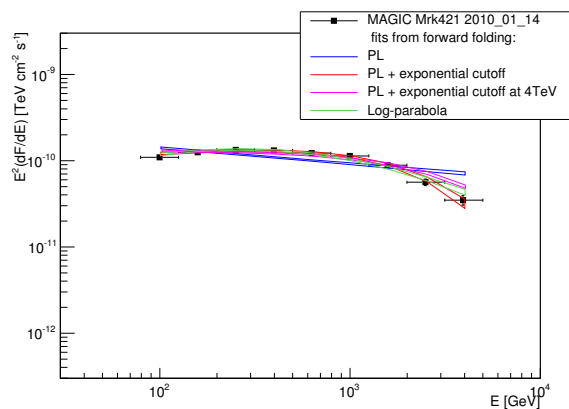
Figure B.1.: Mrk 421 daily VHE spectra from MAGIC during 2010 and 2011. The fit functions are explained in Section 4.2. The resulted fit parameters are listed in Tables B.1 to B.4.



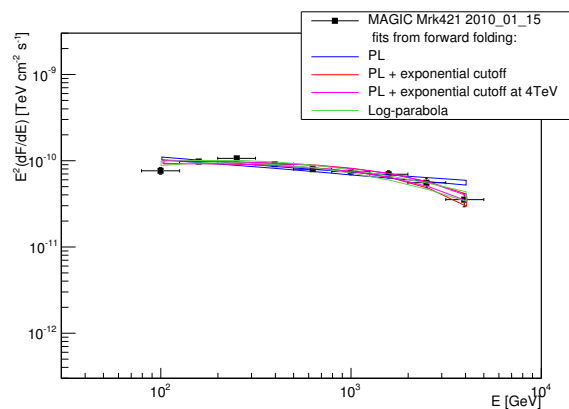
(a) 2010.01.12



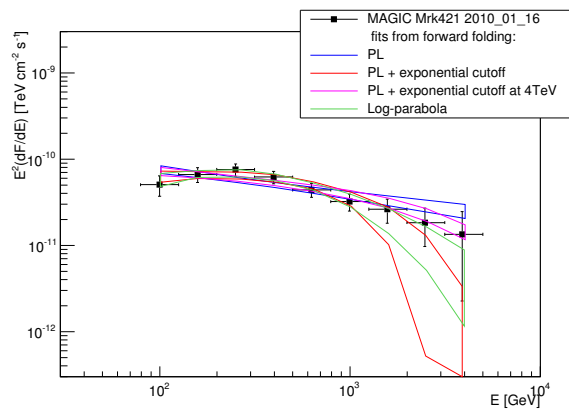
(b) 2010.01.13



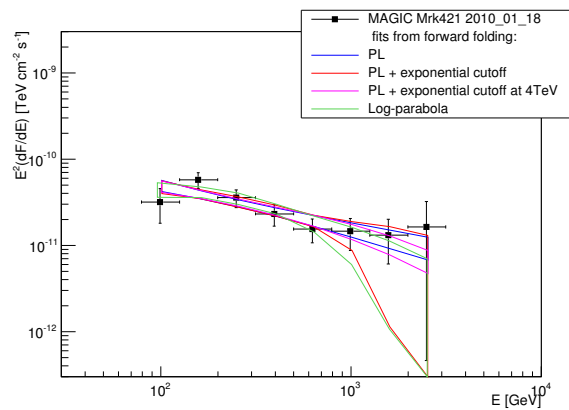
(c) 2010.01.14



(d) 2010.01.15

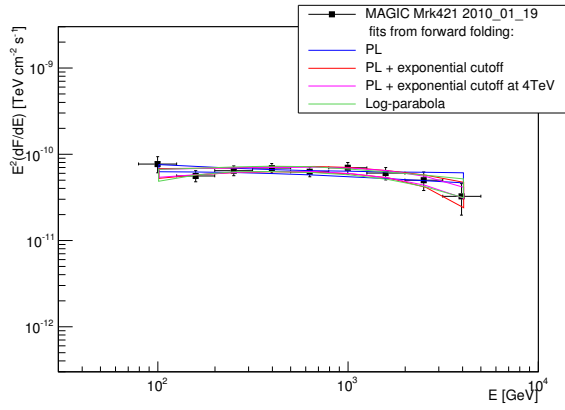


(e) 2010.01.16

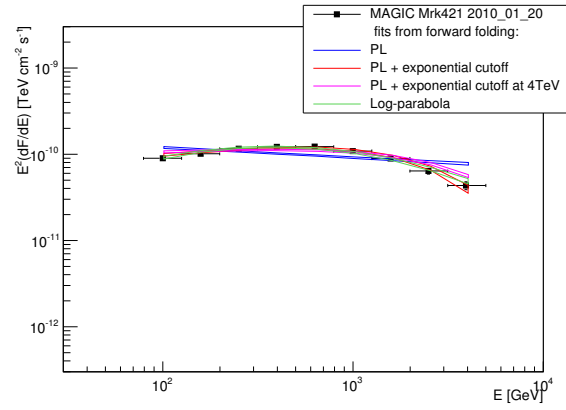


(f) 2010.01.18

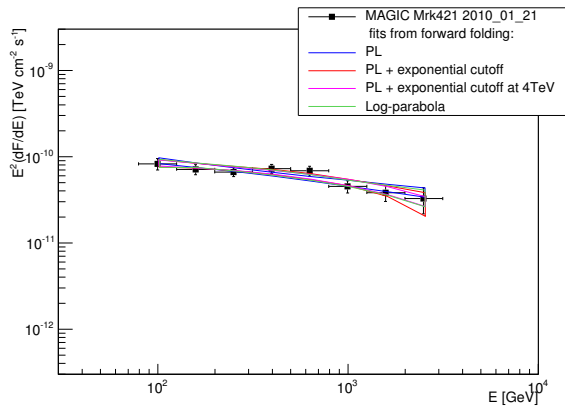
Figure B.2.: Mrk 421 daily VHE spectra from MAGIC during 2010 and 2011. The fit functions are explained in Section 4.2. The resulted fit parameters are listed in Tables B.1 to B.4.



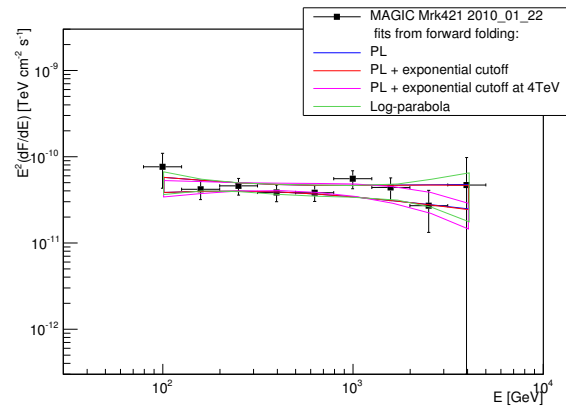
(a) 2010.01.19



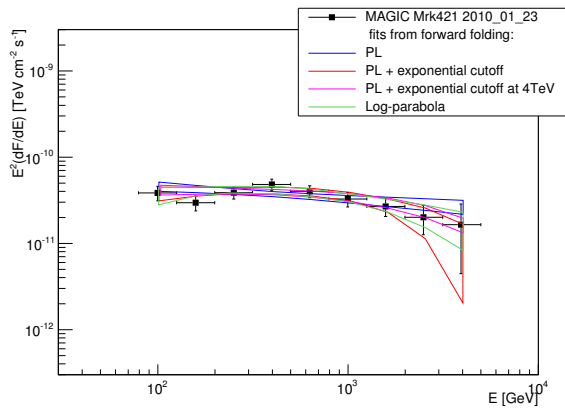
(b) 2010.01.20



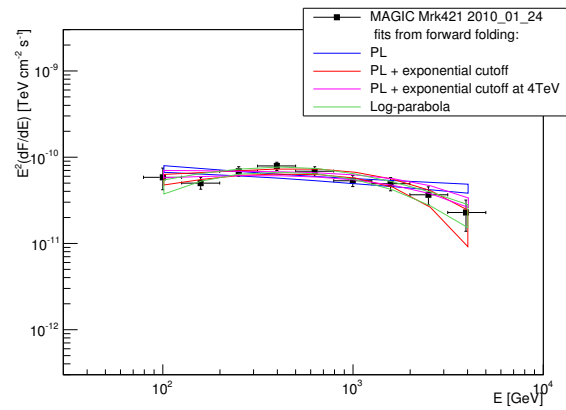
(c) 2010.01.21



(d) 2010.01.22

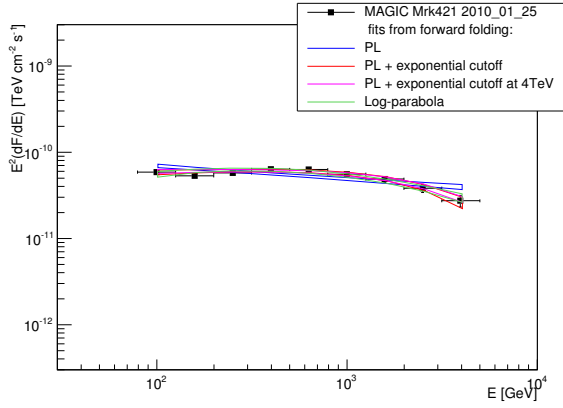


(e) 2010.01.23

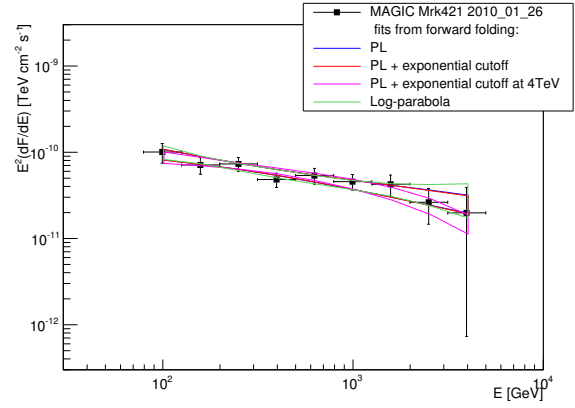


(f) 2010.01.24

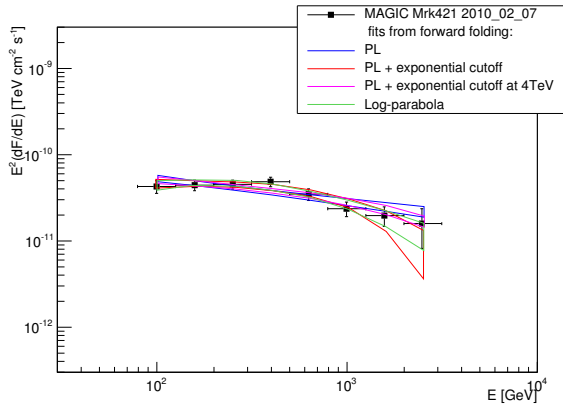
Figure B.3.: Mrk 421 daily VHE spectra from MAGIC during 2010 and 2011. The fit functions are explained in Section 4.2. The resulted fit parameters are listed in Tables B.1 to B.4.



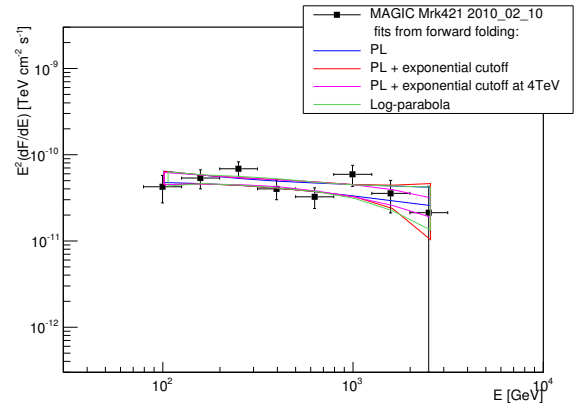
(a) 2010.01.25



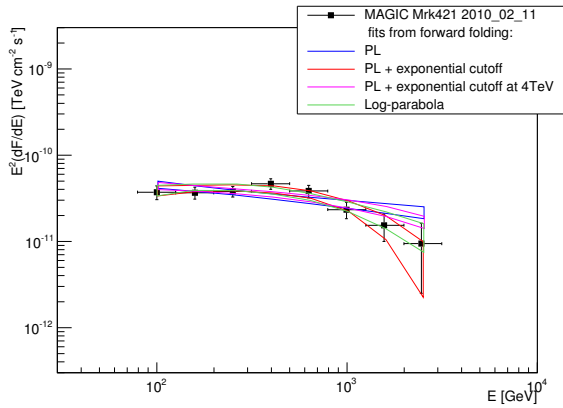
(b) 2010.01.26



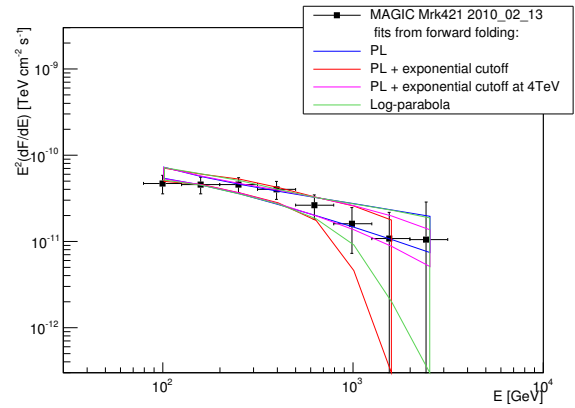
(c) 2010.02.07



(d) 2010.02.10

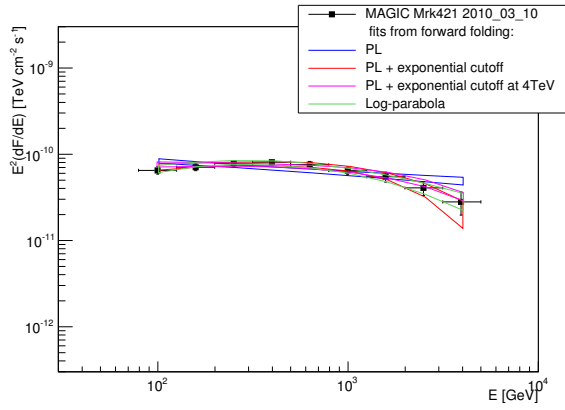


(e) 2010.02.11

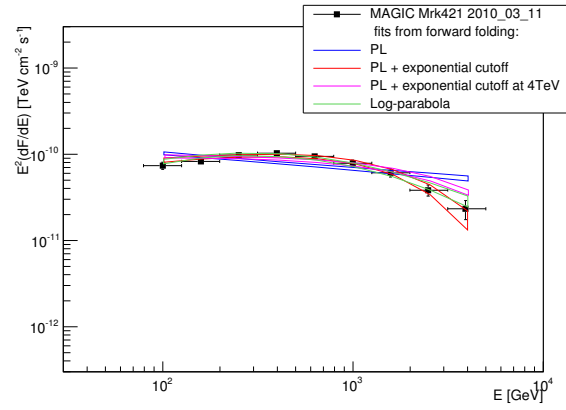


(f) 2010.02.13

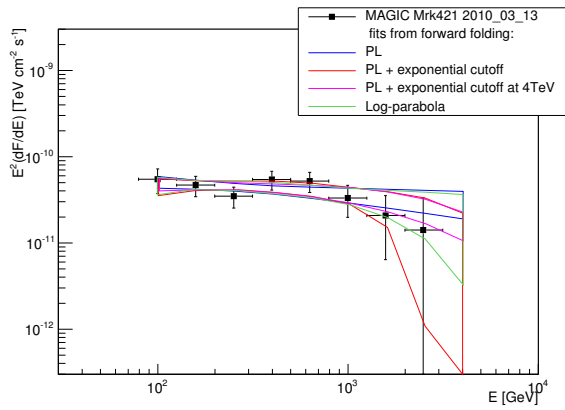
Figure B.4.: Mrk 421 daily VHE spectra from MAGIC during 2010 and 2011. The fit functions are explained in Section 4.2. The resulted fit parameters are listed in Tables B.1 to B.4.



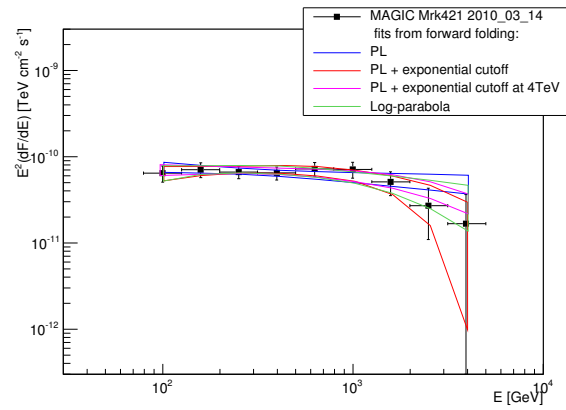
(a) 2010.03.10



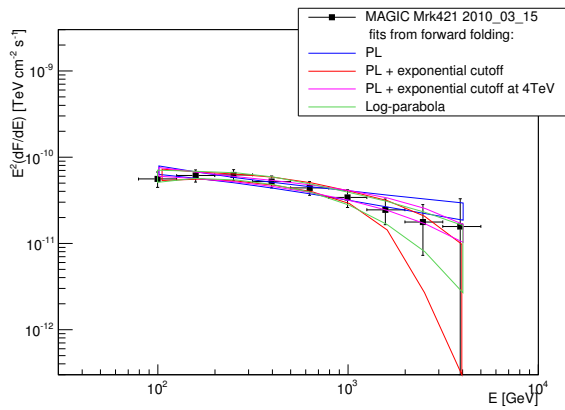
(b) 2010.03.11



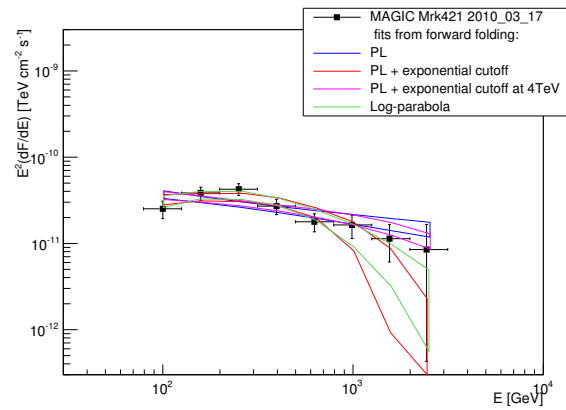
(c) 2010.03.13



(d) 2010.03.14



(e) 2010.03.15



(f) 2010.03.17

Figure B.5.: Mrk 421 daily VHE spectra from MAGIC during 2010 and 2011. The fit functions are explained in Section 4.2. The resulted fit parameters are listed in Tables B.1 to B.4.

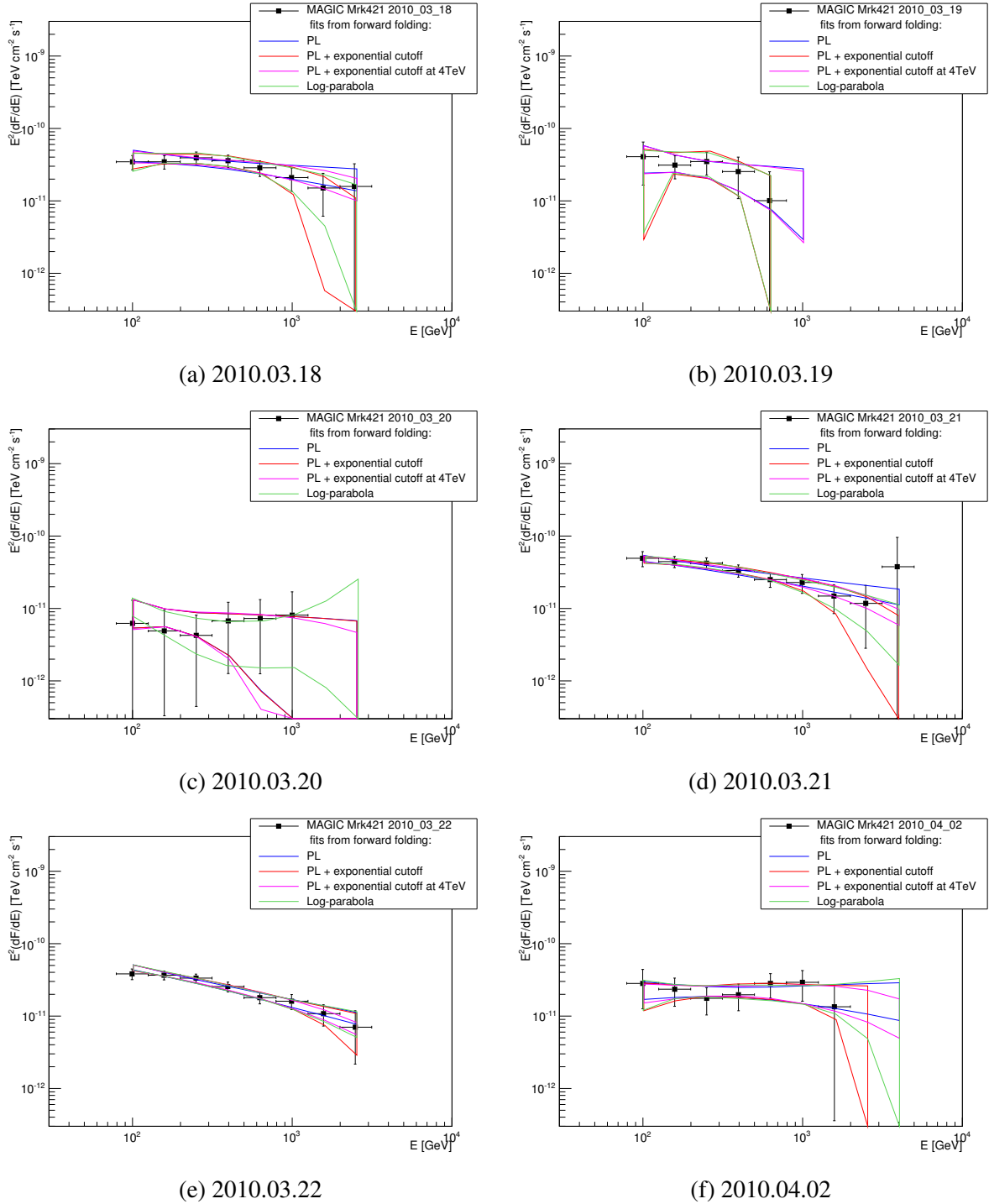
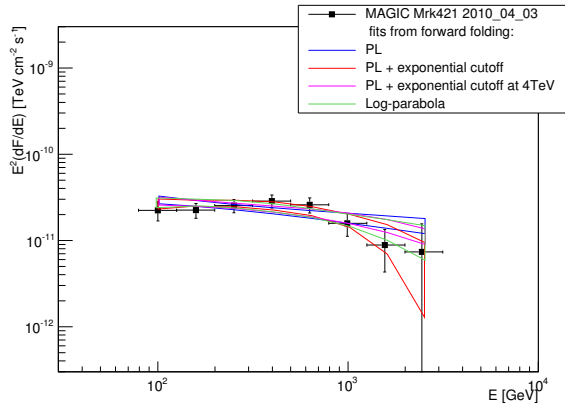
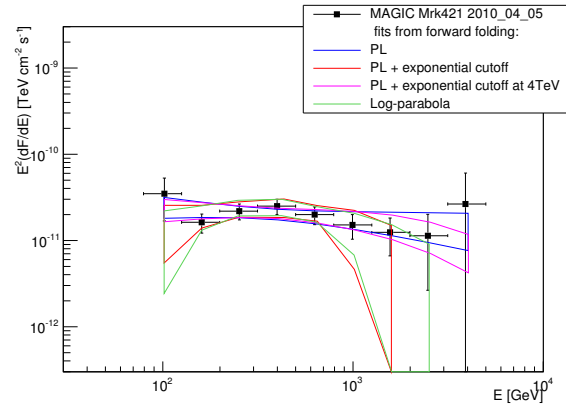


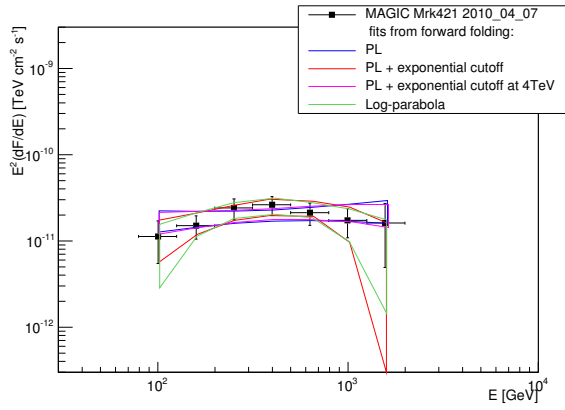
Figure B.6.: Mrk 421 daily VHE spectra from MAGIC during 2010 and 2011. The fit functions are explained in Section 4.2. The resulted fit parameters are listed in Tables B.1 to B.4. The 2010.03.20 data was affected by bad weather, and the SED does not fully agree to that from another independent analysis (cross-check).



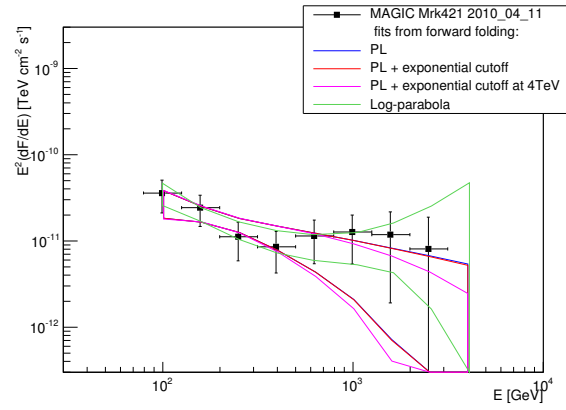
(a) 2010.04.03



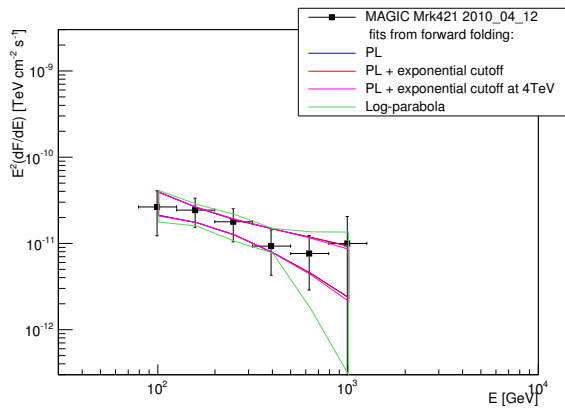
(b) 2010.04.05



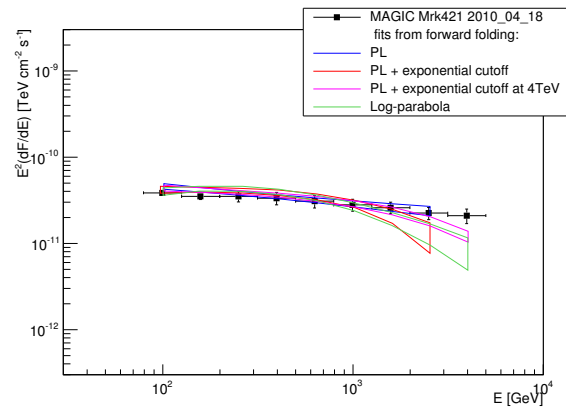
(c) 2010.04.07



(d) 2010.04.11



(e) 2010.04.12



(f) 2010.04.18

Figure B.7.: Mrk 421 daily VHE spectra from MAGIC during 2010 and 2011. The fit functions are explained in Section 4.2. The resulted fit parameters are listed in Tables B.1 to B.4.

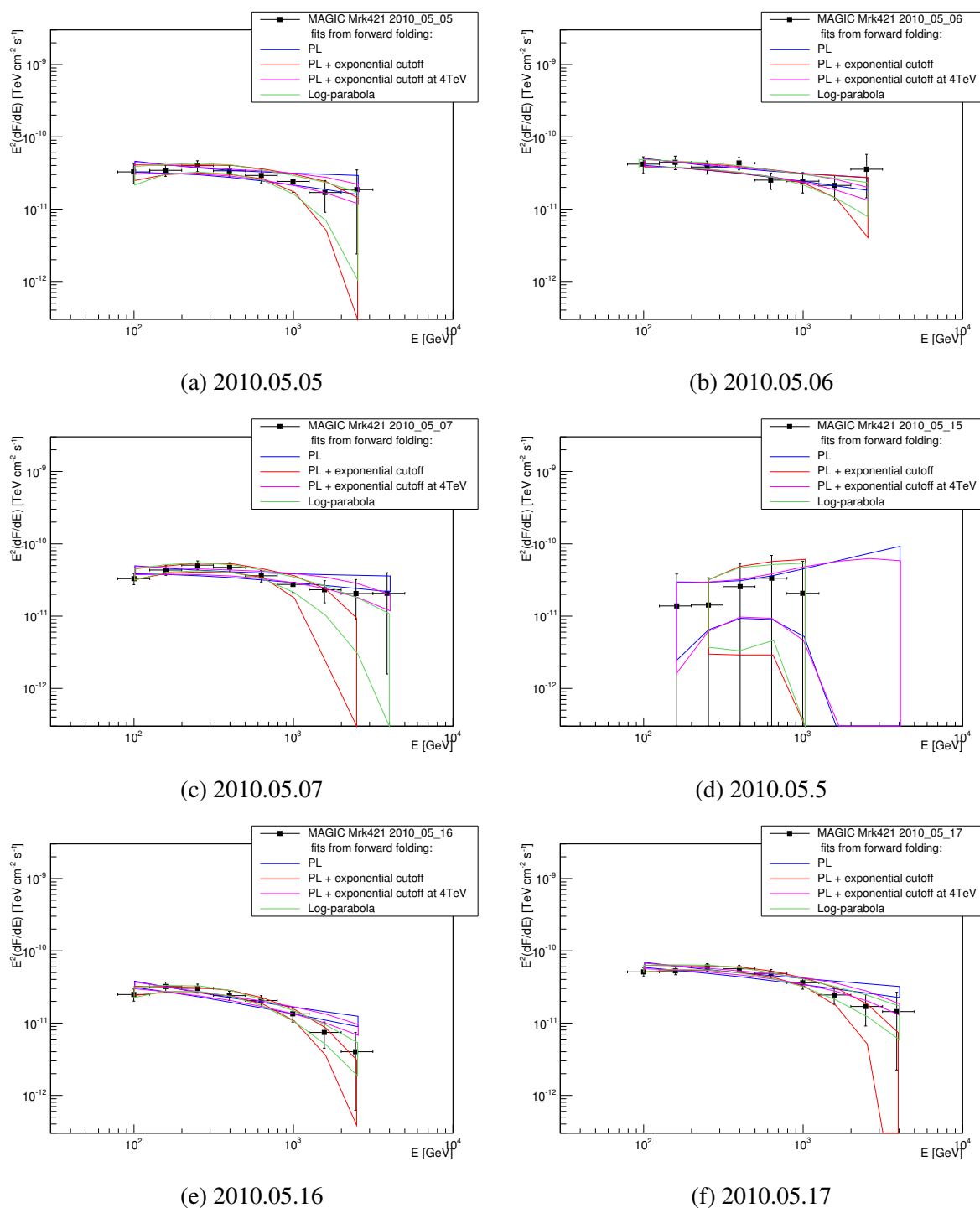
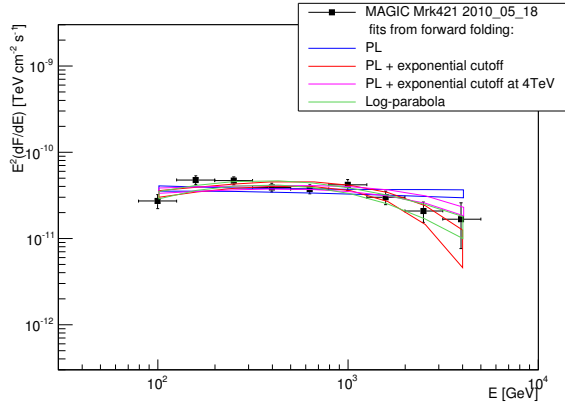
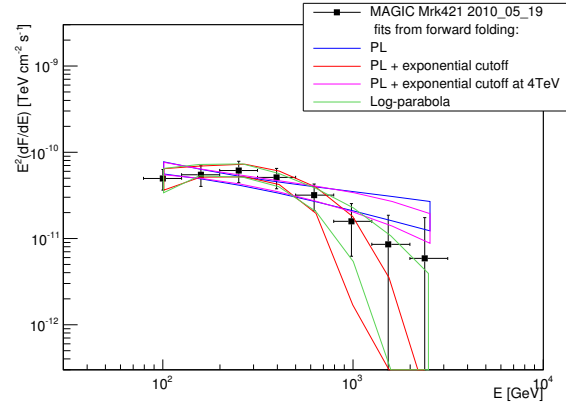


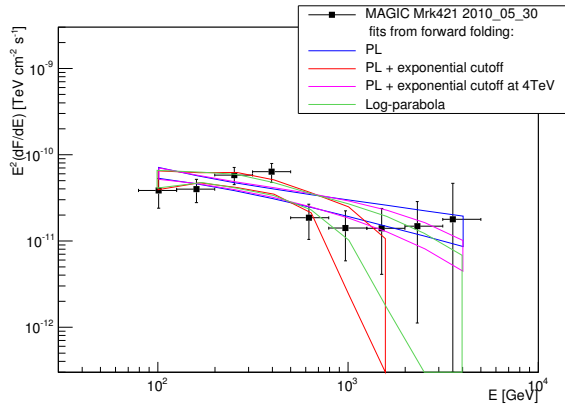
Figure B.8.: Mrk 421 daily VHE spectra from MAGIC during 2010 and 2011. The fit functions are explained in Section 4.2. The resulted fit parameters are listed in Tables B.1 to B.4.



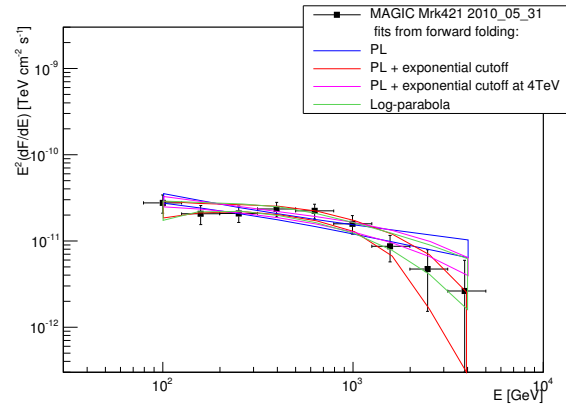
(a) 2010.05.18



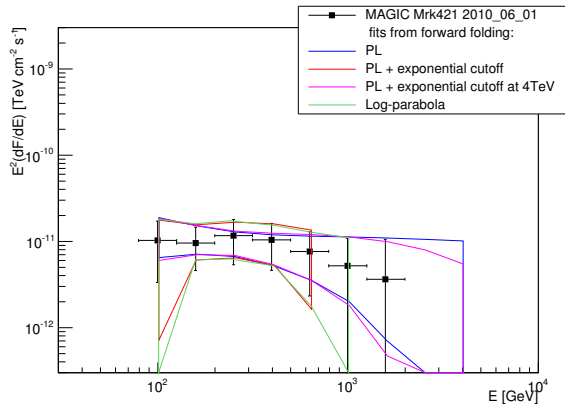
(b) 2010.05.19



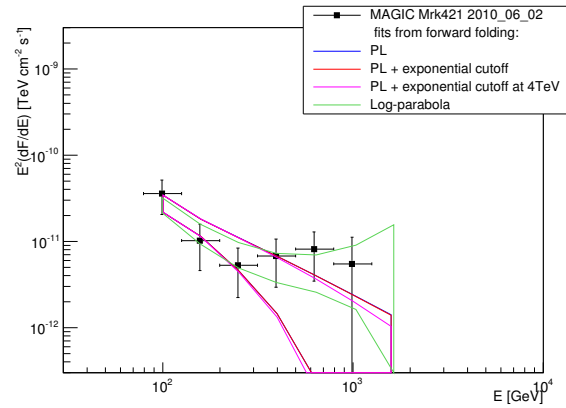
(c) 2010.05.30



(d) 2010.05.31



(e) 2010.06.01



(f) 2010.06.02

Figure B.9.: Mrk 421 daily VHE spectra from MAGIC during 2010 and 2011. The fit functions are explained in Section 4.2. The resulted fit parameters are listed in Tables B.1 to B.4.

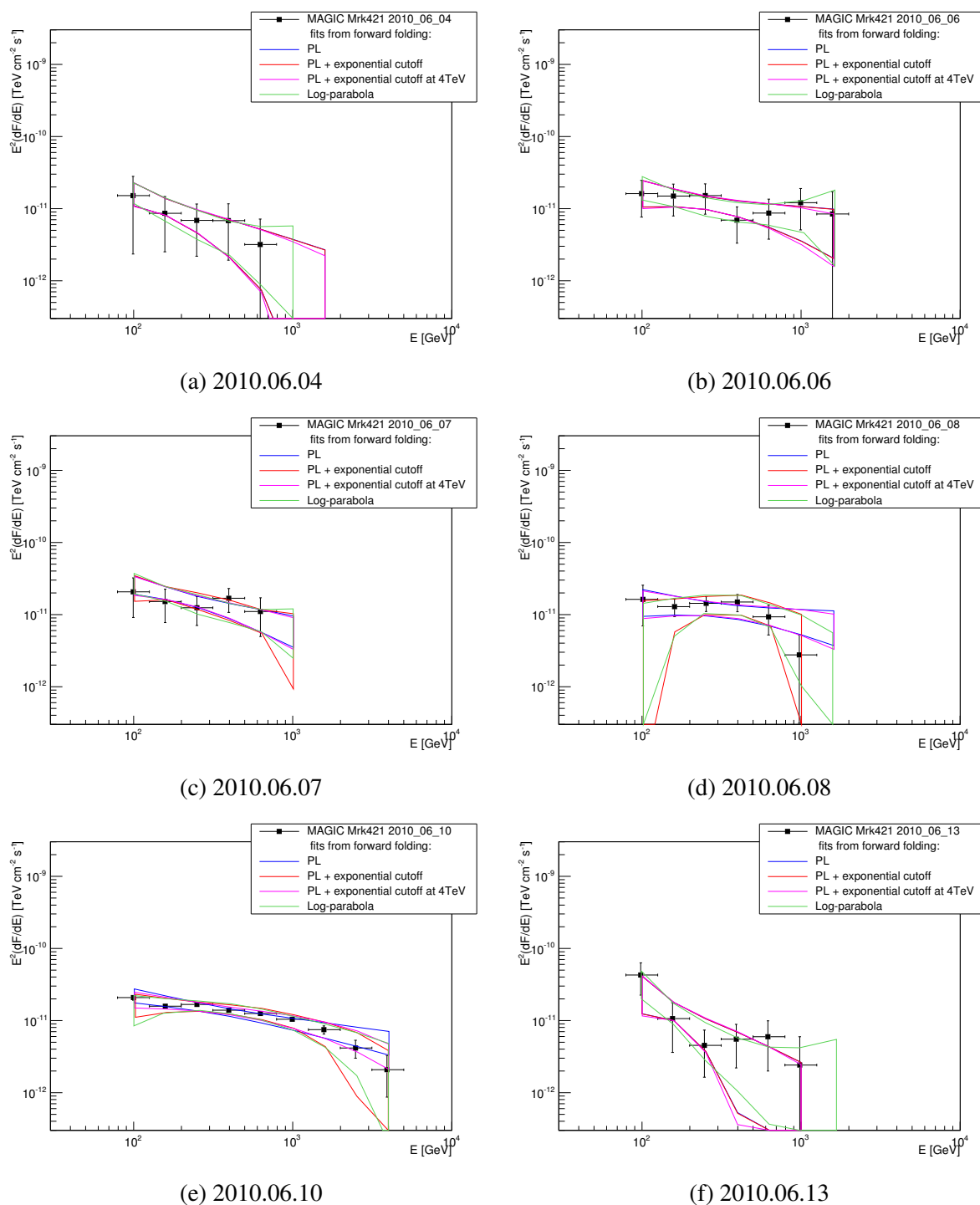
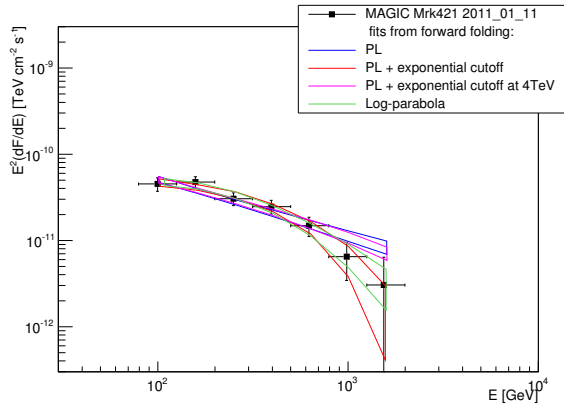
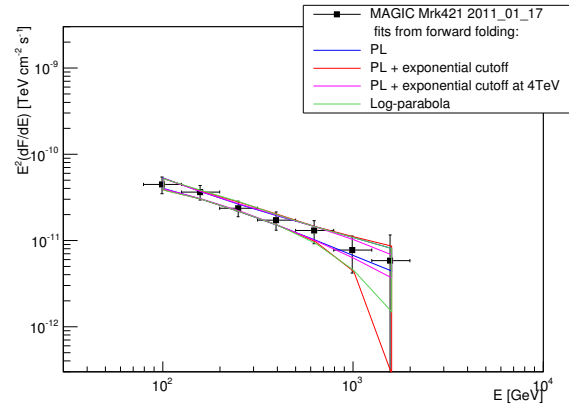


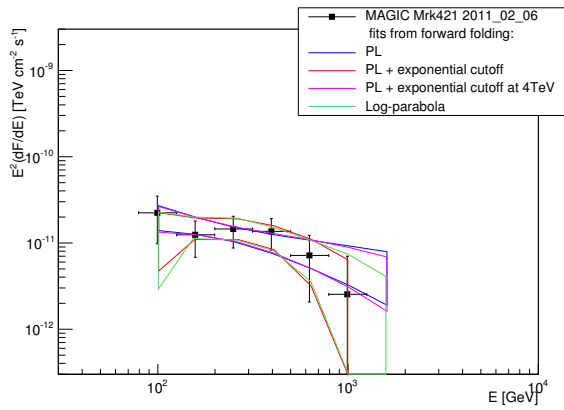
Figure B.10.: Mrk 421 daily VHE spectra from MAGIC during 2010 and 2011. The fit functions are explained in Section 4.2. The resulted fit parameters are listed in Tables B.1 to B.4.



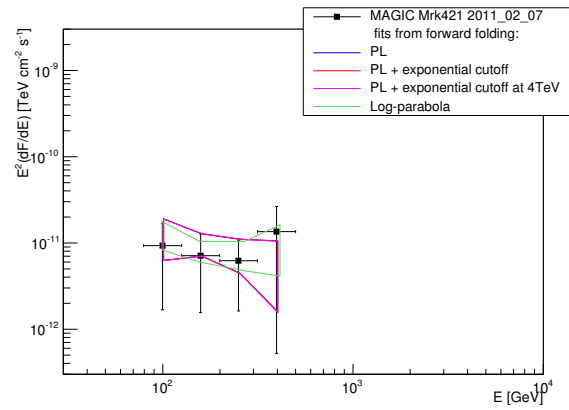
(a) 2011.01.11



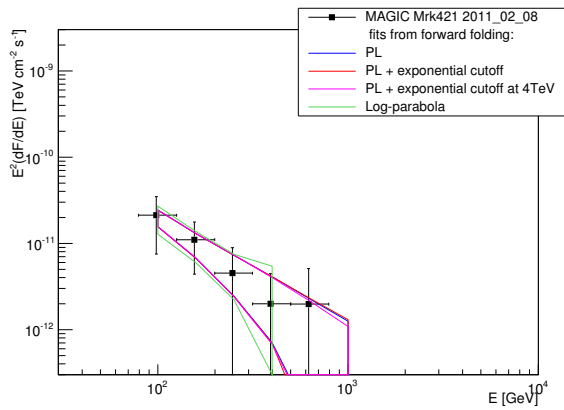
(b) 2011.01.17



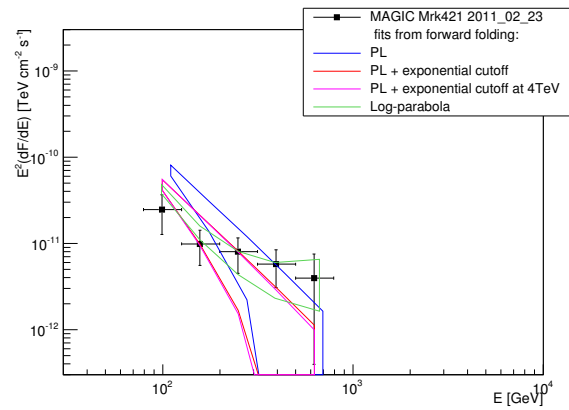
(c) 2011.02.06



(d) 2011.02.07

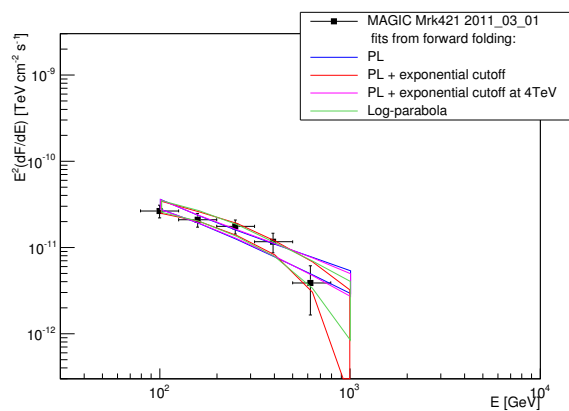


(e) 2011.02.08

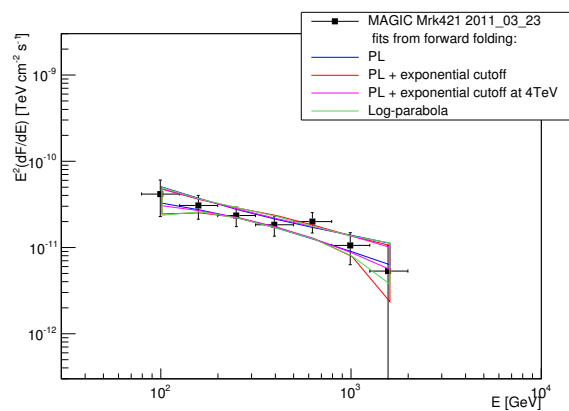


(f) 2011.02.23

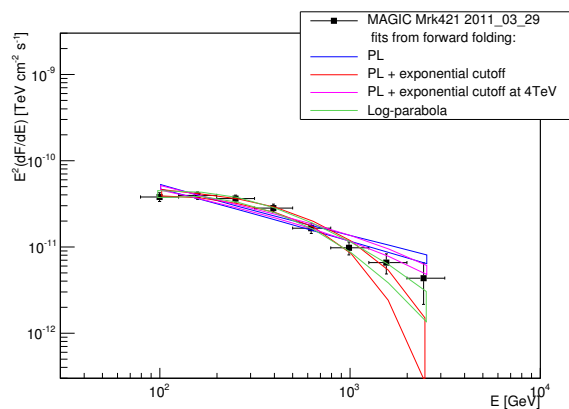
Figure B.11.: Mrk 421 daily VHE spectra from MAGIC during 2010 and 2011. The fit functions are explained in Section 4.2. The resulted fit parameters are listed in Tables B.1 to B.4.



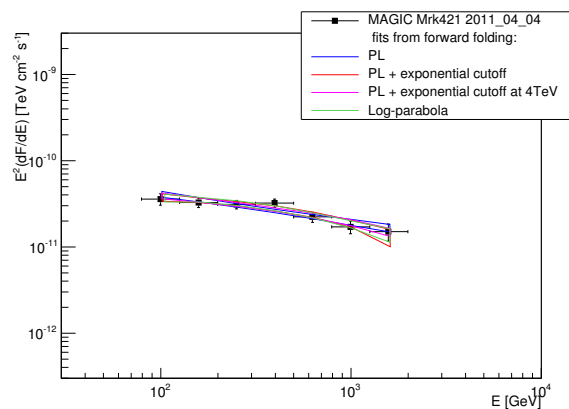
(a) 2011.03.01



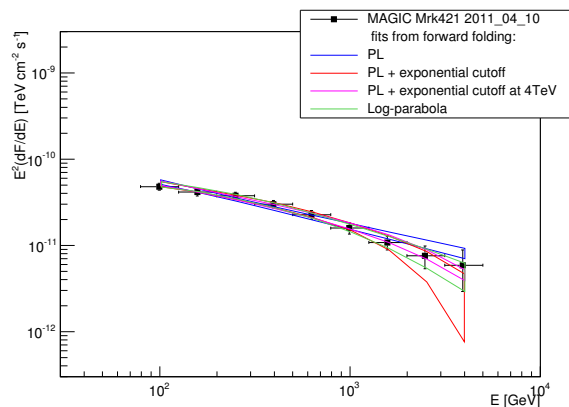
(b) 2011.03.23



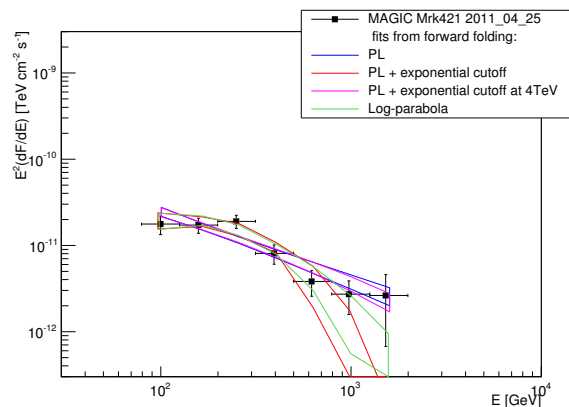
(c) 2011.03.29



(d) 2011.04.04

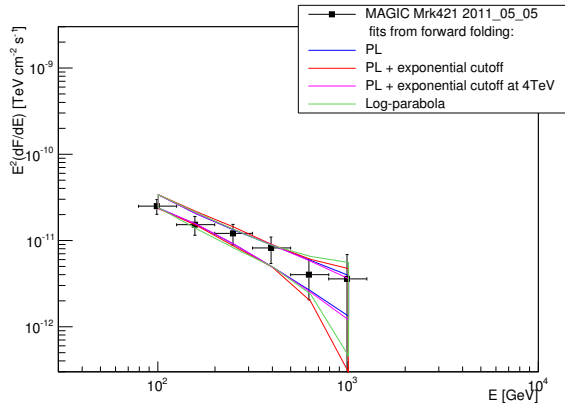


(e) 2011.04.10

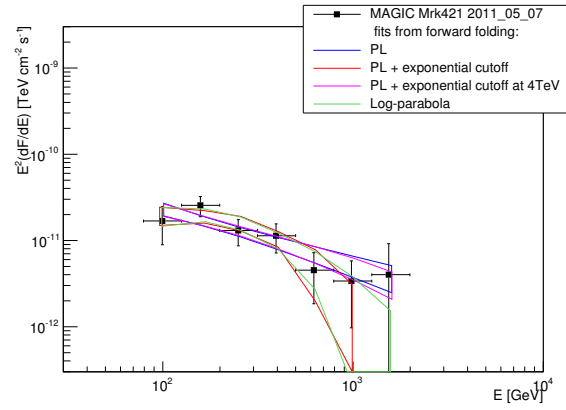


(f) 2011.04.25

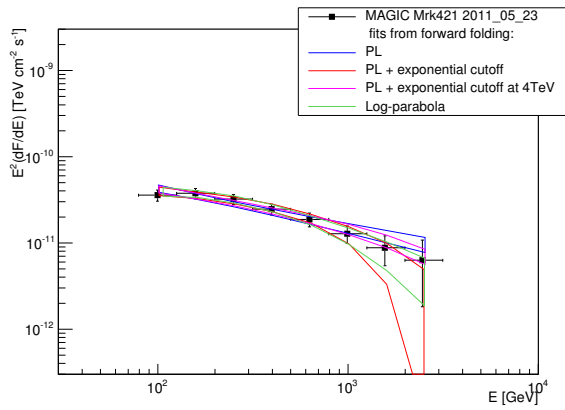
Figure B.12.: Mrk 421 daily VHE spectra from MAGIC during 2010 and 2011. The fit functions are explained in Section 4.2. The resulted fit parameters are listed in Tables B.1 to B.4.



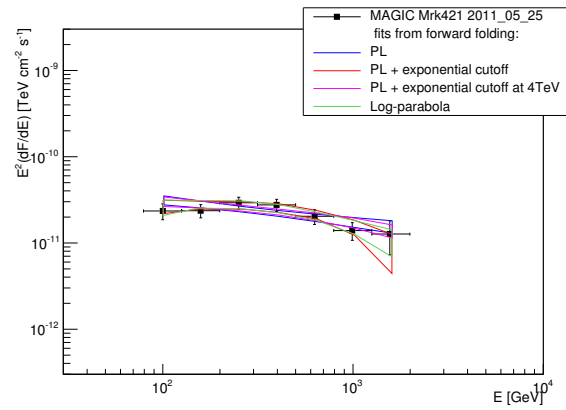
(a) 2011.05.05



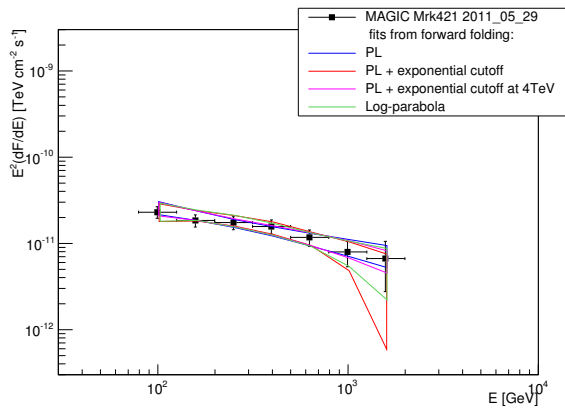
(b) 2011.05.07



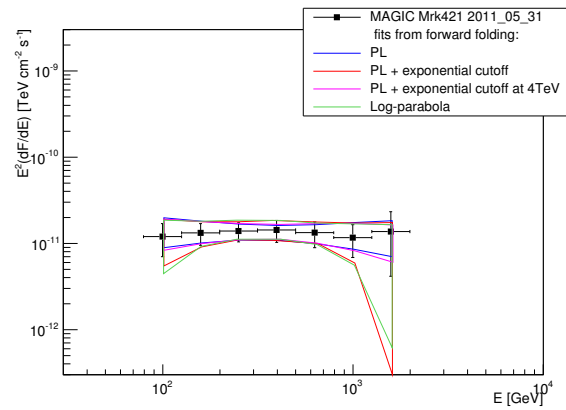
(c) 2011.05.23



(d) 2011.05.25



(e) 2011.05.29



(f) 2011.05.31

Figure B.13.: Mrk 421 daily VHE spectra from MAGIC during 2010 and 2011. The fit functions are explained in Section 4.2. The resulted fit parameters are listed in Tables B.1 to B.4.

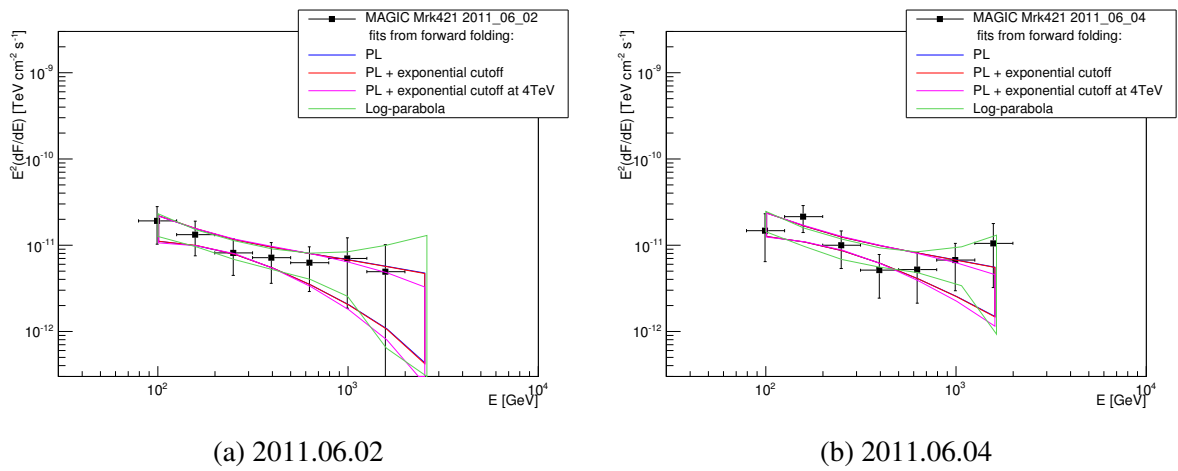


Figure B.14.: Mrk 421 daily VHE spectra from MAGIC during 2010 and 2011. The fit functions are explained in Section 4.2. The resulted fit parameters are listed in Tables B.1 to B.4.

Table B.1. Fit Parameters from the Fit Function 4.1 (power-law) for the MAGIC daily spectra during 2010 and 2011 in Figures B.1 to B.14.

Date	$f_0[\text{TeV cm}^{-2}\text{s}^{-1}]$	α	χ^2/ndf	Prob.	Sig.
2010.01.08	$(6.79 \pm 0.32) \times 10^{-11}$	-2.23 ± 0.03	47.1/12	4.3×10^{-6}	4.59
2010.01.11	$(7.40 \pm 0.27) \times 10^{-11}$	-2.33 ± 0.02	71.5/14	1.0×10^{-9}	6.11
2010.01.12	$(4.86 \pm 0.52) \times 10^{-11}$	-2.43 ± 0.06	15.6/12	2.1×10^{-1}	1.25
2010.01.13	$(4.22 \pm 0.32) \times 10^{-11}$	-2.32 ± 0.04	20.9/13	7.4×10^{-2}	1.78
2010.01.14	$(9.22 \pm 0.21) \times 10^{-11}$	-2.18 ± 0.01	136./13	8.8×10^{-23}	9.82
2010.01.15	$(7.11 \pm 0.27) \times 10^{-11}$	-2.17 ± 0.02	41.8/13	6.8×10^{-5}	3.98
2010.01.16	$(3.82 \pm 0.41) \times 10^{-11}$	-2.30 ± 0.07	12.2/12	4.2×10^{-1}	0.79
2010.01.18	$(1.54 \pm 0.31) \times 10^{-11}$	-2.51 ± 0.13	10.5/9	3.1×10^{-1}	1.01
2010.01.19	$(5.92 \pm 0.43) \times 10^{-11}$	-2.06 ± 0.05	16.5/12	1.6×10^{-1}	1.37
2010.01.20	$(9.15 \pm 0.19) \times 10^{-11}$	-2.11 ± 0.01	129./12	6.2×10^{-22}	9.63
2010.01.21	$(4.94 \pm 0.41) \times 10^{-11}$	-2.26 ± 0.05	13.0/10	2.2×10^{-1}	1.23
2010.01.22	$(4.03 \pm 0.64) \times 10^{-11}$	-2.07 ± 0.13	7.0/8	5.3×10^{-1}	0.62
2010.01.23	$(3.27 \pm 0.33) \times 10^{-11}$	-2.14 ± 0.07	16.3/12	1.7×10^{-1}	1.36
2010.01.24	$(5.29 \pm 0.35) \times 10^{-11}$	-2.14 ± 0.05	20.7/11	3.6×10^{-2}	2.09
2010.01.25	$(4.88 \pm 0.18) \times 10^{-11}$	-2.15 ± 0.02	30.4/13	4.0×10^{-3}	2.88
2010.01.26	$(4.21 \pm 0.53) \times 10^{-11}$	-2.35 ± 0.09	16.0/11	1.3×10^{-1}	1.48
2010.02.05	$(3.21 \pm 10.2) \times 10^{-11}$	-2.44 ± 2.84	0.2/3	9.7×10^{-1}	0.03
2010.02.07	$(2.83 \pm 0.27) \times 10^{-11}$	-2.27 ± 0.06	14.0/10	1.7×10^{-1}	1.37
2010.02.10	$(3.91 \pm 0.62) \times 10^{-11}$	-2.15 ± 0.11	12.9/10	2.2×10^{-1}	1.21
2010.02.11	$(2.70 \pm 0.29) \times 10^{-11}$	-2.23 ± 0.06	15.9/12	1.9×10^{-1}	1.30
2010.02.13	$(2.10 \pm 0.68) \times 10^{-11}$	-2.47 ± 0.17	5.5/10	8.5×10^{-1}	0.18
2010.03.10	$(5.99 \pm 0.35) \times 10^{-11}$	-2.14 ± 0.03	17.2/14	2.4×10^{-1}	1.17
2010.03.11	$(6.76 \pm 0.27) \times 10^{-11}$	-2.18 ± 0.02	60.6/13	3.9×10^{-8}	5.49
2010.03.13	$(3.61 \pm 0.73) \times 10^{-11}$	-2.15 ± 0.13	9.6/11	5.6×10^{-1}	0.58
2010.03.14	$(5.78 \pm 0.80) \times 10^{-11}$	-2.12 ± 0.09	9.2/11	6.0×10^{-1}	0.52
2010.03.15	$(3.62 \pm 0.47) \times 10^{-11}$	-2.29 ± 0.08	4.7/11	9.4×10^{-1}	0.07
2010.03.17	$(1.91 \pm 0.26) \times 10^{-11}$	-2.28 ± 0.08	18.5/10	4.6×10^{-2}	2.00
2010.03.18	$(2.54 \pm 0.58) \times 10^{-11}$	-2.22 ± 0.15	7.5/11	7.5×10^{-1}	0.32
2010.03.19	$(1.54 \pm 1.32) \times 10^{-11}$	-2.42 ± 0.51	1.1/4	8.8×10^{-1}	0.15
2010.03.20	$(3.70 \pm 4.33) \times 10^{-12}$	-2.39 ± 0.64	4.9/11	9.3×10^{-1}	0.09
2010.03.21	$(2.33 \pm 0.32) \times 10^{-11}$	-2.32 ± 0.08	10.2/10	4.2×10^{-1}	0.81
2010.03.22	$(1.50 \pm 0.19) \times 10^{-11}$	-2.50 ± 0.07	11.3/11	4.1×10^{-1}	0.82
2010.04.02	$(2.03 \pm 0.59) \times 10^{-11}$	-2.05 ± 0.21	5.8/10	8.2×10^{-1}	0.22
2010.04.03	$(1.82 \pm 0.25) \times 10^{-11}$	-2.21 ± 0.08	17.2/11	1.0×10^{-1}	1.64
2010.04.05	$(1.75 \pm 0.42) \times 10^{-11}$	-2.15 ± 0.19	3.1/8	9.2×10^{-1}	0.10
2010.04.07	$(2.17 \pm 0.50) \times 10^{-11}$	-1.90 ± 0.18	7.1/8	5.2×10^{-1}	0.64
2010.04.08	$(1.48 \pm 1.97) \times 10^{-11}$	-1.78 ± 0.89	6.5/8	5.9×10^{-1}	0.54
2010.04.11	$(6.15 \pm 4.33) \times 10^{-12}$	-2.66 ± 0.44	4.5/9	8.7×10^{-1}	0.16
2010.04.12	$(5.87 \pm 3.76) \times 10^{-12}$	-2.71 ± 0.38	1.9/7	9.6×10^{-1}	0.05
2010.04.18	$(2.88 \pm 0.24) \times 10^{-11}$	-2.20 ± 0.05	52.1/12	5.9×10^{-7}	4.99
2010.04.19	$(1.00 \pm 101.) \times 10^{-15}$	-5.49 ± 0.93	0.1/13	$1.0 \times 10^{+0}$	0.00
2010.05.04	$(2.62 \pm 12.5) \times 10^{-11}$	-1.53 ± 2.85	0.3/5	9.9×10^{-1}	0.00
2010.05.05	$(2.64 \pm 0.51) \times 10^{-11}$	-2.17 ± 0.13	5.6/8	6.9×10^{-1}	0.40
2010.05.06	$(2.77 \pm 0.37) \times 10^{-11}$	-2.21 ± 0.08	11.7/10	3.0×10^{-1}	1.03
2010.05.07	$(3.37 \pm 0.49) \times 10^{-11}$	-2.11 ± 0.09	9.3/12	6.7×10^{-1}	0.42
2010.05.15	$(2.51 \pm 2.04) \times 10^{-11}$	-1.75 ± 0.70	5.4/9	7.9×10^{-1}	0.26
2010.05.16	$(1.50 \pm 0.17) \times 10^{-11}$	-2.36 ± 0.07	15.4/11	1.6×10^{-1}	1.39
2010.05.17	$(3.77 \pm 0.39) \times 10^{-11}$	-2.23 ± 0.06	11.9/12	4.4×10^{-1}	0.76
2010.05.18	$(3.49 \pm 0.22) \times 10^{-11}$	-2.03 ± 0.04	32.7/12	1.0×10^{-3}	3.27
2010.05.19	$(2.79 \pm 0.74) \times 10^{-11}$	-2.38 ± 0.15	8.9/9	4.4×10^{-1}	0.76
2010.05.30	$(2.45 \pm 0.57) \times 10^{-11}$	-2.40 ± 0.13	18.1/12	1.1×10^{-1}	1.59
2010.05.31	$(1.37 \pm 0.18) \times 10^{-11}$	-2.36 ± 0.09	10.4/12	5.8×10^{-1}	0.55
2010.06.01	$(6.65 \pm 4.89) \times 10^{-12}$	-2.28 ± 0.46	1.3/11	$1.0 \times 10^{+0}$	0.00
2010.06.02	$(1.13 \pm 1.43) \times 10^{-12}$	-3.39 ± 0.60	11.1/8	1.9×10^{-1}	1.30
2010.06.03	$(4.73 \pm 1.95) \times 10^{-12}$	-2.64 ± 0.24	5.0/8	7.5×10^{-1}	0.32

Table B.1 (cont'd)

Date	$f_0[\text{TeV cm}^{-2}\text{s}^{-1}]$	α	χ^2/ndf	Prob.	Sig.
2010.06.04	$(1.90 \pm 2.01) \times 10^{-12}$	-2.94 ± 0.55	11.3/10	3.2×10^{-1}	0.98
2010.06.05	$(5.57 \pm 1.23) \times 10^{-12}$	-2.49 ± 0.14	13.3/11	2.7×10^{-1}	1.10
2010.06.06	$(7.14 \pm 3.80) \times 10^{-12}$	-2.39 ± 0.37	8.2/9	5.1×10^{-1}	0.66
2010.06.07	$(6.57 \pm 3.25) \times 10^{-12}$	-2.61 ± 0.30	9.7/8	2.8×10^{-1}	1.08
2010.06.08	$(8.52 \pm 3.45) \times 10^{-12}$	-2.26 ± 0.30	4.3/7	7.3×10^{-1}	0.34
2010.06.09	$(7.74 \pm 2.42) \times 10^{-12}$	-2.54 ± 0.20	12.9/11	2.9×10^{-1}	1.05
2010.06.10	$(9.03 \pm 1.78) \times 10^{-12}$	-2.39 ± 0.15	9.5/13	7.2×10^{-1}	0.35
2010.06.11	$(1.54 \pm 466.) \times 10^{-12}$	-1.22 ± 14.2	0.3/13	$1.0 \times 10^{+0}$	0.00
2010.06.12	$(7.05 \pm 4.15) \times 10^{-12}$	-2.58 ± 0.37	5.2/10	8.7×10^{-1}	0.16
2010.06.13	$(9.84 \pm 18.6) \times 10^{-13}$	-3.43 ± 1.04	10.2/7	1.7×10^{-1}	1.36
2010.06.14	$(4.52 \pm 3.33) \times 10^{-12}$	-2.86 ± 0.42	5.6/8	6.8×10^{-1}	0.40
2010.06.16	$(6.94 \pm 4.72) \times 10^{-12}$	-2.45 ± 0.46	2.6/10	9.8×10^{-1}	0.01
2011.01.11	$(1.13 \pm 0.17) \times 10^{-11}$	-2.65 ± 0.08	12.9/9	1.6×10^{-1}	1.38
2011.01.17	$(8.80 \pm 2.22) \times 10^{-12}$	-2.72 ± 0.14	3.6/8	8.8×10^{-1}	0.14
2011.02.06	$(6.24 \pm 3.21) \times 10^{-12}$	-2.51 ± 0.32	2.5/7	9.2×10^{-1}	0.10
2011.02.07	$(3.76 \pm 5.77) \times 10^{-12}$	-2.52 ± 0.85	1.7/3	6.1×10^{-1}	0.50
2011.02.08	$(5.85 \pm 7.56) \times 10^{-13}$	-3.53 ± 0.55	9.7/8	2.8×10^{-1}	1.07
2011.02.23	$(1.50 \pm 3.00) \times 10^{-13}$	-4.49 ± 0.84	8.5/6	1.9×10^{-1}	1.29
2011.03.01	$(4.17 \pm 1.33) \times 10^{-12}$	-2.88 ± 0.17	3.8/6	6.9×10^{-1}	0.40
2011.03.23	$(1.14 \pm 0.25) \times 10^{-11}$	-2.56 ± 0.17	6.0/8	6.3×10^{-1}	0.47
2011.03.29	$(1.26 \pm 0.10) \times 10^{-11}$	-2.59 ± 0.05	22.6/10	1.2×10^{-2}	2.50
2011.04.04	$(1.93 \pm 0.15) \times 10^{-11}$	-2.32 ± 0.05	12.0/9	2.1×10^{-1}	1.25
2011.04.10	$(1.66 \pm 0.13) \times 10^{-11}$	-2.51 ± 0.04	15.2/12	2.3×10^{-1}	1.20
2011.04.25	$(3.82 \pm 0.78) \times 10^{-12}$	-2.81 ± 0.12	17.3/8	2.6×10^{-2}	2.21
2011.05.05	$(2.64 \pm 1.44) \times 10^{-12}$	-3.04 ± 0.27	5.9/7	5.4×10^{-1}	0.60
2011.05.07	$(5.15 \pm 1.53) \times 10^{-12}$	-2.65 ± 0.17	9.7/8	2.8×10^{-1}	1.08
2011.05.23	$(1.48 \pm 0.20) \times 10^{-11}$	-2.46 ± 0.08	6.5/12	8.8×10^{-1}	0.15
2011.05.25	$(1.75 \pm 0.23) \times 10^{-11}$	-2.25 ± 0.09	11.1/10	3.4×10^{-1}	0.95
2011.05.29	$(9.11 \pm 2.15) \times 10^{-12}$	-2.45 ± 0.15	3.1/8	9.2×10^{-1}	0.10
2011.05.31	$(1.29 \pm 0.45) \times 10^{-11}$	-2.04 ± 0.28	4.5/8	8.0×10^{-1}	0.24
2011.06.02	$(4.41 \pm 2.53) \times 10^{-12}$	-2.57 ± 0.36	4.5/9	8.6×10^{-1}	0.16
2011.06.04	$(4.64 \pm 2.24) \times 10^{-12}$	-2.59 ± 0.31	9.1/9	4.2×10^{-1}	0.80

Note. — Prob. is the probability for χ^2 to be larger; if it is smaller than 0.05, the model significantly (with a 95% confidence level) deviates from the data. Sig. is the significance of the deviation, in unit of σ .

Table B.2. Fit Parameters from the Fit Function 4.2 (power-law with an exponential cutoff) for the MAGIC daily spectra during 2010 and 2011 in Figures B.1 to B.14.

Date	$f_0[\text{TeV cm}^{-2}\text{s}^{-1}]$	α	$E_0[\text{TeV}]$	χ^2/ndf	Prob.	Sig.
2010.01.08	$(1.40 \pm 0.11) \times 10^{-09}$	-1.80 ± 0.09	$(1.44 \pm 0.34) \times 10^{+0}$	11.6/11	3.8×10^{-1}	0.86
2010.01.11	$(1.74 \pm 0.10) \times 10^{-09}$	-1.96 ± 0.05	$(1.51 \pm 0.27) \times 10^{+0}$	12.2/13	5.0×10^{-1}	0.67
2010.01.12	$(1.46 \pm 0.41) \times 10^{-09}$	-2.03 ± 0.23	$(8.96 \pm 5.63) \times 10^{-1}$	11.1/11	4.2×10^{-1}	0.79
2010.01.13	$(1.06 \pm 0.21) \times 10^{-09}$	-1.89 ± 0.18	$(1.06 \pm 0.52) \times 10^{+0}$	11.5/12	4.8×10^{-1}	0.70
2010.01.14	$(1.67 \pm 0.05) \times 10^{-09}$	-1.84 ± 0.03	$(2.05 \pm 0.25) \times 10^{+0}$	8.6/12	7.3×10^{-1}	0.34
2010.01.15	$(1.12 \pm 0.05) \times 10^{-09}$	-1.98 ± 0.05	$(3.68 \pm 1.05) \times 10^{+0}$	23.2/12	2.5×10^{-2}	2.23
2010.01.16	$(1.02 \pm 0.33) \times 10^{-09}$	-1.76 ± 0.30	$(8.14 \pm 5.33) \times 10^{-1}$	6.1/11	8.6×10^{-1}	0.17
2010.01.18	$(3.83 \pm 1.96) \times 10^{-10}$	-2.34 ± 0.42	$(2.03 \pm 5.25) \times 10^{+0}$	10.3/8	2.4×10^{-1}	1.16
2010.01.19	$(7.93 \pm 0.72) \times 10^{-10}$	-1.86 ± 0.13	$(3.87 \pm 2.60) \times 10^{+0}$	13.4/11	2.6×10^{-1}	1.12
2010.01.20	$(1.46 \pm 0.04) \times 10^{-09}$	-1.77 ± 0.03	$(2.23 \pm 0.27) \times 10^{+0}$	7.5/11	7.5×10^{-1}	0.31
2010.01.21	$(8.54 \pm 1.14) \times 10^{-10}$	-2.11 ± 0.15	$(3.49 \pm 3.42) \times 10^{+0}$	11.9/9	2.1×10^{-1}	1.24
2010.01.22	$(4.93 \pm 0.52) \times 10^{-10}$	-2.07 ± 0.13	$(9.99 \pm 9.26) \times 10^{+1}$	7.0/7	4.2×10^{-1}	0.79
2010.01.23	$(5.37 \pm 0.93) \times 10^{-10}$	-1.82 ± 0.23	$(1.92 \pm 1.45) \times 10^{+0}$	13.6/11	2.5×10^{-1}	1.15
2010.01.24	$(8.76 \pm 0.96) \times 10^{-10}$	-1.72 ± 0.16	$(1.77 \pm 0.76) \times 10^{+0}$	9.6/10	4.7×10^{-1}	0.72
2010.01.25	$(7.47 \pm 0.34) \times 10^{-10}$	-1.89 ± 0.06	$(3.34 \pm 0.91) \times 10^{+0}$	8.9/12	7.1×10^{-1}	0.37
2010.01.26	$(7.19 \pm 0.55) \times 10^{-10}$	-2.34 ± 0.09	$(9.99 \pm 5.41) \times 10^{+1}$	16.0/10	9.8×10^{-2}	1.65
2010.02.05	$(6.16 \pm 5.29) \times 10^{-10}$	-2.44 ± 2.84	$(9.97 \pm 5.02) \times 10^{+1}$	0.2/2	8.9×10^{-1}	0.14
2010.02.07	$(6.34 \pm 1.35) \times 10^{-10}$	-1.88 ± 0.21	$(1.17 \pm 0.68) \times 10^{+0}$	9.2/9	4.1×10^{-1}	0.82
2010.02.10	$(5.60 \pm 1.32) \times 10^{-10}$	-2.08 ± 0.25	$(6.48 \pm 19.0) \times 10^{+0}$	12.8/9	1.7×10^{-1}	1.37
2010.02.11	$(6.54 \pm 1.56) \times 10^{-10}$	-1.72 ± 0.24	$(8.80 \pm 4.37) \times 10^{-1}$	9.1/11	6.1×10^{-1}	0.51
2010.02.13	$(6.55 \pm 5.05) \times 10^{-10}$	-2.12 ± 0.60	$(8.40 \pm 14.6) \times 10^{-1}$	5.0/9	8.3×10^{-1}	0.21
2010.03.10	$(9.92 \pm 0.86) \times 10^{-10}$	-1.83 ± 0.10	$(2.15 \pm 0.79) \times 10^{+0}$	4.1/13	9.9×10^{-1}	0.01
2010.03.11	$(1.28 \pm 0.08) \times 10^{-09}$	-1.77 ± 0.07	$(1.62 \pm 0.33) \times 10^{+0}$	12.2/12	4.2×10^{-1}	0.80
2010.03.13	$(6.09 \pm 2.08) \times 10^{-10}$	-1.88 ± 0.38	$(1.79 \pm 2.57) \times 10^{+0}$	8.9/10	5.4×10^{-1}	0.61
2010.03.14	$(9.37 \pm 1.85) \times 10^{-10}$	-1.80 ± 0.25	$(1.81 \pm 1.47) \times 10^{+0}$	7.0/10	7.2×10^{-1}	0.35
2010.03.15	$(7.84 \pm 2.12) \times 10^{-10}$	-1.96 ± 0.27	$(1.36 \pm 1.19) \times 10^{+0}$	2.4/10	9.9×10^{-1}	0.01
2010.03.17	$(6.80 \pm 3.29) \times 10^{-10}$	-1.59 ± 0.39	$(4.96 \pm 3.17) \times 10^{-1}$	12.4/9	1.8×10^{-1}	1.32
2010.03.18	$(6.11 \pm 3.55) \times 10^{-10}$	-1.74 ± 0.54	$(7.88 \pm 9.39) \times 10^{-1}$	6.3/10	7.8×10^{-1}	0.27
2010.03.19	$(3.24 \pm 14.3) \times 10^{-09}$	-0.50 ± 3.41	$(1.35 \pm 4.46) \times 10^{-1}$	0.6/3	8.7×10^{-1}	0.15
2010.03.20	$(6.68 \pm 3.05) \times 10^{-11}$	-2.39 ± 0.64	$(1.00 \pm 0.96) \times 10^{+2}$	4.9/10	8.9×10^{-1}	0.14
2010.03.21	$(4.92 \pm 1.28) \times 10^{-10}$	-2.11 ± 0.22	$(1.72 \pm 1.82) \times 10^{+0}$	8.9/9	4.4×10^{-1}	0.77
2010.03.22	$(3.40 \pm 0.68) \times 10^{-10}$	-2.40 ± 0.17	$(4.03 \pm 7.03) \times 10^{+0}$	11.0/10	3.5×10^{-1}	0.93
2010.04.02	$(2.88 \pm 1.15) \times 10^{-10}$	-1.80 ± 0.57	$(2.29 \pm 4.99) \times 10^{+0}$	5.6/9	7.7×10^{-1}	0.29
2010.04.03	$(3.80 \pm 1.04) \times 10^{-10}$	-1.85 ± 0.27	$(1.16 \pm 8.76) \times 10^{+0}$	14.6/10	1.4×10^{-1}	1.46
2010.04.05	$(5.21 \pm 6.12) \times 10^{-10}$	-1.18 ± 1.30	$(4.53 \pm 6.77) \times 10^{-1}$	2.1/7	9.5×10^{-1}	0.06
2010.04.07	$(5.02 \pm 3.98) \times 10^{-10}$	-0.94 ± 0.88	$(4.51 \pm 4.36) \times 10^{-1}$	5.1/7	6.4×10^{-1}	0.47
2010.04.08	$(3.40 \pm 2.10) \times 10^{-09}$	0.84 ± 1.51	$(1.00 \pm 16.3) \times 10^{-1}$	6.5/7	4.7×10^{-1}	0.71
2010.04.11	$(1.52 \pm 0.36) \times 10^{-10}$	-2.66 ± 0.44	$(1.00 \pm 0.51) \times 10^{+2}$	4.5/8	8.0×10^{-1}	0.25
2010.04.12	$(1.54 \pm 0.38) \times 10^{-10}$	-2.71 ± 0.38	$(9.99 \pm 9.58) \times 10^{+1}$	1.9/6	9.2×10^{-1}	0.10
2010.04.18	$(5.35 \pm 0.79) \times 10^{-10}$	-1.92 ± 0.15	$(1.69 \pm 0.93) \times 10^{+0}$	47.4/11	1.8×10^{-6}	4.78
2010.04.19	$(1.01 \pm 0.04) \times 10^{-15}$	-9.14 ± 2.29	$(1.00 \pm 668.) \times 10^{-1}$	0.0/12	$1.0 \times 10^{+0}$	0.00
2010.05.04	$(5.39 \pm 9.55) \times 10^{-09}$	1.35 ± 4.46	$(1.00 \pm 26.8) \times 10^{-1}$	0.2/4	9.9×10^{-1}	0.01
2010.05.05	$(5.49 \pm 2.38) \times 10^{-10}$	-1.72 ± 0.44	$(9.50 \pm 9.91) \times 10^{-1}$	4.0/7	7.7×10^{-1}	0.29
2010.05.06	$(4.51 \pm 1.18) \times 10^{-10}$	-2.09 ± 0.24	$(3.43 \pm 6.78) \times 10^{+0}$	11.4/9	2.4×10^{-1}	1.15
2010.05.07	$(8.69 \pm 4.62) \times 10^{-10}$	-1.50 ± 0.45	$(6.09 \pm 5.00) \times 10^{-1}$	5.7/11	8.8×10^{-1}	0.14
2010.05.15	$(5.11 \pm 18.8) \times 10^{-10}$	-0.25 ± 5.46	$(3.68 \pm 22.3) \times 10^{-1}$	5.3/8	7.2×10^{-1}	0.36
2010.05.16	$(4.92 \pm 1.38) \times 10^{-10}$	-1.72 ± 0.27	$(6.53 \pm 3.02) \times 10^{-1}$	6.4/10	7.7×10^{-1}	0.28
2010.05.17	$(8.15 \pm 1.69) \times 10^{-10}$	-1.84 ± 0.20	$(1.17 \pm 0.65) \times 10^{+0}$	6.4/11	8.4×10^{-1}	0.20
2010.05.18	$(5.62 \pm 0.61) \times 10^{-10}$	-1.66 ± 0.11	$(1.51 \pm 0.51) \times 10^{+0}$	17.5/11	9.3×10^{-2}	1.68
2010.05.19	$(2.40 \pm 2.39) \times 10^{-09}$	-1.05 ± 0.83	$(2.35 \pm 1.60) \times 10^{-1}$	4.1/8	8.4×10^{-1}	0.19
2010.05.30	$(1.19 \pm 1.30) \times 10^{-09}$	-1.57 ± 0.90	$(3.90 \pm 4.61) \times 10^{-1}$	16.7/11	1.1×10^{-1}	1.58
2010.05.31	$(3.50 \pm 0.89) \times 10^{-10}$	-1.82 ± 3.34	$(1.05 \pm 0.69) \times 10^{+0}$	6.2/11	8.5×10^{-1}	0.18
2010.06.01	$(2.98 \pm 7.77) \times 10^{-10}$	-1.27 ± 2.37	$(3.54 \pm 9.27) \times 10^{-1}$	1.0/10	$1.0 \times 10^{+0}$	0.00
2010.06.02	$(6.76 \pm 3.78) \times 10^{-11}$	-3.39 ± 0.60	$(9.99 \pm 8.31) \times 10^{+1}$	11.1/7	1.3×10^{-1}	1.51
2010.06.03	$(3.16 \pm 0.74) \times 10^{-09}$	-0.32 ± 0.42	$(1.00 \pm 1.08) \times 10^{-1}$	2.49/7	9.2×10^{-1}	0.09

Table B.2 (cont'd)

Date	$f_0[\text{TeV cm}^{-2}\text{s}^{-1}]$	α	$E_0[\text{TeV}]$	χ^2/ndf	Prob.	Sig.
2010.06.04	$(6.66 \pm 3.01) \times 10^{-11}$	-2.94 ± 0.55	$(9.93 \pm 5.00) \times 10^{+1}$	11.3/9	2.5×10^{-1}	1.15
2010.06.05	$(3.83 \pm 3.03) \times 10^{-10}$	-1.24 ± 0.78	$(3.19 \pm 2.24) \times 10^{-1}$	7.9/10	6.3×10^{-1}	0.48
2010.06.06	$(1.27 \pm 0.2) \times 10^{-10}$	-2.38 ± 0.37	$(1.00 \pm 0.65) \times 10^{+2}$	8.2/8	4.1×10^{-1}	0.82
2010.06.07	$(1.96 \pm 2.31) \times 10^{-10}$	-2.38 ± 1.07	$(1.48 \pm 8.03) \times 10^{+0}$	9.7/7	2.0×10^{-1}	1.27
2010.06.08	$(4.78 \pm 7.86) \times 10^{-10}$	-0.76 ± 1.85	$(2.75 \pm 3.63) \times 10^{-1}$	2.9/6	8.1×10^{-1}	0.23
2010.06.09	$(5.58 \pm 0.93) \times 10^{-09}$	0.43 ± 0.42	$(1.00 \pm 0.86) \times 10^{-1}$	7.5/10	6.7×10^{-1}	0.42
2010.06.10	$(2.05 \pm 0.62) \times 10^{-10}$	-1.98 ± 0.44	$(1.59 \pm 1.87) \times 10^{+0}$	8.1/12	7.7×10^{-1}	0.28
2010.06.11	$(0.00 \pm 1.32) \times 10^{-08}$	-1.09 ± 14.4	$(1.00 \pm 710.) \times 10^{-1}$	0.3/12	$1.0 \times 10^{+0}$	0.00
2010.06.12	$(4.66 \pm 1.39) \times 10^{-09}$	0.06 ± 0.68	$(1.00 \pm 2.00) \times 10^{-1}$	3.6/9	9.3×10^{-1}	0.08
2010.06.13	$(6.19 \pm 4.23) \times 10^{-11}$	-3.43 ± 1.05	$(9.98 \pm 9.92) \times 10^{+1}$	10.2/6	1.1×10^{-1}	1.58
2010.06.14	$(3.85 \pm 1.44) \times 10^{-09}$	-0.54 ± 0.66	$(1.00 \pm 0.76) \times 10^{-1}$	3.4/7	8.3×10^{-1}	0.20
2010.06.16	$(2.00 \pm 57.1) \times 10^{-09}$	0.09 ± 6.40	$(1.28 \pm 13.4) \times 10^{-1}$	2.0/9	9.9×10^{-1}	0.01
2011.01.11	$(6.67 \pm 2.78) \times 10^{-10}$	-1.99 ± 0.31	$(4.39 \pm 2.24) \times 10^{-1}$	5.6/8	6.8×10^{-1}	0.41
2011.01.17	$(2.80 \pm 1.38) \times 10^{-10}$	-2.58 ± 0.40	$(2.09 \pm 5.54) \times 10^{+0}$	3.4/7	8.3×10^{-1}	0.21
2011.02.06	$(4.81 \pm 9.03) \times 10^{-10}$	-1.27 ± 1.72	$(2.72 \pm 4.05) \times 10^{-1}$	1.7/6	9.4×10^{-1}	0.07
2011.02.07	$(7.91 \pm 4.46) \times 10^{-11}$	-2.52 ± 0.85	$(9.98 \pm 5.52) \times 10^{+1}$	1.7/2	4.1×10^{-1}	0.82
2011.02.08	$(4.12 \pm 2.90) \times 10^{-11}$	-3.53 ± 0.56	$(8.24 \pm 5.40) \times 10^{+1}$	9.7/7	2.0×10^{-1}	1.26
2011.02.23	$(2.98 \pm 2.97) \times 10^{-11}$	-4.52 ± 0.84	$(1.00 \pm 0.59) \times 10^{+2}$	8.8/5	1.1×10^{-1}	1.57
2011.03.01	$(3.48 \pm 3.14) \times 10^{-10}$	-2.19 ± 0.66	$(3.73 \pm 3.66) \times 10^{-1}$	2.3/5	7.9×10^{-1}	0.26
2011.03.23	$(3.16 \pm 1.46) \times 10^{-10}$	-2.27 ± 0.55	$(1.57 \pm 2.96) \times 10^{+0}$	5.7/7	5.7×10^{-1}	0.57
2011.03.29	$(5.82 \pm 1.46) \times 10^{-10}$	-1.96 ± 0.21	$(5.98 \pm 2.29) \times 10^{-1}$	7.5/9	5.8×10^{-1}	0.55
2011.04.04	$(3.94 \pm 0.69) \times 10^{-10}$	-2.10 ± 0.18	$(1.92 \pm 1.53) \times 10^{+0}$	10.4/8	2.3×10^{-1}	1.19
2011.04.10	$(4.27 \pm 0.62) \times 10^{-10}$	-2.31 ± 0.13	$(2.17 \pm 1.49) \times 10^{+0}$	11.9/11	3.6×10^{-1}	0.90
2011.04.25	$(7.11 \pm 10.1) \times 10^{-10}$	-1.39 ± 1.06	$(1.93 \pm 1.61) \times 10^{-1}$	13.3/7	6.5×10^{-2}	1.84
2011.05.05	$(1.23 \pm 1.39) \times 10^{-10}$	-2.91 ± 0.80	$(1.92 \pm 17.1) \times 10^{+0}$	5.9/6	4.3×10^{-1}	0.78
2011.05.07	$(5.82 \pm 8.36) \times 10^{-10}$	-1.50 ± 1.04	$(2.30 \pm 2.33) \times 10^{-1}$	7.6/7	3.6×10^{-1}	0.91
2011.05.23	$(4.38 \pm 1.34) \times 10^{-10}$	-2.10 ± 0.26	$(9.89 \pm 7.45) \times 10^{-1}$	3.7/11	9.7×10^{-1}	0.03
2011.05.25	$(4.26 \pm 1.47) \times 10^{-10}$	-1.77 ± 0.35	$(8.50 \pm 6.25) \times 10^{-1}$	8.6/9	4.7×10^{-1}	0.72
2011.05.29	$(2.59 \pm 1.39) \times 10^{-10}$	-2.09 ± 0.51	$(1.00 \pm 1.39) \times 10^{+0}$	2.4/7	9.2×10^{-1}	0.09
2011.05.31	$(2.12 \pm 1.67) \times 10^{-10}$	-1.67 ± 0.90	$(1.13 \pm 2.62) \times 10^{+0}$	4.2/7	7.4×10^{-1}	0.32
2011.06.02	$(9.83 \pm 2.21) \times 10^{-11}$	-2.57 ± 0.36	$(9.99 \pm 9.95) \times 10^{+1}$	4.5/8	8.0×10^{-1}	0.25
2011.06.04	$(1.05 \pm 0.21) \times 10^{-10}$	-2.59 ± 0.31	$(1.00 \pm 0.89) \times 10^{+2}$	9.1/8	3.3×10^{-1}	0.97

Note. — See the comments under Table B.1 for detail explanation.

Table B.3. Fit Parameters from the Fit Function 4.3 (power-law with the exponential cutoff fixed at 4 TeV) for the MAGIC daily spectra during 2010 and 2011 in Figures B.1 to B.14.

Date	$f_0[\text{TeV cm}^{-2}\text{s}^{-1}]$	α	χ^2/ndf	Prob.	Sig.
2010.01.08	$(1.14 \pm 0.03) \times 10^{-09}$	-2.05 ± 0.03	22.8/12	2.8×10^{-2}	2.19
2010.01.11	$(1.42 \pm 0.03) \times 10^{-09}$	-2.17 ± 0.02	29.9/14	7.8×10^{-3}	2.66
2010.01.12	$(1.01 \pm 0.06) \times 10^{-09}$	-2.33 ± 0.06	13.3/12	3.4×10^{-1}	0.95
2010.01.13	$(7.84 \pm 0.37) \times 10^{-10}$	-2.19 ± 0.05	15.3/13	2.8×10^{-1}	1.06
2010.01.14	$(1.49 \pm 0.02) \times 10^{-09}$	-1.99 ± 0.01	30.5/13	3.9×10^{-3}	2.89
2010.01.15	$(1.11 \pm 0.03) \times 10^{-09}$	-1.99 ± 0.02	23.3/13	3.7×10^{-2}	2.08
2010.01.16	$(6.85 \pm 0.47) \times 10^{-10}$	-2.17 ± 0.07	9.1/12	6.8×10^{-1}	0.40
2010.01.18	$(3.49 \pm 0.35) \times 10^{-10}$	-2.42 ± 0.13	10.3/9	3.2×10^{-1}	0.99
2010.01.19	$(7.91 \pm 0.46) \times 10^{-10}$	-1.87 ± 0.06	13.4/12	3.3×10^{-1}	0.96
2010.01.20	$(1.34 \pm 0.02) \times 10^{-09}$	-1.90 ± 0.01	24.4/12	1.7×10^{-2}	2.38
2010.01.21	$(8.41 \pm 0.41) \times 10^{-10}$	-2.12 ± 0.06	11.9/10	2.8×10^{-1}	1.06
2010.01.22	$(5.39 \pm 0.58) \times 10^{-10}$	-1.92 ± 0.14	7.3/8	5.0×10^{-1}	0.67
2010.01.23	$(4.82 \pm 0.36) \times 10^{-10}$	-1.98 ± 0.08	14.2/12	2.8×10^{-1}	1.07
2010.01.24	$(7.76 \pm 0.45) \times 10^{-10}$	-1.93 ± 0.05	12.1/11	3.5×10^{-1}	0.93
2010.01.25	$(7.32 \pm 0.23) \times 10^{-10}$	-1.93 ± 0.03	9.3/13	7.4×10^{-1}	0.32
2010.01.26	$(7.93 \pm 0.61) \times 10^{-10}$	-2.21 ± 0.10	16.7/11	1.1×10^{-1}	1.57
2010.02.05	$(6.65 \pm 5.71) \times 10^{-10}$	-2.34 ± 2.90	0.2/3	9.7×10^{-1}	0.04
2010.02.07	$(4.91 \pm 0.28) \times 10^{-10}$	-2.15 ± 0.06	11.3/10	3.3×10^{-1}	0.97
2010.02.10	$(5.82 \pm 0.53) \times 10^{-10}$	-2.04 ± 0.12	12.8/10	2.3×10^{-1}	1.20
2010.02.11	$(4.46 \pm 0.29) \times 10^{-10}$	-2.10 ± 0.07	12.8/12	3.7×10^{-1}	0.88
2010.02.13	$(4.61 \pm 0.69) \times 10^{-10}$	-2.40 ± 0.18	5.3/10	8.7×10^{-1}	0.16
2010.03.10	$(9.02 \pm 0.38) \times 10^{-10}$	-1.96 ± 0.04	6.1/14	9.6×10^{-1}	0.05
2010.03.11	$(1.08 \pm 0.03) \times 10^{-09}$	-1.99 ± 0.02	25.1/13	2.2×10^{-2}	2.28
2010.03.13	$(5.37 \pm 0.56) \times 10^{-10}$	-2.02 ± 0.14	9.1/11	6.1×10^{-1}	0.51
2010.03.14	$(8.29 \pm 0.70) \times 10^{-10}$	-1.97 ± 0.10	7.6/11	7.4×10^{-1}	0.32
2010.03.15	$(6.41 \pm 0.48) \times 10^{-10}$	-2.17 ± 0.09	3.3/11	9.8×10^{-1}	0.02
2010.03.17	$(3.36 \pm 0.26) \times 10^{-10}$	-2.18 ± 8.77	16.5/10	8.4×10^{-2}	1.72
2010.03.18	$(4.11 \pm 0.49) \times 10^{-10}$	-2.11 ± 0.15	7.0/11	7.9×10^{-1}	0.26
2010.03.19	$(3.13 \pm 1.00) \times 10^{-10}$	-2.35 ± 0.52	1.1/4	8.8×10^{-1}	0.14
2010.03.20	$(7.25 \pm 3.52) \times 10^{-11}$	-2.33 ± 0.70	5.1/11	9.2×10^{-1}	0.09
2010.03.21	$(4.29 \pm 0.32) \times 10^{-10}$	-2.23 ± 0.08	9.3/10	5.0×10^{-1}	0.67
2010.03.22	$(3.40 \pm 0.23) \times 10^{-10}$	-2.40 ± 0.08	11.0/11	4.4×10^{-1}	0.77
2010.04.02	$(2.68 \pm 0.42) \times 10^{-10}$	-1.91 ± 0.23	5.7/10	8.4×10^{-1}	0.20
2010.04.03	$(2.94 \pm 0.22) \times 10^{-10}$	-2.10 ± 0.09	15.8/11	1.4×10^{-1}	1.45
2010.04.05	$(2.57 \pm 0.38) \times 10^{-10}$	-2.02 ± 0.20	2.8/8	9.4×10^{-1}	0.07
2010.04.07	$(2.38 \pm 0.37) \times 10^{-10}$	-1.79 ± 0.19	6.6/8	5.7×10^{-1}	0.55
2010.04.08	$(1.38 \pm 0.74) \times 10^{-10}$	-1.71 ± 0.91	6.5/8	5.9×10^{-1}	0.54
2010.04.11	$(1.64 \pm 0.40) \times 10^{-10}$	-2.61 ± 0.47	4.8/9	8.4×10^{-1}	0.19
2010.04.12	$(1.68 \pm 0.42) \times 10^{-10}$	-2.65 ± 0.38	1.9/7	9.6×10^{-1}	0.05
2010.04.18	$(4.56 \pm 0.23) \times 10^{-10}$	-2.08 ± 0.05	48.5/13	5.2×10^{-6}	4.55
2010.04.19	$(1.00 \pm 388.) \times 10^{-15}$	-8.96 ± 1.15	0.0/13	$1.0 \times 10^{+0}$	0.00
2010.05.04	$(1.82 \pm 3.68) \times 10^{-10}$	-1.46 ± 2.88	0.3/5	9.9×10^{-1}	0.00
2010.05.05	$(4.01 \pm 0.43) \times 10^{-10}$	-2.05 ± 0.14	4.8/8	7.7×10^{-1}	0.29
2010.05.06	$(4.43 \pm 0.33) \times 10^{-10}$	-2.11 ± 0.09	11.4/10	3.2×10^{-1}	0.98
2010.05.07	$(4.87 \pm 0.44) \times 10^{-10}$	-2.00 ± 0.09	7.8/12	7.9×10^{-1}	0.26
2010.05.15	$(2.26 \pm 1.40) \times 10^{-10}$	-1.58 ± 0.75	5.3/9	7.9×10^{-1}	0.25
2010.05.16	$(2.90 \pm 0.20) \times 10^{-10}$	-2.24 ± 0.07	12.1/11	3.5×10^{-1}	0.93
2010.05.17	$(6.26 \pm 0.38) \times 10^{-10}$	-2.10 ± 0.06	8.7/12	7.2×10^{-1}	0.35
2010.05.18	$(4.64 \pm 0.22) \times 10^{-10}$	-1.88 ± 0.04	22.3/12	3.4×10^{-2}	2.12
2010.05.19	$(5.47 \pm 0.73) \times 10^{-10}$	-2.28 ± 0.15	8.1/9	5.2×10^{-1}	0.64
2010.05.30	$(4.95 \pm 0.58) \times 10^{-10}$	-2.31 ± 0.14	17.7/12	1.2×10^{-1}	1.54
2010.05.31	$(2.64 \pm 0.22) \times 10^{-10}$	-2.20 ± 0.09	8.1/12	7.7×10^{-1}	0.29
2010.06.01	$(1.15 \pm 0.40) \times 10^{-10}$	-2.17 ± 0.48	1.2/11	$1.0 \times 10^{+0}$	0.00
2010.06.02	$(7.10 \pm 4.10) \times 10^{-11}$	-3.37 ± 0.62	11.2/8	1.8×10^{-1}	1.32
2010.06.03	$(1.26 \pm 0.2.) \times 10^{-10}$	-2.57 ± 0.24	4.8/8	7.7×10^{-1}	0.29

Table B.3 (cont'd)

Date	$f_0[\text{TeV cm}^{-2}\text{s}^{-1}]$	α	χ^2/ndf	Prob.	Sig.
2010.06.04	$(7.25 \pm 3.31) \times 10^{-11}$	-2.88 ± 0.57	11.4/10	3.2×10^{-1}	0.98
2010.06.05	$(1.25 \pm 0.16) \times 10^{-10}$	-2.36 ± 0.15	12.0/11	3.6×10^{-1}	0.92
2010.06.06	$(1.39 \pm 0.31) \times 10^{-10}$	-2.30 ± 0.39	8.4/9	4.9×10^{-1}	0.68
2010.06.07	$(1.67 \pm 0.34) \times 10^{-10}$	-2.52 ± 0.31	9.7/8	2.8×10^{-1}	1.07
2010.06.08	$(1.44 \pm 0.32) \times 10^{-10}$	-2.15 ± 0.32	4.1/7	7.6×10^{-1}	0.30
2010.06.09	$(1.84 \pm 0.31) \times 10^{-10}$	-2.43 ± 0.21	12.3/11	3.3×10^{-1}	0.96
2010.06.10	$(1.79 \pm 0.23) \times 10^{-10}$	-2.21 ± 0.17	8.5/13	8.0×10^{-1}	0.24
2010.06.11	$(0.95 \pm 276.) \times 10^{-11}$	-1.07 ± 14.4	0.3/13	$1.0 \times 10^{+0}$	0.00
2010.06.12	$(1.74 \pm 0.47) \times 10^{-10}$	-2.49 ± 0.39	5.1/10	8.8×10^{-1}	0.15
2010.06.13	$(6.69 \pm 4.78) \times 10^{-11}$	-3.37 ± 1.11	10.2/7	1.7×10^{-1}	1.36
2010.06.14	$(1.55 \pm 0.52) \times 10^{-10}$	-2.78 ± 0.43	5.5/8	6.9×10^{-1}	0.39
2010.06.16	$(1.47 \pm 0.48) \times 10^{-10}$	-2.32 ± 0.48	2.5/10	9.9×10^{-1}	0.01
2011.01.11	$(3.09 \pm 0.23) \times 10^{-10}$	-2.57 ± 0.08	11.1/9	2.6×10^{-1}	1.11
2011.01.17	$(2.57 \pm 0.28) \times 10^{-10}$	-2.64 ± 0.15	3.5/8	8.9×10^{-1}	0.13
2011.02.06	$(1.42 \pm 0.31) \times 10^{-10}$	-2.42 ± 0.33	2.4/7	9.3×10^{-1}	0.09
2011.02.07	$(8.48 \pm 4.80) \times 10^{-11}$	-2.48 ± 0.86	1.8/3	6.1×10^{-1}	0.50
2011.02.08	$(4.40 \pm 2.90) \times 10^{-11}$	-3.49 ± 0.55	9.7/8	2.8×10^{-1}	1.07
2011.02.23	$(3.53 \pm 3.41) \times 10^{-11}$	-4.48 ± 0.83	8.6/6	1.9×10^{-1}	1.30
2011.03.01	$(1.48 \pm 0.21) \times 10^{-10}$	-2.81 ± 0.17	3.6/6	7.3×10^{-1}	0.34
2011.03.23	$(2.74 \pm 0.30) \times 10^{-10}$	-2.44 ± 0.18	5.8/8	6.6×10^{-1}	0.44
2011.03.29	$(3.24 \pm 0.15) \times 10^{-10}$	-2.49 ± 0.05	17.1/10	7.0×10^{-2}	1.81
2011.04.04	$(3.53 \pm 0.16) \times 10^{-10}$	-2.21 ± 0.06	10.7/9	2.9×10^{-1}	1.06
2011.04.10	$(3.88 \pm 0.18) \times 10^{-10}$	-2.39 ± 0.05	12.4/12	4.1×10^{-1}	0.82
2011.04.25	$(1.25 \pm 0.12) \times 10^{-10}$	-2.73 ± 0.12	16.6/8	3.4×10^{-2}	2.12
2011.05.05	$(1.12 \pm 0.27) \times 10^{-10}$	-2.97 ± 0.28	5.9/7	5.4×10^{-1}	0.60
2011.05.07	$(1.39 \pm 0.20) \times 10^{-10}$	-2.57 ± 0.17	9.4/8	3.0×10^{-1}	1.02
2011.05.23	$(3.21 \pm 0.24) \times 10^{-10}$	-2.36 ± 0.08	5.1/12	9.5×10^{-1}	0.06
2011.05.25	$(2.94 \pm 0.23) \times 10^{-10}$	-2.14 ± 0.09	10.1/10	4.3×10^{-1}	0.79
2011.05.29	$(1.94 \pm 0.22) \times 10^{-10}$	-2.36 ± 0.16	2.8/8	9.4×10^{-1}	0.07
2011.05.31	$(1.67 \pm 0.34) \times 10^{-10}$	-1.93 ± 0.29	4.4/8	8.2×10^{-1}	0.23
2011.06.02	$(1.07 \pm 0.24) \times 10^{-10}$	-2.50 ± 0.38	4.7/9	8.5×10^{-1}	0.18
2011.06.04	$(1.14 \pm 0.23) \times 10^{-10}$	-2.53 ± 0.32	9.3/9	4.0×10^{-1}	0.83

Note. — See the comments under Table B.1 for detail explanation.

Table B.4. Fit Parameters from the Fit Function 4.4 (log-parabola) for the MAGIC daily spectra during 2010 and 2011 in Figures B.1 to B.14.

Date	$f_0[\text{TeV cm}^{-2}\text{s}^{-1}]$	α	β	χ^2/ndf	Prob.	Sig.
2010.01.08	$(1.18 \pm 0.05) \times 10^{-09}$	-2.06 ± 0.04	$(-4.48 \pm 0.90) \times 10^{-1}$	13.7/11	2.4×10^{-1}	1.16
2010.01.11	$(1.46 \pm 0.04) \times 10^{-09}$	-2.24 ± 0.02	$(-3.74 \pm 0.59) \times 10^{-1}$	18.4/13	1.4×10^{-1}	1.47
2010.01.12	$(1.04 \pm 0.08) \times 10^{-09}$	-2.44 ± 0.08	$(-4.23 \pm 2.23) \times 10^{-1}$	10.8/11	4.5×10^{-1}	0.75
2010.01.13	$(8.38 \pm 0.58) \times 10^{-10}$	-2.24 ± 0.06	$(-5.55 \pm 1.88) \times 10^{-1}$	7.1/12	8.4×10^{-1}	0.19
2010.01.14	$(1.50 \pm 0.03) \times 10^{-09}$	-2.04 ± 0.02	$(-3.53 \pm 0.37) \times 10^{-1}$	17.8/12	1.2×10^{-1}	1.56
2010.01.15	$(1.07 \pm 0.03) \times 10^{-09}$	-2.08 ± 0.03	$(-2.38 \pm 0.61) \times 10^{-1}$	22.9/12	2.8×10^{-2}	2.20
2010.01.16	$(7.48 \pm 0.73) \times 10^{-10}$	-2.20 ± 0.10	$(-7.11 \pm 3.24) \times 10^{-1}$	3.8/11	9.7×10^{-1}	0.03
2010.01.18	$(3.58 \pm 0.55) \times 10^{-10}$	-2.57 ± 0.20	$(-5.74 \pm 6.35) \times 10^{-1}$	9.3/8	3.1×10^{-1}	1.01
2010.01.19	$(7.49 \pm 0.50) \times 10^{-10}$	-1.95 ± 0.10	$(-2.07 \pm 1.49) \times 10^{-1}$	14.3/11	2.1×10^{-1}	1.24
2010.01.20	$(1.34 \pm 0.02) \times 10^{-09}$	-1.91 ± 0.02	$(-3.81 \pm 0.40) \times 10^{-1}$	7.4/11	7.6×10^{-1}	0.30
2010.01.21	$(7.83 \pm 0.55) \times 10^{-10}$	-2.22 ± 0.07	$(-1.28 \pm 1.60) \times 10^{-1}$	12.3/9	1.9×10^{-1}	1.30
2010.01.22	$(4.84 \pm 0.62) \times 10^{-10}$	-2.11 ± 0.18	$(8.33 \pm 31.8) \times 10^{-2}$	6.9/7	4.3×10^{-1}	0.78
2010.01.23	$(4.71 \pm 0.45) \times 10^{-10}$	-2.00 ± 0.13	$(-3.33 \pm 2.60) \times 10^{-1}$	14.3/11	2.1×10^{-1}	1.25
2010.01.24	$(7.84 \pm 0.52) \times 10^{-10}$	-1.85 ± 0.10	$(-5.31 \pm 1.79) \times 10^{-1}$	7.9/10	6.3×10^{-1}	0.47
2010.01.25	$(7.04 \pm 0.25) \times 10^{-10}$	-2.00 ± 0.04	$(-2.57 \pm 0.69) \times 10^{-1}$	13.5/12	3.2×10^{-1}	0.98
2010.01.26	$(6.99 \pm 0.71) \times 10^{-10}$	-2.38 ± 0.11	$(9.06 \pm 21.7) \times 10^{-2}$	15.9/10	1.0×10^{-1}	1.63
2010.02.05	$(5.61 \pm 4.63) \times 10^{-10}$	-2.91 ± 2.05	$(2.00 \pm 2.87) \times 10^{+0}$	0.1/2	9.3×10^{-1}	0.09
2010.02.07	$(5.05 \pm 0.42) \times 10^{-10}$	-2.19 ± 0.08	$(-4.65 \pm 2.28) \times 10^{-1}$	8.5/9	4.7×10^{-1}	0.71
2010.02.10	$(5.44 \pm 0.68) \times 10^{-10}$	-2.14 ± 0.12	$(-1.32 \pm 3.11) \times 10^{-1}$	12.7/9	1.7×10^{-1}	1.36
2010.02.11	$(4.64 \pm 0.43) \times 10^{-10}$	-2.16 ± 0.09	$(-4.68 \pm 2.38) \times 10^{-1}$	10.7/11	4.6×10^{-1}	0.74
2010.02.13	$(4.40 \pm 0.87) \times 10^{-10}$	-2.51 ± 0.22	$(-2.38 \pm 5.85) \times 10^{-1}$	5.3/9	8.0×10^{-1}	0.25
2010.03.10	$(8.98 \pm 0.48) \times 10^{-10}$	-2.00 ± 0.06	$(-3.48 \pm 1.13) \times 10^{-1}$	4.7/13	9.8×10^{-1}	0.02
2010.03.11	$(1.11 \pm 0.04) \times 10^{-09}$	-2.01 ± 0.04	$(-4.15 \pm 0.74) \times 10^{-1}$	17.8/12	1.2×10^{-1}	1.55
2010.03.13	$(5.07 \pm 0.72) \times 10^{-10}$	-2.11 ± 0.16	$(-1.86 \pm 3.61) \times 10^{-1}$	9.3/10	4.9×10^{-1}	0.68
2010.03.14	$(7.98 \pm 0.84) \times 10^{-10}$	-2.03 ± 0.13	$(-2.62 \pm 2.54) \times 10^{-1}$	7.9/10	6.3×10^{-1}	0.48
2010.03.15	$(6.46 \pm 0.67) \times 10^{-10}$	-2.23 ± 0.11	$(-4.12 \pm 2.95) \times 10^{-1}$	2.0/10	9.9×10^{-1}	0.01
2010.03.17	$(3.87 \pm 0.43) \times 10^{-10}$	-2.33 ± 0.13	$(-9.37 \pm 4.26) \times 10^{-1}$	10.2/9	3.2×10^{-1}	0.98
2010.03.18	$(4.25 \pm 0.74) \times 10^{-10}$	-2.20 ± 0.19	$(-5.74 \pm 6.06) \times 10^{-1}$	6.3/10	7.8×10^{-1}	0.27
2010.03.19	$(3.41 \pm 1.36) \times 10^{-10}$	-2.80 ± 0.95	$(-1.98 \pm 3.43) \times 10^{+0}$	0.7/3	8.5×10^{-1}	0.19
2010.03.20	$(4.93 \pm 2.95) \times 10^{-11}$	-2.39 ± 0.35	$(8.77 \pm 7.51) \times 10^{-1}$	4.0/10	9.4×10^{-1}	0.07
2010.03.21	$(4.20 \pm 0.42) \times 10^{-10}$	-2.34 ± 0.10	$(-2.98 \pm 2.56) \times 10^{-1}$	8.5/9	4.7×10^{-1}	0.71
2010.03.22	$(3.12 \pm 0.29) \times 10^{-10}$	-2.50 ± 0.08	$(-7.66 \pm 20.0) \times 10^{-2}$	11.2/10	3.3×10^{-1}	0.96
2010.04.02	$(2.48 \pm 0.49) \times 10^{-10}$	-2.02 ± 0.29	$(-1.02 \pm 5.47) \times 10^{-1}$	5.8/9	7.5×10^{-1}	0.31
2010.04.03	$(2.85 \pm 0.31) \times 10^{-10}$	-2.18 ± 0.09	$(-2.56 \pm 2.62) \times 10^{-1}$	16.1/10	9.6×10^{-2}	1.66
2010.04.05	$(2.80 \pm 0.63) \times 10^{-10}$	-1.88 ± 0.34	$(-1.17 \pm 1.17) \times 10^{+0}$	1.6/7	9.7×10^{-1}	0.03
2010.04.07	$(2.75 \pm 0.60) \times 10^{-10}$	-1.66 ± 0.32	$(-1.24 \pm 0.97) \times 10^{+0}$	4.8/7	6.8×10^{-1}	0.41
2010.04.08	$(1.57 \pm 0.86) \times 10^{-10}$	-2.06 ± 1.30	$(-2.00 \pm 2.18) \times 10^{+0}$	6.5/7	4.7×10^{-1}	0.71
2010.04.11	$(1.32 \pm 0.36) \times 10^{-10}$	-2.64 ± 0.27	$(7.50 \pm 5.20) \times 10^{-1}$	3.3/8	9.1×10^{-1}	0.11
2010.04.12	$(1.58 \pm 0.55) \times 10^{-10}$	-2.75 ± 0.64	$(-1.95 \pm 28.1) \times 10^{-1}$	1.9/6	9.2×10^{-1}	0.10
2010.04.18	$(4.70 \pm 0.33) \times 10^{-10}$	-2.15 ± 0.06	$(-4.24 \pm 1.67) \times 10^{-1}$	44.8/12	1.0×10^{-5}	4.40
2010.04.19	$(1.00 \pm 537.) \times 10^{-15}$	-7.13 ± 5.75	$(1.99 \pm 3.85) \times 10^{+0}$	0.0/12	$1.0 \times 10^{+0}$	0.00
2010.05.04	$(2.30 \pm 0.43) \times 10^{-10}$	-1.79 ± 3.81	$(-2.00 \pm 2.95) \times 10^{+0}$	0.3/4	9.9×10^{-1}	0.01
2010.05.05	$(4.17 \pm 0.63) \times 10^{-10}$	-2.09 ± 0.17	$(-6.15 \pm 5.33) \times 10^{-1}$	3.7/7	8.0×10^{-1}	0.24
2010.05.06	$(4.27 \pm 0.47) \times 10^{-10}$	-2.20 ± 0.10	$(-2.33 \pm 2.80) \times 10^{-1}$	10.9/9	2.8×10^{-1}	1.08
2010.05.07	$(5.39 \pm 0.72) \times 10^{-10}$	-2.09 ± 0.13	$(-6.74 \pm 4.04) \times 10^{-1}$	4.7/11	9.4×10^{-1}	0.07
2010.05.15	$(2.30 \pm 1.71) \times 10^{-10}$	-1.17 ± 2.24	$(-1.23 \pm 3.27) \times 10^{+0}$	5.3/8	7.2×10^{-1}	0.36
2010.05.16	$(3.20 \pm 0.29) \times 10^{-10}$	-2.28 ± 0.10	$(-7.45 \pm 2.95) \times 10^{-1}$	5.9/10	8.1×10^{-1}	0.23
2010.05.17	$(6.37 \pm 0.54) \times 10^{-10}$	-2.17 ± 0.08	$(-3.90 \pm 2.03) \times 10^{-1}$	7.1/11	7.8×10^{-1}	0.27
2010.05.18	$(4.88 \pm 0.29) \times 10^{-10}$	-1.92 ± 0.06	$(-4.61 \pm 1.26) \times 10^{-1}$	14.2/11	2.1×10^{-1}	1.23
2010.05.19	$(6.56 \pm 1.21) \times 10^{-10}$	-2.47 ± 0.26	$(-1.36 \pm 0.85) \times 10^{+0}$	4.8/8	7.7×10^{-1}	0.29
2010.05.30	$(5.27 \pm 1.03) \times 10^{-10}$	-2.42 ± 0.18	$(-6.62 \pm 7.34) \times 10^{-1}$	16.9/11	1.1×10^{-1}	1.60
2010.05.31	$(2.66 \pm 0.29) \times 10^{-10}$	-2.18 ± 0.15	$(-4.54 \pm 3.16) \times 10^{-1}$	7.6/11	7.4×10^{-1}	0.33
2010.06.01	$(1.29 \pm 0.66) \times 10^{-10}$	-2.23 ± 0.71	$(-1.13 \pm 2.19) \times 10^{+0}$	1.0/10	$1.0 \times 10^{+0}$	0.00
2010.06.02	$(6.96 \pm 2.62) \times 10^{-11}$	-2.75 ± 0.32	$(1.16 \pm 0.64) \times 10^{+0}$	9.6/7	2.1×10^{-1}	1.25
2010.06.03	$(1.46 \pm 0.32) \times 10^{-10}$	-3.17 ± 0.38	$(-2.00 \pm 2.92) \times 10^{+0}$	2.3/7	9.3×10^{-1}	0.08

Table B.4 (cont'd)

Date	f_0 [TeV cm ⁻² s ⁻¹]	α	β	χ^2/ndf	Prob.	Sig.
2010.06.04	$(6.27 \pm 3.10) \times 10^{-11}$	-2.85 ± 0.59	$(3.54 \pm 11.8) \times 10^{-1}$	11.3/9	2.5×10^{-1}	1.14
2010.06.05	$(1.51 \pm 0.26) \times 10^{-10}$	-2.32 ± 0.25	$(-1.37 \pm 0.77) \times 10^{+0}$	7.7/10	6.5×10^{-1}	0.45
2010.06.06	$(1.13 \pm 0.35) \times 10^{-10}$	-2.39 ± 0.28	$(5.04 \pm 7.37) \times 10^{-1}$	7.9/8	4.4×10^{-1}	0.77
2010.06.07	$(1.44 \pm 0.48) \times 10^{-10}$	-2.60 ± 0.29	$(2.24 \pm 10.1) \times 10^{-1}$	9.7/7	2.0×10^{-1}	1.27
2010.06.08	$(1.67 \pm 0.51) \times 10^{-10}$	-1.95 ± 0.59	$(-1.68 \pm 2.60) \times 10^{+0}$	2.9/6	8.1×10^{-1}	0.24
2010.06.09	$(2.45 \pm 0.39) \times 10^{-10}$	-2.60 ± 0.34	$(-2.00 \pm 0.86) \times 10^{+0}$	7.5/10	6.7×10^{-1}	0.42
2010.06.10	$(1.76 \pm 0.27) \times 10^{-10}$	-2.18 ± 0.26	$(-4.65 \pm 4.84) \times 10^{-1}$	8.2/12	7.6×10^{-1}	0.30
2010.06.12	$(2.12 \pm 0.59) \times 10^{-10}$	-2.87 ± 0.59	$(-2.00 \pm 3.08) \times 10^{+0}$	3.6/9	9.3×10^{-1}	0.09
2010.06.13	$(5.26 \pm 0.36) \times 10^{-11}$	-3.29 ± 0.62	$(1.02 \pm 1.30) \times 10^{+0}$	9.9/6	1.2×10^{-1}	1.52
2010.06.14	$(1.79 \pm 0.64) \times 10^{-10}$	-3.38 ± 0.60	$(-2.00 \pm 2.68) \times 10^{+0}$	3.6/7	8.2×10^{-1}	0.22
2010.06.16	$(1.78 \pm 0.58) \times 10^{-10}$	-2.35 ± 0.83	$(-2.00 \pm 2.85) \times 10^{+0}$	1.9/9	9.9×10^{-1}	0.01
2011.01.11	$(3.32 \pm 0.32) \times 10^{-10}$	-2.80 ± 0.14	$(-7.78 \pm 3.46) \times 10^{-1}$	5.6/8	6.8×10^{-1}	0.41
2011.01.17	$(2.43 \pm 0.34) \times 10^{-10}$	-2.76 ± 0.19	$(-2.04 \pm 4.77) \times 10^{-1}$	3.4/7	8.4×10^{-1}	0.20
2011.02.06	$(1.57 \pm 0.49) \times 10^{-10}$	-2.49 ± 0.46	$(-1.24 \pm 2.32) \times 10^{+0}$	1.9/6	9.2×10^{-1}	0.09
2011.02.07	$(8.79 \pm 0.40) \times 10^{-11}$	-1.48 ± 0.59	$(2.00 \pm 3.42) \times 10^{+0}$	1.1/2	5.7×10^{-1}	0.56
2011.02.08	$(4.11 \pm 3.43) \times 10^{-11}$	-3.53 ± 2.01	$(-0.63 \pm 294.) \times 10^{-2}$	9.7/7	2.0×10^{-1}	1.26
2011.02.23	$(5.59 \pm 2.19) \times 10^{-11}$	-2.95 ± 0.32	$(2.00 \pm 0.74) \times 10^{+0}$	4.6/5	4.6×10^{-1}	0.74
2011.03.01	$(1.49 \pm 0.26) \times 10^{-10}$	-3.06 ± 0.30	$(-6.70 \pm 7.02) \times 10^{-1}$	2.8/5	7.2×10^{-1}	0.35
2011.03.23	$(2.59 \pm 0.40) \times 10^{-10}$	-2.51 ± 0.21	$(-2.19 \pm 5.71) \times 10^{-1}$	5.9/7	5.4×10^{-1}	0.60
2011.03.29	$(3.60 \pm 0.24) \times 10^{-10}$	-2.57 ± 0.07	$(-7.47 \pm 2.21) \times 10^{-1}$	5.0/9	8.3×10^{-1}	0.21
2011.04.04	$(3.41 \pm 0.24) \times 10^{-10}$	-2.29 ± 0.06	$(-2.56 \pm 1.94) \times 10^{-1}$	10.2/8	2.4×10^{-1}	1.16
2011.04.10	$(3.77 \pm 0.24) \times 10^{-10}$	-2.49 ± 0.05	$(-2.47 \pm 1.41) \times 10^{-1}$	11.4/11	4.0×10^{-1}	0.83
2011.04.25	$(1.45 \pm 0.21) \times 10^{-10}$	-3.02 ± 0.27	$(-1.39 \pm 0.84) \times 10^{+0}$	12.3/7	8.8×10^{-2}	1.70
2011.05.05	$(1.00 \pm 0.27) \times 10^{-10}$	-2.99 ± 0.38	$(1.57 \pm 8.27) \times 10^{-1}$	5.9/6	4.3×10^{-1}	0.78
2011.05.07	$(1.55 \pm 0.28) \times 10^{-10}$	-2.92 ± 0.41	$(-1.31 \pm 0.97) \times 10^{+0}$	6.9/7	4.3×10^{-1}	0.78
2011.05.23	$(3.28 \pm 0.33) \times 10^{-10}$	-2.48 ± 0.11	$(-4.55 \pm 2.86) \times 10^{-1}$	3.2/11	9.8×10^{-1}	0.02
2011.05.25	$(3.02 \pm 0.35) \times 10^{-10}$	-2.19 ± 0.12	$(-5.00 \pm 3.73) \times 10^{-1}$	8.8/9	4.4×10^{-1}	0.76
2011.05.29	$(1.89 \pm 0.32) \times 10^{-10}$	-2.45 ± 0.17	$(-3.13 \pm 5.42) \times 10^{-1}$	2.8/7	9.0×10^{-1}	0.12
2011.05.31	$(1.67 \pm 0.43) \times 10^{-10}$	-1.98 ± 0.36	$(-4.85 \pm 9.03) \times 10^{-1}$	4.1/7	7.5×10^{-1}	0.31
2011.06.02	$(9.12 \pm 2.51) \times 10^{-11}$	-2.53 ± 0.29	$(3.69 \pm 6.40) \times 10^{-1}$	4.3/8	8.2×10^{-1}	0.22
2011.06.04	$(9.36 \pm 2.68) \times 10^{-11}$	-2.50 ± 0.24	$(5.38 \pm 6.79) \times 10^{-1}$	8.6/8	3.7×10^{-1}	0.89

Note. — See the comments under Table B.1 for detail explanation.

C. Test and Cross-check for MAGIC Markarian 421 Data Analysis

C.1. Analysis Chain Testing on the Crab Nebula Very-High-Energy Spectrum

The following plots show the test results of several hadronness cuts of different efficiencies. See more explanation on "Gamma-Hadron Separation" in Section 3.2.

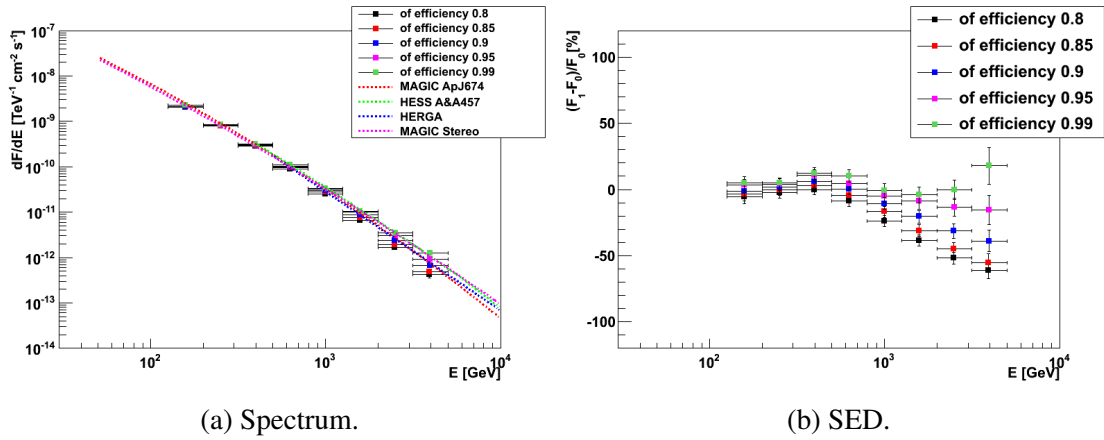


Figure C.1.: The Crab Nebula data with the zenith angle 5–28 degrees.

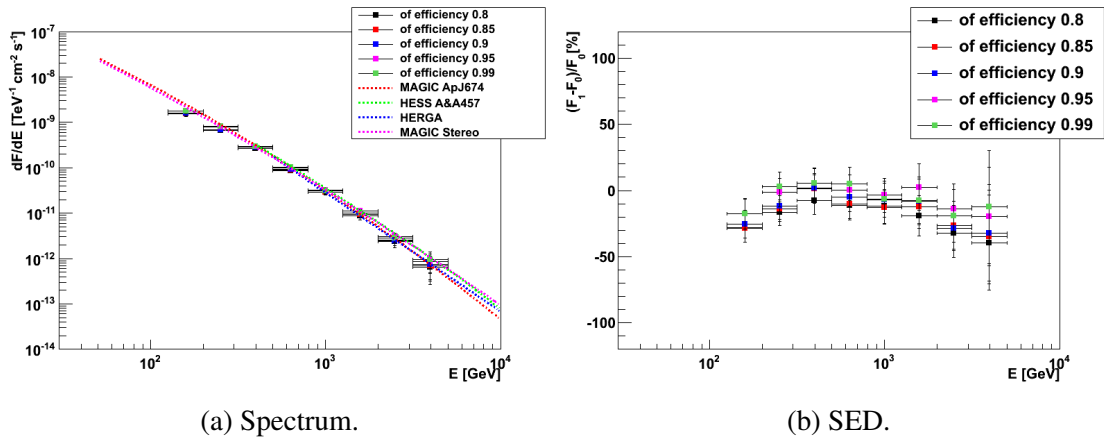


Figure C.2.: The Crab Nebula data with the zenith angle 28–40 degrees.

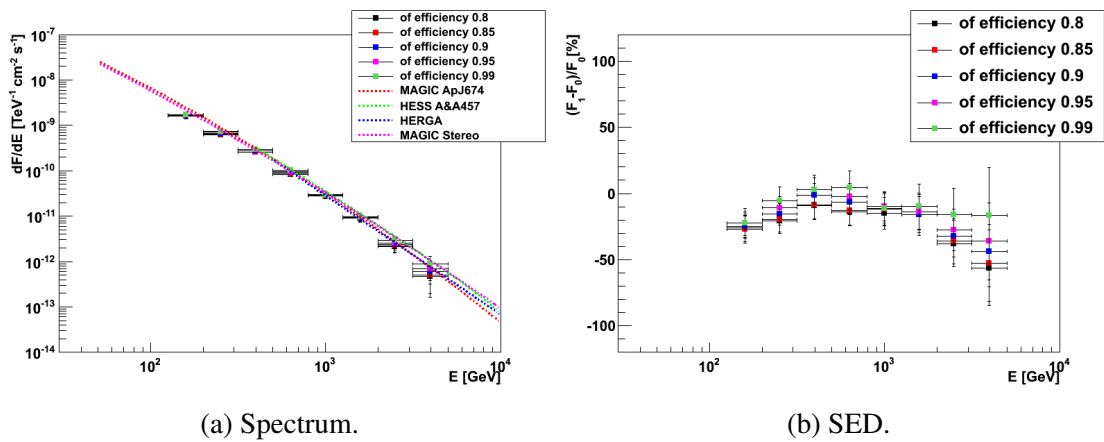


Figure C.3.: The Crab Nebula data with the zenith angle 40–50 degrees.

C.2. Markarian 421 Very-High-Energy Light Curve Cross-check with Other Analyzers

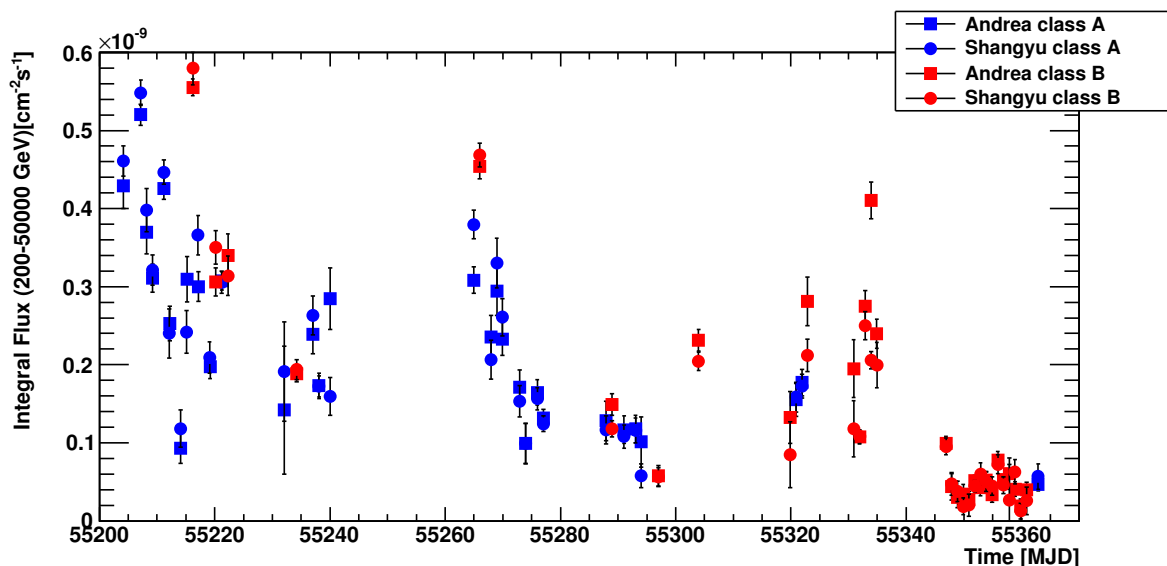


Figure C.4.: The 2010-LC cross-check.

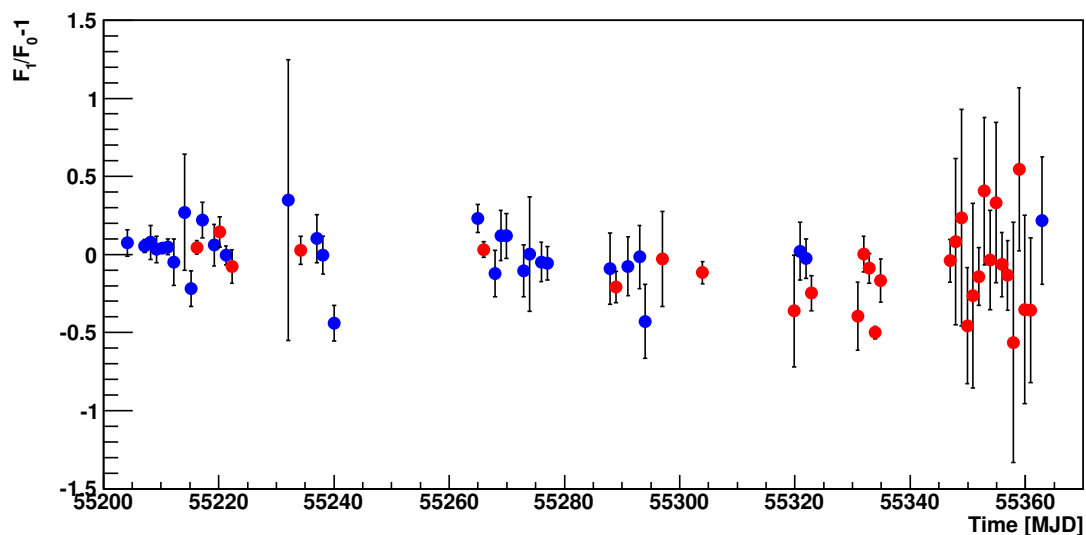


Figure C.5.: The 2010-LC cross-check: residual of the two LCs.

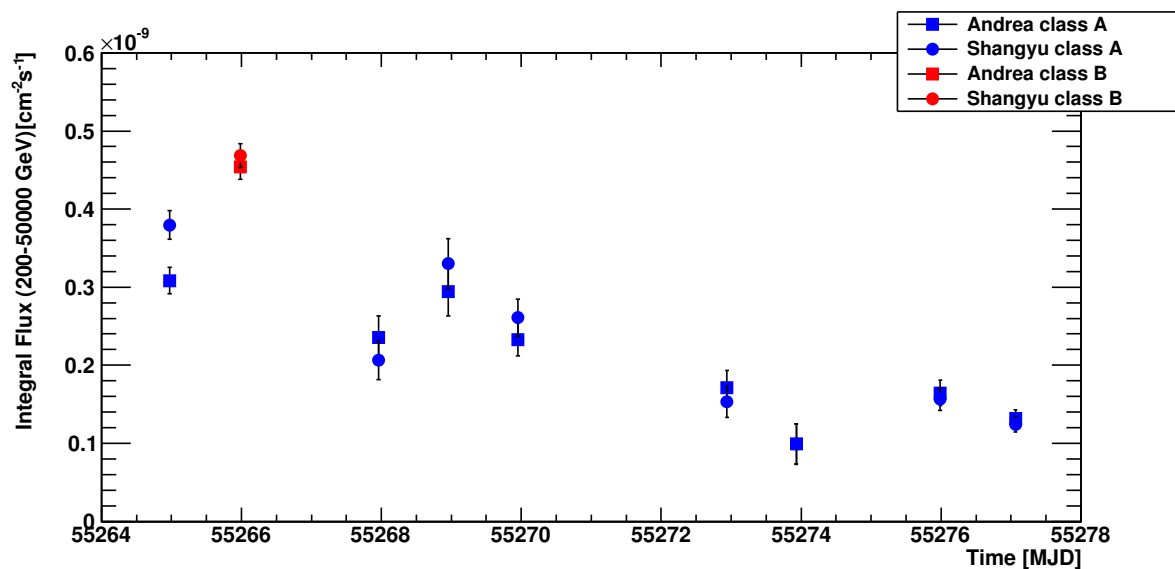


Figure C.6.: The March-2010-LC cross-check.

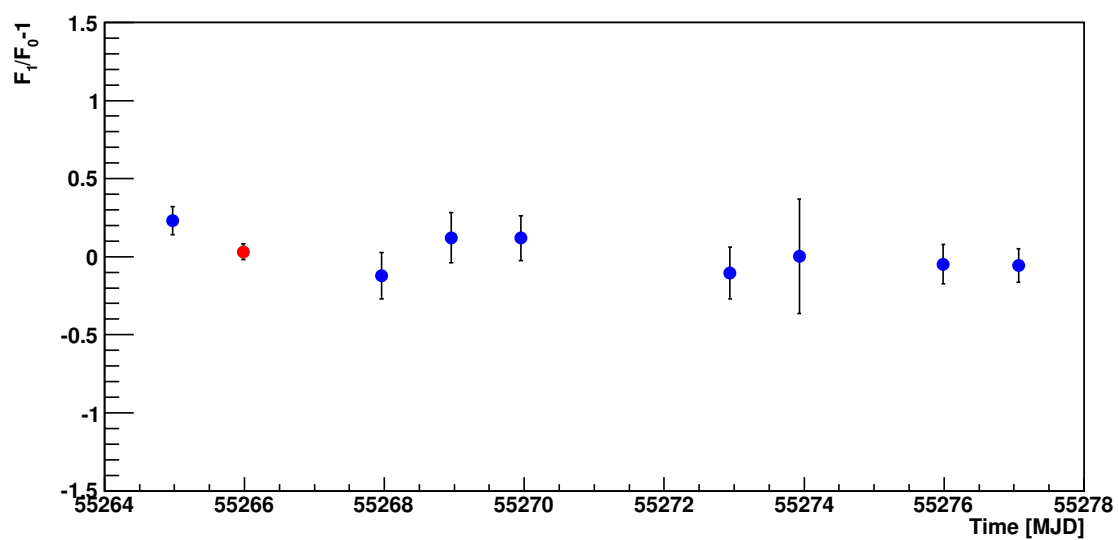


Figure C.7.: The March-2010-LC cross-check: residual of the two LCs.

C.3. Markarian 421 Very-High-Energy Spectrum Cross-check with Other Analyzers

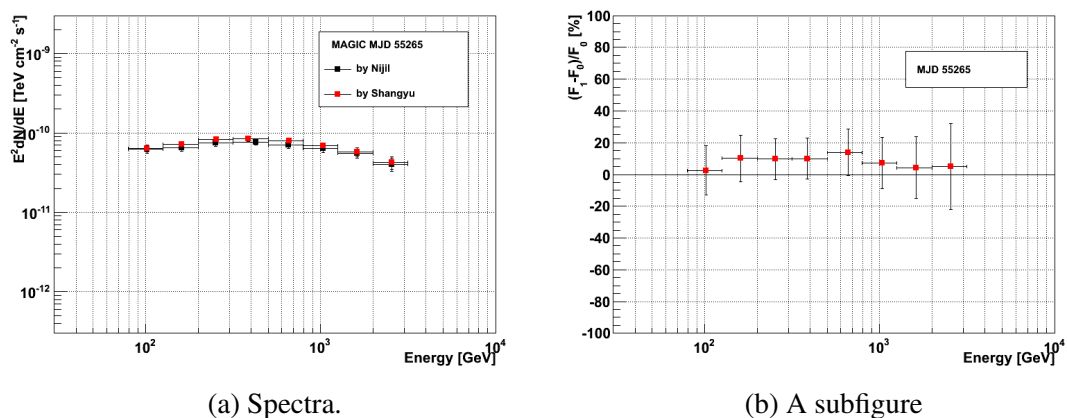


Figure C.8.: Cross-check on the spectrum of 2010.03.10.

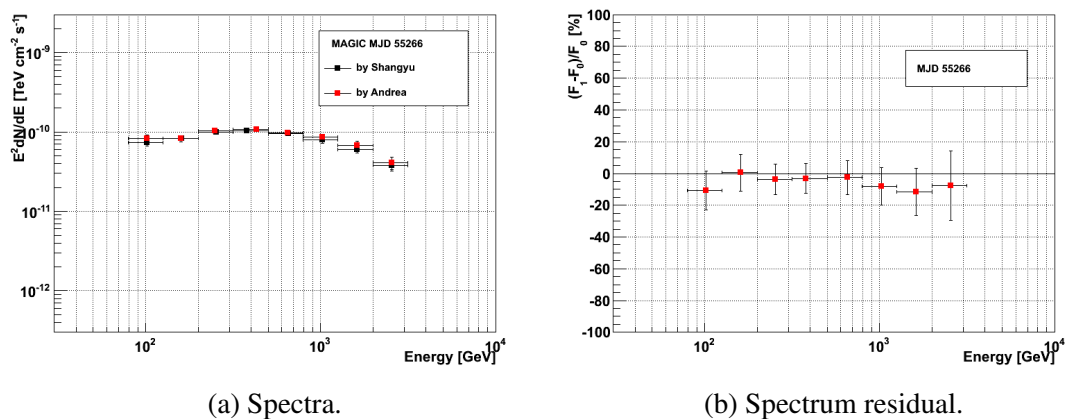


Figure C.9.: Cross-check on the spectrum of 2010.03.11.

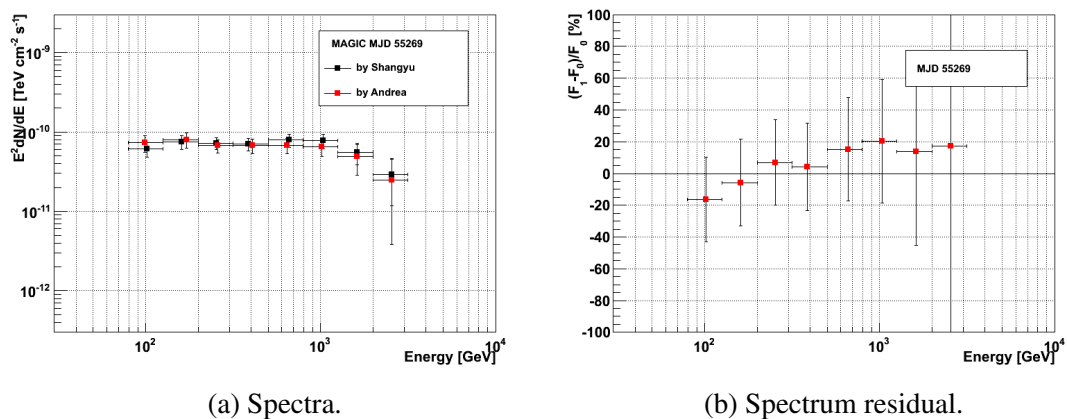


Figure C.10.: Cross-check on the spectrum of 2010.03.14.

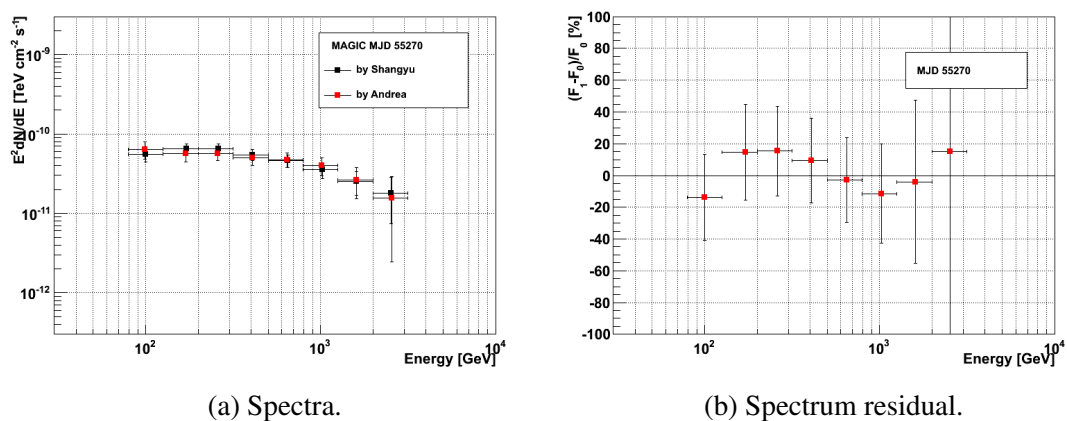


Figure C.11.: Cross-check on the spectrum of 2010.03.15.

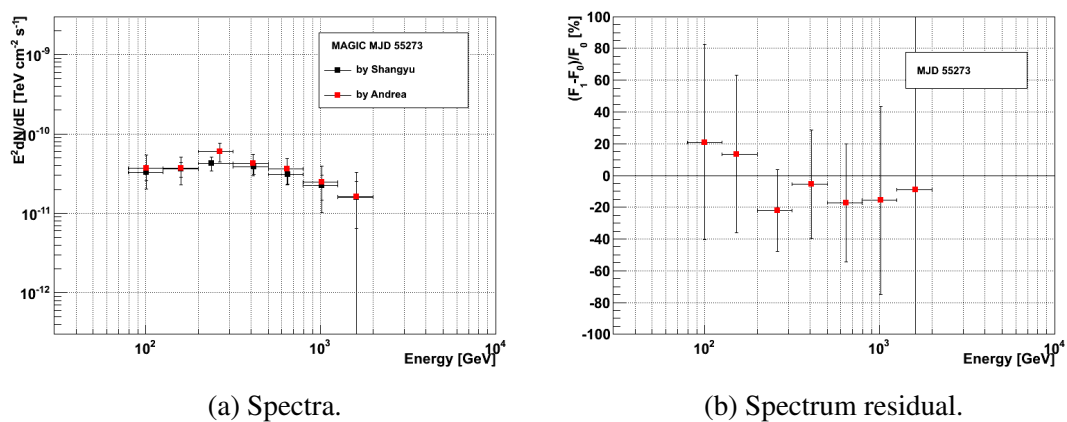


Figure C.12.: Cross-check on the spectrum of 2010.03.18.

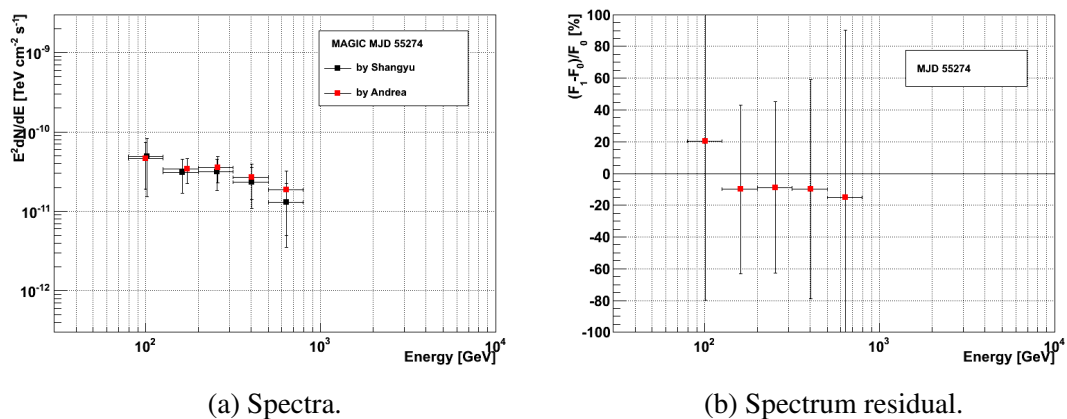


Figure C.13.: Cross-check on the spectrum of 2010.03.19.

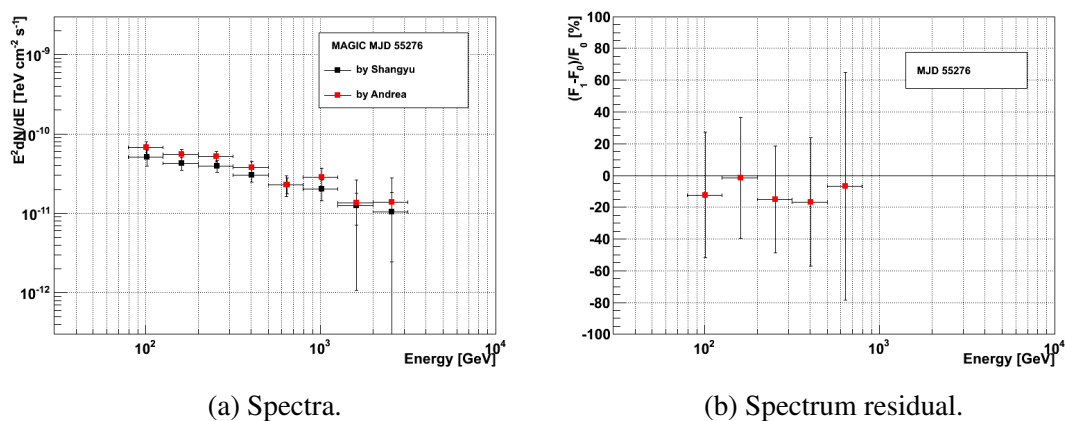


Figure C.14.: Cross-check on the spectrum of 2010.03.21.

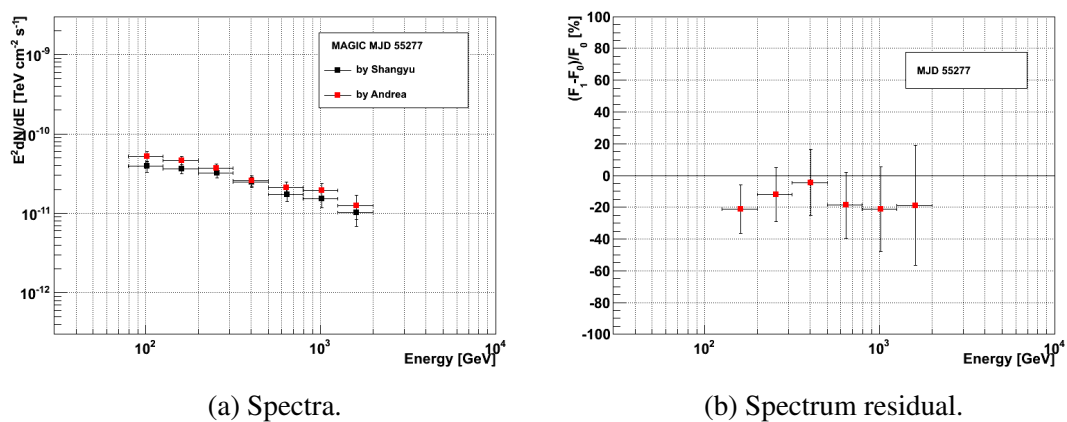
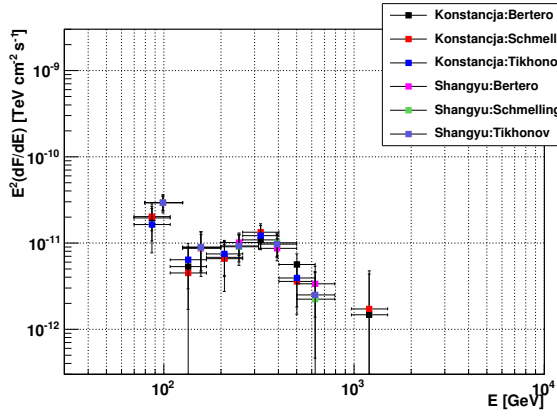
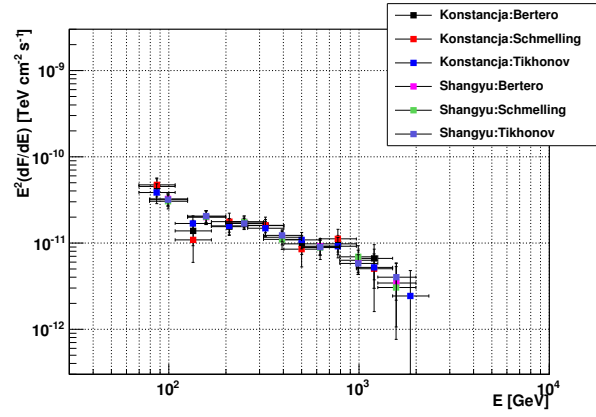


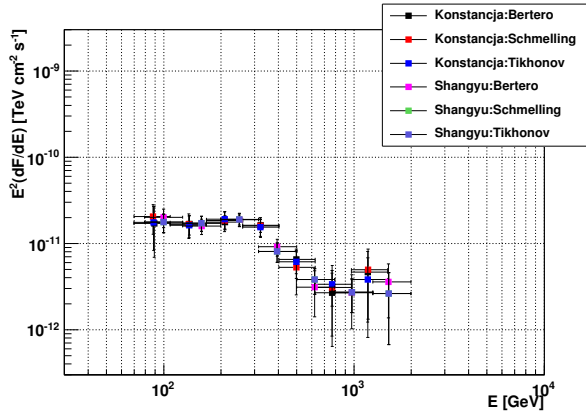
Figure C.15.: Cross-check on the spectrum of 2010.03.22.



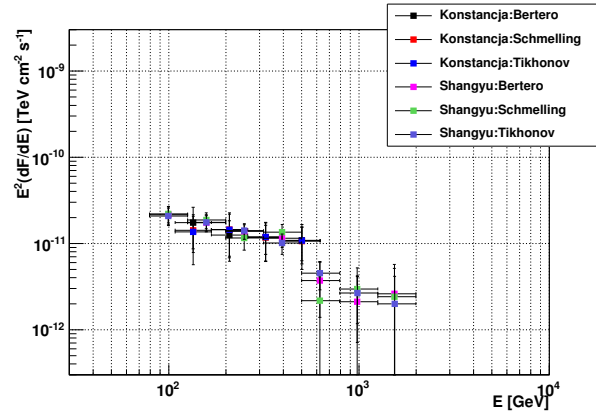
(a) 02.06+02.07+02.08



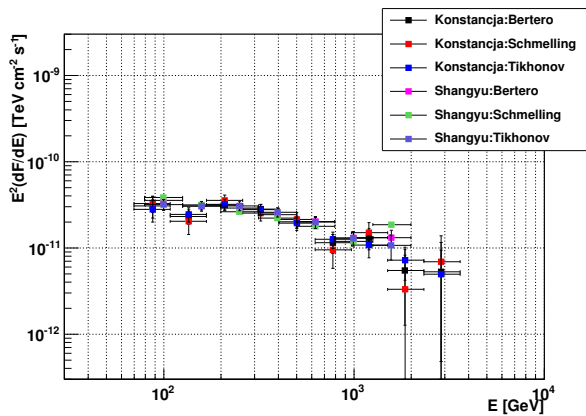
(b) 02.23+03.01+03.23



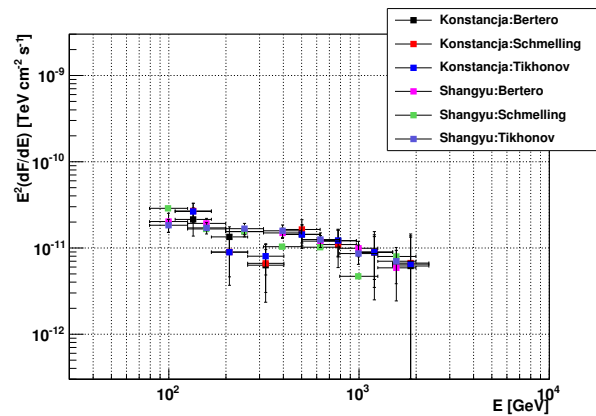
(c) 04.25



(d) 05.05

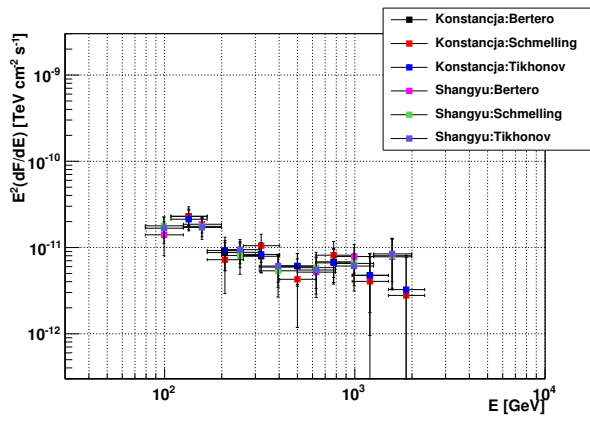


(e) 05.23+05.25



(f) 05.29+05.31

Figure C.16.: Cross-check on 2011 spectra.



(a) 06.02+06.04

Figure C.17.: Cross-check on 2011 spectra.

Bibliography

- [Abdo et al., 2010] Abdo, A. A. et al. (2010). *ApJ*, 716:30.
- [Abdo et al., 2011] Abdo, A. A. et al. (2011). *ApJ*, 736:131.
- [Abdo, 2014] Abdo, A. A., e. a. T. F. c. (2014). Fermi Large Area Telescope Third Source Catalog. *in preparation*.
- [Acciari, 2011] Acciari, V. (2011). PhD thesis, Galway-Mayo Institute of Technology.
- [Acciari et al., 2011] Acciari, V. A., Aliu, E., Arlen, T., Aune, T., Beilicke, M., Benbow, W., Boltuch, D., Bradbury, S. M., Buckley, J. H., Bugaev, V., Byrum, K., Cannon, A., Cesarini, A., Ciupik, L., Cui, W., Dickherber, R., Duke, C., Falcone, A., Finley, J. P., Finnegan, G., Fortson, L., Furniss, A., Galante, N., Gall, D., Gillanders, G. H., Godambe, S., Grube, J., Guenette, R., Gyuk, G., Hanna, D., Holder, J., Hui, C. M., Humensky, T. B., Imran, A., Kaaret, P., Karlsson, N., Kertzman, M., Kieda, D., Konopelko, A., Krawczynski, H., Krennrich, F., Lang, M. J., Maier, G., McArthur, S., McCutcheon, M., Moriarty, P., Ong, R. A., Otte, A. N., Ouellette, M., Pandel, D., Perkins, J. S., Pichel, A., Pohl, M., Quinn, J., Ragan, K., Reyes, L. C., Reynolds, P. T., Roache, E., Rose, H. J., Rovero, A. C., Schroedter, M., Sembroski, G. H., Senturk, G. D., Steele, D., Swordy, S. P., Theiling, M., Thibadeau, S., Varlotta, A., Vassiliev, V. V., Vincent, S., Wagner, R. G., Wakely, S. P., Ward, J. E., Weekes, T. C., Weinstein, A., Weisgarber, T., Williams, D. A., Wissel, S., Wood, M., Zitzer, B., Garson, III, A., Lee, K., Sadun, A. C., Carini, M., Barnaby, D., Cook, K., Maune, J., Pease, A., Smith, S., Walters, R., Berdyugin, A., Lindfors, E., Nilsson, K., Pasanen, M., Sainio, J., Sillanpaa, A., Takalo, L. O., Villforth, C., Montaruli, T., Baker, M., Lahteenmaki, A., Tornikoski, M., Hovatta, T., Nieppola, E., Aller, H. D., and Aller, M. F. (2011). TeV and Multi-wavelength Observations of Mrk 421 in 2006-2008. *ApJ*, 738:25.
- [Acciari et al., 2014] Acciari, V. A., Arlen, T., Aune, T., Benbow, W., Bird, R., Bouvier, A., Bradbury, S. M., Buckley, J. H., Bugaev, V., de la Calle Perez, I., Carter-Lewis, D. A., Cesarini, A., Ciupik, L., Collins-Hughes, E., Connolly, M. P., Cui, W., Duke, C., Dumm, J., Falcone, A., Federici, S., Fegan, D. J., Fegan, S. J., Finley, J. P., Finnegan, G., Fortson, L., Gaidos, J., Galante, N., Gall, D., Gibbs, K., Gillanders, G. H., Griffin, S., Grube, J., Gyuk, G., Hanna, D., Horan, D., Humensky, T. B., Kaaret, P., Kertzman, M., Khassen, Y., Kieda, D., Krawczynski, H., Krennrich, F., Lang, M. J., McEnery, J. E., Madhavan, A. S., Moriarty, P., Nelson, T., O’Faoláin de Bhróithe, A., Ong, R. A., Orr, M., Otte, A. N., Perkins, J. S., Petry, D., Pichel, A., Pohl, M., Quinn, J., Ragan, K., Reynolds, T., Roache, E., Rovero, A., Schroedter, M., Sembroski, G. H., Smith, A., Telezhinsky, I., Theiling, M., Toner, J., Tyler,

- J., Varlotta, A., Vivier, M., Wakely, S. P., Ward, J. E., Weekes, T. C., Weinstein, A., Welsing, R., Williams, D. A., and Wissel, S. (2014). Observation of Markarian 421 in TeV gamma rays over a 14-year time span. *Astroparticle Physics*, 54:1–10.
- [Ackermann et al., 2012] Ackermann, M., Ajello, M., Albert, A., Allafort, A., Atwood, W. B., Axelsson, M., Baldini, L., Ballet, J., Barbiellini, G., Bastieri, D., Bechtol, K., Bellazzini, R., Bissaldi, E., Blandford, R. D., Bloom, E. D., Bogart, J. R., Bonamente, E., Borgland, A. W., Bottacini, E., Bouvier, A., Brandt, T. J., Bregeon, J., Brigida, M., Bruel, P., Buehler, R., Burnett, T. H., Buson, S., Caliandro, G. A., Cameron, R. A., Caraveo, P. A., Casandjian, J. M., Cavazzuti, E., Cecchi, C., Çelik, Ö., Charles, E., Chaves, R. C. G., Chekhtman, A., Cheung, C. C., Chiang, J., Ciprini, S., Claus, R., Cohen-Tanugi, J., Conrad, J., Corbet, R., Cutini, S., D’Ammando, F., Davis, D. S., de Angelis, A., DeKlotz, M., de Palma, F., Dermer, C. D., Digel, S. W., Silva, E. d. C. e., Drell, P. S., Drlica-Wagner, A., Dubois, R., Favuzzi, C., Fegan, S. J., Ferrara, E. C., Focke, W. B., Fortin, P., Fukazawa, Y., Funk, S., Fusco, P., Gargano, F., Gasparrini, D., Gehrels, N., Giebels, B., Giglietto, N., Giordano, F., Giroletti, M., Glanzman, T., Godfrey, G., Grenier, I. A., Grove, J. E., Guiriec, S., Hadasch, D., Hayashida, M., Hays, E., Horan, D., Hou, X., Hughes, R. E., Jackson, M. S., Jogler, T., Jóhannesson, G., Johnson, R. P., Johnson, T. J., Johnson, W. N., Kamae, T., Katagiri, H., Kataoka, J., Kerr, M., Knödseder, J., Kuss, M., Lande, J., Larsson, S., Latronico, L., Lavalley, C., Lemoine-Goumard, M., Longo, F., Loparco, F., Lott, B., Lovellette, M. N., Lubrano, P., Mazziotta, M. N., McConville, W., McEnery, J. E., Mehault, J., Michelson, P. F., Mitthumsiri, W., Mizuno, T., Moiseev, A. A., Monte, C., Monzani, M. E., Morselli, A., Moskalenko, I. V., Murgia, S., Naumann-Godo, M., Nemmen, R., Nishino, S., Norris, J. P., Nuss, E., Ohno, M., Ohsugi, T., Okumura, A., Omodei, N., Orienti, M., Orlando, E., Ormes, J. F., Paneque, D., Panetta, J. H., Perkins, J. S., Pesce-Rollins, M., Pierbattista, M., Piron, F., Pivato, G., Porter, T. A., Racusin, J. L., Rainò, S., Rando, R., Razzano, M., Razzaque, S., Reimer, A., Reimer, O., Reposeur, T., Reyes, L. C., Ritz, S., Rochester, L. S., Romoli, C., Roth, M., Sadrozinski, H. F.-W., Sanchez, D. A., Saz Parkinson, P. M., Sbarra, C., Scargle, J. D., Sgrò, C., Siegal-Gaskins, J., Siskind, E. J., Spandre, G., Spinelli, P., Stephens, T. E., Suson, D. J., Tajima, H., Takahashi, H., Tanaka, T., Thayer, J. G., Thayer, J. B., Thompson, D. J., Tibaldo, L., Tinivella, M., Tosti, G., Troja, E., Usher, T. L., Vandenbroucke, J., Van Klaveren, B., Vasileiou, V., Vianello, G., Vitale, V., Waite, A. P., Wallace, E., Winer, B. L., Wood, D. L., Wood, K. S., Wood, M., Yang, Z., and Zimmer, S. (2012). The Fermi Large Area Telescope on Orbit: Event Classification, Instrument Response Functions, and Calibration. *ApJS*, 203:4.
- [Ackermann et al., 2011a] Ackermann, M., Ajello, M., Allafort, A., Angelakis, E., Axelsson, M., Baldini, L., Ballet, J., Barbiellini, G., Bastieri, D., Bellazzini, R., Berenji, B., Blandford, R. D., Bloom, E. D., Bonamente, E., Borgland, A. W., Bouvier, A., Bregeon, J., Brez, A., Brigida, M., Bruel, P., Buehler, R., Buson, S., Caliandro, G. A., Cameron, R. A., Cannon, A., Caraveo, P. A., Casandjian, J. M., Cavazzuti, E., Cecchi, C., Charles, E., Chekhtman, A., Cheung, C. C., Ciprini, S., Claus, R., Cohen-Tanugi, J., Cutini, S., de Palma, F., Dermer, C. D., Silva, E. d. C. e., Drell, P. S., Dubois, R., Dumora, D., Escande, L., Favuzzi, C., Fegan, S. J., Focke, W. B., Fortin, P., Frailis, M., Fuhrmann, L., Fukazawa, Y., Fusco,

- P., Gargano, F., Gasparrini, D., Gehrels, N., Giglietto, N., Giommi, P., Giordano, F., Giroletti, M., Glanzman, T., Godfrey, G., Grandi, P., Grenier, I. A., Guiriec, S., Hadasch, D., Hayashida, M., Hays, E., Healey, S. E., Jóhannesson, G., Johnson, A. S., Kamae, T., Katagiri, H., Kataoka, J., Knödlseeder, J., Kuss, M., Lande, J., Lee, S.-H., Longo, F., Loparco, F., Lott, B., Lovellette, M. N., Lubrano, P., Makeev, A., Max-Moerbeck, W., Mazziotta, M. N., McEnery, J. E., Mehault, J., Michelson, P. F., Mizuno, T., Monte, C., Monzani, M. E., Morselli, A., Moskalenko, I. V., Murgia, S., Naumann-Godo, M., Nishino, S., Nolan, P. L., Norris, J. P., Nuss, E., Ohsugi, T., Okumura, A., Omodei, N., Orlando, E., Ormes, J. F., Ozaki, M., Paneque, D., Pavlidou, V., Pelassa, V., Pepe, M., Pesce-Rollins, M., Pierbattista, M., Piron, F., Porter, T. A., Rainò, S., Razzano, M., Readhead, A., Reimer, A., Reimer, O., Richards, J. L., Romani, R. W., Sadrozinski, H. F.-W., Scargle, J. D., Sgrò, C., Siskind, E. J., Smith, P. D., Spandre, G., Spinelli, P., Strickman, M. S., Suson, D. J., Takahashi, H., Tanaka, T., Taylor, G. B., Thayer, J. G., Thayer, J. B., Thompson, D. J., Torres, D. F., Tosti, G., Tramacere, A., Troja, E., Vandenbroucke, J., Vianello, G., Vitale, V., Waite, A. P., Wang, P., Winer, B. L., Wood, K. S., Yang, Z., and Ziegler, M. (2011a). The Radio/Gamma-Ray Connection in Active Galactic Nuclei in the Era of the Fermi Large Area Telescope. *ApJ*, 741:30.
- [Ackermann et al., 2011b] Ackermann, M., Ajello, M., Allafort, A., Antolini, E., Atwood, W. B., Axelsson, M., Baldini, L., Ballet, J., Barbiellini, G., Bastieri, D., Bechtol, K., Bellazzini, R., Berenji, B., Blandford, R. D., Bloom, E. D., Bonamente, E., Borgland, A. W., Bottacini, E., Bouvier, A., Bregeon, J., Brigida, M., Bruel, P., Buehler, R., Burnett, T. H., Buson, S., Caliendo, G. A., Cameron, R. A., Caraveo, P. A., Casandjian, J. M., Cavazzuti, E., Cecchi, C., Charles, E., Cheung, C. C., Chiang, J., Ciprini, S., Claus, R., Cohen-Tanugi, J., Conrad, J., Costamante, L., Cutini, S., de Angelis, A., de Palma, F., Dermer, C. D., Digel, S. W., Silva, E. d. C. e., Drell, P. S., Dubois, R., Escande, L., Favuzzi, C., Fegan, S. J., Ferrara, E. C., Finke, J., Focke, W. B., Fortin, P., Frailis, M., Fukazawa, Y., Funk, S., Fusco, P., Gargano, F., Gasparrini, D., Gehrels, N., Germani, S., Giebels, B., Giglietto, N., Giommi, P., Giordano, F., Giroletti, M., Glanzman, T., Godfrey, G., Grenier, I. A., Grove, J. E., Guiriec, S., Gustafsson, M., Hadasch, D., Hayashida, M., Hays, E., Healey, S. E., Horan, D., Hou, X., Hughes, R. E., Iafate, G., Jóhannesson, G., Johnson, A. S., Johnson, W. N., Kamae, T., Katagiri, H., Kataoka, J., Knödlseeder, J., Kuss, M., Lande, J., Larsson, S., Latronico, L., Longo, F., Loparco, F., Lott, B., Lovellette, M. N., Lubrano, P., Madejski, G. M., Mazziotta, M. N., McConville, W., McEnery, J. E., Michelson, P. F., Mitthumsiri, W., Mizuno, T., Moiseev, A. A., Monte, C., Monzani, M. E., Moretti, E., Morselli, A., Moskalenko, I. V., Murgia, S., Nakamori, T., Naumann-Godo, M., Nolan, P. L., Norris, J. P., Nuss, E., Ohno, M., Ohsugi, T., Okumura, A., Omodei, N., Orienti, M., Orlando, E., Ormes, J. F., Ozaki, M., Paneque, D., Parent, D., Pesce-Rollins, M., Pierbattista, M., Piranomonte, S., Piron, F., Pivato, G., Porter, T. A., Rainò, S., Rando, R., Razzano, M., Razzaque, S., Reimer, A., Reimer, O., Ritz, S., Rochester, L. S., Romani, R. W., Roth, M., Sanchez, D. A., Sbarra, C., Scargle, J. D., Schalk, T. L., Sgrò, C., Shaw, M. S., Siskind, E. J., Spandre, G., Spinelli, P., Strong, A. W., Suson, D. J., Tajima, H., Takahashi, H., Takahashi, T., Tanaka, T., Thayer, J. G., Thayer, J. B., Thompson, D. J., Tibaldo, L., Tinivella, M., Torres, D. F., Tosti, G., Troja, E., Uchiyama, Y.,

- Vandenbroucke, J., Vasileiou, V., Vianello, G., Vitale, V., Waite, A. P., Wallace, E., Wang, P., Winer, B. L., Wood, D. L., Wood, K. S., and Zimmer, S. (2011b). The Second Catalog of Active Galactic Nuclei Detected by the Fermi Large Area Telescope. *ApJ*, 743:171.
- [Aharonian et al., 2002] Aharonian, F. et al. (2002). *A&A*, 393:89.
- [Aharonian et al., 2003] Aharonian, F. et al. (2003). *A&A*, 410:813.
- [Aharonian et al., 2005] Aharonian, F. et al. (2005). *A&A*, 437:95.
- [Aharonian et al., 1997] Aharonian, F. A., Hofmann, W., Konopelko, A. K., and Völk, H. J. (1997). The potential of ground based arrays of imaging atmospheric Cherenkov telescopes. I. Determination of shower parameters. *Astroparticle Physics*, 6:343–368.
- [Albert et al., 2007a] Albert, J. et al. (2007a). *ApJ*, 663:125.
- [Albert et al., 2007b] Albert, J. et al. (2007b). *Nucl. Instr. Meth.*, A583:494.
- [Aleksić et al., 2012a] Aleksić, J., Alvarez, E. A., Antonelli, L. A., Antoranz, P., Asensio, M., Backes, M., Barrio, J. A., Bastieri, D., Becerra González, J., Bednarek, W., Berdyugin, A., Berger, K., Bernardini, E., Biland, A., Blanch, O., Bock, R. K., Boller, A., Bonoli, G., Borla Tridon, D., Braun, I., Bretz, T., Cañellas, A., Carmona, E., Carosi, A., Colin, P., Colombo, E., Contreras, J. L., Cortina, J., Cossio, L., Covino, S., Dazzi, F., de Angelis, A., de Caneva, G., de Cea Del Pozo, E., de Lotto, B., Delgado Mendez, C., Diago Ortega, A., Doert, M., Domínguez, A., Dominis Prester, D., Dorner, D., Doro, M., Elsaesser, D., Ferenc, D., Fonseca, M. V., Font, L., Fruck, C., García López, R. J., Garczarczyk, M., Garrido, D., Giavitto, G., Godinović, N., Hadasch, D., Häfner, D., Herrero, A., Hildebrand, D., Höhne-Mönch, D., Hose, J., Hrupec, D., Huber, B., Jogler, T., Kellermann, H., Klepser, S., Krähenbühl, T., Krause, J., La Barbera, A., Lelas, D., Leonardo, E., Lindfors, E., Lombardi, S., López, M., López-Oramas, A., Lorenz, E., Makariev, M., Maneva, G., Mankuzhiyil, N., Mannheim, K., Maraschi, L., Mariotti, M., Martínez, M., Mazin, D., Meucci, M., Miranda, J. M., Mirzoyan, R., Miyamoto, H., Moldón, J., Moralejo, A., Munar-Adrover, P., Nieto, D., Nilsson, K., Orito, R., Oya, I., Paneque, D., Paoletti, R., Pardo, S., Paredes, J. M., Partini, S., Pasanen, M., Pauss, F., Perez-Torres, M. A., Persic, M., Peruzzo, L., Pilia, M., Pochon, J., Prada, F., Prada Moroni, P. G., Prandini, E., Puljak, I., Reichardt, I., Reinthal, R., Rhode, W., Ribó, M., Rico, J., Rügamer, S., Saggion, A., Saito, K., Saito, T. Y., Salvati, M., Satalecka, K., Scalzotto, V., Scapin, V., Schultz, C., Schweizer, T., Shayduk, M., Shore, S. N., Sillanpää, A., Sitarek, J., Snidaric, I., Sobczynska, D., Spanier, F., Spiro, S., Stamatescu, V., Stamerra, A., Steinke, B., Storz, J., Strah, N., Surić, T., Takalo, L., Takami, H., Tavecchio, F., Temnikov, P., Terzić, T., Tesaro, D., Teshima, M., Tibolla, O., Torres, D. F., Treves, A., Uellenbeck, M., Vankov, H., Vogler, P., Wagner, R. M., Weitzel, Q., Zabalza, V., Zandanel, F., and Zanin, R. (2012a). Performance of the MAGIC stereo system obtained with Crab Nebula data. *Astroparticle Physics*, 35:435–448.
- [Aleksić et al., 2012b] Aleksić, J., Alvarez, E. A., Antonelli, L. A., Antoranz, P., Asensio, M., Backes, M., Barrio, J. A., Bastieri, D., Becerra González, J., Bednarek, W., Berdyugin, A.,

Berger, K., Bernardini, E., Biland, A., Blanch, O., Bock, R. K., Boller, A., Bonnoli, G., Borla Tridon, D., Braun, I., Bretz, T., Cañellas, A., Carmona, E., Carosi, A., Colin, P., Colombo, E., Contreras, J. L., Cortina, J., Cossio, L., Covino, S., Dazzi, F., De Angelis, A., De Caneva, G., De Cea del Pozo, E., De Lotto, B., Delgado Mendez, C., Diago Ortega, A., Doert, M., Domínguez, A., Dominis Prester, D., Dorner, D., Doro, M., Elsaesser, D., Ferenc, D., Fonseca, M. V., Font, L., Fruck, C., García López, R. J., Garczarczyk, M., Garrido, D., Giavitto, G., Godinović, N., Hadasch, D., Häfner, D., Herrero, A., Hildebrand, D., Höhne-Mönch, D., Hose, J., Hrupec, D., Huber, B., Jogler, T., Kellermann, H., Klepser, S., Krähenbühl, T., Krause, J., La Barbera, A., Lelas, D., Leonardo, E., Lindfors, E., Lombardi, S., López, A., López, M., Lorenz, E., Makariev, M., Maneva, G., Mankuzhiyil, N., Mannheim, K., Maraschi, L., Mariotti, M., Martínez, M., Mazin, D., Meucci, M., Miranda, J. M., Mirzoyan, R., Miyamoto, H., Moldón, J., Moralejo, A., Munar-Adrover, P., Nieto, D., Nilsson, K., Orito, R., Oya, I., Paneque, D., Paoletti, R., Pardo, S., Paredes, J. M., Partini, S., Pasanen, M., Pauss, F., Perez-Torres, M. A., Persic, M., Peruzzo, L., Pilia, M., Pochon, J., Prada, F., Prada Moroni, P. G., Prandini, E., Puljak, I., Reichardt, I., Reinthal, R., Rhode, W., Ribó, M., Rico, J., Rügamer, S., Saggion, A., Saito, K., Saito, T. Y., Salvati, M., Satalecka, K., Scalzotto, V., Scapin, V., Schultz, C., Schweizer, T., Shayduk, M., Shore, S. N., Sillanpää, A., Sitarek, J., Sobczynska, D., Spanier, F., Spiro, S., Stamerra, A., Steinke, B., Storz, J., Strah, N., Surić, T., Takalo, L., Takami, H., Tavecchio, F., Temnikov, P., Terzić, T., Tescaro, D., Teshima, M., Tibolla, O., Torres, D. F., Treves, A., Uellenbeck, M., Vankov, H., Vogler, P., Wagner, R. M., Weitzel, Q., Zabalza, V., Zandanel, F., and Zanin, R. (2012b). Mrk 421 active state in 2008: the MAGIC view, simultaneous multi-wavelength observations and SSC model constrained. *A&A*, 542:A100.

[Aleksić et al., 2012c] Aleksić, J., Alvarez, E. A., Antonelli, L. A., Antoranz, P., Asensio, M., Backes, M., Barrio, J. A., Bastieri, D., Becerra González, J., Bednarek, W., Berdyugin, A., Berger, K., Bernardini, E., Biland, A., Blanch, O., Bock, R. K., Boller, A., Bonnoli, G., Borla Tridon, D., Braun, I., Bretz, T., Cañellas, A., Carmona, E., Carosi, A., Colin, P., Colombo, E., Contreras, J. L., Cortina, J., Cossio, L., Covino, S., Dazzi, F., de Angelis, A., de Caneva, G., de Cea Del Pozo, E., de Lotto, B., Delgado Mendez, C., Diago Ortega, A., Doert, M., Domínguez, A., Dominis Prester, D., Dorner, D., Doro, M., Elsaesser, D., Ferenc, D., Fonseca, M. V., Font, L., Fruck, C., García López, R. J., Garczarczyk, M., Garrido, D., Giavitto, G., Godinović, N., Hadasch, D., Häfner, D., Herrero, A., Hildebrand, D., Höhne-Mönch, D., Hose, J., Hrupec, D., Huber, B., Jogler, T., Kellermann, H., Klepser, S., Krähenbühl, T., Krause, J., La Barbera, A., Lelas, D., Leonardo, E., Lindfors, E., Lombardi, S., López, M., López-Oramas, A., Lorenz, E., Makariev, M., Maneva, G., Mankuzhiyil, N., Mannheim, K., Maraschi, L., Mariotti, M., Martínez, M., Mazin, D., Meucci, M., Miranda, J. M., Mirzoyan, R., Miyamoto, H., Moldón, J., Moralejo, A., Munar-Adrover, P., Nieto, D., Nilsson, K., Orito, R., Oya, I., Paneque, D., Paoletti, R., Pardo, S., Paredes, J. M., Partini, S., Pasanen, M., Pauss, F., Perez-Torres, M. A., Persic, M., Peruzzo, L., Pilia, M., Pochon, J., Prada, F., Prada Moroni, P. G., Prandini, E., Puljak, I., Reichardt, I., Reinthal, R., Rhode, W., Ribó, M., Rico, J., Rügamer, S., Saggion, A., Saito, K., Saito, T. Y., Salvati, M., Satalecka, K., Scalzotto, V., Scapin, V., Schultz, C., Schweizer, T., Shayduk, M., Shore, S. N., Sillanpää, A., Sitarek,

- J., Snidaric, I., Sobczynska, D., Spanier, F., Spiro, S., Stamatescu, V., Stamerra, A., Steinke, B., Storz, J., Strah, N., Surić, T., Takalo, L., Takami, H., Tavecchio, F., Temnikov, P., Terzić, T., Tesaro, D., Teshima, M., Tibolla, O., Torres, D. F., Treves, A., Uellenbeck, M., Vankov, H., Vogler, P., Wagner, R. M., Weitzel, Q., Zabalza, V., Zandanel, F., and Zanin, R. (2012c). Performance of the MAGIC stereo system obtained with Crab Nebula data. *Astroparticle Physics*, 35:435–448.
- [Aller et al., 1985] Aller, H. D., Aller, M. F., Latimer, G. E., and Hodge, P. E. (1985). Spectra and linear polarizations of extragalactic variable sources at centimeter wavelengths. *ApJS*, 59:513–768.
- [Asano et al., 2014] Asano, K., Takahara, F., Kusunose, M., Toma, K., and Kakuwa, J. (2014). Time-dependent Models for Blazar Emission with the Second-order Fermi Acceleration. *ApJ*, 780:64.
- [Atwood et al., 2009] Atwood, W. B., Abdo, A. A., Ackermann, M., Althouse, W., Anderson, B., Axelsson, M., Baldini, L., Ballet, J., Band, D. L., Barbiellini, G., and et al. (2009). The Large Area Telescope on the Fermi Gamma-Ray Space Telescope Mission. *ApJ*, 697:1071–1102.
- [Bartoli et al., 2013] Bartoli, B., Bernardini, P., Bi, X. J., Bolognino, I., Branchini, P., Budano, A., Calabrese Melcarne, A. K., Camarri, P., Cao, Z., Cardarelli, R., Catalanotti, S., Chen, S. Z., Chen, T. L., Creti, P., Cui, S. W., Dai, B. Z., D’Amone, A., Danzengluobu, De Mitri, I., D’Ettore Piazzoli, B., Di Girolamo, T., Di Sciascio, G., Feng, C. F., Feng, Z., Feng, Z., Gou, Q. B., Guo, Y. Q., He, H. H., Hu, H., Hu, H., Iacovacci, M., Iuppa, R., Jia, H. Y., Labaciren, Li, H. J., Liguori, G., Liu, C., Liu, J., Liu, M. Y., Lu, H., Ma, X. H., Mancarella, G., Mari, S. M., Marsella, G., Martello, D., Mastroianni, S., Montini, P., Ning, C. C., Panareo, M., Panico, B., Perrone, L., Pistilli, P., Ruggieri, F., Salvini, P., Santonico, R., Sbrano, S. N., Shen, P. R., Sheng, X. D., Shi, F., Surdo, A., Tan, Y. H., Vallania, P., Vernetto, S., Vigorito, C., Wang, H., Wu, C. Y., Wu, H. R., Xue, L., Yan, Y. X., Yang, Q. Y., Yang, X. C., Yao, Z. G., Yuan, A. F., Zha, M., Zhang, H. M., Zhang, L., Zhang, X. Y., Zhang, Y., Zhaxiciren, Zhaxisangzhu, Zhou, X. X., Zhu, F. R., Zhu, Q. Q., and Zizzi, G. (2013). Medium scale anisotropy in the TeV cosmic ray flux observed by ARGO-YBJ. *Phys. Rev. D*, 88(8):082001.
- [Bhattacharjee and Sigl, 2000] Bhattacharjee, P. and Sigl, G. (2000). *Phys.Rept.*, 327:109.
- [Błażejowski, 2005] Błażejowski (2005). *ApJ*, 630:130.
- [Bloom and Marscher, 1996] Bloom, S. D. and Marscher, A. P. (1996). An Analysis of the Synchrotron Self-Compton Model for the Multi-Wave Band Spectra of Blazars. *ApJ*, 461:657.
- [Bock et al., 2001] Bock, R. K. et al. (2001). *Nuclear Instruments and Methods in Physics Research A*, 516:511.
- [Boettcher et al., 2012] Boettcher, M., Harris, D. E., and Krawczynski, H., editors (2012). *Relativistic Jets from Active Galactic Nuclei*. WILEY-VCH.

- [Bradt et al., 1993] Bradt, H. V., Rothschild, R. E., and Swank, J. H. (1993). X-ray timing explorer mission. *A&AS*, 97:355–360.
- [Brigida and Fermi LAT Collaboration, 2011] Brigida, M. and Fermi LAT Collaboration (2011). Moon and quiet Sun detection with Fermi-LAT observatory. *Nuclear Instruments and Methods in Physics Research A*, 630:140–142.
- [Burrows et al., 2005] Burrows, D. N., Hill, J. E., Nousek, J. A., Kennea, J. A., Wells, A., Osborne, J. P., Abbey, A. F., Beardmore, A., Mukerjee, K., Short, A. D. T., Chincarini, G., Campana, S., Citterio, O., Moretti, A., Pagani, C., Tagliaferri, G., Giommi, P., Capalbi, M., Tamburelli, F., Angelini, L., Cusumano, G., Bräuninger, H. W., Burkert, W., and Hartner, G. D. (2005). The Swift X-Ray Telescope. *Space Sci. Rev.*, 120:165–195.
- [Celotti and Ghisellini, 2008] Celotti, A. and Ghisellini, G. (2008). The power of blazar jets. *MNRAS*, 385:283–300.
- [Cogan, 2006] Cogan, P. (2006). PhD thesis, School of Physics, University College Dublin.
- [Daniel, 2008] Daniel, M. K. (2008). The VERITAS standard data analysis. *International Cosmic Ray Conference*, 3:1325–1328.
- [de Mello Neto and Pierre Auger Collaboration, 2013] de Mello Neto, J. and Pierre Auger Collaboration (2013). Anisotropy studies with the Pierre Auger Observatory. *Journal of Physics Conference Series*, 409(1):012108.
- [de Vaucouleurs et al., 1991] de Vaucouleurs, G., de Vaucouleurs, A., Corwin, Jr., H. G., Buta, R. J., Paturel, G., and Fouqué, P. (1991). *Third Reference Catalogue of Bright Galaxies. Volume I: Explanations and references. Volume II: Data for galaxies between 0^h and 12^h. Volume III: Data for galaxies between 12^h and 24^h.*
- [Dermer and Schlickeiser, 1993] Dermer, C. D. and Schlickeiser, R. (1993). Model for the High-Energy Emission from Blazars. *ApJ*, 416:458.
- [Domínguez et al., 2011] Domínguez, A. et al. (2011). *MNRAS*, 410:2556.
- [Donato et al., 2001] Donato, D., Ghisellini, G., Tagliaferri, G., and Fossati, G. (2001). Hard X-ray properties of blazars. *A&A*, 375:739–751.
- [Finke et al., 2008a] Finke, J. D., Dermer, C. D., and Böttcher, M. (2008a). Synchrotron Self-Compton Analysis of TeV X-Ray-Selected BL Lacertae Objects. *ApJ*, 686:181–194.
- [Finke et al., 2008b] Finke, J. D., Dermer, C. D., and Böttcher, M. (2008b). Synchrotron Self-Compton Analysis of TeV X-Ray-Selected BL Lacertae Objects. *ApJ*, 686:181–194.
- [Finke and Razzaque, 2010] Finke, J. D. and Razzaque, S. (2010). *ApJ*, 712:238.
- [Fitzpatrick, 1999] Fitzpatrick, E. L. (1999). Correcting for the Effects of Interstellar Extinction. *PASP*, 111:63–75.

- [Fomin et al., 1994] Fomin, V. P., Fennell, S., Lamb, R. C., Lewis, D. A., Punch, M., and Weekes, T. C. (1994). New methods of atmospheric Cherenkov imaging for gamma-ray astronomy. II. The differential position method. *Astroparticle Physics*, 2:151–159.
- [Fossati et al., 2008] Fossati, G. et al. (2008). *ApJ*, 677:906.
- [Franceschini et al., 2008] Franceschini, A. et al. (2008). *A&A*, 487:837.
- [Fukugita et al., 1995] Fukugita, M., Shimasaku, K., and Ichikawa, T. (1995). *PASP*, 107:945.
- [Fukushima et al., 2013] Fukushima, M. et al. (2013). TA anisotropy summary. *International Cosmic Ray Conference*.
- [Gaidos et al., 1996] Gaidos, J. A., Akerlof, C. W., Biller, S., Boyle, P. J., Breslin, A. C., Buckley, J. H., Carter-Lewis, D. A., Catanese, M., Cawley, M. F., Fegan, D. J., Finley, J. P., Gordo, J. B., Hillas, A. M., Krennrich, F., Lamb, R. C., Lessard, R. W., McEnery, J. E., Masterson, C., Mohanty, G., Moriarty, P., Quinn, J., Rodgers, A. J., Rose, H. J., Samuelson, F., Schubnell, M. S., Sembroski, G. H., Srinivasan, R., Weekes, T. C., Wilson, C. L., and Zweerink, J. (1996). Extremely rapid bursts of TeV photons from the active galaxy Markarian 421. *Nature*, 383:319–320.
- [Georganopoulos and Kazanas, 2003] Georganopoulos, M. and Kazanas, D. (2003). Decelerating Flows in TeV Blazars: A Resolution to the BL Lacertae-FR I Unification Problem. *ApJ*, 594:L27–L30.
- [Ghisellini, 2013] Ghisellini, G., editor (2013). *Radiative Processes in High Energy Astrophysics*, volume 873 of *Lecture Notes in Physics*, Berlin Springer Verlag.
- [Ghisellini et al., 1998] Ghisellini, G., Celotti, A., Fossati, G., Maraschi, L., and Comastri, A. (1998). A theoretical unifying scheme for gamma-ray bright blazars. *MNRAS*, 301:451–468.
- [Ghisellini et al., 2005] Ghisellini, G., Tavecchio, F., and Chiaberge, M. (2005). Structured jets in TeV BL Lac objects and radiogalaxies. Implications for the observed properties. *A&A*, 432:401–410.
- [Gini, 1921] Gini, C. (1921). *Economic Journal*, 31:22.
- [Gorham, 2005] Gorham, P. (2005). 1st International Workshop on the Saltdome Shower Array (SalSA), SLAC.
- [Greisen, 1966] Greisen, K. (1966). End to the cosmic ray spectrum? *Phys. Rev. Lett.*, 16:748.
- [Gruppen, 2005] Gruppen, C. (2005). *Astroparticle Physics*.
- [Hillas, 1985a] Hillas, A. M. (1985a). Cherenkov light images of EAS produced by primary gamma. *International Cosmic Ray Conference*, 3:445–448.

- [Hillas, 1985b] Hillas, A. M. (1985b). Cerenkov light images of EAS produced by primary gamma. *International Cosmic Ray Conference*, 3:445–448.
- [Holder, 2012] Holder, J. (2012). TeV gamma-ray astronomy: A summary. *Astroparticle Physics*, 39:61–75.
- [Horan et al., 2009] Horan, D. et al. (2009). *ApJ*, 695:596.
- [Kalberla et al., 2005] Kalberla, P. M. W., Burton, W. B., Hartmann, D., Arnal, E. M., Bajaja, E., Morras, R., and Pöppel, W. G. L. (2005). The Leiden/Argentine/Bonn (LAB) Survey of Galactic HI. Final data release of the combined LDS and IAR surveys with improved stray-radiation corrections. *A&A*, 440:775–782.
- [Katarzyński et al., 2005] Katarzyński, K., Ghisellini, G., Tavecchio, F., Maraschi, L., Fossati, G., and Mastichiadis, A. (2005). *A&A*, 433:479.
- [Katarzyński et al., 2003] Katarzyński, K., Sol, H., and Kus, A. (2003). *A&A*, 410:101.
- [Kildea et al., 2007] Kildea, J., Atkins, R. W., Badran, H. M., Blaylock, G., Bond, I. H., Bradbury, S. M., Buckley, J. H., Carter-Lewis, D. A., Celik, O., Chow, Y. C. K., Cui, W., Cogan, P., Daniel, M. K., de la Calle Perez, I., Dowdall, C., Duke, C., Falcone, A. D., Fegan, D. J., Fegan, S. J., Finley, J. P., Fortson, L. F., Gall, D., Gillanders, G. H., Grube, J., Gutierrez, K. J., Hall, J., Hall, T. A., Holder, J., Horan, D., Hughes, S. B., Jordan, M., Jung, I., Kenny, G. E., Kertzman, M., Knapp, J., Konopelko, A., Kosack, K., Krawczynski, H., Krennrich, F., Lang, M. J., LeBohec, S., Lloyd-Evans, J., Millis, J., Moriarty, P., Nagai, T., Ogden, P. A., Ong, R. A., Perkins, J. S., Petry, D., Pizlo, F., Pohl, M., Quinn, J., Quinn, M., Rebillot, P. F., Rose, H. J., Schroedter, M., Sembroski, G. H., Smith, A. W., Syson, A., Toner, J. A., Valcarcel, L., Vassiliev, V. V., Wakely, S. P., Weekes, T. C., and White, R. J. (2007). The Whipple Observatory 10 m gamma-ray telescope, 1997–2006. *Astroparticle Physics*, 28:182–195.
- [Kneiske et al., 2004] Kneiske, T. M., Bretz, T., Mannheim, K., and Hartmann, D. H. (2004). *A&A*, 413:807.
- [Komissarov and Falle, 1997] Komissarov, S. S. and Falle, S. A. E. G. (1997). Simulations of Superluminal Radio Sources. *MNRAS*, 288:833–848.
- [Krawczynski et al., 2006] Krawczynski, H., Carter-Lewis, D. A., Duke, C., Holder, J., Maier, G., Le Bohec, S., and Sembroski, G. (2006). Gamma hadron separation methods for the VERITAS array of four imaging atmospheric Cherenkov telescopes. *Astroparticle Physics*, 25:380–390.
- [Krennrich et al., 2002] Krennrich, F., Bond, I. H., Bradbury, S. M., Buckley, J. H., Carter-Lewis, D. A., Cui, W., de la Calle Perez, I., Fegan, D. J., Fegan, S. J., Finley, J. P., Gaidos, J. A., Gibbs, K., Gillanders, G. H., Hall, T. A., Hillas, A. M., Holder, J., Horan, D., Jordan, M., Kertzman, M., Kieda, D., Kildea, J., Knapp, J., Kosack, K., Lang, M. J., LeBohec, S., Moriarty, P., Müller, D., Ong, R. A., Pallassini, R., Petry, D., Quinn, J., Reay, N. W., Reynolds,

- P. T., Rose, H. J., Sembroski, G. H., Sidwell, R., Stanton, N., Swordy, S. P., Vassiliev, V. V., Wakely, S. P., and Weekes, T. C. (2002). Discovery of Spectral Variability of Markarian 421 at TeV Energies. *ApJ*, 575:L9–L13.
- [Lefa et al., 2011] Lefa, E., Rieger, F. M., and Aharonian, F. (2011). Formation of Very Hard Gamma-Ray Spectra of Blazars in Leptonic Models. *ApJ*, 740:64.
- [Li and Ma, 1983] Li, T. P. and Ma, Y. Q. (1983). Analysis methods for results in γ -ray astronomy. *Astrophys. Journal*, 272:317.
- [Lin et al., 1992] Lin, Y. C., Bertsch, D. L., Chiang, J., Fichtel, C. E., Hartman, R. C., Hunter, S. D., Kanbach, G., Kniffen, D. A., Kwok, P. W., Mattox, J. R., Mayer-Hasselwander, H. A., Michelson, P. F., von Montigny, C., Nolan, P. L., Pinkau, K., Schneid, E., Sreekumar, P., and Thompson, D. J. (1992). Detection of high-energy gamma-ray emission from the BL Lacertae object Markarian 421 by the EGRET telescope on the Compton Observatory. *ApJ*, 401:L61–L64.
- [Maier et al., 2005] Maier, G., Antoni, T., Apel, W. D., Badea, A. F., Bekk, K., Bercuci, A., Blümer, H., Bozdog, H., Brancus, I. M., Büttner, C., Chilingarian, A., Daumiller, K., Doll, P., Engel, R., Engler, J., Feßler, F., Gils, H. J., Glasstetter, R., Haungs, A., Heck, D., Hörandel, J. R., Kampert, K.-H., Klages, H. O., Mathes, H. J., Mayer, H. J., Milke, J., Müller, M., Obenland, R., Oehlschläger, J., Ostapchenko, S., Petcu, M., Rebel, H., Risse, A., Risse, M., Roth, M., Schatz, G., Schieler, H., Scholz, J., Thouw, T., Ulrich, H., van Buren, J., Vardanyan, A., Weindl, A., Wochele, J., and Zabierowski, J. (2005). Cosmic Ray Anisotropy with the KASCADE Experiment. *International Journal of Modern Physics A*, 20:6840–6842.
- [Mankuzhiyil et al., 2011] Mankuzhiyil, N., Ansoldi, S., Persic, M., and Tavecchio, F. (2011). The Environment and Distribution of Emitting Electrons as a Function of Source Activity in Markarian 421. *ApJ*, 733:14.
- [Mannheim, 1993] Mannheim, K. (1993). The proton blazar. *A&A*, 269:67–76.
- [Maraschi et al., 1999] Maraschi, L., Fossati, G., Tavecchio, F., Chiappetti, L., Celotti, A., Ghisellini, G., Grandi, P., Pian, E., Tagliaferri, G., Treves, A., Breslin, A. C., Buckley, J. H., Carter-Lewis, D. A., Catanese, M., Cawley, M. F., Fegan, D. J., Fegan, S., Finley, J., Gaidos, J., Hall, T., Hillas, A. M., Krennrich, F., Lessard, R. W., Masterson, C., Moriarty, P., Quinn, J., Rose, J., Samuelson, F., Weekes, T. C., Urry, C. M., and Takahashi, T. (1999). Simultaneous X-Ray and TEV Observations of a Rapid Flare from Markarian 421. *ApJ*, 526:L81–L84.
- [Maraschi et al., 1992] Maraschi, L., Ghisellini, G., and Celotti, A. (1992). A jet model for the gamma-ray emitting blazar 3C 279. *ApJ*, 397:L5–L9.
- [Marscher, 2014] Marscher, A. P. (2014). Turbulent, Extreme Multi-zone Model for Simulating Flux and Polarization Variability in Blazars. *ApJ*, 780:87.

- [Mattox et al., 1996] Mattox, J. R., Bertsch, D. L., Chiang, J., Dingus, B. L., Digel, S. W., Esposito, J. A., Fierro, J. M., Hartman, R. C., Hunter, S. D., Kanbach, G., Kniffen, D. A., Lin, Y. C., Macomb, D. J., Mayer-Hasselwander, H. A., Michelson, P. F., von Montigny, C., Mukherjee, R., Nolan, P. L., Ramanamurthy, P. V., Schneid, E., Sreekumar, P., Thompson, D. J., and Willis, T. D. (1996). The Likelihood Analysis of EGRET Data. *ApJ*, 461:396.
- [Moralejo et al., 2009] Moralejo, A., Gaug, M., Carmona, E., Colin, P., Delgado, C., Lombardi, S., Mazin, D., Scalzotto, V., Sitarek, J., Tescaro, D., and for the MAGIC collaboration (2009). MARS, the MAGIC Analysis and Reconstruction Software. *ArXiv e-prints*.
- [Mücke et al., 2003] Mücke, A., Protheroe, R. J., Engel, R., Rachen, J. P., and Stanev, T. (2003). BL Lac objects in the synchrotron proton blazar model. *Astroparticle Physics*, 18:593–613.
- [Nilsson et al., 2007] Nilsson, K. et al. (2007). *A&A*, 475:199.
- [Nolan et al., 2012] Nolan, P. L., Abdo, A. A., Ackermann, M., Ajello, M., Allafort, A., Antolini, E., Atwood, W. B., Axelsson, M., Baldini, L., Ballet, J., and et al. (2012). Fermi Large Area Telescope Second Source Catalog. *ApJS*, 199:31.
- [Okumura et al., 2002] Okumura, K., Asahara, A., Bicknell, G. V., Edwards, P. G., Enomoto, R., Gunji, S., Hara, S., Hara, T., Hayashi, S., Itoh, C., Kabuki, S., Kajino, F., Katagiri, H., Kataoka, J., Kawachi, A., Kifune, T., Kubo, H., Kushida, J., Maeda, S., Maeshiro, A., Matsubara, Y., Mizumoto, Y., Mori, M., Moriya, M., Muraishi, H., Muraki, Y., Naito, T., Nakase, T., Nishijima, K., Ohishi, M., Patterson, J. R., Sakurazawa, K., Suzuki, R., Swaby, D. L., Takano, K., Takano, T., Tanimori, T., Tokanai, F., Tsuchiya, K., Tsunoo, H., Uruma, K., Watanabe, A., Yanagita, S., Yoshida, T., and Yoshikoshi, T. (2002). Observation of Gamma Rays Greater than 10 TeV from Markarian 421. *ApJ*, 579:L9–L12.
- [Perkins et al., 2009] Perkins, J. S., Maier, G., and The VERITAS Collaboration (2009). VERITAS Telescope 1 Relocation: Details and Improvements. *ArXiv e-prints*.
- [Piner et al., 2010] Piner, B. G., Pant, N., and Edwards, P. G. (2010). The Jets of TeV Blazars at Higher Resolution: 43 GHz and Polarimetric VLBA Observations from 2005 to 2009. *ApJ*, 723:1150–1167.
- [Poole et al., 2008] Poole, T. S., Breeveld, A. A., Page, M. J., Landsman, W., Holland, S. T., Roming, P., Kuin, N. P. M., Brown, P. J., Gronwall, C., Hunsberger, S., Koch, S., Mason, K. O., Schady, P., vanden Berk, D., Blustin, A. J., Boyd, P., Broos, P., Carter, M., Chester, M. M., Cucchiara, A., Hancock, B., Huckle, H., Immler, S., Ivanushkina, M., Kennedy, T., Marshall, F., Morgan, A., Pandey, S. B., de Pasquale, M., Smith, P. J., and Still, M. (2008). Photometric calibration of the Swift ultraviolet/optical telescope. *MNRAS*, 383:627–645.
- [Poutanen et al., 2008] Poutanen, J., Zdziarski, A. A., and Ibragimov, A. (2008). Superorbital variability of X-ray and radio emission of Cyg X-1 - II. Dependence of the orbital modulation and spectral hardness on the superorbital phase. *MNRAS*, 389:1427–1438.

- [Punch et al., 1992] Punch, M., Akerlof, C. W., Cawley, M. F., Chantell, M., Fegan, D. J., Fennell, S., Gaidos, J. A., Hagan, J., Hillas, A. M., Jiang, Y., Kerrick, A. D., Lamb, R. C., Lawrence, M. A., Lewis, D. A., Meyer, D. I., Mohanty, G., O’Flaherty, K. S., Reynolds, P. T., Rovero, A. C., Schubnell, M. S., Sembroski, G., Weekes, T. C., and Wilson, C. (1992). Detection of TeV photons from the active galaxy Markarian 421. *Nature*, 358:477.
- [Rebillot et al., 2006] Rebillot, P. F., Badran, H. M., Blaylock, G., Bradbury, S. M., Buckley, J. H., Carter-Lewis, D. A., Celik, O., Chow, Y. C., Cogan, P., Cui, W., Daniel, M., Duke, C., Falcone, A., Fegan, S. J., Finley, J. P., Fortson, L. F., Gillanders, G. H., Grube, J., Gutierrez, K., Gyuk, G., Hanna, D., Holder, J., Horan, D., Hughes, S. B., Kenny, G. E., Kertzman, M., Kieda, D., Kildea, J., Kosack, K., Krawczynski, H., Krennrich, F., Lang, M. J., Le Bohec, S., Linton, E., Maier, G., Moriarty, P., Perkins, J., Pohl, M., Quinn, J., Ragan, K., Reynolds, P. T., Rose, H. J., Schroedter, M., Sembroski, G. H., Steele, G., Swordy, S. P., Valcarcel, L., Vassiliev, V. V., Wakely, S. P., Weekes, T. C., Zweerink, J., VERITAS Collaboration, Aller, M., Aller, H., Boltwood, P., Jung, I., Kranich, D., Nilsson, K., Pasanen, M., Sadun, A., and Sillanpaa, A. (2006). Multiwavelength Observations of the Blazar Markarian 421 in 2002 December and 2003 January. *ApJ*, 641:740–751.
- [Richards et al., 2011] Richards, J. L., Max-Moerbeck, W., Pavlidou, V., King, O. G., Pearson, T. J., Readhead, A. C. S., Reeves, R., Shepherd, M. C., Stevenson, M. A., Weintraub, L. C., Fuhrmann, L., Angelakis, E., Zensus, J. A., Healey, S. E., Romani, R. W., Shaw, M. S., Grainge, K., Birkinshaw, M., Lancaster, K., Worrall, D. M., Taylor, G. B., Cotter, G., and Bustos, R. (2011). Blazars in the Fermi Era: The OVRO 40 m Telescope Monitoring Program. *ApJS*, 194:29.
- [Roming et al., 2005] Roming, P. W. A., Kennedy, T. E., Mason, K. O., Nousek, J. A., Ahr, L., Bingham, R. E., Broos, P. S., Carter, M. J., Hancock, B. K., Huckle, H. E., Hunsberger, S. D., Kawakami, H., Killough, R., Koch, T. S., McLelland, M. K., Smith, K., Smith, P. J., Soto, J. C., Boyd, P. T., Breeveld, A. A., Holland, S. T., Ivanushkina, M., Pryzby, M. S., Still, M. D., and Stock, J. (2005). The Swift Ultra-Violet/Optical Telescope. *Space Sci. Rev.*, 120:95–142.
- [Schlegel et al., 1998] Schlegel, D. J., Finkbeiner, D. P., and Davis, M. (1998). Maps of Dust Infrared Emission for Use in Estimation of Reddening and Cosmic Microwave Background Radiation Foregrounds. *ApJ*, 500:525.
- [Schlickeiser, 1985] Schlickeiser, R. (1985). A viable mechanism to establish relativistic thermal particle distribution functions in cosmic sources. *A&A*, 143:431–434.
- [Shockley and Pierce, 1938] Shockley, W. and Pierce, J. R. (1938). A Theory of Noise for Electron Multipliers. *Proc. Inst. Radio Eng.*, 26:321.
- [Sokolov et al., 2004] Sokolov, A., Marscher, A. P., and McHardy, I. M. (2004). Synchrotron Self-Compton Model for Rapid Nonthermal Flares in Blazars with Frequency-dependent Time Lags. *ApJ*, 613:725–746.

- [Stawarz and Petrosian, 2008] Stawarz, Ł. and Petrosian, V. (2008). On the Momentum Diffusion of Radiating Ultrarelativistic Electrons in a Turbulent Magnetic Field. *ApJ*, 681:1725–1744.
- [Tagliaferri et al., 2008] Tagliaferri, G., Foschini, L., Ghisellini, G., Maraschi, L., Tosti, G., Albert, J., Aliu, E., Anderhub, H., Antoranz, P., Baixeras, C., Barrio, J. A., Bartko, H., Bastieri, D., Becker, J. K., Bednarek, W., Bedyugin, A., Berger, K., Bigongiari, C., Biland, A., Bock, R. K., Bordas, P., Bosch-Ramon, V., Bretz, T., Britvitch, I., Camara, M., Carmona, E., Chilingarian, A., Coarasa, J. A., Commichau, S., Contreras, J. L., Cortina, J., Costado, M. T., Curtef, V., Danielyan, V., Dazzi, F., De Angelis, A., Delgado, C., de los Reyes, R., De Lotto, B., Dorner, D., Doro, M., Errando, M., Fagiolini, M., Ferenc, D., Fernández, E., Firpo, R., Fonseca, M. V., Font, L., Fuchs, M., Galante, N., García-López, R. J., Garczarczyk, M., Gaug, M., Giller, M., Goebel, F., Hakobyan, D., Hayashida, M., Hengstebeck, T., Herrero, A., Höhne, D., Hose, J., Huber, S., Hsu, C. C., Jacon, P., Jogler, T., Kosyra, R., Kranich, D., Kritzer, R., Laille, A., Lindfors, E., Lombardi, S., Longo, F., López, M., Lorenz, E., Majumdar, P., Maneva, G., Mannheim, K., Mariotti, M., Martínez, M., Mazin, D., Merck, C., Meucci, M., Meyer, M., Miranda, J. M., Mirzoyan, R., Mizobuchi, S., Moralejo, A., Nieto, D., Nilsson, K., Ninkovic, J., Oña-Wilhelmi, E., Otte, N., Oya, I., Panniello, M., Paoletti, R., Paredes, J. M., Pasanen, M., Pascoli, D., Pauss, F., Pegna, R., Persic, M., Peruzzo, L., Piccioli, A., Prandini, E., Puchades, N., Raymers, A., Rhode, W., Ribó, M., Rico, J., Rissi, M., Robert, A., Rügamer, S., Saggion, A., Saito, T. Y., Sánchez, A., Sartori, P., Scalzotto, V., Scapin, V., Schmitt, R., Schweizer, T., Shayduk, M., Shinozaki, K., Shore, S. N., Sidro, N., Sillanpää, A., Sobczynska, D., Spanier, F., Stamerra, A., Stark, L. S., Takalo, L., Tavecchio, F., Temnikov, P., Tesaro, D., Teshima, M., Torres, D. F., Turini, N., Vankov, H., Venturini, A., Vitale, V., Wagner, R. M., Wibig, T., Wittek, W., Zandanel, F., Zanin, R., Zapatero, J., and MAGIC Collaboration (2008). Simultaneous Multiwavelength Observations of the Blazar 1ES 1959+650 at a Low TeV Flux. *ApJ*, 679:1029–1039.
- [Takami, 2011] Takami (2011). *MNRAS*, 413:1845.
- [Tavecchio et al., 1998] Tavecchio, F., Maraschi, L., and Ghisellini, G. (1998). Constraints on the Physical Parameters of TeV Blazars. *ApJ*, 509:608–619.
- [Teraesranta et al., 1998] Teraesranta, H., Tornikoski, M., Mujunen, A., Karlamaa, K., Valtonen, T., Henelius, N., Urpo, S., Lainela, M., Pursimo, T., Nilsson, K., Wiren, S., Lahteenmaeki, A., Korpi, M., Rekola, R., Heinaemaeki, P., Hanski, M., Nurmi, P., Kokkonen, K., Keinaenen, P., Joutsamo, O., Oksanen, J., Pietilae, H., Valtaoja, E., Valtonen, M., and Koenonen, P. (1998). Fifteen years monitoring of extragalactic radio sources at 22, 37 and 87 GHz. *A&AS*, 132:305–331.
- [Torres and Anchordoqui, 2004] Torres, D. and Anchordoqui, L. (2004). *Rep. Prog. Phys.*, 67:1663–1730.
- [Vaughan et al., 2003] Vaughan, S. et al. (2003). *MNRAS*, 345:1271.

- [Villata et al., 2009] Villata, M., Raiteri, C. M., Gurwell, M. A., Larionov, V. M., Kurtanidze, O. M., Aller, M. F., Lähteenmäki, A., Chen, W. P., Nilsson, K., Agudo, I., Aller, H. D., Arkharov, A. A., Bach, U., Bachev, R., Beltrame, P., Benítez, E., Buemi, C. S., Böttcher, M., Calcidese, P., Capezzali, D., Carosati, D., da Rio, D., di Paola, A., Dolci, M., Dultzin, D., Forné, E., Gómez, J. L., Hagen-Thorn, V. A., Halkola, A., Heidt, J., Hiriart, D., Hovatta, T., Hsiao, H.-Y., Jorstad, S. G., Kimeridze, G. N., Konstantinova, T. S., Kopatskaya, E. N., Koptelova, E., Leto, P., Ligustri, R., Lindfors, E., Lopez, J. M., Marscher, A. P., Mommert, M., Mujica, R., Nikolashvili, M. G., Palma, N., Pasanen, M., Roca-Sogorb, M., Ros, J. A., Roustazadeh, P., Sadun, A. C., Saino, J., Sigua, L. A., Sorcia, M., Takalo, L. O., Tornikoski, M., Trigilio, C., Turchetti, R., and Umama, G. (2009). The GASP-WEBT monitoring of 3C 454.3 during the 2008 optical-to-radio and γ -ray outburst. *A&A*, 504:L9–L12.
- [Villata et al., 1998] Villata, M., Raiteri, C. M., Lanteri, L., Sobrito, G., and Cavallone, M. (1998). BVR photometry of comparison stars in selected blazar fields. I. Photometric sequences for 10 BL Lacertae objects. *A&AS*, 130:305–310.
- [Villata et al., 2008] Villata, M., Raiteri, C. M., Larionov, V. M., Kurtanidze, O. M., Nilsson, K., Aller, M. F., Tornikoski, M., Volvach, A., Aller, H. D., Arkharov, A. A., Bach, U., Beltrame, P., Bhatta, G., Buemi, C. S., Böttcher, M., Calcidese, P., Carosati, D., Castro-Tirado, A. J., da Rio, D., di Paola, A., Dolci, M., Forné, E., Frasca, A., Hagen-Thorn, V. A., Heidt, J., Hiriart, D., Jelínek, M., Kimeridze, G. N., Konstantinova, T. S., Kopatskaya, E. N., Lanteri, L., Leto, P., Ligustri, R., Lindfors, E., Lähteenmäki, A., Marilli, E., Nieppola, E., Nikolashvili, M. G., Pasanen, M., Ragozzine, B., Ros, J. A., Sigua, L. A., Smart, R. L., Sorcia, M., Takalo, L. O., Tavani, M., Trigilio, C., Turchetti, R., Uckert, K., Umama, G., Vercellone, S., and Webb, J. R. (2008). Multifrequency monitoring of the blazar 0716+714 during the GASP-WEBT-AGILE campaign of 2007. *A&A*, 481:L79–L82.
- [Weekes et al., 2002] Weekes, T. C., Badran, H., Biller, S. D., Bond, I., Bradbury, S., Buckley, J., Carter-Lewis, D., Catanese, M., Criswell, S., Cui, W., Dowkontt, P., Duke, C., Fegan, D. J., Finley, J., Fortson, L., Gaidos, J., Gillanders, G. H., Grindlay, J., Hall, T. A., Harris, K., Hillas, A. M., Kaaret, P., Kertzman, M., Kieda, D., Krennrich, F., Lang, M. J., LeBohec, S., Lessard, R., Lloyd-Evans, J., Knapp, J., McKernan, B., McEnery, J., Moriarty, P., Muller, D., Ogden, P., Ong, R., Petry, D., Quinn, J., Reay, N. W., Reynolds, P. T., Rose, J., Salamon, M., Sembroski, G., Sidwell, R., Slane, P., Stanton, N., Swordy, S. P., Vassiliev, V. V., and Wakely, S. P. (2002). VERITAS: the Very Energetic Radiation Imaging Telescope Array System. *Astroparticle Physics*, 17:221–243.
- [Zanin, 2011] Zanin, R. (2011). MAGIC measurement of the Crab Nebula spectrum over three decades in energy. *International Cosmic Ray Conference*, 7:71.
- [Zatsepin and Kuzmin, 1966] Zatsepin, G. T. and Kuzmin, V. A. (1966). Upper limit of the spectrum of cosmic rays. *JETP Lett*, 4:78.
- [Zier and Biermann, 2002] Zier, C. and Biermann, P. L. (2002). *A&A*, 396:91.